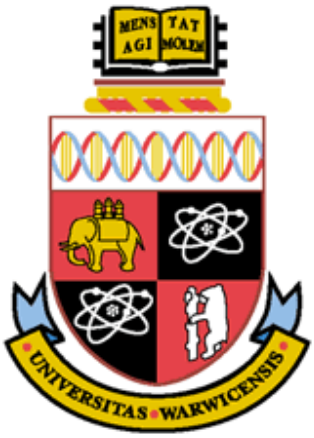

Mathematical Modelling and Analysis of Cerebrospinal Mechanics: An Investigation Into the Pathogenesis of Syringomyelia

Novak Samuel Jon Elliott

BSc(Hons) BE(Hons) MBiomedE

This report is submitted as partial fulfilment

of the requirements for the PhD Programme of the

School of Engineering

University of Warwick

August 2009

THE UNIVERSITY OF
WARWICK

AUTHOR: **Novak Samuel Jon Elliott** DEGREE: **PhD**

TITLE: **Mathematical Modelling and Analysis of Cerebrospinal Mechanics: An Investigation Into the Pathogenesis of Syringomyelia**

DATE OF DEPOSIT: .....

I agree that this thesis shall be available in accordance with the regulations governing the University of Warwick theses.

I agree that the summary of this thesis may be submitted for publication.

I **agree** that the thesis may be photocopied (single copies for study purposes only).

Theses with no restriction on photocopying will also be made available to the British Library for microfilming. The British Library may supply copies to individuals or libraries. subject to a statement from them that the copy is supplied for non-publishing purposes. All copies supplied by the British Library will carry the following statement:

> "Attention is drawn to the fact that the copyright of this thesis rests with its author. This copy of the thesis has been supplied on the condition that anyone who consults it is understood to recognise that its copyright rests with its author and that no quotation from the thesis and no information derived from it may be published without the author's written consent."

AUTHOR'S SIGNATURE: .....

USER'S DECLARATION

1. I undertake not to quote or make use of any information from this thesis without making acknowledgement to the author.
2. I further undertake to allow no-one else to use this thesis while it is in my care.

DATE SIGNATURE ADDRESS

.....

.....

.....

.....

.....

This thesis is dedicated to the memory of Professor Peter Carpenter who taught me to challenge accepted wisdom in the pursuit of scientific rigour.

Abstract

Syringomyelia is a disease in which fluid-filled cavities, called syrinxes, form in the spinal cord causing progressive loss of sensory and motor functions. Invasive monitoring of pressure waves in the spinal subarachnoid space implicates a hydrodynamic origin. Poor treatment outcomes have led to myriad hypotheses for its pathogenesis, which unfortunately are often based on small numbers of patients due to the relative rarity of the disease. However, only recently have models begun to appear based on the principles of mechanics. One such model is the mathematically rigorous work of Carpenter and colleagues. They suggest that a pressure wave due to a cough or sneeze could form a shock-like elastic jump, which when incident at a stenosis, such as a hindbrain tonsil, would generate a transient region of high pressure within the spinal cord and lead to fluid accumulation. The salient physiological parameters of this model are reviewed from the literature and the assumptions and predictions re-evaluated from a mechanical standpoint. It is found that, while the spinal geometry does allow for elastic jumps to occur, their effects are likely to be weak and subsumed by the small amounts of damping that have been measured in the subarachnoid space. The analysis presented here does not support the elastic-jump hypothesis for syrinx formation. Furthermore, the site of maximum transpial pressure differential due to a cough-induced pulse is most likely to be at the site of pulse origin—not,

as supposed, at a distant reflection site. This suggests that there must be some other localising factor more critical to providing the necessary conditions for syrinx formation. Two coaxial tube models are developed that incorporate Darcy's law separately in the pial membrane and the spinal cord tissue. It is shown that permeability plays opposing roles in the spinal cord and pia for wave attenuation; the propagation of a pressure wave is aided by a less-permeable pia but a more-permeable spinal cord. This may have implications in a syringomyelic cord. To understand the dynamic interaction of the fluid and solid components of the spinal cord tissue Biot's theory of poroelasticity is employed. It is concluded that physiological frequencies are probably too low for poroelastic dissipation to be of significance in such a soft and weak material as the spinal cord. Accumulating evidence in the last decade from animal studies implicates arterial pulsations in syrinx formation. In particular, Bilston and colleagues suggested that a phase difference between the pressure pulse in the spinal subarachnoid space and the perivascular spaces, due to a pathologically disturbed blood supply, could result in a net influx of cerebrospinal fluid into the spinal cord. A lumped-parameter model is developed of the cerebrospinal system to investigate this conjecture. It is found that although this phase-lag mechanism may operate, it requires the spinal cord to have an intrinsic storage capacity due to the collapsibility of the contained venous reservoir. If this storage requirement is met then the results presented here suggest that, on mechanical grounds, a syringo-subarachnoid shunt may be a better surgical treatment option than a subarachnoid bypass for post-traumatic syringomyelia.

Keywords: syringomyelia, syrinx formation, collapsible tubes, pressure waves, poroelasticity, lumped-parameter

List of Publications

Parts of this work were presented in the following publications.

Articles in refereed journals

Elliott, N.S.J., Lockerby, D.A. & Brodbelt, A.R. (2009) The pathogenesis of syringomyelia: a re-evaluation of the elastic jump hypothesis, *Journal of Biomechanical Engineering*, **131**(4): 044503-1–6.

Published conference papers

Elliott, N.S.J., Carpenter, P.W. & Brodbelt, A.R. (2007) The role of pial permeability on pressure wave propagation in a model of syringomyelia, *Proceedings of the International Symposium Syringomyelia 2007 Abstracts of Free Papers*, Rugby, U.K., 24 Oct; published in *British Journal of Neurosurgery*, **21**(5):430.

Elliott, N.S.J., Lockerby, D.A. & Brodbelt, A.R. (Paper accepted) A lumped-parameter model of the cerebrospinal system for simulating syringomyelia, *Proceedings of the 2009 Micro and Nano Flows Conference*, London, U.K., 1–2 Sep.

Elliott, N.S.J., Lockerby, D.A. & Brodbelt, A.R. (Paper accepted) Arterial-pulsation driven flow in syringomyelia—A lumped-parameter model, *Proceedings of the 2009 World Congress on Medical Physics and Biomedical Engineering*, Munich, Germany, 7–12 Sep.

Conference posters

Elliott, N.S.J. & Carpenter, P.W. (2006) Pressure propagation in the spinal cord and the origins of syringomyelia, *World Congress on Medical Physics & Biomedical Engineering*, Seoul, South Korea, 27 Aug–1 Sept.

Elliott, N.S.J. & Carpenter, P.W. (2007) Modelling syringomyelia using wave propagation in collapsible tubes, *Fifth Physiological Flow Network Meeting*, Imperial College, University of London, 3–4 September.

Carpenter, P.W. & Elliott, N.S.J. (2007) A simple biomechanical model for syringomyelia, *Syringomyelia International Symposium*, Rugby, United Kingdom, 24–26 October.

Talks / Colloquia

Elliott, N.S.J. (2006) Pressure-wave propagation in the spinal cord and the origins of syringomyelia, *Post-graduate Student Colloquium*, School of Engineering, University of Warwick, Coventry, U.K., 14 June.

Elliott, N.S.J. & Carpenter, P.W. (2006) Pressure waves in the spinal cord and the origins of syringomyelia, *Fluid Dynamics Research Group Seminar*, Department of Mechanical Engineering, Curtin University, Perth, Australia, 15 December. [Invited]

Elliott, N.S.J. & Carpenter, P.W. (2007) Coughing up a storm: syringomyelia and wave propagation in the spinal cord, *Workshop on Computation of Biomedical Processes*, Simula Research Laboratory, Oslo, Norway, 11 June. [Invited, expenses paid]

Acknowledgements

During my PhD project I have been fortunate enough to receive invaluable advice, encouragement and inspiration from many people, to whom I would like to say "thank you". There isn't room enough here to list the names of everyone but in particular I would like to mention (in alphabetical order): Chris Bertram, Mark Brend, Andrew Brodbelt, Peter Carpenter, Mark Evernden, Matthias Heil, Richard Howell, James Jewkes, Duncan Lockerby, Tony Lucey, Bryn Martin, Astrid Nordin, Mark Pitman, Sarah Waters and Robert Whittaker. To my family, friends and fellow PhD students, you have been an endless source of support and I thank you all for your time.

I would also like to acknowledge the following institutions and people for funding my research: Graduate School, University of Warwick (Warwick Postgraduate Research Fellowship, Overseas Research Student Award); School of Engineering, University of Warwick (Postgraduate Bursaries, from the School itself and from Duncan Lockerby); Royal Academy of Engineers (International Travel Grant for attending the World Congress on Medical Physics & Biomedical Engineering 2006), Physiological Flow Network (Travel Bursary for attending the Fifth Physiological Flow Network Meeting) and Simula Research Laboratory (expenses paid for an invited presentation at the Workshop on Computation of Biomedical Processes 2007).

Contents

List of Tables

List of Figures

List of Acronyms

CC ..... central canal

CSF ..... cerebrospinal fluid

ECF ..... extracellular fluid

FT ..... filum terminale

ICP ..... intracranial pressure

ISF ..... interstitial fluid

MRI ..... magnetic resonance imaging

PVS ..... perivascular space(s)

SC ..... spinal cord

SSS ..... spinal subarachnoid space

Part I

Problem Definition & Background

Synopsis

This Part commences by defining syringomyelia and describing available treatment options and the current prognosis for sufferers (Chapter 1). A brief account of the salient anatomy and physiology is given which builds a picture of the biomechanical system. This sets the context for a review of the pathogenesis hypotheses proposed to date (Chapter 2). Finally, having established the current state of research, the particulars are given for the methods that were chosen in this investigation.

CHAPTER 1

Introduction

"Syringomyelia is in general considered to be a slowly progressive degenerative disease, the outlook of which is in the long run hopeless" — Boman & Iivanainen (1967; p.61).

1.1 Disease definition

Syringomyelia[1] is a disease in which fluid-filled cavities, called *syrinxes*, form and enlarge within the spinal cord (SC); an example is shown in Fig. 1.1(a) and (b). The progressive expansion of these syrinxes over many years compresses the surrounding nerve fibres and blood vessels, which is associated with neurological damage. The classical clinical sign of a syrinx is a dissociated sensory loss—loss of pain and temperature sensation with preservation of light touch and proprioception. Since the SC connects the brain to nerves in the extremities this damage usually affects the arms and legs. The specific location of function impairment coincides with the location of nerve root damage in the SC and, as syrinxes are typically found in the neck region, damage more commonly affects the arms. The wasting away of muscle is common, as are headaches, and lower-limb paralysis may ensue as a late-stage debilitation. Some of these effects

[1]The word derives from the Latin root syrinx which in itself comes from the Greek *surinx*, meaning 'musical pan pipe', together with the Greek root *muelos*, meaning 'marrow, innermost or essential part'. One can thus make the analogy between a syrinx of the muelos to an elongated cavity (pipe) of the spinal cord (marrow). The more commonly accepted plural of syrinx is *syrinxes* (Oxford English Dictionary) but some sources advocate *syringes* (e.g., Stedman's Medical Dictionary).

(a)

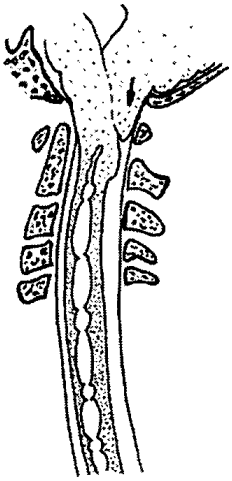

(b)

(c)

(d)

Fig. 1.1: (a) Magnetic resonance imaging scan showing a syrinx and associated Chiari malformation; (b) schematic interpretation; (c) patient with syringomyelia showing severe muscular wasting and lateral curvature of the spine; (d) hands of the same patient. Panels (c) and (d) reproduced from Curschmann (1894), Plates 18 and 21, respectively.

can be seen in Fig. 1.1(c) and (d).

Syringomyelia is rare[2] with prevalence estimates ranging from 8.4 to 85 cases per

[2]In the E. U. a rare disease is defined to have a prevalence of less than 5 per 10 000 (European Commission, 2004) equating to approximately 246 000 persons; similarly in the U. S. A. a prevalence of less than 200 000 individuals qualifies as a rare disease (Rare Diseases Act of 2002) which is equivalent to less that 7 per 10 000 in 2009.

100 000 (Brewis *et al.*, 1966; Speer *et al.*, 2003; respectively). When associated with a congenital defect, the disease usually appears in the third or fourth decade of life, with a mean age of onset of around 30 years (Brickell *et al.*, 2006). Rarely, syringomyelia may develop in childhood or late adulthood, except following traumatic injury to the SC. Surgical treatment often relieves some symptoms, such as headaches and stiffness, but irreversible cord damage means that the more severe impairments like weakness and paralysis tend to persist (Levine, 2004). The prognosis is especially bleak for patients with spinal injuries—reported cases demonstrate that only half will improve after treatment (Brodbelt, Stoodley, Watling, Tu, Burke & Jones, 2003). Clinical evidence suggests that syrinx formation has a mechanical basis but despite much conjecture the pathogenesis of syringomyelia remains unknown.

1.2 Anatomy and physiology

The salient features of the human cerebrospinal system are now given. Except where specific articles are cited, this section is compiled from standard medical reference works (Gray, 1918; Marieb, 2000; Crossman & Neary, 2001; Martin, 2003; England & Wakeley, 2006).

The SC lies within the upper two thirds of the vertebral canal and is continuous above with the hindbrain (functionally divided into the medulla oblongata, pons and cerebellum) and the midbrain, which connects to the hemispheres of the forebrain (the brain proper) upon entering the skull. The SC and brain are collectively referred to as the central nervous system. The length of the SC is about 40–45 cm and has a mass of approximately 30 g. The SC receives information from, and controls, the trunk and limbs. This is achieved through 31 pairs of spinal nerves, which join the cord at intervals along its length. From top to bottom there are eight pairs of cervical nerves (C1–C8), twelve thoracic (T1–T12), five lumbar (L1–L5), five sacral (S1–S5) and one coccygeal (Co1). As a consequence of the relative inequality in rates of growth of the SC and vertebral column, the nerve roots in the lumbar and sacral regions descend

almost vertically to reach their exit points. Their appearance has been likened to that of a horses tail and consequently these nerves are collectively referred to as the cauda equina.

The central nervous system is supported and protected by the bones of the vertebral column and skull. Within this bony casing they are entirely ensheathed by three layers of membranes—non-nervous tissue called the meninges (Fig. 1.2). The outermost membrane is the dura mater, a fibrous inelastic coat that surrounds the brain and SC like a loose-fitting bag. The cranial dura is fused to the skull whereas the spinal dura is lubricated by the contents of the epidural space to allow articulation of the spine. Beneath the dura lies the arachnoid mater, the two sometimes being separated by a thin subdural space that is created by the separation of the arachnoid from the dura as the result of trauma or some ongoing pathological process. The arachnoid is a translucent, collagenous membrane, named for its likeness to a spider's web. Like the dura, the arachnoid loosely envelops the brain and SC. The innermost of the meninges is the pia mater, a delicate membrane of microscopic thickness that is firmly adherent to the surface of the brain and SC, closely following their contours. The pia membrane is perforated by all the blood vessels as they enter or leave the central nervous system. At the lower end the SC tapers into a cone and the pia continues as the filum terminale (FT), a ligament that extends through the dural sheath and anchors to the first segment of the coccyx.

The brain and SC have a highly heterogeneous structure in terms of the distribution of nerve cell bodies and their fibres. Some regions are relatively enriched in nerve cell bodies (e.g., the central portion of the SC and the surface of the brain hemispheres) and are referred to as grey matter. Other regions contain mostly nerve fibres. These are often ensheathed in myelin, an electrical insulator, which confers a paler colouration hence the term white matter. The grey and white matter constitute the functional tissue of the central nervous system and thus may be referred to as its parenchyma.

Between the arachnoid and the pia is the subarachnoid space, traversed by delicate fibrous trabeculae and filled with cerebrospinal fluid (CSF). The enlargement of the

subarachnoid space between the conical end of the SC and the lower extent of the FT is referred to as the lumbar cistern. Since the pia mater immediately adheres to the surface of the brain and spinal cord, the space is greatly widened wherever the brain surface exhibits a deep depression. There are three of these widenings around the level of the *craniocervical junction*, where the spine articulates with the skull, which are named the cisterna magna, the pontine cistern and the interpeduncular cistern. The subarachnoid space is continuous with the four cavities of the brain, called ventricles, where most CSF is produced. The choroid plexuses are small proliferations of blood vessels that secrete CSF causing it to flow from the pair of lateral ventricles down through the third and into the fourth ventricle, from where it exits the brain into the subarachnoid space, flowing around the SC and brain and finally being reabsorbed into the blood by the thin membranes of the arachnoid villi that protrude into the cranial subarachnoid space. A significant proportion of CSF is also probably absorbed around cranial nerves into the lymphatic system (Brodbelt & Stoodley, 2007). Since CSF is derived from blood plasma it is essentially water with some proteins, salts and sugars added (Bloomfield *et al.*, 1998). CSF is produced at a rate of around 500 ml/day in human adults (Bradbury, 1993) and, as the storage vessels only have a collective volume of about 150 ml (35 ml from the ventricles and the balance mainly from the subarachnoid space and lumbar cistern; Brodbelt & Stoodley, 2007), the CSF reservoir must be renewed several times daily (Nolte, 2002). The SC also contains an internal fluid space, the central canal (CC), which is often thought of as a spinal equivalent to the cranial ventricles. However, recent studies have demonstrated that—although this narrow passageway, which extends the length of the SC, evolves with an opening to the fourth ventricle above called the obex—the entire canal all but disappears by adult age (e.g., Milhorat *et al.*, 1994). Moreover, CSF production within the SC has not been proven. CSF provides a hydraulic cushion for the brain and SC and also functions as a medium for the exchange of substances between the brain and the rest of the body.

The brain receives its blood supply from the internal carotid and the vertebral arteries, which join together to form the circle of Willis on the base of the brain. The

vertebral arteries also supply the SC, reinforced by radicular arteries derived from segmental vessels. The arteries and veins serving the brain and SC run for part of their course in the subarachnoid space, perforating the pia to form a connection thus completing the circulatory loop. In the parenchyma the *central arteries* reside within tubular sheaths that extend inward from the pial surface, and the intervening annular cavities are called *perivascular spaces* (PVS)[3]. The PVS contain the same fluid that occupies the spaces between cells—*interstitial fluid* (ISF)—which is essentially water with a few salts and proteins. ISF has a similar make up to CSF, which is not surprising considering that the pial surface has leaky cellular junctions at the interface with the PVS; i.e., the PVS and the subarachnoid space are a single continuous fluid compartment (Rennels *et al.*, 1985; Stoodley *et al.*, 1996). In fact, it has been estimated that some 10–30% of the total CSF flow is associated with the bulk flow of cranial ISF, secreted from endothelial cells of the brain microvessels into the PVS (Redzic *et al.*, 2005). This is effectively flow through a porous medium—the cranial parenchyma. In addition to CSF, blood plasma may be filtered into the PVS through the permeable arterial walls (the so-called blood-brain barrier, which also applies to the SC) under the influence of a pressure or concentration gradient. This intravascular fluid is distinguished from ISF by its significantly higher protein concentration. The interstitial and intravascular fluids are collectively referred to as *extracellular fluid* (ECF), although curiously the term 'extracellular space' does not include the noncellular blood volume.

The heart and breathing cycles are transmitted to the CSF through the arteries and veins, respectively, superimposing a pulsatile component over the mean flow in the subarachnoid space and ventricles.

1.3 Pathology and treatment

Syringomyelia occurs in association with almost every other disorder of the SC (Table 1.1). Clinical analysis will usually reveal either an obstruction to CSF flow, teth-

[3]Also called Virchow-Robin spaces.

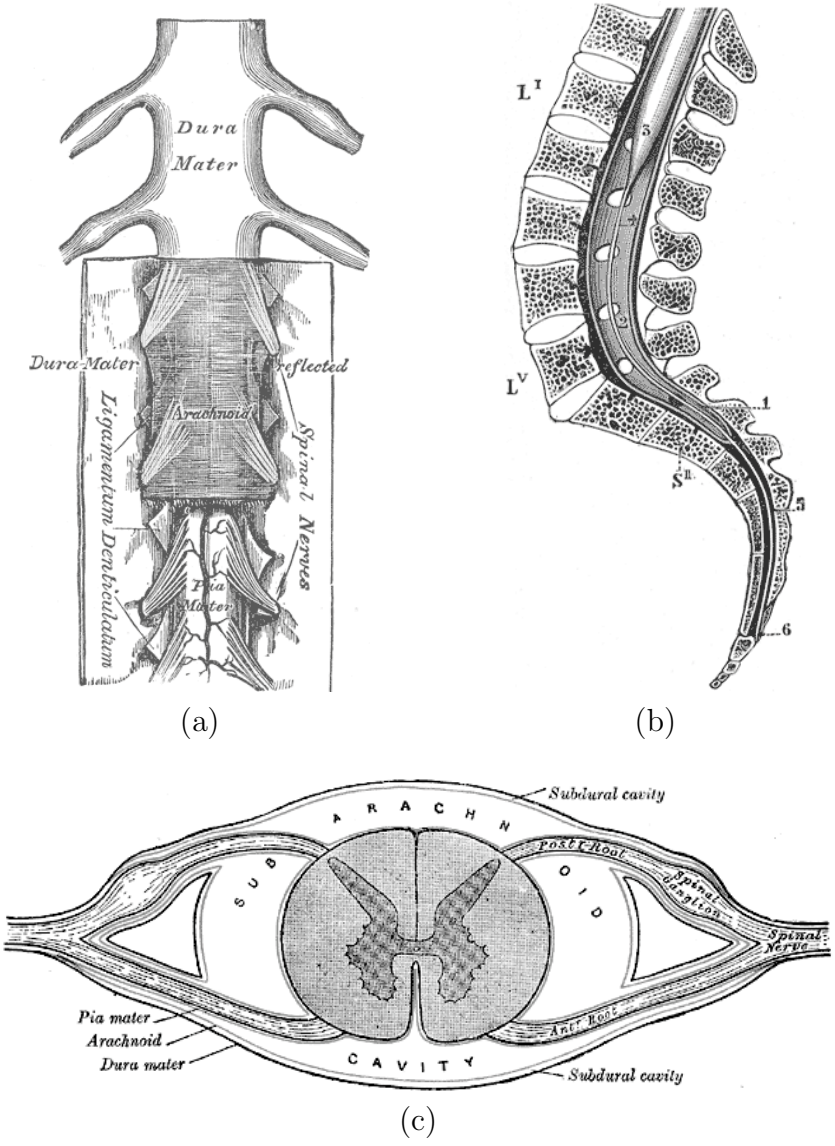

Fig. 1.2: Illustrations of the spinal cord anatomy. (a) longitudinal view showing the path of the spinal nerves through the dura, arachnoid and pia mater; (b) Midline section of the spinal canal showing the lower end of the SC and the filum terminale. Annotations: Li, Lv., first and fifth lumbar vertebrae; Sii, Second sacral vertebra; 1, dura mater; 2, lower part of tube of dura mater; 3, lower extremity of SC; 4, intradural, and 5, extradural portions of filum terminale; 6, attachment of filum terminale to first segment of coccyx. (c) Transverse section of the SC and its membranes. Panels (a), (b) and (c) reproduced from Gray (1918), Figures 767, 661 and 770, respectively.

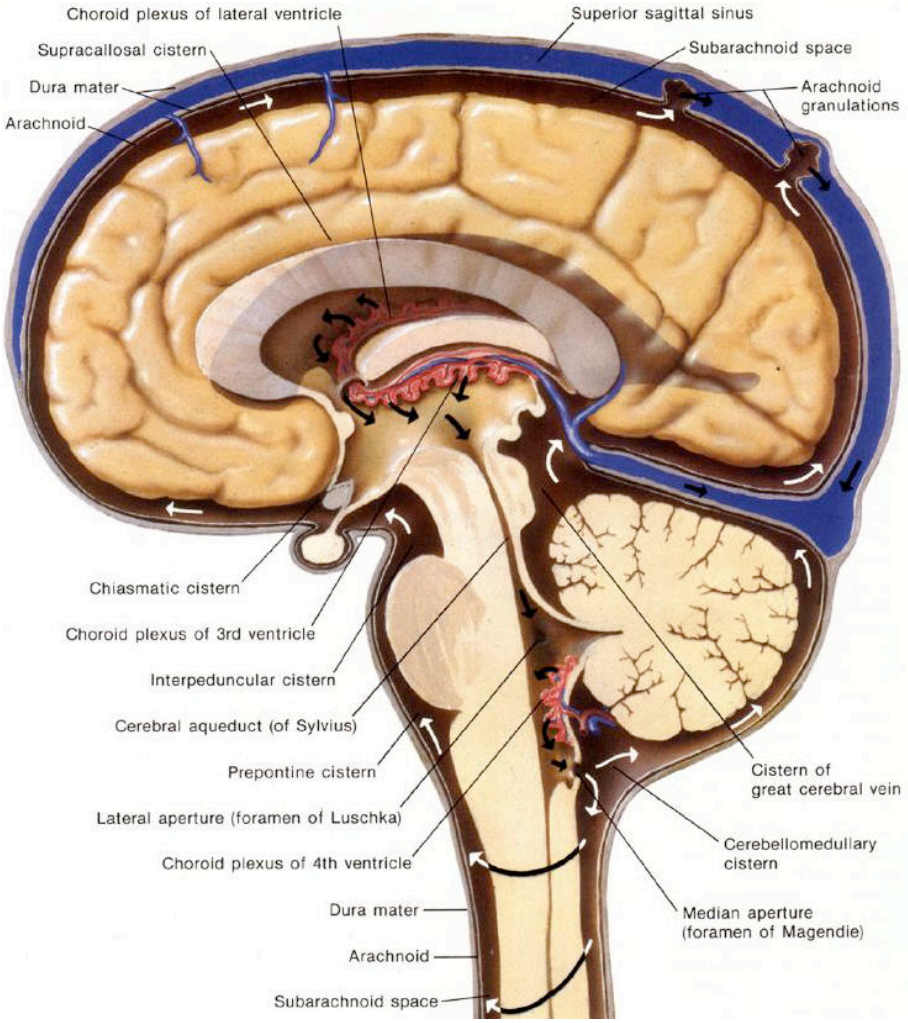

Fig. 1.3: The cerebrospinal fluid circulation. Reproduced from Rubin & Safdieh (2007; p. 87).

Table 1.1: Diseases that are known to occur in combination with syringomyelia. Adapted from Klekamp (2002).

	Spinal canal	Craniocervical junction
Malformations	**Spina bifida**: embryologic failure of fusion of one or more vertebral arches, often exposing SC	**Chiari**: downward displacement of hindbrain through the main aperture of the base of the skull
	Tethered cord syndrome: abnormal tissue attachments that stretch and limit the movement of the SC in the longitudinal direction	**Basilar invagination**: upward deformation of the base of the skull
	Diastematomyelia: splitting of the SC in the longitudinal direction	**Posterior fossa**: abnormalities of the cavity containing the brainstem
		Rhombencephalic: abnormalities of the hindbrain (lower brainstem)
Tumours	**Intramedullary**: within the SC	**Posterior fossa**: Within the cavity containing the brainstem
	Extramedullary: outside the SC but within the dura	**Supratentorial**: Above the cavity containing the brainstem
	Extradural: outside the dura	
Arachnoid pathologies	**Posttraumatic**: following a physical injury, either a direct wound or a concussion. **Postmenengitic**: following inflammation of the meninges, usually caused by viral or bacterial infection **Postsurgical**: following surgery, usually an invasive and/or reconstructive procedure **Posthaemorrhagic**: following internal bleeding	
Degenerations	**Disc disease**: dehydration of the intervertebral disc reducing the shock-absorbing capacity	
	Scoliosis: sideward curvature of the spine	
	Kyphosis: excessive forward curvature of the spine (hump-backed)	
	Spinal stenosis: blockage of the spinal subarachnoid space inhibiting/preventing CSF flow	

ering of the SC or a spinal tumour (Klekamp, 2002). Before the arrival of magnetic resonance imaging (MRI) in the 1980s the diagnosis of syringomyelia was difficult, if not impossible. Given the relative rarity of the disease, historically this has led to a plethora of hypotheses for the causes of the syringomyelia, often based on the autopsy findings of only a few patients. Today dynamic MR imaging (cardiac-gated cine-MRI) allows CSF flow not only to be visualised, facilitating diagnosis, but also to be measured, providing numerical data for validation of biomechanical models (e.g., Loth *et al.*, 2001; Martin *et al.*, 2005).

Syrinx cavities come in various shapes, sizes, locations and quantities, which to a large extent determines the physical signs of the disease. There may be a single oblong

cavity, or a large cavity may have several interconnected compartments, or a number of adjacent cavities may form, each separated by nervous tissue. Cavities may taper to a thin strand or have round, bulb-like ends. The syrinx may be a dilated CC communicating with the fourth ventricle, termed *communicating syringomyelia* (often called hydromyelia), or noncommunicating syrinxes may form in either isolated segments of the CC or the surrounding cord tissue, termed *noncommunicating syringomyelia*. Syringomyelia usually occurs in the cervical segments of the SC but can involve the entire length of the cord and occasionally progresses up into the brainstem (the frontal portion of the hindbrain and the midbrain; syringobulbia). Numerous classification schemes have been devised (e.g., Williams, 1990; Milhorat, 2000) but perhaps the most important mechanical division is in the terms of the hindbrain. From a database of 535 patients Williams (1990) found that about three quarters of all cases were associated with an Arnold-Chiari deformity, commonly referred to as a *Chiari malformation*. In this congenital disorder the hindbrain tonsils—the pair of rounded lobules on the undersurface of the cerebellum—protrude through the main aperture of the skull (foramen magnum), which tends to obstruct the entrance to the spinal subarachnoid space (SSS) and inhibit the flow of CSF between the spinal canal and the head. Chiari malformations are graded on a scale of I to IV according to the severity of the defects and related symptoms (Soleau *et al.*, 2007). Those cases graded as Chiari I commonly have noncommunicating syringomyelia with syrinxes being dilatations of the CC, while for the more severe Chiari II malformations the associated syringomyelia is usually communicating with the fourth ventricle. Chiari III and IV are very rare and need not be considered here. Of Williams's (1990) patients without hindbrain hernia most involved inflammation of the arachnoid membrane (arachnoiditis) due to a traumatic event to the spinal canal. Syrinxes in post-traumatic syringomyelia are typically noncommunicating and extracanalicular in nature. Arachnoiditis can lead to scar tissue formation that may also obstruct the SSS.

While the literature abounds with opposing theories for the pathogenesis of syringomyelia, there is considerably more agreement on the treatment. Most surgeons

today advocate that CSF flow obstructions and abnormal cord tethers should be removed—i.e., the fluid and solid mechanics should be returned to normal. This advice is based on favourable patient outcomes. In the case of a Chiari malformation the usual procedure is to remove a piece of the base of the skull and enlarge the dural sheath so as to decompress the hindbrain, thereby unblocking the fluid passage between the head and the spinal canal; most surgeons also open the arachnoid membrane, which may contain a fibrous band at this location (Brodbelt & Stoodley, 2003). If the exits to the fourth ventricle (foraminae of Luschka and Magendie) are blocked then these may be re-established, likewise any scar tissue blocking the SSS is usually cut out. Perforating the SC to drain a syrinx is common but not a universally accepted practice (Heiss *et al.*, 1999). An assortment of tubes (usually made from polyethylene, a thermoplastic) have been devised to shunt CSF around an obstruction, or to another part of the body (often to reduce CSF pressure, as in hydrocephalus), or to allow permanent syrinx drainage into the SSS.

1.4 The present investigation

In the next chapter a review is presented of the hypotheses for the pathogenesis of syringomyelia that have been proposed to date. By comparing human and animal observations with predictions from engineering models a set of requirements is established for syrinx formation based on the principles of mechanics. This leads to two proposed routes of investigation: pressure-wave propagation in the spinal canal using continuum approaches based on collapsible tubes and the theory of poroelasticity, and lumped-parameter modelling of the pressure-flow-rate characteristics of the craniospinal system.

The continuum modelling begins with a re-evaluation of the elastic jump hypothesis (Berkouk *et al.*, 2003; Carpenter *et al.*, 2003) in Chapter 3. This analysis leads to a closer look at the poroelastic nature of the SC in Chapter 4. As the distributed dynamics of the spinal canal do not appear to offer many clues as to a mechanism for

syrinx formation, a lumped-parameter model is developed in Chapter 5. Sensitivity studies for this model are performed in Chapter 6 which provide the foundations for simulating disease states and treatments in Chapter 7.

All of the results in Part II (chapters 3–7) are discussed in Chapter 8 with respect to the literature reviewed in Chapter 2. This dissertation draws to a close in Chapter 9 with concluding remarks and recommendations for further research. While the prognosis for sufferers of syringomyelia is still far from acceptable, it is shown that much insight can be gained through mathematical models and the outlook is far from "hopeless" as put by Boman & Iivanainen (1967).

CHAPTER 2

Literature review

"Discussion of the pathogenesis of syringomyelia involves considering the origin of the fluid and also the forces which cause that fluid to break down the structure of the cord." — Williams (1980; p. 805).

2.1 Overview

In this chapter a review is presented of the major pathogenesis hypotheses for syringomyelia that have been put forward over the last two centuries. These hypotheses are organised into *biological* and *biomechanical* categories, depending on whether the pathological process predominantly involves the living function or the mechanical interaction, of the anatomy, respectively; within each category hypotheses are placed in chronological order. Of course medicine and science doesn't evolve into such a discrete organisation so there is some overlap between the various theories. A number of reviews of syringomyelia have appeared in the medical literature which were particularly useful in compiling the biological-based hypotheses; e.g., Tauber & Langworthy (1935), Williams (1980) and Klekamp (2002). In contrast, engineering studies arrived relatively late on the scene and are reviewed here for the first time, focussing on their contribution to our understanding of the pathological mechanism of syringomyelia.

2.2 Biological-based hypotheses

2.2.1 Dysraphic hypotheses

In 1700 Brunner published a report on a newborn treated for syringomyelia. The syrinx was punctured but later the patient developed hydrocephalus, a condition in which CSF accumulates in the cerebral ventricles at high pressure, and died. The autopsy revealed that several of the vertebral arches had failed to fuse—a *dysraphic* state—allowing a bifurcating protrusion of the SC to form; i.e., spina bifida. The association of the syrinx with these congenital defects led Brunner to the conclusion that the syrinx either constituted a malformation in itself or had to be seen as part of the lumbosacral malformation complex. Likewise Morgagni (1769) observed syrinxes at the site of dysraphic malformations in adults and children, and half a century later Ollivier D'Angers (1827) reached similar conclusions to Brunner from his own experience.

Cleland elaborated on the dysraphic process propounding a defective development of the brainstem as being responsible for (what later became known as) the Chiari I malformation, which would lead to hydrocephalus, a dilated CC and its rupture into the herniated SC (Cleland, 1874; 1883). Although this concept is inherently biological in nature, Cleland believed that "structures are modified in their development by alterations in their mechanical relations", and considered four possible mechanisms:

1. *exposure* of one tissue to another,
2. *pressure* of fluids on tissues,
3. *exhaustion* of the tissue elements, and
4. *stretching* of tissues.

Over time, experience proved that syringomyelia may occur without such gross deformities. Following a similar line of reason Hinsdale (1897) proposed that syringomyelia constituted a developmental defect of the cells lining the CC (ependyma) and of the cells interspersed between the nerve fibres (glia). This argument was based

on microscale examinations (histology) that were thought to prove that a syrinx always started inside the CC; the overgrowth around the cyst wall (gliosis) was interpreted as degeneration of glial and ependymal cells. Thus the dysraphic concept of syringomyelia was transformed from the macro- to the microscale. However, a case of identical twins, with only one having syringomyelia, suggested that embryological abnormalities are probably not the cause—diseases of the derm plasm are usually found in both of identical twins (Tauber & Langworthy, 1935).

It is worth drawing to attention at this point that a syrinx is a fluid-filled cavity in the SC, which may be closed—as in a cyst—or have an open communication to another fluid compartment, such as the subarachnoid space. Thus the terms syrinx and cyst are not interchangeable.

2.2.2 Neoplastic hypotheses

Many thought that the role of a foetal disturbance in syringomyelia was to displace cells from their region of origin (a cell rest) which could then proliferate later on in life forming a glial *neoplasm*, more commonly known as a tumour. The tumour was thought to cavitate due to insufficient blood supply, thus the thickening (gliosis) around the syrinx wall was believed to be the remnants of the tumour (Virchow, 1863). The idea was popular in the German literature from the mid 1800s through to the late 1920s (Riley, 1930; and references therein). Some proponents of the neoplastic concept thought that the tumour could be acquired postnatally, negating the dysraphic element entirely (Simon, 1875; Hassin, 1920). Holmes & Kennedy (1909) believed that "a satisfactory pathological definition of syringomyelia can be scarcely given", and in a case involving both a syrinx and a tumour they thought it improbable that the tumour itself was a causal factor in the development of the syringomyelia. Rather, the two conditions were thought to arise independent from another, but perhaps from a common neoplastic defect in the central nervous system.

In whichever version of events the key feature was the neoplastic genesis of the

syrinx and this concept proved popular as it offered a form of treatment: radiotherapy. Reports began to appear in the literature of symptomatic improvement in the majority of so-treated patients (e.g., Delherm & Morel-Kahn, 1930). However, many remained sceptical. Grinker (1934), in his seminal monograph, stipulated that radiation may be useful but this form of therapy is difficult to evaluate since the disease progresses slowly with frequent stationary periods. Tauber & Langworthy (1935) analysed three cases and concluded that the cavity is surrounded by glial scar tissue rather than by tumour cells, making radiotherapy without any logical basis. Borysowicz (1967) agreed that radiotherapy was not an effective treatment for syringomyelia but still with a neoplastic mechanism in mind instead promoted the use of chemotherapy based on a study of 50 patients. Nevertheless, Borysowicz cautioned that "no prominent results of any treatment can be expected in a progressing and late recognized disease", citing small cohorts and short follow-up periods, amongst other factors, as impeding a definite and accurate evaluation of the obtained results of treatment.

Finally a 45-year study appeared which showed that radiotherapy made no difference to the long-term course of syringomyelia (Boman & Iivanainen, 1967). Although a few more retrospective studies appeared in favour of a neoplastic hypothesis (e.g., Ferry *et al.*, 1969), by the end of the 1960s radiotherapy was abandoned as a treatment strategy and the neoplastic concept lost favour. Notwithstanding, 50% or more of patients with a spinal cord tumour will have a syrinx (Klekamp *et al.*, 2001), suggesting that a tumour may contribute to syrinx formation by some other mechanism, such as obstruction of CSF pathways.

2.2.3 Ischaemic hypotheses

In parallel with the aforementioned theories, there was early speculation from post-mortem examinations that meningitis was accountable for venous obstruction and arterial clotting (thrombosis), which led to *ischaemic* damage of the SC and was presumed to have caused a subsequent syringomyelia (Charcot & Joffroy, 1869; Joffroy

& Achard, 1887). However, the first animal studies (canine) intended to corroborate meningitic ischaemia as a causative mechanism produced death of arachnoid cells and death of regions of SC tissue, effecting a softening of the SC (myelomalacia) rather than the cavitation characteristic of syringomyelia (e.g., Camus & Roussy, 1914; McLaurin *et al.*, 1954).

More successful experiments were those involving SC compression (L'Hermitte & Boveri, 1912) or constriction (ligature) of the anterior spinal artery (Tauber & Langworthy, 1935). This led to the hypothesis that syringomyelia developed as a consequence of obstruction of the anterior spinal artery at the foramen magnum in patients with a Chiari malformation (Lichtenstein, 1943). In other words, the ischaemia was now seen as a result of external compression, rather than inflammation, of the containing tissues. Many other investigators adopted this animal model (e.g., Tarlov *et al.*, 1953, see Fig. 2.1; McGrath, 1965), including a variation with venous obstruction (Martinez-Arizala *et al.*, 1990; 1995), who considered these cavities to resemble syringomyelia. Netsky (1953) thought the ischaemia was due to vascular anomalies within the SC itself; e.g., abnormal development of blood vessels of the SC, which of course draws upon the original dysraphic concept.

If compression is able to produce ischaemia then the expansion of a syrinx may actually be the precursor; i.e., ischaemic damage of the SC could be the effect or the cause of a syrinx. However, even though vascular factors will contribute to any disorder of the SC, especially those stemming from arachnoiditis or spinal cord compression, the progressive expansion of syrinxes over years cannot be explained by ischaemia and necrosis alone. Syringomyelia must be distinguished from myelomalacia (Klekamp, 2002).

2.2.4 Haematomyelic hypothesis

This is another blood-based theory but instead of insufficient supply the problem was thought to be a case of 'too much' and 'in the wrong place'. Syringomyelia was believed

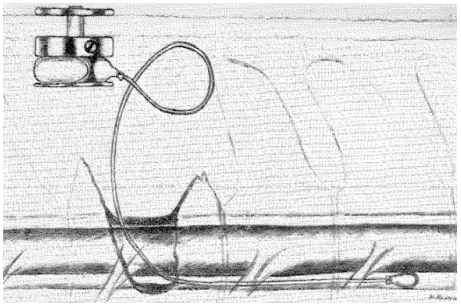

(a)

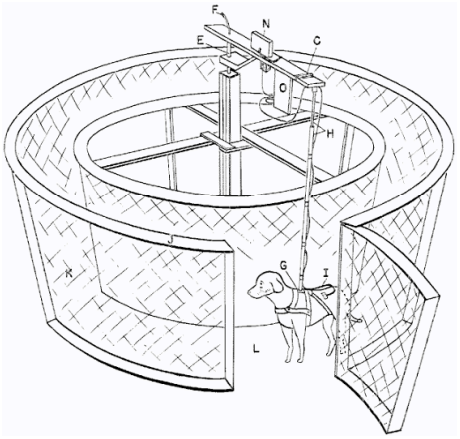

(b)

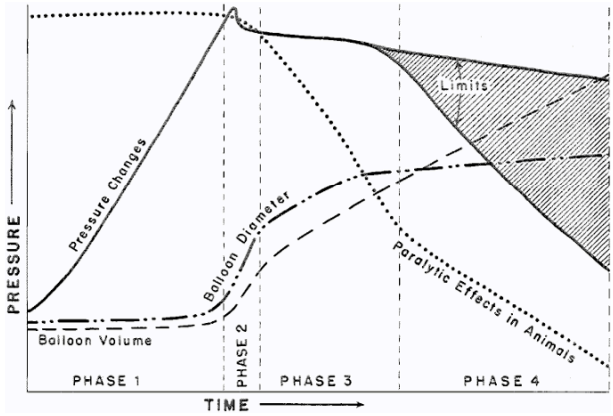

(c)

Fig. 2.1: Example of an animal model for testing pathogenesis theories based upon spinal cord compression, such as the ischaemic hypothesis. (a) balloon for inducing compressive ischaemia; (b) animal *in situ*; (c) qualitative experimental findings. Syrinx formation is correlated with paralytic effects. Reproduced from Tarlov *et al.* (1953).

by some to develop from a *haematoma* (blood clot) within the SC caused by a traumatic event; i.e., a bruise (Bastian, 1867). The inner region of the clot was thought to liquify, transforming it into a syrinx. The first experimental paper appeared in 1890 (Schmaus) and many animal models followed using various methods to inflict SC trauma; e.g., crushing with fingers (McVeigh, 1923), dropping weights (Allen, 1911; Freeman & Wright, 1953; Assenmacher & Ducker, 1971; Noble & Wrathall, 1989), applying a clip (Tator & Deecke, 1973; Fehlings *et al.*, 1989; Tator, 1991), or injecting amino acids (Yezierski *et al.*, 1993). All of these protocols yielded a lesion of the SC and usually an accompanying SC cavity at the level of the trauma.

Williams (1980) remarked that "these blood clots are common and are known to spread in sites of structural weakness, along the grey matter, particularly the dorsal horns". And Klekamp (2002) offered the same advice on the haematomyelic hypothesis as for the ischaemic hypothesis. Namely, that these models explain myelomalacia but not syringomyelia, which may develop without spinal cord trauma or a blood clot. Even so, the reproducibility of syrinxes at trauma sites, independent of the trauma protocol, suggests that trauma as a precursor to syringomyelia warrants further investigation.

2.2.5 Secretory hypotheses

Despite being one of the pioneers in the field, Morgagni (1769) showed remarkable insight. In addition to dysraphism, he first postulated that fluid may be *secreted* in either the head or SC and that the fluid accumulation in one location may be due to insufficient drainage, or alternately, increased production with adequate drainage might cause accumulation at the other site. Barnett (1973) echoed these sentiments but even with two centuries of accumulated knowledge he was not able to elaborate upon any specific mechanism. The measured similarity of syrinx fluid to CSF led some surgeons to the conclusion that ependymal cells secrete CSF, accumulating in the CC and causing a syrinx if the CC is obstructed (Rice-Edwards, 1977; Wiedemayer *et al.*, 1990).

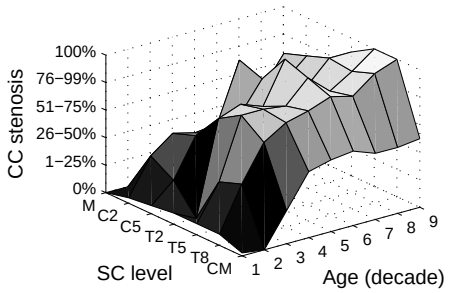

Fig. 2.2: Incidence and extent of central canal stenosis in 228 autopsy cases. Data from Milhorat *et al.* (1994), Table 1.

But around this time evidence surfaced that the CC in humans appears to gradually occlude with age in the vast majority of otherwise healthy individuals (Kasantikul *et al.*, 1979; Milhorat *et al.*, 1994), as illustrated in Fig. 2.2. Therefore if this theory was valid then syringomyelia would be one of the most common neurological diseases.

2.2.6 Transudation hypothesis

Holmes (1915) reported on his postmortem experience with spinal injuries incurred in World War I. Of particular interest and found in more than half of some 50 cases were "curious cavities, roughly cylindrical or oval in cross section, in the segments of the spinal cord adjoining the lesion, either in those above or below it, or in both". Despite the extenuating circumstances of injury and treatment, Holmes ruled out infection and haemorrhage as possible causes. Rather, it was conjectured that the syrinxes originated from the accumulation under pressure of *transuded* fluid and degeneration products from the primary lesion. There has also been some discussion of a transudation mechanism with cystic tumours as the fluid source (Williams, 1970; 1980; 1986; Lohle *et al.*, 1994).

Gardner (1965) compared the protein content of syrinxes with that of lumbar CSF from a series of patients. In three cases of cystic tumours of the cervical SC with symptoms suggesting syringomyelia, the fluid was "thick and yellow" with a protein content about two orders of magnitude higher than CSF, a clear colourless fluid. The

fluid accumulating in such neural tumours was therefore believed to be intercellular in origin—the result of plasma diffusing through the walls of perfusing capillaries into the spaces between the cells of the tissues—and to be distinguished from the CSF-filled syrinxes of syringomyelia. Lohle *et al.* (1994) pointed out that tumour fluid may escape into the CC, also giving the appearance of syringomyelia. This explanation would account for some patients diagnosed with syringomyelia benefitting from radiotherapy (Gardner, 1965).

However, even limiting this theory to cases with *intramedullary* tumours (within the SC), 50% of which will have an associated syrinx (Klekamp *et al.*, 2001; Table 4.16, p. 159), it does not explain why syringomyelia is more frequently associated with tumours at the cervical level than those at lower levels of the same histology (Samii & Klekamp, 1994).

2.3 Biomechanical-based hypotheses

2.3.1 Hydrodynamic hypothesis

In 1862, Gull reported on a case of progressive wasting away of the muscles of the hands. This atrophy was accompanied with an enlargement of the "ventricle of the cord" and dwindling of the surrounding grey matter at the cervical level—a so-called "hydromyelus". Gull thought that the dilatation of the SC was due to fluid accumulation in the CC. Towards the close of the century Chiari hypothesised that the hindbrain malformation, which now bears his name, was caused by prenatal hydrocephalus (Chiari, 1891; 1896). Ogryzlo (1942) put these two ideas together—hydrocephalus might be responsible for the Chiari malformation and this would force fluid into the CC, thereby dilating it.

Lichtenstein (1943) agreed with much of the above logic yet drew different conclusions. He suggested that a Chiari malformation would block the openings (foraminae) of the fourth ventricle and cause fluid to accumulate in the CC, with some escaping

into the parenchyma to form a syrinx. The Chiari malformation was also thought to compress the spinal arteries and veins, leading to ischaemic damage of the SC; together these effects were described as a "syringomyelic syndrome". Lichtenstein stated emphatically "I do not wish here to discuss that controversial subject—the pathogenesis and pathology of true syringomyelia", as he believed "true" syringomyelia to be a condition intrinsic to the SC.

Gardner & Goodall, in 1950, reviewed a series of 17 patients with Chiari malformation; in three quarters of these a cervical syrinx was found and drained during surgery. Having acknowledged the work of their predecessors, Gardner & Goodall described the condition as "congenital obstructive hydrocephalomyelia with foraminal hernia". A prenatal hydrocephalus, due to obstruction of the foraminae of the fourth ventricle, was thought to cause foraminal herniation—Chiari malformation—which would then force CSF into the CC via the obex where it would accumulate, dilating the CC; i.e. the state referred to at the time as hydromyelia.

This theory was presented formally as the *hydrodynamic* hypothesis for the pathogenesis of syringomyelia in the landmark paper by Gardner & Angel (1959). Believing that the CC in humans progressively occludes with age, Gardner interpreted a patent CC as a dysraphism[1] required for the development of syringomyelia; he also postulated that each syrinx required at least an intermittent hydrocephalus. Gardner considered the hydrodynamic force to be purely pulsatile. The arterial pulsations of the choroid plexus were thought to cause permeable membranes covering the foraminae of the fourth ventricle to flex, giving rise to a gentle water-hammer effect on the CSF; this was thought to cause "hydrodissection" in the SC—the mechanism for syrinx expansion. Such a concept did not require a raised intracranial pressure (Gardner, 1965), although presumably even partial obstructions of the CSF pathways would perturb the normal pressure levels.

Gardner's theory attracted many followers because he introduced a surgical treatment based on it, which was quite successful:

[1] as did Ollivier D'Angers in 1827.

1. removal of a portion of the base of the skull (medial suboccipital craniectomy) to accommodate the malformed hindbrain,

2. opening of the fourth ventricle to allow passage of CSF,

3. closure of the obex with a piece of muscle to prevent CSF from entering the CC, and

4. reconstruction of the dura mater (duraplasty) to accommodate the extra volume of the hindbrain, thereby unblocking the connection between the cranial and spinal fluid spaces.

Furthermore, syringomyelia could be demonstrated in animals according to Gardner's hypothesis (Becker *et al.*, 1972; Hall *et al.*, 1975; 1976; 1980).

The success of the procedure was attributed to the occlusion of the obex rather than the decompression of the craniocervical junction (craniectomy and duraplasty), an existing contemporary treatment for hydrocephalus associated with Chiari malformation and spina bifida. However, Gardner's procedure worked just as well if the obex was not closed with muscle (Ball & Dayan, 1972; Klekamp, 2002). Moreover, a patent connection between the fourth ventricle and CC via the obex could not be demonstrated in the majority of patients with syringomyelia, nor did each of them (122 patients) have evidence or a history of hydrocephalus (Williams, 1980). Since the CC does remain patent in a number of mammal species it may play a different role than in humans, making the predictions from previous animal models questionable (Kasantikul *et al.*, 1979; Milhorat *et al.*, 1994).

It was around the time of the hydrodynamic hypothesis that the first mathematical models of the CSF system arrived. Agarwal *et al.* (1969) developed a lumped-parameter model of the cranial contents to study hydrocephalus and the interactions of the CSF and blood compartments; the spinal canal was omitted. One of the contributions of Agarwal *et al.*'s work was in estimating the parameter values for the various fluid compartments. Resistances were approximated from published values for mean

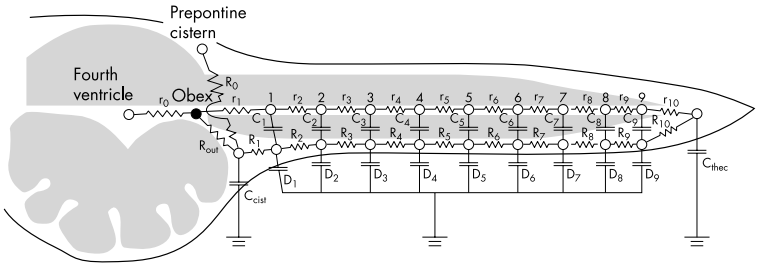

Fig. 2.3: A schematic diagram of the lumped-parameter model by Chang & Nakagawa (2003), represented by an electric circuit analogue.

compartment pressures and flow rates; compliances were determined experimentally by simulating the electrical model and matching approximately the vascular-pressure curves published elsewhere. Marmarou *et al.* (1975) developed an empirical method for estimating the net compliance and resistance of the spinal and cranial compartments based on a lumped-parameter model. In cats the cerebral compartment accounted for about two thirds of total compliance and about one sixth of total conductance.

Chang & Nakagawa (2003) recently resurrected the hydrodynamic hypothesis, with some modifications, using a lumped-parameter model of the craniospinal system. The electric circuit analogy of their model is shown in Fig. 2.3. Chang & Nakagawa suggested that the cisterna magna acts as a "shock absorber" against the pulsatile CSF waves from the cranium, and that the loss of this compliance due to crowding of the base of the skull (e.g., due to a Chiari) causes an increase in the pressure in the CC, leading to syringomyelia. The reliance on a patent CC is an obvious limitation but this compartment could, perhaps, be reinterpreted as the extracellular space within the SC.

2.3.2 Pressure dissociation hypothesis

Williams (1969) admired Gardner's work but argued that obstruction of the foraminae of the fourth ventricle usually leads to gross hydrocephalus affecting all parts of the brain, which would dominate the clinical picture, rather than a mild hydrocephalus leading to a dilated CC. He stated that to explain the pathological findings a mechanism

is needed which can be observed to set up a significant pressure difference between the inside and outside of the cord without altering the relative pressures inside and outside the brain. To this end, Williams believed that the venous pressure wave, excited by occasional events such as coughing, rather than the arterial pressure wave, produced continuously by the choroid plexus, was the main mechanism for the normal displacement of CSF from the cranium to the spinal canal. In regard to the pathogenesis of syringomyelia Williams (1969) first proposed the following "venous mechanism". In the healthy person there exists a dynamic equilibrium between venous distension in the head and the flow of CSF into the spine and back again. A partial SSS obstruction at the craniocervical junction could act as a one-way valve such that, in combination with a patent CC, would allow a venous compression/reflux, due to say, a cough, to raise CSF pressure everywhere except in the SSS, thereby creating a raised SC pressure relative to that in the SSS. The basic concept is illustrated in Fig. 2.4(a,b). This view was supported by clinical descriptions of patients who sometimes experienced quite severe exacerbations of their symptoms with such manoeuvres. The maintenance of this pressure differential, intermittently over many years, was thought to ensure the progression of the disease.

Like Gardner, Williams (1969; 1970) assumed that syrinxes "communicating" with the CSF pathways could do so only via a patent connection between the CC and the fourth ventricle. Other "noncommunicating" syrinxes were taken to be those containing yellow-coloured fluid, which may be exudate from a tumour. By adopting these definitions Williams thus avoided the criticism of his theory not accounting for noncommunicating syringomyelia. He later explicitly dismissed perivascular flow as a possible source of syrinx fluid on mechanical grounds, stating that "Fluid may not, however, be forced along the perivascular spaces to initiate or inflate a syrinx because uniformly raised pressure around the cord must tend to compress rather than expand it" (Williams, 1980).

Although Williams's initial theory was mere speculation this situation was quickly remedied. Simultaneous lumbar and cisternal pressure recordings in the sitting position

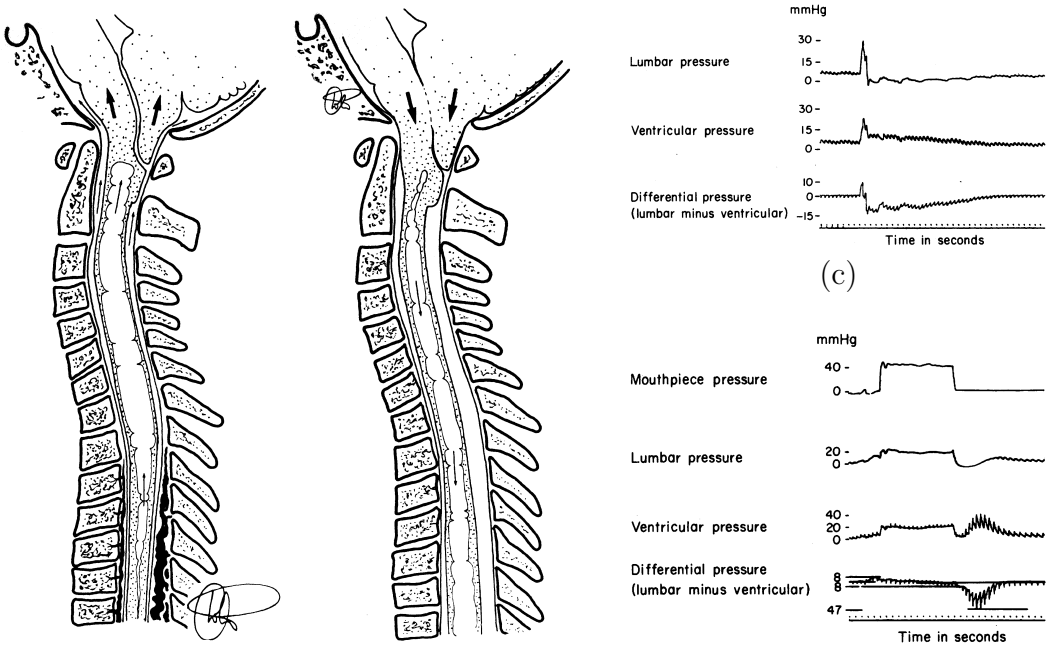

Fig. 2.4: Williams's "suck" mechanism for syrinx formation. See text for detailed explanation. Panels (a) and (b) reproduced from Williams (1990), Fig. 7; panels (c) and (d) reproduced from Williams (1980), Figures 1 and 2, respectively.

were carried out on 17 patients suffering from various diseases of the SC (myelopathies) in the cervical region (Williams, 1972; 1976). Cough impulses of about 0.7 s duration and 15–75 mmHg amplitude were measured. The cisternal wave always arrived after the lumbar wave, with a lesser amplitude, and rose and fell more slowly giving it a longer duration. All of these features were more pronounced when there was a partial spinal block compared to otherwise healthy patients. These pressure recordings were intended to demonstrate the so-called craniospinal *pressure dissociation* mechanism (also referred to as "suck"; Williams, 1980). Referring to Fig. 2.4(c), the differential pressure trace shows that after the cough pulse passes the cisternal transducer the cranial and spinal compartments become dissociated—there is a negative pressure acting across the hindbrain, peaking at around 10 mmHg and gradually attenuating over half a minute. This suction pressure was thought to be maintained by the hindbrain plugging the SSS and alleviated by CSF flowing into the CC [as per 2.4(a,b)]. The dissociation effect was more pronounced after the patient had maintained a constant lung pressure by performing a *Valsalva manoeuvre* [Fig. 2.4(d)], which involves attempted expiration against a closed glottis or closed mouth and nose. When the SSS blockage was due to a tumour within the SC the dissociation effect was also observable (Williams, 1980; Fig. 3).

Before the days of medical imaging physicians used the *Queckenstedt test* to determine spinal block, which involved compression of the jugular vein and measurement of lumbar fluid pressure by column manometer. In a healthy person jugular compression causes an increase in the pressure of the spinal fluid in the lumbar region within 10 to 12 seconds, and an equally rapid fall to normal on release of the pressure on the vein; when there is a block of the subarachnoid channels, compression of the vein causes little or no increase of pressure in the CSF. Williams (1972) proposed that his invasive cough pressure measurements would be a more sensitive method for determining spinal block than the Queckenstedt test, owing to the higher pressures and shorter timescales involved. However, Williams also acknowledged that the Queckenstedt test was largely superseded by myelography (an X-ray with contrast media injected into

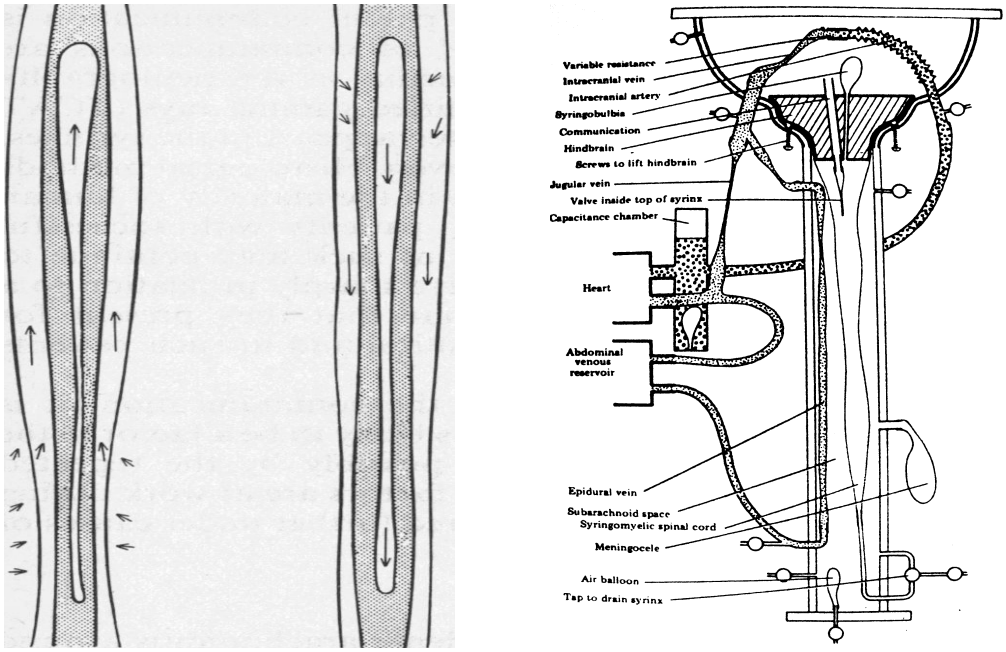

(a) (b)

Fig. 2.5: Schematics pertaining to Williams's *pressure dissociation hypothesis* of syringomyelia pathogenesis. (a) An illustration of the proposed "slosh" mechanism for syrinx expansion. Distension of the epidural veins compresses the spinal subarachnoid space and squeezes the spinal cord, which was thought to force syrinx fluid to be displaced upwards, thereby damaging the cord tissue and thus elongate the syrinx (left); a similar but diminished effect was proposed for the downward direction (right). (b) DAVID, the Demonstration Analogue for Ventricular and Intraspinal Dynamics. Panels (a) and (b) reproduced from Williams (1980), Figure 4, and Williams (1974), Figure 1, respectively.

the SSS), and did not comment on the comparison of his method with this diagnostic imaging technique.

In addition to syrinx formation, Williams suggested a mechanism for the longitudinal expansion of so-formed syrinxes. Compression of the SSS due to distension of the epidural veins tends to squeeze the SC, forcing the syrinx fluid to be displaced upwards. This gross fluid movement was readily observable by radiological screening. The surge of fluid was thought to damage the SC tissue and thus elongate the syrinx cavity; a similar but diminished effect was described for the downward direction. This so-called "slosh" mechanism is illustrated in Fig. 2.5(a).

To add weight to his argument Williams (1974) built a physical model of the cran-

iospinal fluid system which was nicknamed DAVID—a Demonstration Analogue for Ventricular and Intraspinal Dynamics [shown in Fig. 2.5(b)]. He was able to demonstrate movement of CSF in the SSS due to pulsations in the epidural veins, leading to craniospinal pressure dissociation as a result of the hindbrain valve effect, and filling of a communicating syrinx when the intrasyrinx pressure was lower than intracranial pressure (ICP). The syrinx continued to fill when the mean intrasyrinx pressure exceeded the cranial pressure because a mitral valve was fitted at the entrance to the syrinx. This was supposed to simulate a natural one-way valve presumed to operate in the upper CC due to the external SC compression imposed by the hindbrain. Adding extra SSS capacitance in the form of an outpouching through the rigid spinal canal (representative of a meningocele, see Fig. 2.5) tended to damp intraspinal pulsations and lessen the pressure dissociation mechanism. Venous pulsations were more readily transmitted to the CSF when the epidural vein was just collapsed.

The CSF pressure recordings mentioned earlier showed that the cisternal amplitude was lower than the lumbar amplitude [Fig. 2.4(c,d)]. To Williams (1976) this suggested that in the sitting position the compliance of the veins of the upper thorax and neck is sufficient to absorb the upward thrust of venous distension, at least over the short sharp coughs that were studied, and that intracranial compliance is also high. These pressure-volume characteristics of the cerebrospinal system were considered to be sufficient to overcome any localised pressure amplification due to the superposition of waves reflected from the head. However, the possibility of viscous dissipation was not mentioned by Williams (1976). In related theoretical work Lockey *et al.* (1975)[2] investigated the transmission of pressure pulse waves in the SSS. The continuum model consisted of an annular tube with rigid inner surface (representing the SC), flexible outer surface (representing the dura), and the intervening fluid (representing the CSF) was set to be inviscid purely on grounds of mathematical tractability. Permutations of open/closed end conditions were studied with variation of dural thickness and the degree and location of an imposed SSS blockage. The open-closed and closed-closed end

[2]also directed by Williams

conditions yielded attenuation factors increasing with degree of blockage, which may be relevant to syringomyelia. The wave speed was chiefly determined by the thickness of the dura, which is to be expected, though, as it was the only source of compliance in the model.

DAVID's duck-billed valve appeared to be in operation in dogs according to a study by Hall *et al.* (1980). They measured mean intrasyrinx pressure to be greater than mean intracranial pressure, even when hydrocephalus was present. Syringeal pressure rose with ICP but did not fall when ICP was lowered by aspiration of ventricular fluid. This was thought to demonstrate that a one-way valve mechanism might operate to allow fluid to accumulate in the syrinx from transient rises in ICP.

Häckel *et al.* (2001) recently performed invasive pressure monitoring in patients with indications of Chiari malformation to confirm pressure dissociation in cases where MR images were inconclusive. However, although the pressure dissociation phenomenon was measured, almost all cases with a blockage and a syrinx could be confirmed with MR only, making the more invasive diagnostic procedure questionable. The difficulty in taking fluid pressure measurements, especially in humans, is a significant obstacle in the study of syringomyelia.

2.3.3 Piston hypothesis

In 1970, Ellertsson & Greitz measured intrasyrinx pressure under resting conditions to be greater than SSS pressure but with lower pulse amplitude. During Queckenstedt and Valsalva manoeuvres the syrinx pressure rose later and persisted longer than the SSS pressure. This suggested to the investigators that there exists a pathway between the CSF and syrinx spaces other than the CC[3], and that a transiently favourable pressure gradient at the syrinx "inlet" in combination with defective syrinx drainage accounted for the persistence of raised syrinx pressure.

An alternative CSF pathway was soon found. Ball & Dayan (1972) established the

[3]making the descriptions 'communicating' and 'noncommunicating' syringomyelia slightly ambiguous

PVS as a fluid conduit connecting the SSS with the syrinx. This important discovery was made by injecting water-soluble contrast media into the SSS which then accumulated in the PVS and syrinx; the PVS were dilated in histological sections indicating a raised lumen pressure.

Oldfield *et al.* (1994) and Heiss *et al.* (1999) formulated a theory for syrinx formation and progression based on perivascular flow. They proposed that systolic pulsations in the head created a *piston*-like action on the hindbrain tonsils which excites caudal-moving (toward the tailbone) pressure waves that squeeze the SC, forcing fluid into the SC via PVS to originate a syrinx, and propelling intrasyrinx fluid downwards maintaining its progression. This process is illustrated in Fig. 2.6. In support of their theory Heiss *et al.* (1999) presented a study on 20 patients with Chiari malformation and signs of syringomyelia, and 18 healthy volunteers for comparison. MRI (static and dynamic), ultrasound and invasive pressure measurements were taken in all subjects and these measurements were repeated on patients during surgery and 6 months later. Compared to the volunteers, the patients had obstructed CSF flow and impaired pressure transmission between the head and spinal canal, and the SSS had a lower compliance. Flow in the SSS was downward during systole and upward during diastole, which was synchronised with hindbrain tonsil movements. Syrinx compression coincided with raised SSS pressure and descent of the tonsils. The gross deformations of the SC and syrinx cavity illustrated in Fig.2.6 were observable with ultrasonography. Patients were treated by decompression of the hindbrain but the syrinx was left intact. After surgery the piston-like action of the hindbrain ceased, SSS compliance increased, pressure and flow characteristics normalised, and the syrinx diameter decreased. Although symptoms tended to persist this was presumed to be because irreversible damage had been done to the SC.

As part of their investigation Heiss *et al.* (1999) evaluated the theories of Gardner & Angel (1959) and Williams (1969). Only one patient had evidence of a connection between the fourth ventricle and CC which largely dismisses both of these hypotheses. Furthermore, the syrinx tended to be compressed during systole, rather than distended

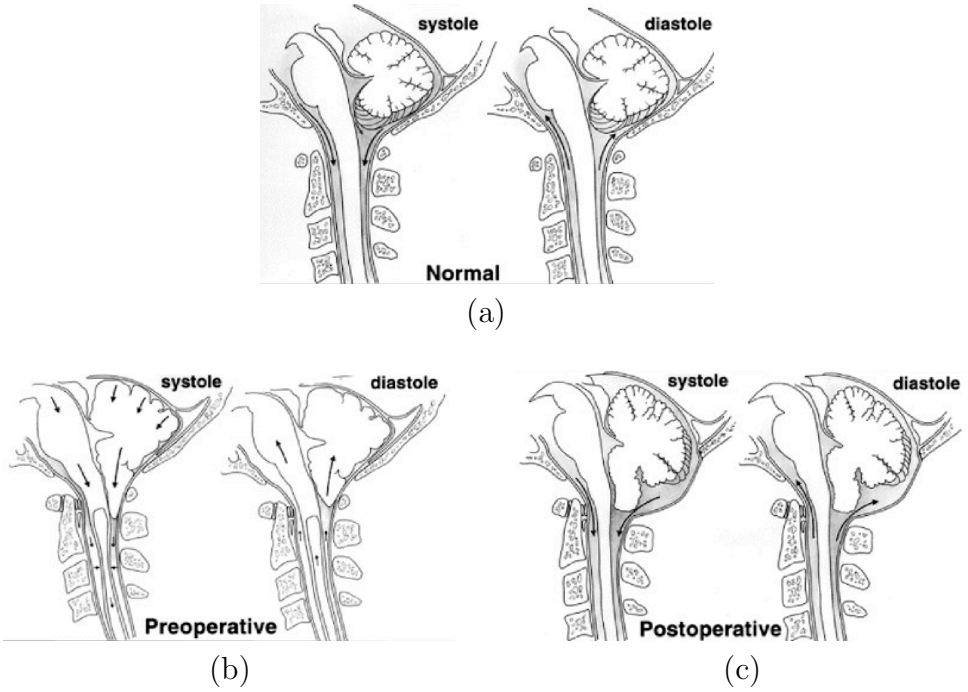

Fig. 2.6: An illustration of the *piston hypothesis* put forth by Oldfield, Heiss and coworkers. (a) Normal cerebrospinal fluid flux between cranial and spinal cavities. (b) The piston-like action of a malformed hindbrain, driven by systolic pulsations in the head, which excite caudal-moving pressure waves that squeeze the spinal cord, forcing fluid into the spinal cord via perivascular spaces to originate a syrinx, and propelling intrasyrinx fluid downwards maintaining its progression. (c) Restoration of the cerebrospinal fluid flux to normal by surgical treatment at the craniocervical junction. Reproduced from Heiss *et al.* (1999), Figure 8.

as Gardner's hydrodynamic mechanism requires, and the syrinx diameter did not increase during the Valsalva manoeuvre as predicted by Williams's pressure dissociation hypothesis.

2.3.4 Oedema hypothesis

This theory is somewhat complementary to the other hypotheses but has received enough attention to stand on its own. And as with the secretory hypothesis (§2.2.5) it was Morgagni (1769) who made the initial suggestion. He proposed that syringomyelia, besides being associated with dysraphic malformations, was analogous to hydrocephalus, beginning initially as *oedema*. Such an accumulation of fluid in cells or intercellular

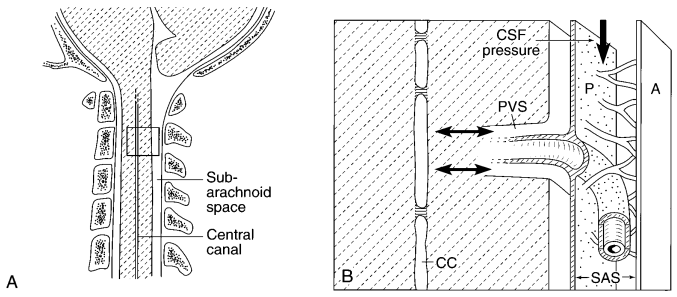

Fig. 2.7: An illustration of how cerebrospinal fluid (CSF) may be exchanged between the central canal (CC) and the spinal subarachnoid space (SAS here but SSS elsewhere in the text) by a pathway through a perivascular space (PVS). The subarachnoid space is bounded by the arachnoid mater (A) and the pia mater (P). Reproduced from Fischbein *et al.* (1999), Figure 5.

tissues must be driven mechanically, either by a hydraulic or osmotic pressure gradient. Tannenberg (1924) and Liber & Lisa (1937) elaborated upon this idea, demanding a blockage of the CSF pathways be present, either in the CC or the PVS, respectively.

Fischbein *et al.* (1999; 2000) suggested that there may exist a normal dynamic equilibrium of flow between the SSS and SC via the PVS, as shown in Fig. 2.7. The normal situation was also assumed to include a CC stenosed into isolated segments. However, Fischbein's group argued that if the SSS pressure is periodically raised by systolic pulsations of a hindbrain hernia [Fig. 2.8(a)], then there may be a net inflow of CSF into the SC. Patent segments of CC were thought to inflate to form syrinxes [panels (b) and (c)] but if no such segments existed then CSF would diffuse into the cord tissue resulting in oedema and cord swelling [panel (d)]. Fischbein and colleagues treated a small number of Chiari patients by surgically removing the CSF obstruction which led to resolution of cord swelling and neurological improvement. Based on these findings and the similarity of MRI responses to oedema and syrinxes they proposed that SC oedema was a reversible "pre-syrinx" state. In many respects the oedema theory presented by Fischbein *et al.* (1999; 2000) is simply a different interpretation of the piston theory that places greater emphasis on the reversibility of the disease process than on the mechanical force that drives it.

The introduction of MR imaging led to the discovery that only a minority of sy-

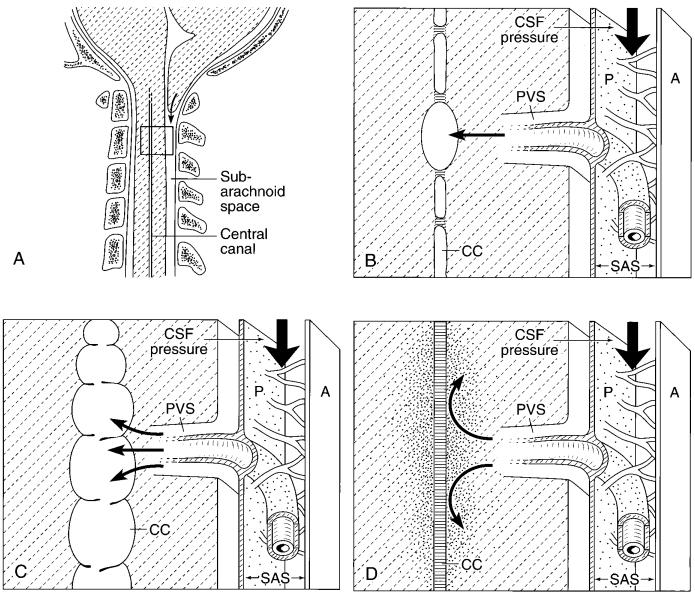

Fig. 2.8: An illustration of Fischbein and coworkers's *oedema hypothesis*. The normal situation was thought to include a dynamic equilibrium of cerebrospinal fluid (CSF) flow between the spinal subarachnoid space (SAS here but SSS elsewhere in the text) and spinal cord via the perivascular spaces (PVS), and a central canal (CC) stenosed into isolated segments. It was proposed that if (a) the subarachnoid-space pressure is periodically raised by systolic pulsations of a hindbrain hernia then (b) there may be a net inflow of CSF into the SC, entering the patent segments of CC which would (c) inflate to form syrinxes, but if no such segments existed then (d) CSF would diffuse into the cord tissue resulting in oedema and cord swelling, thought to be a reversible "pre-syrinx" state. Reproduced from Fischbein *et al.* (1999), Figure 6.

rinxes communicate directly with the fourth ventricle, motivating the search for a new mechanism to replace those of Gardner and Williams. Milhorat (1999) generally agreed with Fischbein's proposal and suggested that treatment should be aimed at identifying and correcting CSF obstruction. Although Häckel *et al.* (2001) championed the pressure dissociation hypothesis they believed that the route the CSF takes into the syrinx is the path of least resistance and this is more likely to be along the PVS rather than through the CC.

2.3.5 Intramedullary pulse pressure hypothesis

Greitz (2006) recently presented an ambitious attempt to explain the pathogenesis of syringomyelia in all its guises; e.g., in association with Chiari malformation, spinal trauma or arachnoiditis, as well as occurring secondary to tumours in both the spinal canal or the base of the skull. This grand unifying theory, of sorts, was first conceived of in 1995 and then refined over the course of the proceeding decade (Greitz, 1995; Greitz *et al.*, 1999; Josephson *et al.*, 2001; Greitz & Flodmark, 2004; Greitz, 2006). As the name suggests, the emphasis was on the pulse pressure of capillaries within the SC (medulla).

Figure 2.9 shows Greitz's graphic description of the intramedullary pulse pressure hypothesis for the case of posttraumatic syringomyelia. The proposed mechanism was as follows. The systolic expansion of arteries within the base of the skull was thought to set up a pair of coupled pressure waves—one in the SC and another in the CSF within the SSS. These waves would propagate down the spinal canal and under normal physiology it was assumed that there would be no significant pressure differential between them. Greitz argued diagrammatically that an obstruction in the SSS wouldn't affect the SC wave and so this would be transmitted [panel (a)], while the SSS wave would be reflected from the obstruction [panel (b)]. On this basis, at a location downstream of the obstruction there would be a net pressure distending the SC due to the transmitted SC wave and upstream the reflected SSS wave would be "reflected into"

the SC thereby distending the cord just higher up. If the obstruction were only partial then a venturi effect was supposed to operate causing a suction on the SC which would act to distend it. Effects mirrored about the level of the stenosis were presumed to occur for cranially-moving waves in diastole, coughing and the Valsalva manoeuvre. Syringomyelia was hypothesised to develop in the distended cord by accumulation of ECF *derived from blood plasma*, rather than from CSF, by the mechanism shown in Fig. 2.9(d). What this diagram attempted to convey was that the ECF flows down a pressure gradient from the intramedullary capillaries, through the capillary walls, and into the syrinx; the pressure of the syrinx would then exert a compressive force on the venous outflow network which would increase venous resistance, increase arterial pressure, thereby reinforcing the pressure gradient driving the extracellular flow into the syrinx.

In support of their theory Greitz's group presented some empirical observations. Dynamic MRI measurements in humans showed that CSF velocity increases through a partial obstruction in the SSS (Greitz *et al.*, 1999), and animal experiments demonstrated that a constriction of the SSS (by ligature) may lead to syrinxes forming at adjacent sites above and below (Josephson *et al.*, 2001; Greitz & Flodmark, 2004). However, the animal model did come under scrutiny. Although the ligature was designed to produce an obstruction of the CSF flow, Milhorat argued that the ligature almost certainly upsets the intramedullary circulation that is integral to Greitz's theory, resulting in ischaemia of the SC, which would explain the presence of acute paraplegia seen in surviving animals, amongst other effects (Josephson *et al.*, 2001; see Milhorat's review comments, p. 646).

Also relevant here is the work of Chang and Nakagawa. Their lumped-parameter model for studying Chiari malformation (Chang & Nakagawa, 2003), described earlier (see Fig. 2.3), was subsequently reapplied to study flow obstruction in the SSS representative of arachnoiditis (Chang & Nakagawa, 2004). The results predicted a raised SC pressure with respect to the SSS just below the obstruction. This lends some support to the intramedullary pulse pressure hypothesis.

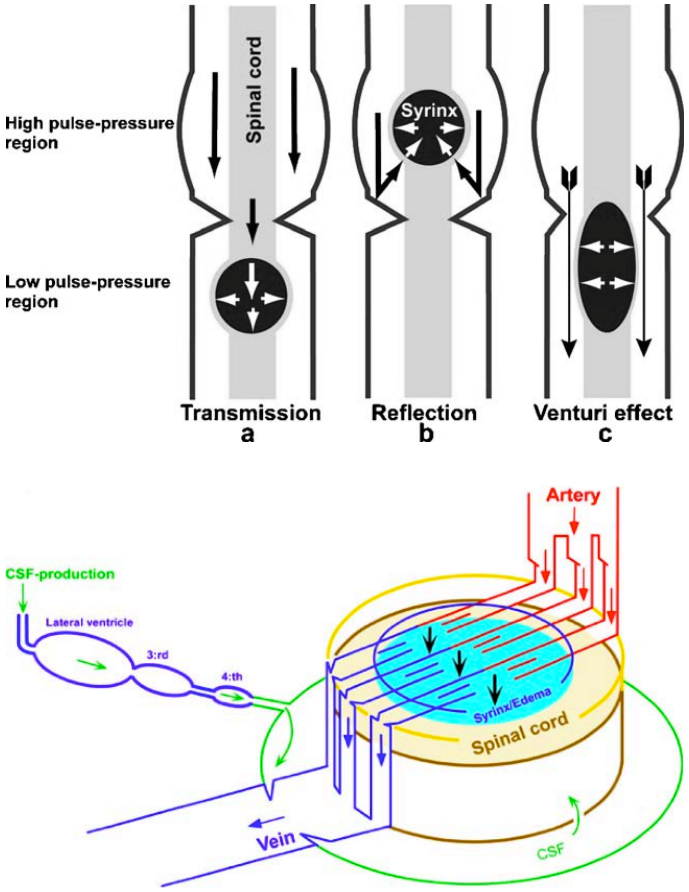

(d)

Fig. 2.9: A schematic description of Greitz's *intramedullary pulse pressure hypothesis* for syrinx formation. See text for detailed description. Reproduced from Greitz (2006), Figures 1 and 3.

2.3.6 Elastic jump hypothesis

In 2003, Carpenter and colleagues presented a pair of papers describing a pathogenesis hypothesis for syringomyelia which was based on classical theory of flow through elastic tubes (Berkouk *et al.*, 2003; Carpenter *et al.*, 2003). This work was the culmination of several earlier attempts (Carpenter *et al.*, 1996; Berkouk, 1999; Carpenter *et al.*, 1999). The model consisted of a pair of fluid-filled coaxial tubes, the inner tube being flexible, the outer rigid, and the enclosed and intervening fluid inviscid. The outer tube represented the dura mater and surrounding structures and the annular fluid space corresponded to the SSS. As their investigation was motivated by the work of Williams (§2.3.2), the flexible tube was originally interpreted as the SC and the cylindrical fluid space within was thus the CC (Berkouk *et al.*, 2003; and earlier papers). Upon realising the limited applicability of a model dependent on a patent CC, the flexible tube was reinterpreted as the pia mater and the contained fluid became an approximation of the SC tissue (Carpenter *et al.*, 2003).

By making a long-wave assumption, Berkouk *et al.* (2003) reduced the one-dimensional governing equations to a classic wave equation for small-amplitude disturbances. Using asymptotic analysis a weakly-nonlinear theory was then developed for pressure-wave propagation along the rostrocaudal axis (i.e., the axis running from the head to the tail, encompassing the longitudinal axis of the SC). As the wave speed is a strong function of the ratio of the tubes' cross-sectional areas, Berkouk *et al.* (2003) was able to prove that the leading edge of a pressure pulse steepens to form a shock-like *elastic jump*. This phenomenon is akin to a wave breaking at the beach as it reaches shallow water. When such an elastic jump reflects from a stenosis of the SSS it forms a transient localised region of high pressure within the SC, which for a cough-induced pulse was estimated to be 50–70 mm Hg or more above the normal level in the SSS; this concept is illustrated in Fig. 2.10. Carpenter *et al.* (2003) proposed this as a new mechanism whereby pressure pulses created by coughing or sneezing can generate syrinxes.

The mathematical model that the elastic jump hypothesis was founded on was ana-

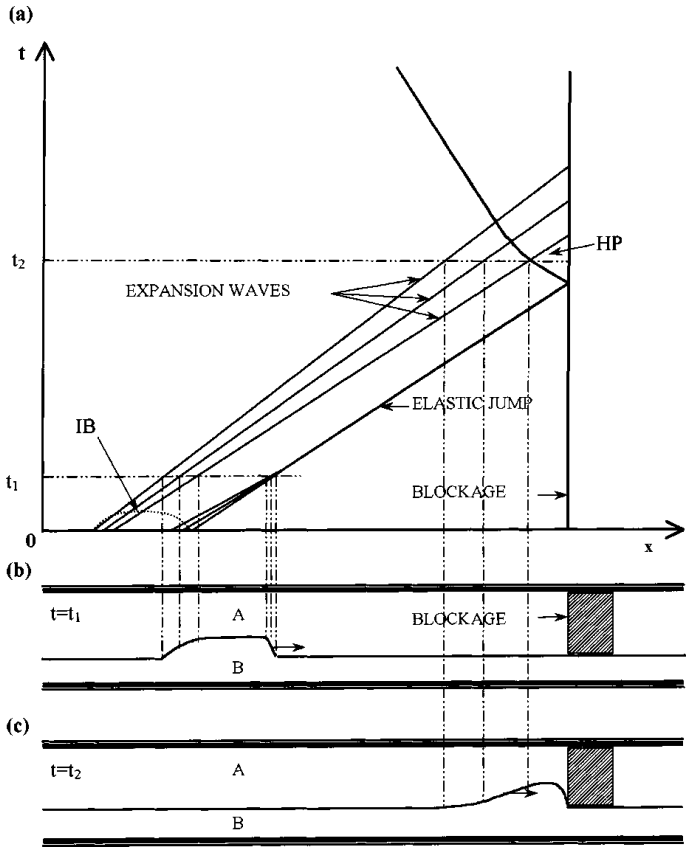

Fig. 2.10: A schematic illustration of the elastic jump concept. (a) A wave diagram of a pressure pulse propagating through a coaxial tube system and incident on a blockage at the right. The characteristic lines show that the leading edge of the pulse steepens with time to form an elastic jump. The dotted line denotes the initial bump deformation of the tube wall (IB). As the elastic jump reflects from the blockage a transient, localized region of high pressure is generated (HP). The forms of the tube-wall displacement at times $t = t_1$ and $t = t_2$ are shown in panels (b) and (c), respectively. Reproduced from Carpenter *et al.* (2003), Figure 3.

lytical in nature, which revealed the underlying mechanical relations and thus could be used to evaluate other biomechanical-based theories. Carpenter *et al.* (2003) found that their analysis did not support syrinx formation by the pressure dissociation hypothesis (Williams, 1969) nor by the piston hypothesis (Oldfield *et al.*, 1994; Heiss *et al.*, 1999), although they did show some support for the latter mechanism in syrinx progression.

The inviscid assumption made in the coaxial tube model was controversial—both for the CSF and as an approximation of the SC tissue. The earlier work of Loth *et al.* (2001) provided some support though. Realistic SSS geometry was reconstructed from axial slice data of the Visual Human Project (U. S. National Library of Medicine, n.d.) and the velocity profile was measured at C2 via dynamic phase contrast MRI in a healthy volunteer. The hydraulic diameter varied significantly down the length of the cord from 5–15 mm, with narrower passage occurring into the central portion. Inertial effects tended to dominate the flow under normal conditions with Reynolds numbers ranging from 150–450 and Womersley numbers from 5–17. These findings were corroborated by a pair of computational fluid dynamics (CFD) models of the SSS although the meningeal boundaries were set to be rigid.

From the same research group Martin *et al.* (2005) followed up this work with a physical analogue of the spinal canal, this time including the SC, which was validated with MRI measurements from a patient with syringomyelia (see Fig. 2.11). Interestingly, flow waveforms in the model only matched those *in vivo* when the syrinx was open to atmospheric pressure. The pulse wave velocity varied in time (between 0 and 25 m/s), and so did the flexible tube cross-section, which might indicate the presence of elastic jumps. A favourable pressure gradient for flow of CSF from the SSS into the syrinx only existed for a fraction of the cardiac cycle. The similarity of *in vivo* and *in vitro* MRI measurements indicated to the authors that the coaxial tube analogy captures some of the salient fluid and solid mechanics in syringomyelia (Martin *et al.*, 2005).

The SC is a fluid-saturated poroelastic solid which Carpenter *et al.* (2003) approximated rather crudely as inviscid fluid. Bertram *et al.* (2005), in a computational fluid-

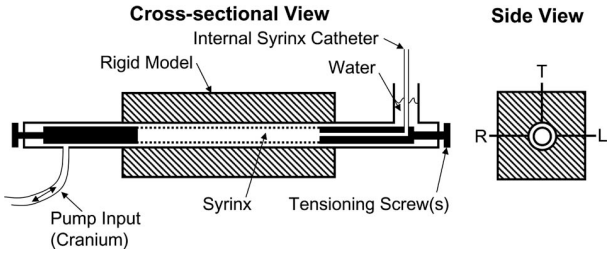

Fig. 2.11: A schematic of the physical analogue model used by Martin and coworkers for investigating flow waveforms in the subarachnoid space and in a syrinx. Reproduced from Martin *et al.* (2005), Figure 3.

structure-interaction (FSI) model, investigated the opposite extreme—approximating the SC as a linear elastic solid. They neglected the pia mater but allowed the fluid to be viscous and the dura was made flexible to account for spinal canal compliance. The stated aim of this paper was to show that in the SC "there is little opportunity for shock formation". The study consisted of exciting the mechanical system with pressure impulses equivalent to arterial pulsation and coughing, then observing the wave propagation and reflection characteristics. They found that at cardiac frequencies the dynamic response was that of a "lumped" system with the pressure along the the length of the SSS rising and falling in synchrony. A more distributed response was observed in the higher frequencies found in cough pulses. However, as the system was dispersive the wave speed was frequency dependent, and at none of the frequencies studied did the wave speed fall to sufficiently low values for the SC to be long relative to the wavelength. On this basis Bertram *et al.* (2005) argued that shock formation from wave steepening was unlikely to be of great significance in syringomyelia.

While Bertram *et al.*'s conclusion is consistent with their results the model upon which it is based differs from Carpenter *et al.*'s in a non-trivial way. The SC is largely water by mass yet only about 20% of the volume is available for the free passage of fluid. This seeming contradiction has led to two very different approximations—the pure fluid approach of Carpenter *et al.* (2003) and the pure solid approach of Bertram *et al.* (2005). The actual physics, however, lies somewhere in between.

Bertram *et al.* (2005) determined the speed of the dominant wave in their simula-

tions to be 12.2 m/s through inspection of the plots of pressure and radial displacement on the inner SSS surface. By performing numerical experiments in which the cord and dura, in turn, were set to be rigid, the compliance of the cord and dura were identified as making relatively equal contributions to this wave speed value. Complementary to these findings is the recent work of Cirovic (2009), which was essentially an analytical approach to the same problem and thus bears some resemblance to the methods of Berkouk *et al.* (2003) and Carpenter *et al.* (2003). The model differed slightly from that of Bertram *et al.* (2005) though by including a central fluid canal within the SC, and the fluid in this and the SSS was set to be inviscid.[4] From the roots of the dispersion equation Cirovic was able to derive expressions for four distinct wave modes; for the chosen 'normal' parameter values these corresponded to speeds of 13 m/s, 14.7 m/s, 30.3 m/s and 124.5 m/s. The slowest and fastest modes were attributed to the dura and the SC, respectively, whereas the remaining two modes involved some degree of coupling between the two structures. Interestingly, when the thickness of the SC was reduced below its normal value, the speed of the first mode dropped significantly and was also dominant in terms of the induced movement of CSF. This finding suggested to Cirovic (2009) that a syrinx may be characterized by an abnormally low speed of the CSF pulse.

2.3.7 Tethering hypothesis

In a follow-up study Bertram and coworkers added to their model three different attributes representing possible effects of localised cord tethering by arachnoiditis (Bertram *et al.*, 2008). The disease-affected region was a short section of computational cells lining the outer surface of the SC, located midway along the length. The cell vertices on the side facing the SSS were either prevented from motion in the radial direction ('pure radial tethering'), prevented from motion in the axial direction ('pure axial tethering'), or attached to the dura on the opposite side of the SSS by

[4]Bertram *et al.* (2005) also considered a model with a CC but this was not the focus of the investigation.

spring elements that were stiff in tension but had zero compressive stiffness ('inextensible strings'). When the system was excited by a pressure pulse at one end of the SSS, in the case of the inextensible strings the authors observed transients of tensile radial stress and negative pressure[5] in the SC. The pure radial and axial tethering cases produced less noteworthy results, although radial tension was possible in the latter case if the cranial end of the cord was left unconstrained. This led Bertram *et al.* (2008) to the hypothesis that cord-to-dura movements associated with tethering could cause transient tensile radial stress and negative pressure in the SC, as pressure waves propagate. Furthermore, they postulated that the repeated action of the tensile stress may produce a syrinx and that lowered hydrostatic pressure, corresponding to pressure in the interstitial fluid, may contribute to the enlargement of such a syrinx. All of the above-mentioned effects of the tethering occurred in juxtaposition to the region of simulated arachnoiditis, which is consistent with syringomyelia pathology.

2.3.8 Peristaltic hypothesis

This hypothesis evolved from a large number of animal experiments by Stoodley and coworkers who sought to trace the path of syrinx fluid and how this was affected by perturbations in the hydrodynamic environment. The experimental protocol was established by Stoodley *et al.* (1996) in a study on rats. Horseradish peroxidase was used as a CSF tracer molecule which, due to its size (5–6 nm) and molecular weight (43 kD), resists simple diffusion but is able to pass, under a pressure gradient, between the pial and ependymal cells separating the CSF spaces from the extracellular spaces within the SC (and brain). Tracer was injected into each animal (at mid-SSS or cisterna magna) and allowed to flow for a set time (0, 10 or 30 minutes) before the animal was sacrificed. The tissue was fixed by perfusion of aldehyde and then processed using standard techniques to produce glass-mounted tissue sections suitable for microscope analysis. By observing where and how quickly tracer accumulated in the tissues it was

[5]Strictly speaking, a negative 'pressure' equates to a positive value for the average of the mutually orthogonal normal stresses, since the cord material was an elastic solid.

possible to determine the route and time course of the CSF flow within the SC. Stoodley *et al.* (1996) found that in rats CSF flows through the PVS, across the interstitial space and into the CC; no CSF path was found between the fourth ventricle and the CC and the CC was stenosed into isolated segments. They believed this flow to be driven by *arterial pulsations*, in accordance with the pioneering work on the brain by Rennels *et al.* (1985), rather than as a "free transfer" of fluid. Furthermore, Stoodley *et al.* (1996) also suggested that such a mechanism could lead to accumulation of fluid and development of syrinxes in cases of isolated CC segments.

Evidence in support of the arterial-pulsation idea was provided by Stoodley *et al.* (1997) in a subsequent study on sheep. They demonstrated that CSF flow from the SSS to the CC via the PVS is abolished when the SC arterial pulsation is reduced while maintaining mean arterial pressure (a partial ligation technique).

However, to evaluate this mechanism in syringomyelia a reliable method for producing syrinxes was needed. For this task Stoodley *et al.* (1999) used kaolin (a fine white clay) after Milhorat *et al.* (1993). When post-traumatic syringomyelia was induced in rats by kaolin injection in the SSS, there was evidence that CSF takes the same flow path into the syrinxes as into the CC. Since the syrinxes were simply dilated segments of the CC this might not seem surprising. Nevertheless, CSF made its way into these syrinxes even when the surrounding tissue was visibly compressed, presumably due to raised lumen pressure. The kaolin also caused a SSS blockage which, it was speculated, may induce increased arterial pulsation at rostral locations (towards the head). Similar observations were made when syrinxes were induced separate from the CC using an excitotoxic amino acid[6] (Stoodley *et al.*, 2000; Yang *et al.*, 2001; Brodbelt, Stoodley, Watling, Rogan, Tu, Brown, Burke & Jones, 2003). These extra-canalicular syrinxes enlarged when a subarachnoid block due to arachnoiditis was present. In fact, CSF flowed preferentially into the syrinx, ahead of perivascular flow into the rostral portions of the SC (Brodbelt, Stoodley, Watling, Tu & Jones, 2003).

[6]Excitotoxic amino acids are released at the time of cord injury and are likely to be important in initial syrinx formation.

The experiences of Stoodley and colleagues in the operating theatre and laboratory suggested to them that the effects of adhesive arachnoiditis that potentiate syrinx formation are likely to be CSF flow obstruction, cord tethering and/or a change in SSS compliance. Brodbelt, Stoodley, Watling, Tu, Burke & Jones (2003) examined the effects of altering the total SSS compliance by shunting the CSF into the abdomen while maintaining any obstructive or tethering effects of localised arachnoiditis. Since the shunt produced no significant change in syrinx formation and the SSS blockage did not inhibit the CSF flow appreciably, the authors concluded that the main effect of arachnoiditis is to effect a localised change in SSS compliance which preferentially diverts CSF into the SC and syrinxes. These ideas are in keeping with an earlier conjecture that the success of hindbrain decompression surgery for syringomyelia in combination with Chiari malformation might be due to the increase in SSS compliance and concomitant reduction in SSS pulse pressure and perivascular flow, rather than removal of the so-called piston mechanism (Stoodley *et al.*, 1997).

Although Stoodley and colleagues implicated arterial pulsation in the pathogenesis of syringomyelia, up to this point they had not elaborated on a driving mechanism. Their first such proposal was demonstrated using a CFD model (Bilston *et al.*, 2003). The idea was simple—the pressure wave travelling down a spinal artery can set up a *peristaltic* flow into the SC through the surrounding PVS. This CSF pump functioned even against a moderate pressure gradient which could explain how fluid is able to flow 'up hill' into a syrinx. Pumping is facilitated by larger amplitudes and speeds of arterial-wall pulsation, by narrow PVS and by shorter wavelengths. The phasing of the transpial pressure gradient would also determine how much fluid is pumped, which would need to be determined experimentally (if feasible).

2.3.9 Phase-lag hypothesis

As an alternative to peristalsis, Stoodley's group also proposed a variable-resistance-valve mechanism to effect an arterial-pressure-driven flow (Bilston *et al.*, 2007). CSF

may be exchanged between the SC and the SSS via the network of fenestrating PVS. The resistance of these conduits is set by the inflation of the intruding vessel, which in turn is set by the cardiac pulse—the same pressure source that provides the CSF with its pulsation. Bilston *et al.* (2007) constructed a CFD model of a PVS represented as an annular cylinder. The inner surface of the PVS deformed with a simulated cardiac pulse and SSS pulse pressure was applied to one end (and a zero pressure boundary condition at the other end). They found that having a *phase lag* between the two pulses permits a net PVS inflow, which could accumulate as a syrinx. Alterations to normal phase difference might occur as a result of scar tissue, associated with syrinxes, interrupting the local blood supply (Bilston *et al.*, 2007).

2.4 Summary

The history of syringomyelia is rich with theories for the formation and expansion of syrinxes. More than a dozen have been presented here, which are considered to be representative of the literature. Initially, these hypotheses were formulated on the basis of autopsy findings of just a handful of patients but with advances in technology, speculation gave way to scientific endeavour, and in doing so emphasised the mechanical nature of syringomyelia. In humans the chief investigative tool today is MRI. Static images can be used to diagnose the disease and also to evaluate treatment options by following syrinx development over long periods postoperatively. Dynamic MR imaging, although still not ubiquitous, is now beginning to provide useful quantitative information on the flow of CSF within the spinal canal. However, the description of the fluid mechanics *in situ* remains incomplete because invasive pressure measurements are problematic. Animal experiments have not overcome this limitation but instead have allowed the influx of syrinx fluid to be traced in a reproducible form of post-traumatic syringomyelia. Engineering studies have taken two routes: (i) continuum models that mainly seek to characterize the wave-bearing properties of the spinal canal, or (ii) lumped-parameter models that attempt to capture the effects of compliance and resistance on the cere-

brospinal system as a whole.

Syringomyelia occurs with a large constellation of symptoms which can probably be attributed to an equally large number of associated disorders (recall Table 1.1). So, is syringomyelia one disease? Or are there many pathologically distinct diseases that merely appear the same due to a similar cystic outcome? This is a moot point. However, what is certain is that the principles of mechanics must apply.

The main energy sources for pressure fluctuations in the cerebrospinal system are the impulses set up by isolated, percussive respiratory events such as coughing and sneezing, which are mostly transmitted through the venous system, and the cardiac cycle, which provides smaller but continuous oscillations that are mostly transmitted through the arteries. A cough produces a short sharp pressure rise within the major body cavities of the thorax and abdomen. Beginning with the diaphragm relaxed and the glottis closed, the intra-abdominal pressure is then raised by contraction of the trunk muscles and continues to rise until the glottis relaxes, releasing air from the lungs whereafter the pressure drops to atmospheric and the cough is over. As the pressure in the thorax and abdomen rise during coughing, or any similar manoeuvre, the veins within the major body cavities are subjected to a high pressure and blood moves into the epidural veins transmitting most of that rise in pressure. Within the spinal canal the pressure rise will be transmitted across the membranes forming the wall of the veins and across the dura and arachnoid to effect a pressure rise in the CSF within the SSS (Lockey *et al.*, 1975). The cardiac cycle may excite CSF pulsations by direct transfer of vascular pressure from arteries passing through the SSS, or indirectly by the pulsatile expansion of the brain and SC due to perfusing vessels (Henry-Feugeas *et al.*, 2000).

Fluid can flow into the syrinx in two possible ways: (i) it can flow passively down a pressure gradient, implying that there must be some other source of high-pressure fluid; or (ii) it can be actively pumped up a pressure gradient. If the responsible mechanism is only transiently present then some sort of one-way valve would be required for fluid to remain and thus accumulate in the syrinx. CSF flow obstructions and loss of SSS

compliance are likely to encourage syrinx development, and all mechanical phenomena involved must be localised to be consistent with the disease progression.

The aim of this project is to provide insight into the pathogenesis of syringomyelia using simple mathematical models. Given the large number of hypotheses that have been proposed over the last three centuries there is considerable scope for investigation. In this thesis the focus is on the elastic jump and phase lag hypotheses which is based on the following rationale. Since each of the biological-based hypotheses were introduced much empirical evidence has accumulated in opposition, as detailed in §2.2. While none of these theories can be formally disproved, it would seem that the underlying mechanisms are more likely to make second-order contributions to the pathogenesis of syringomyelia. The ischaemic concept in particular may be applicable to most forms of syringomyelia, as a disrupted blood supply, either through trauma or syrinx expansion, is likely to feature at some point in the disease process. As for the biomechanical-based approaches, the hydrodynamic and pressure dissociation hypotheses are dismissed on the grounds that they rely on a patent CC which rarely exists in humans of adult age. This leaves seven candidates want of further analysis. To account for a cough-based pressure source exciting the wave-bearing properties of the cerebrospinal system, the coaxial tube model from the elastic jump hypothesis is adopted. Carpenter's predictions are re-evaluated through parameter estimation and asymptotic analysis before making novel modifications to this model to study questions relating to transpial flow. This work constitutes Chapter 3 and the beginning of the present investigation. Poroelasticity has not been attempted in any of the engineering models to date and is thus the second topic addressed from a continuum standpoint (Chapter 4). The emphasis here is on the frequency-dependence of wave speed and attenuation in SC tissue. Following on, a lumped-parameter model is developed for determining the feasibility of the phase-lag mechanism for syrinx formation (Chapters 5–7). This model, driven by a continuous cardiac source, attempts to overcome a limitation of Bilston's preliminary CFD model—namely the omission of the greater part of the cerebrospinal system, all of which would normally be in direct hydraulic communication with the small section

that was modelled. The lumped-parameter approach is suitable to the low arterial frequencies involved and also allows specific disease states and surgical treatment options to be simulated, which constitute Chapter 7. The modelling presented in Part II covers many of the mechanical concepts of the more promising theories reviewed in this chapter. The remaining five hypotheses based on the piston, oedema, intramedullary pulse pressure, tethering and peristaltic concepts are addressed in the subsequent discussion in Part III.

Part II

Methods & Results of Investigation

Synopsis

In this part a series of mathematical models and analysis is presented which are used to investigate the pathogenesis of syringomyelia. The methods involve classical 1-d theory of flow through collapsible tubes (Chapter 3), the theory of poroelasticity (Chapter 4) and lumped-parameter hydraulics (Chapters 5, 6 & 7). Nomenclature is listed at the end of Chapters 3, 4 and 5 for reference.

CHAPTER 3

The elastic jump hypothesis and 1-d continuum modelling

The elastic jump hypothesis was based on a quasi-1-d theory for flow through fluid-filled coaxial tubes. The salient physiological parameters of this model are reviewed here using sources from the literature and the assumptions and predictions of this model are re-evaluated from a mechanical standpoint. Novel modifications are then made to the coaxial tube model to investigate the effects of tissue permeability on pressure wave propagation.

3.1 Introduction

Carpenter and colleagues introduced a theoretical model for pressure-wave propagation in the spinal canal based on a pair of fluid-filled coaxial tubes (Berkouk *et al.*, 2003; Carpenter *et al.*, 2003). This model, in their "preferred interpretation" for the intraspinal system (Carpenter *et al.*, 2003), is shown in Fig. 3.1. The outer rigid tube represents the dura mater, the inner flexible tube the pia mater, the intervening fluid in 'space A' (annular cylinder) corresponds to the CSF in the SSS, and the inner fluid core in 'space B' (circular cylinder) is an approximation of the SC parenchyma. (The alternative interpretation, in which the flexible tube represents the SC and the central

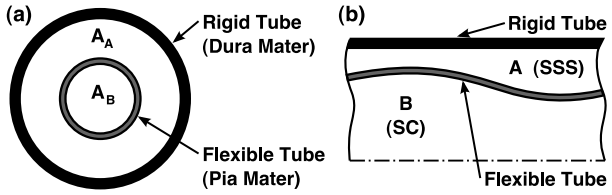

Fig. 3.1: A schematic diagram of the coaxial tubes model used in the elastic jump hypothesis: (a) end view; (b) side view. The contents of the spinal subarachnoid space (SSS) and spinal cord (SC) are represented by inviscid fluid.

canal being the fluid space within, has limited application and will not be discussed here.) To make progress mathematically several assumptions were made. Chiefly, the CSF in the SSS, a viscous fluid, and the SC, a poroelastic solid saturated with CSF-like fluid, were both approximated as inviscid fluid. Radial and circumferential variations in flow variables were omitted, and any changes in the x-direction were assumed to be gradual (long-wave assumption), making the model quasi-1-d. In the undisturbed state the fluid was assumed to be stationary and the cross-sectional areas constant. A pressure-area relation was assigned to the flexible tube, meaning that wall inertia and end effects of the pia were ignored; and the compliance of the dura mater and surrounding tissues were omitted in favour of the rigid tube.

A pressure impulse in the SSS, due to say, a cough, will set up a pressure differential across the pia membrane, $\Delta p = p_{\mathrm{B}} - p_{\mathrm{A}}$, which is expected to split into two waves moving in opposite directions, each having half the original amplitude. In the linear model the speed of these waves will be

$$c_0 = \sqrt{\frac{\alpha_0(1-\alpha_0)}{\rho D}} \tag{3.1}$$

[Berkouk *et al.*, 2003; Eq. (7)], where ρ, D and α_0 are respectively the density of the fluid, the distensibility of the flexible tube, and the nondimensional cross-sectional area of the annular fluid space A ($\alpha_0 = A_{\mathrm{A}0}/A_{\mathrm{T}}$, $A_{\mathrm{T}} = A_{\mathrm{A}} + A_{\mathrm{B}}$ and additional '0' subscripts indicate an equilibrium value). A weakly nonlinear model was developed based on the small parameter $\varepsilon = D\,|\Delta P|$ (i.e. $\varepsilon \ll 1$), where ΔP ($= P_{\mathrm{B}} - P_{\mathrm{A}}$) is the initial

pressure impulse[1], which was used to establish the existence of shock-like elastic jumps originating from pressure waves due to coughs or sneezes. An elastic jump reflecting at a complete blockage of the SSS [e.g., Chiari malformation; Carpenter *et al.* (2003) did not model post-traumatic syringomyelia] would cause a transient region of high Δp to form adjacent to the blockage with amplification factor

$$\Delta_{\mathrm{r}} = \frac{\Delta p_{\mathrm{r}}}{\Delta p_{\mathrm{i}}} = 2 + \frac{2\alpha_0 - 1}{\alpha_0(1-\alpha_0)}\varepsilon + \mathrm{O}(\varepsilon^2) \qquad (3.2\mathrm{a,b})$$

[Carpenter *et al.*, 2003; Eq. (9)]; i.e., the ratio of reflected-to-incident pressure amplitudes. In the linear model a pressure differential Δp will double upon striking a reflection site, yielding $\Delta_{\mathrm{r}} = 2$; i.e., re-attaining the unattenuated Δp at the source location (ΔP) which would be the normal level experienced in a healthy person during a cough. The effect of the weak nonlinearity in (3.2b) is thus to increase the amplification potential of a reflection site (> 2), possibly to values that could damage the SC.

Carpenter *et al.* (2003) calculated the distensibility to be $D = 10^{-5}$ Pa^{-1} from the linear wave speed relation (3.1) by setting $\rho = 10^3$ kg/m^3, $\alpha_0 = 0.2$ and $c_0 = 4$ m/s. For a cough corresponding to a pressure differential $\Delta P = 3$ kPa (22.5 mmHg), the small parameter was $\varepsilon = 0.03$, and $\Delta_{\mathrm{r}} = 2.2,\ 2.33$ and 2.63 for $\alpha_0 = 0.2,\ 0.1$ and 0.05, respectively. Thus the weak nonlinearity could account for a nonphysiological pressure differential of up to 30% above the normal level. The elastic-jump hypothesis (EJH) suggests that elevated pressure within the SC due to an elastic jump reflecting from a stenosis could damage the SC and lead to syrinx formation—a possible mechanism for the pathogenesis of syringomyelia.

Next a renewed survey is presented of the physiological parameters used in the coax-

[1]Carpenter and colleagues used lowercase notation for the general governing equations but swapped to a mixture of lowercase and uppercase notation when modelling the elastic jump to distinguish the various regions of the pressure wave (Berkouk *et al.*, 2003; Carpenter *et al.*, 2003); lowercase is used throughout the present analysis for pressure variables (p_{A}, p_{B}, Δp) and their uppercase counterparts denote constant values associated with the initial impulse (P_{A}, P_{B}, ΔP). Negative ΔP will be dealt with in §3.2.3

Table 3.1: Parameter values used in the present analysis of the elastic jump hypothesis.

Parameter	Value	Parameter	Value
r_{B0}	4 mm	$\lvert\Delta P\rvert$	3 kPa
r_T	7.5 mm	$\lvert\varepsilon\rvert$	0.03
α_0	0.7	τ	0.1 s
D	1×10^{-5} Pa^{-1}	μ	0.85 mPa·s
c_0	5 m/s	ρ	1000 kg/m^3

ial tube model (summarized in Table 3.1). From this the assumptions and predictions of the EJH will be re-evaluated.

3.2 Physiological parameters

3.2.1 Gross geometry: α_0

The mean equilibrium radius of the SC is here defined as r_{B0} and that of the SSS as r_T, hence the geometric parameter becomes $\alpha_0 = (r_T^2 - r_{B0}^2)/r_T^2$. These three parameters were computed—unaveraged—for published anatomical data (Donaldson & Davis, 1903; Elliott, 1945; Lockey *et al.*, 1975; Thijssen *et al.*, 1979; Yu *et al.*, 1985; Fujiwara *et al.*, 1988; Okada *et al.*, 1994; Kameyama *et al.*, 1996; Inoue *et al.*, 1996; Ros *et al.*, 1998; Carpenter *et al.*, 2003; Ko *et al.*, 2004; U. S. National Library of Medicine, n.d.; England & Wakeley, 2006; Zaaroor *et al.*, 2006) by matching cross-sectional area, and are plotted in Fig. 3.2 on axes of SC segment[2] (SC length 40–45 cm; England & Wakeley, 2006); i.e., $\alpha_0 = \bar{\alpha}_{0,x}$. Note that α_0 refers only to the unstenosed SSS—the blockage itself is assumed to be rigid, filling the SSS (Carpenter *et al.*, 2003; Fig. 4).

[2]For sources that did not list measurements by value the measurements were computed by digitizing an electronic copy of the relevant figure (be it graph or histological section). The SC segment axis was taken from Fig. 1d of Ko *et al.* (2004), in which the mean segment length was plotted for C3–S5, and supplemented by Donaldson & Davis (1903), Table I, for segments C1 and C2. In cases where measurements were assigned to vertebral level (Thijssen *et al.*, 1979; Yu *et al.*, 1985; Okada *et al.*, 1994; Inoue *et al.*, 1996; Ros *et al.*, 1998; Zaaroor *et al.*, 2006), the equivalent SC segment position was calculated from Fig. 2-1 of Young & Tolbert (2007). The Visible Human data were digitized from Fig. 2 of Bertram *et al.* (2005) and registration on the SC segment axis was achieved with the additional assistance of Fig. 1 of Loth *et al.* (2001).

The prominent features of Fig. 3.2(a) are the cervical (C5–C6) and lumbosacral (L2–S1) enlargements, and the general reduction in $r_{\mathrm{B0},x}$ from head to tail. The data in Fig. 3.2(b) are comparatively sparse as there have been fewer studies on the dimensions of the SSS, especially below cervical level. Panel (c) shows that in the healthy spinal canal $\alpha_{0,x}$ mostly lies in the range 0.4–0.8, but approaches unity at the cauda equina. The area ratio may reduce further approaching a stenosis. In Fig. 3.2 most of the variation between data sets can probably be attributed to the different measurement protocols. Although the standard deviation for these derived quantities was not available, as an indication of variance, length measurements at a given SC segment position often ranged to ±20% of the mean value (Zaaroor *et al.*, 2006); there is also statistically significant variation in the segment lengths themselves (Ko *et al.*, 2004).

A least-squares regression was performed for each plot, weighting data by the sample size of the study (n-value, see legend); trend lines are plotted in bold in each panel. Also plotted in Fig. 3.2 are the theoretical values used in three models of syringomyelia, denoted by dotted lines. The radii chosen by Lockey *et al.* (1975) are closest to the trend lines, and those by Carpenter *et al.* (2003) are quite far from all measured values[3]. Presently, for the coaxial tube model the mean values $r_{\mathrm{B0}} = 4$ mm, $r_{\mathrm{T}} = 7.5$ mm and $\alpha_0 = 0.7$ are chosen as representative of the intraspinal system.

3.2.2 Distensibility: D

Following classical theory for flow through elastic tubes, Berkouk *et al.* (2003) derived the distensibility from a first-order approximation to a Maclaurin series, which expressed transmural pressure purely as a function of cross-sectional area; i.e.,

$$\frac{A_{\mathrm{A}} - A_{\mathrm{A0}}}{A_{\mathrm{T}}} = -D\Delta p \qquad \Longrightarrow \qquad D = \frac{1}{A_{\mathrm{T}}} \left.\frac{dA_{\mathrm{B}}}{d\Delta p}\right|_{\Delta p=0}, \tag{3.3a,b}$$

[3]By comparison, the recent numerical model by Bertram *et al.* (2008), with linearly varying cross-section, agrees well with the anatomical data in Fig. 3.2.

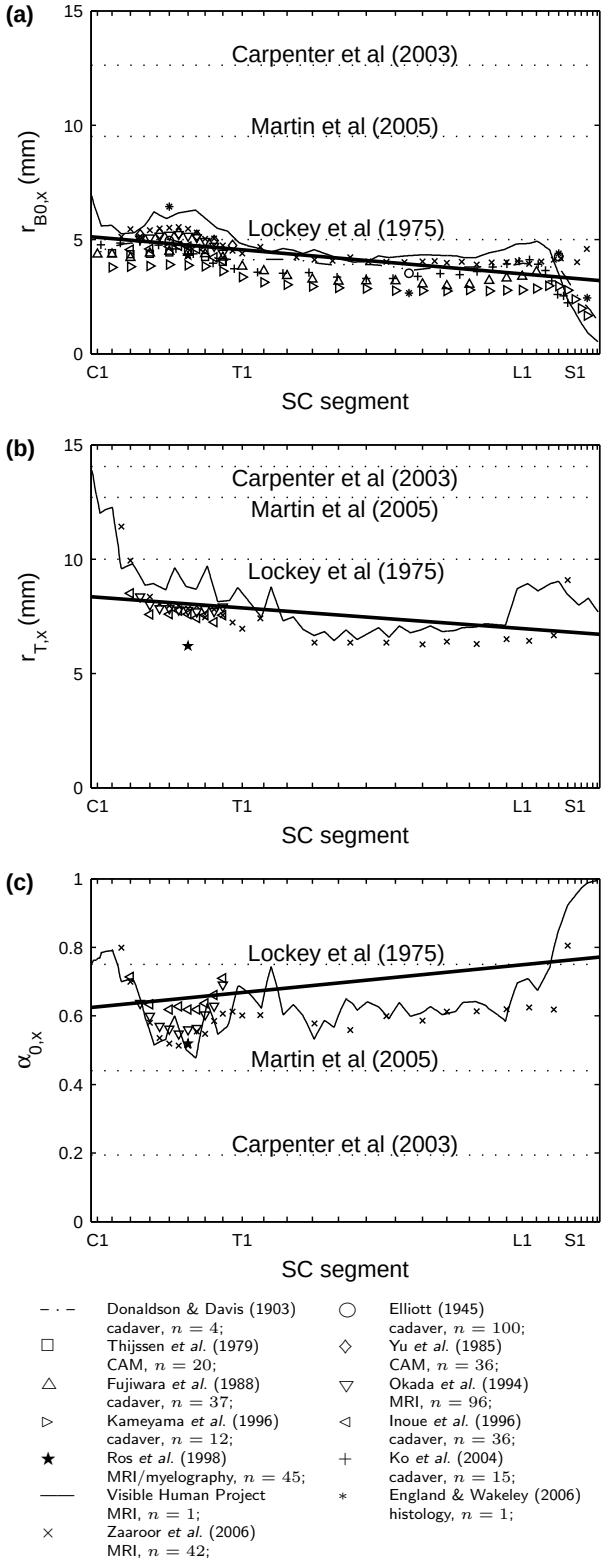

Fig. 3.2: Variation of transverse dimensions of the SC and SSS with SC segment; (a) SC radius, (b) SSS radius, (c) cross-sectional area ratio. The bold line is the sample-weighted least-squares regression line and the three dotted lines correspond to theoretical values used in the indicated papers.

commonly referred to as a 'tube law'. This fixed value of D is equivalent to the reciprocal slope of the curve in Fig. 3.3(a) at zero transmural pressure (where the dashed lines intersect). Since empirical data to construct such a pressure-area curve for the pia were not available, D was simply calculated from Eq. (3.1). However, one can evaluate distensibility independently from the wave speed by applying thin-shell theory, as follows.

The force balance illustrated in Fig. 3.3(b) gives

$$2(\sigma_{\theta\theta}t) - 2\Delta p\, r_{\mathrm{B}} = 0 \qquad \Longrightarrow \qquad \sigma_{\theta\theta} = \frac{r_{\mathrm{B}}}{t}\Delta p, \tag{3.4a,b}$$

which is then used with Hooke's Law to calculate the circumferential strain

$$\epsilon_{\theta\theta} = \frac{\sigma_{\theta\theta}}{E} = \frac{r_{\mathrm{B}}}{Et}\Delta p; \tag{3.5a,b}$$

$\sigma_{\theta\theta}$ is the circumferential stress, E and t are respectively the circumferential elastic modulus and thickness of the flexible tube. However, $\epsilon_{\theta\theta}$ can also be expressed as the differential

$$\epsilon_{\theta\theta} = \frac{\mathrm{d}(2\pi r_{\mathrm{B}})}{2\pi r_{\mathrm{B0}}} = \frac{\mathrm{d}r_{\mathrm{B}}}{r_{\mathrm{B0}}}, \tag{3.6a,b}$$

thus one may write

$$\frac{\mathrm{d}r_{\mathrm{B}}}{r_{\mathrm{B0}}} = \frac{r_{\mathrm{B}}}{Et}\Delta p. \tag{3.7}$$

The relative change in cross-sectional area of the tube lumen due to the pressure difference Δp is:

$$\begin{aligned} \frac{A_{\mathrm{B}} - A_{\mathrm{B0}}}{A_{\mathrm{B0}}} &= \frac{\mathrm{d}A_{\mathrm{B}}}{A_{\mathrm{B0}}} \\ &= \frac{\mathrm{d}(\pi r_{\mathrm{B}}^2)}{\pi r_{\mathrm{B0}}^2} \\ &= 2\frac{r_{\mathrm{B}}}{r_{\mathrm{B0}}}\frac{\mathrm{d}r_{\mathrm{B}}}{r_{\mathrm{B0}}} \\ &= 2\frac{r_{\mathrm{B}}^2}{r_{\mathrm{B0}}Et}\Delta p. \end{aligned} \tag{3.8}$$

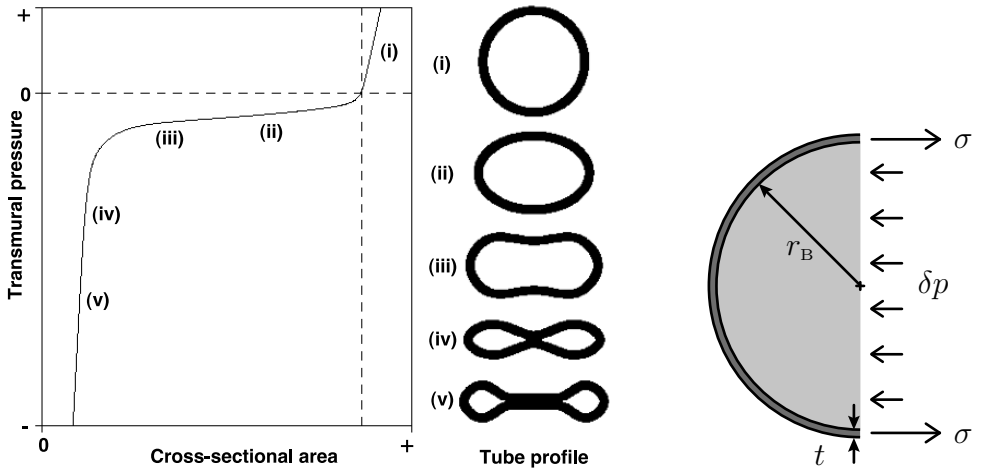

(a) (b)

Fig. 3.3: (a) Tube law and (b) free-body diagram used to calculate the distensibility of a thin-walled tube.

Rearranging Eq. (3.8) in terms of A_{B} and then differentiating with respect to Δp gives

$$\frac{\mathrm{d}A_{\mathrm{B}}}{\mathrm{d}\Delta p} = 2\frac{r_{\mathrm{B}}^2}{r_{\mathrm{B0}}Et}A_{\mathrm{B0}}. \tag{3.9}$$

Noting that $r_{\mathrm{B}} = r_{\mathrm{B0}}$ when $\Delta p = 0$ and $A_{\mathrm{B0}} = A_{\mathrm{T}}(1-\alpha_0)$, the derivative at $\Delta p = 0$ becomes

$$\left.\frac{\mathrm{d}A_{\mathrm{B}}}{\mathrm{d}\Delta p}\right|_{\Delta p=0} = 2\frac{r_{\mathrm{B0}}}{Et}A_{\mathrm{T}}(1-\alpha_0). \tag{3.10}$$

Therefore, substituting (3.10) into (3.3b) gives an expression for distensibility that is independent of the wave speed

$$D = 2\frac{r_{\mathrm{B0}}}{Et}(1-\alpha_0). \tag{3.11}$$

Inserting Eq. (3.11) into (3.1) yields the same wave speed relation as for a 2-d linear axisymmetric model uninhibited by a tube law,

$$c \approx \sqrt{\frac{Et}{2r_{\mathrm{B0}}}\,\frac{\rho_{\mathrm{wall}}}{\rho_{\mathrm{A}}\rho_{\mathrm{B}}}\,\frac{\alpha_0}{1+\alpha_0(\rho_{\mathrm{A}}/\rho_{\mathrm{B}}-1)}} \tag{3.12}$$

(Cirovic *et al.*, 2002), providing that the fluid and solid have matching densities; i.e.,

if $\rho_A = \rho_B = \rho_{wall} = \rho$. Since the flexible tube represents soft tissue and is therefore largely water by mass, and CSF is essentially water [$\rho = 1000$ kg/m^3 (Kiernan, 1998); μ = 0.7–1.0 mPa·s (Bloomfield *et al.*, 1998)], Eq. (3.11) gives a reasonable approximation to the elastic contribution of the flexible tube. The SC is secured by the dentate ligaments which assume enough tension to overcome tethering forces from the filum terminale (Selçuki *et al.*, 2003), likely guarding against SC buckling. Therefore, this approach to determining D should hold for negative as well as positive Δp since the SC will normally be distended.

In addition to the pia mater, the layer of *subpial collagen* further separates the surface of the SC from the SSS (Weller, 1999); these tissues provide the main source of SC elasticity (Yamada *et al.*, 2007). In an electron microscopy study on fresh human cadavers pia thickness was reported at 8–15 μm and subpial thickness to range from 80–90 μm to 130–200 μm (medullary cone and thoracolumbar, respectively; Reina *et al.*, 2004). Therefore, $t = 150$ μm is chosen as a suitable estimate of the combined thickness of the pia mater and subpial tissue, herein collectively referred to as the *pial membrane*. Since $t \ll r_{B0}$ the thin-wall assumption of the coaxial tube model holds.

There is no published value for the elastic modulus of the human spinal pial membrane. The most conservative estimate made here, $E = 2.3$ MPa, is that calculated for the spinal pia mater of rabbits (SC radius 2.5 mm, pia thickness 12 ± 3 μm; Ozawa *et al.*, 2004). In computing D one may choose various permutations of the human and animal parameter values; to order of magnitude, it is found that $D = 1 \times 10^{-5}$ Pa^{-1}. Applying Eq. (3.1) gives $c_0 = 5$ m/s and, although the wave speed is probably not constant [but varies with rostrocaudal position (3.1) and SSS pressure over the cardiac cycle (Martin *et al.*, 2005)], this value compares favourably with clinical estimates of 4–5 m/s (Jackson & Williams, 1979; Greitz *et al.*, 1999). Carpenter *et al.* (2003) fixed the wave speed at 4.0 m/s from the same estimates and then computed D from Eq. (3.1), arriving at the same value.

Although the coaxial tube model assumes the pial membrane to be isotropic and linearly-elastic, there is experimental evidence to the contrary. Measurements of elastic

moduli have demonstrated the viscoelastic nature of the SC and pia mater [e.g., 520–1880 kPa at strain rates of 0.04–0.24 s^{-1} for human SC with pia attached (Bilston & Thibault, 1996); 1400 kPa with and 89 kPa without the pia mater, at rates of 1 and 10 s^{-1} (Mazuchowski & Thibault, 2003); for a viscoelastic model of syringomyelia see Bertram *et al.* (2008)], and at least in the dura mater both anisotropy (e.g., 65–103 MPa longitudinal modulus vs. 4–8 MPa circumferential for human lumbar dura; Runza *et al.*, 1999) and nonlinear elasticity (e.g., 0.4 MPa at 14% strain vs. 46 MPa at 18% for canine thoraco-lumbar dura; Tunturi, 1977) have been confirmed. Since the dura is both stiffer and thicker (≈0.3 mm; Reina *et al.*, 1997) than the pia, and reinforced by bone compared to the pia's milder support from the SC (SC two orders of magnitude less stiff than the pia; Ozawa *et al.*, 2004), the compliance of the pia will dominate the system dynamics making the rigid wall assumption of the coaxial tube model reasonable.

3.2.3 Weak nonlinearity: ε

Coughs studied by Williams were 0.6–0.9 s duration with rise time $\tau = 0.1$ s, and the SSS pressure increased 20–30 mmHg (2.6–4.0 kPa) above resting value (original measurements by Williams, 1972; analysis by Lockey *et al.*, 1975, and Williams, 1976). For such a pulse travelling at 5 m/s in a SC of length 0.5 m, the long-wave assumption is reasonable. When a spinal block was present the SSS pressure measured at the cisternal level was only 23.5% of the value at the lumbar level, compared to 91.5% in otherwise healthy subjects (Lockey *et al.*, 1975). This attenuation takes place over the extra distance the rostral-moving wave has to travel compared to the caudal-moving wave, from the cough epicentre. Carpenter *et al.* (2003) estimated this to be about one third of the length of the SC (15 cm).

The SC is normally distended thus Δp is small but positive. A cough will raise p_{A}

with a concomitant reduction in $p_{\rm B}$ causing Δp to become *negative*; i.e.,

$$p_{\rm A} = -\frac{(1-\alpha_0)}{\alpha_0}\, p_{\rm B} \qquad \Longrightarrow \qquad \Delta p = -\frac{1}{(1-\alpha_0)}\, p_{\rm A} \tag{3.13a,b}$$

(Cirovic *et al.*, 2002). Thus a cough is associated with $p_{\rm A} > 0$ but $p_{\rm B} < 0$ and $\Delta p < 0$; negative $p_{\rm B}$ would be akin to a compressive radial stress in the SC tissue. The weakly-nonlinear theory allows for negative ΔP, providing that $|\varepsilon| \ll 1$ for the asymptotic treatment to hold. Similarly, mass conservation demands that an equal volume of fluid be displaced in opposite directions in the two tubes as a pressure pulse is transmitted. While this might not be realized in the SC due to viscous resistance, the fluid velocities are at least small ($\mathrm{O}(\varepsilon)$) compared to the wave speed so this is probably acceptable [Berkouk *et al.*, 2003; Eq. (14b,c)].

A cough of $P_{\rm A} = 3$ kPa (22.5 mmHg) with $\alpha_0 = 0.7$ equates to $\Delta P = -10$ kPa (75 mmHg). However, when combined with the computed value of D, ε becomes -0.1—not a particularly 'small' parameter. Physically $|\varepsilon|$ must be of the order of a few per cent to ensure that radial strains are small enough for the tube law to remain applicable. To make progress, as the SC parenchyma is plainly not inviscid fluid, the above treatment of Δp is relaxed in the analysis that follows and instead the same magnitude is chosen as used by Carpenter *et al.* (2003): $|\Delta P| = 3$ kPa giving $|\varepsilon| = 0.03$. This may correspond to a 'weaker' cough.

3.3 Hydrodynamic potential of the elastic jump

The prediction of the EJH is manifest in $\Delta_{\rm r}$, which is plotted in Fig. 3.4(a) for positive (solid line) and negative (dash-dot line) values of ΔP ($\varepsilon = \pm 0.03$); the ordinate refers to the leading edge in proximity to a reflection site (3.2b). The elastic jump does not exist at $\alpha_0 = 0.5$ hence $\Delta_{\rm r} = 2$ (dotted line) and corresponds to the linear case of Δp doubling at the reflection site (thereby re-attaining ΔP). The leading edge will steepen, possibly into an elastic jump, when $\Delta P > 0$ and $\alpha_0 > 0.5$ (top-right quadrant), or when

$\Delta P < 0$ and $\alpha_0 < 0.5$ (top-left), resulting in $\Delta_r > 2$ at the leading edge and $\Delta_r < 2$ at the trailing edge (not shown). The reverse is true for steepening at the trailing edge, therefore the weak nonlinearity will always give rise to $\Delta_r > 2$ provided that $\alpha_0 \neq 0.5$.

Over much of the central range, $0.22 < \alpha_0 < 0.78$, the nonlinearity only allows for a 5% change in Δ_r over the linear case; i.e. $|\Delta_r - 2|/2 < 5\%$. In fact, from (3.2b) it is found that the effect of the nonlinearity is $(\Delta_r - 2)/2 < |\varepsilon|$ for $0.29 < \alpha_0 < 0.71$, and $(\Delta_r - 2)/2 < 2|\varepsilon|$ for $0.13 < \alpha_0 < 0.87$. Given that $|\varepsilon| \ll 1$ these are small effects indeed. For significant Δ_r adjacent to a hindbrain tonsil $\alpha_0 \approx 0$ would need to be realized.

Pulsatile viscous flow in an elastic tube can be described by the Womersley number, $\mathrm{Wo} = R\sqrt{\omega/\nu}$ (R is an appropriate length scale, ω is the pulsation frequency, ν is the kinematic viscosity). For the SSS, $R = r_T - r_B$, and for the SC, $R = r_B$ (Loth *et al.*, 2001); an isolated pressure pulse has $\omega = 2\pi/\tau$ (Berkouk *et al.*, 2003)[4]. For viscous effects to be ignored Wo is required to be 'large', typically > 10 (McDonald, 1974). Using the parameter values from Table 3.1, for the SSS it is found that $\alpha_0 > 0.29$ are permissible. (Similarly, an upper limit on α_0 probably exists for the SC but the approximation of a poroelastic solid as a fluid is not amenable to the same quantitative assessment.) The estimate of α_0, 0.7, can be broadened to cover the cervicothoracic range (0.4–0.8, Fig. 3.2(c)) and an allowance can also be made for SSS narrowing towards a stenosis, to give say $0.3 < \alpha_0 < 0.8$; thus the inviscid assumption is reasonable in the SSS.

However, the permissible α_0 fall in the region where the elastic jump is marginal: $(\Delta_r - 2)/2 < |\varepsilon|$; i.e., the potency of the elastic jump is compromised by the inviscid assumption upon which the coaxial tube model is reliant. The weak nonlinearity may thus confer 5% greater amplification at a reflection site than linear pressure-doubling. Nonetheless, clinical measurements indicate that caudorostral attenuation is at least 10% (Lockey *et al.*, 1975). Therefore, even with this marginal nonlinear effect, the

[4]The nondimensional number T used by Berkouk *et al.* [2003; Eq. (10)] to describe the ratio of viscous-to-inertial forces is thus related to the Womersley number as $T = \sqrt{\pi/2}\,/\,\mathrm{Wo}$.

maximum Δp at the reflection site will not exceed the unattenuated pressure differential at the site of the cough pulse generation (ΔP).

Figure 3.4(b) depicts the distance required for an elastic jump to form, s_τ, for a pulse with rise time τ, as a function of α_0. If the base of the wave has speed V_0 and the crest of the wave has speed $V = V_0 + V_1\varepsilon + \mathrm{O}(\varepsilon^2)$, where

$$V_0 = c_0 \qquad \text{and} \qquad V_1 = \frac{3}{4}\frac{(2\alpha_0 - 1)}{\alpha_0(1-\alpha_0)}c_0 \tag{3.14a,b}$$

[Berkouk *et al.*, 2003; Eq. (29a,b)], then an elastic jump will occur when the crest of the wave catches up to the base of the wave which will take place at a distance

$$s_\tau = V_0\tau\left(1 + \frac{V_0}{|V_1\varepsilon|}\right) + \mathrm{O}(\varepsilon^2). \tag{3.15}$$

As would be expected, at $\alpha_0 = 0.5$ there is no elastic jump hence the asymptote, and $s_\tau = 0$ at $\alpha_0 = 0, 1$ corresponds to the theoretical limit of instantaneous wave steepening. Evidently, for the majority of physiological values of α_0 the pressure wave is unlikely to have time to steepen fully within the length of the spinal canal, further reducing the hydrodynamic potential of the elastic jump.

The preceding analysis of elastic jumps applied equally to positive and negative Δp. However, the direction of the pressure gradient dictates both fluid movement and displacement of the flexible tube. For a cough $\Delta p < 0$, so CSF will be drawn into the SC but the pial membrane will also be displaced inward, competing for bulk SC volume. What will determine where fluid accumulates is the balance of viscous CSF resistances in the perivascular spaces and SC with elastic forces sustained in the SC tissue and confining pial membrane. The EJH cited elevated, *positive* Δp as a mechanism for the pathogenesis of syringomyelia. Not only will a cough induce a *negative* Δp, precisely the condition that Carpenter *et al.* (2003) used to argue against other pathogenesis hypotheses (e.g., the piston hypothesis), but the coaxial tube model as it stands does not permit fluid movement across the pial membrane and therefore cannot adequately

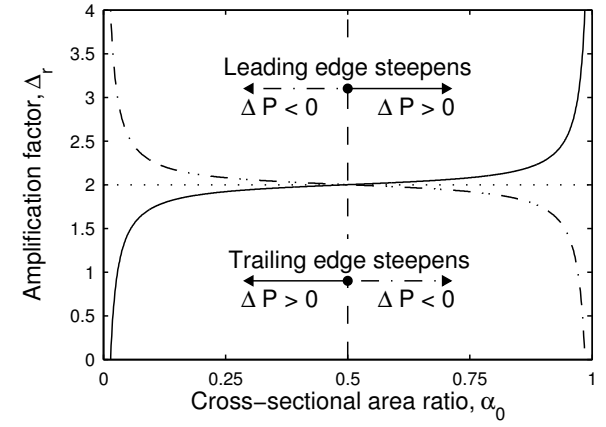

(a)

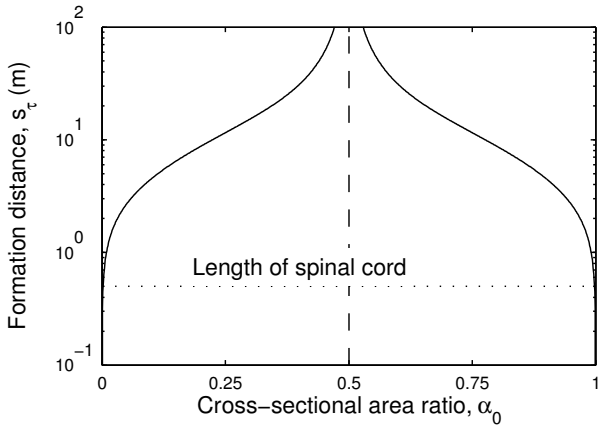

(b)

Fig. 3.4: A demonstration of the asymptotic behaviour of the elastic jump in the coaxial tube model. (a) The amplification factor of an elastic jump reflecting from a reflection site, Δ_r, for the cases of $\Delta p > 0$ (——) and $\Delta p < 0$ (– · –); (b) the distance required for an elastic jump to form, s_τ, compared to the length of the spinal cord (dotted line).

address the issue of syrinx formation.

It has been demonstrated that the peak pressure differential due to a cough or sneeze is likely to occur at the site of origin rather than at a reflection site. Since this is not consistent with the pathology, this suggests that there must be some other localising factor more critical to providing the necessary conditions for syrinx formation than the magnitude of the transpial pressure differential. However, a model must be validated with experiment and the clinical measurements of cough pulses in humans constitute the most reliable data against which to compare. Any model of syringomyelia should be able to predict realistic wave speeds for simulated coughs.

Analytical models such as that of Carpenter and colleagues are desirable as they give a deeper insight into the underlying mechanics. With this in mind, in the next section the coaxial tube model is modified to answer some questions of fundamental significance.

3.4 Novel modifications to the coaxial tube model

3.4.1 Overview

Will a pressure pulse propagating through the SSS excite significant fluid exchange between the SSS and the SC? i.e., bulk flow due to a transpial pressure gradient, rather than due to some sort of valvular or pumping mechanism. Proponents of the piston hypothesis, at least, would say 'yes' but no models or measurements have appeared thus far to substantiate such a claim. Therefore the flexible tube is made permeable using Darcy's law (§3.4.2) and a model of pressure wave attenuation due to transmembrane flow is developed (§3.4.3). The approximation of the SC as inviscid fluid is retained to maximise system compliance and isolate dissipation to the flexible tube.

Following on, the issue of the inviscid SC is addressed next (§3.4.4). The premise for this approximation was that the cylindrical fluid space was originally intended to represent the central canal (Carpenter *et al.*, 1999). Upon realising that the central

canal is seldom present, and noting that the SC tissue is very deformable and has a high water content, the authors reinterpreted this inviscid fluid as the SC itself (Carpenter *et al.*, 2003). In reality the SC is more like a poroelastic solid saturated with viscous fluid. For a transmural pressure wave to propagate the SC must deform, which will tend to displace the fluid in the pores in order to accommodate the tissue. To determine to what extent fluid in the SC flows relative to the confining tissue, the SC is modelled as a permeable solid and Darcy flow is permitted in the longitudinal direction.

3.4.2 Darcy's law

Darcy's law is a phenomologically derived constitutive equation that describes creeping fluid flow through a porous medium.[5] Although this law—an expression of conservation of momentum—was determined experimentally by Darcy, it has since been derived from the Navier-Stokes equations via homogenisation. Darcy's law is a simple proportional relationship between the instantaneous discharge rate through a porous medium, the viscosity of the fluid and the pressure drop over a given distance. The flux (with units of length per unit time) through a permeable material in the x direction is given by

$$q_x = -\frac{\kappa_x}{\mu}\frac{\partial p}{\partial x}, \tag{3.16}$$

where κ_x is the material permeability, μ is the dynamic viscosity of the fluid and $\partial p/\partial x$ is the pressure gradient. Note that a negative pressure gradient is required for a positive flux.

[5]It is analogous to Fourier's law in the field of heat conduction, Ohm's law in the field of electrical networks, or Fick's law in diffusion theory.

3.4.3 Model with a permeable pial membrane

For annular space A and cylindrical space B, the continuity equations are

$$\frac{\partial \alpha}{\partial t} + \frac{\partial (v_{\mathrm{A}} \alpha)}{\partial x} + \frac{2(1-\alpha)^{1/2}}{r_{\mathrm{T}}} q_{\mathrm{AB}} = 0, \tag{3.17a}$$

$$\frac{\partial (1-\alpha)}{\partial t} + \frac{\partial (v_{\mathrm{B}}(1-\alpha))}{\partial x} - \frac{2(1-\alpha)^{1/2}}{r_{\mathrm{T}}} q_{\mathrm{AB}} = 0, \tag{3.17b}$$

respectively; q_{AB} is the flux from space A to space B through the permeable flexible tube, and $2(1-\alpha)^{1/2}/r_{\mathrm{T}}$ is the circumference of the flexible tube ($2\pi r_{\mathrm{B}}$) divided by the cross-sectional area of the rigid tube (A_{T}). The momentum equations are

$$\frac{\partial v_{\mathrm{A}}}{\partial t} + v_{\mathrm{A}} \frac{\partial v_{\mathrm{A}}}{\partial x} = -\frac{1}{\rho_{\mathrm{csf}}} \frac{\partial p_{\mathrm{A}}}{\partial x}, \tag{3.18a}$$

$$\frac{\partial v_{\mathrm{B}}}{\partial t} + v_{\mathrm{B}} \frac{\partial v_{\mathrm{B}}}{\partial x} = -\frac{1}{\rho_{\mathrm{csf}}} \frac{\partial p_{\mathrm{B}}}{\partial x}, \tag{3.18b}$$

$$q_{\mathrm{AB}} = -\frac{\kappa_{\mathrm{pia}}}{\mu} \frac{\Delta p}{t}. \tag{3.18c}$$

If the flexible tube is made impermeable ($\kappa_{\mathrm{pia}} \equiv 0$) then (3.17a,b) reduce to the continuity equations from Berkouk *et al.* [2003; Eqs (2a,b)], as expected. The transmembrane flux does not make a contribution to the axial momentum since to maintain the inviscid assumption within space A and space B the associated $\partial/\partial r$ term must be identically zero. Thus the axial momentum equations (3.18a,b) are the same as those in Berkouk *et al.* [2003; Eqs (3a,b)]. The third momentum equation (3.18c) is Darcy's law applied to the flexible tube with thickness t.

The tube law (3.3a) can be rewritten as

$$\alpha = \alpha_0 - D\Delta p \qquad \Rightarrow \qquad \mathrm{d}\alpha = -D \, \mathrm{d}\Delta p, \tag{3.19a,b}$$

and then, together with (3.18c), can be applied to the continuity equations (3.17a) and

(3.17b) to eliminate the dependence on the geometric variable α:

$$\frac{\partial \Delta p}{\partial t} + v_{\mathrm{A}} \frac{\partial \Delta p}{\partial x} - \left(\frac{\alpha_0}{D} - \Delta p \right) \frac{\partial v_{\mathrm{A}}}{\partial x} + \frac{2\kappa_{\mathrm{pia}}}{\mu l r_{\mathrm{T}}} \frac{[(1-\alpha_0) + D\Delta p]^{1/2}}{D} \Delta p = 0, \tag{3.20a}$$

$$\frac{\partial \Delta p}{\partial t} + v_{\mathrm{B}} \frac{\partial \Delta p}{\partial x} + \left(\frac{1-\alpha_0}{D} + \Delta p \right) \frac{\partial v_{\mathrm{B}}}{\partial x} + \frac{2\kappa_{\mathrm{pia}}}{\mu l r_{\mathrm{T}}} \frac{[(1-\alpha_0) + D\Delta p]^{1/2}}{D} \Delta p = 0. \tag{3.20b}$$

Next, (3.18a) is subtracted from (3.18b) to get a single axial momentum equation

$$\frac{\partial v_{\mathrm{B}}}{\partial t} - \frac{\partial v_{\mathrm{A}}}{\partial t} + v_{\mathrm{B}} \frac{\partial v_{\mathrm{B}}}{\partial x} - v_{\mathrm{A}} \frac{\partial v_{\mathrm{A}}}{\partial x} + \frac{1}{\rho_{\mathrm{csf}}} \frac{\partial \Delta p}{\partial x} = 0. \tag{3.21}$$

We now have three governing equations in three dependent variables: v_{A}, v_{B} and Δp.

For the propagation of *small-amplitude* waves (3.20a,b) and (3.21) can be linearised. Making use of the binomial theorem,

$$\begin{aligned} [(1-\alpha_0) + D\Delta p]^{1/2} &= (1-\alpha_0)^{1/2} \left[1 + \frac{D\Delta p}{1-\alpha_0} \right]^{1/2} \\ &= (1-\alpha_0)^{1/2} \left[1 + \frac{1}{2} \left(\frac{D\Delta p}{1-\alpha_0} \right) - \frac{1}{8} \left(\frac{D\Delta p}{1-\alpha_0} \right)^2 + \dots \right], \end{aligned} \tag{3.22}$$

the modified continuity equations (3.20a,b) become

$$\frac{\partial \Delta p}{\partial t} - \frac{\alpha_0}{D} \frac{\partial v_{\mathrm{A}}}{\partial x} + \beta_0 \Delta p = 0, \tag{3.23a}$$

$$\frac{\partial \Delta p}{\partial t} + \frac{1-\alpha_0}{D} \frac{\partial v_{\mathrm{B}}}{\partial x} + \beta_0 \Delta p = 0, \tag{3.23b}$$

where β_0 is the constant

$$\beta_0 = \frac{2\kappa_{\mathrm{pia}}}{\mu l r_{\mathrm{T}} D} (1-\alpha_0)^{1/2}. \tag{3.24}$$

Similarly, the linearised axial momentum equation is

$$\frac{\partial v_{\mathrm{B}}}{\partial t} - \frac{\partial v_{\mathrm{A}}}{\partial t} + \frac{1}{\rho_{\mathrm{csf}}}\frac{\partial \Delta p}{\partial x} = 0. \tag{3.25}$$

Finally, by differentiating Eq. (3.25) with respect to x,

$$\frac{\partial^2 v_{\mathrm{B}}}{\partial x \partial t} - \frac{\partial^2 v_{\mathrm{A}}}{\partial x \partial t} + \frac{1}{\rho_{\mathrm{csf}}}\frac{\partial^2 \Delta p}{\partial x^2} = 0, \tag{3.26}$$

which may be rewritten as[6]

$$\frac{\partial}{\partial t}\left\{\frac{\partial v_{\mathrm{B}}}{\partial x}\right\} - \frac{\partial}{\partial t}\left\{\frac{\partial v_{\mathrm{A}}}{\partial x}\right\} + \frac{1}{\rho_{\mathrm{csf}}}\frac{\partial^2 \Delta p}{\partial x^2} = 0, \tag{3.27}$$

and then rearranging equations (3.23a,b),

$$\frac{\partial v_{\mathrm{A}}}{\partial x} = \frac{D}{\alpha_0}\left(\frac{\partial \Delta p}{\partial t} + \beta_0 \Delta p\right), \tag{3.28a}$$

$$\frac{\partial v_{\mathrm{B}}}{\partial x} = -\frac{D}{(1-\alpha_0)}\left(\frac{\partial \Delta p}{\partial t} + \beta_0 \Delta p\right), \tag{3.28b}$$

one arrives at the following *damped wave equation*

$$\frac{\partial^2 \Delta p}{\partial t^2} - c_0^2 \frac{\partial^2 \Delta p}{\partial x^2} + \beta_0 \frac{\partial \Delta p}{\partial t} = 0; \tag{3.29}$$

c_0 is the same wave speed as for the impermeable tube model [Eq. (3.1), p. 56] and β_0 is a pressure damping coefficient due to the permeability of the flexible tube (3.24).

Equation (3.29), also known as the *telegrapher's equation*,[7] has an exact general solution for the initial-value problem which can be obtained using a Green's function (details given in §B.1). To assess how much a pressure wave will attenuate over a given distance, we consider the propagation of a longitudinal pressure profile in an otherwise

[6]The interchanging of $\partial^2/\partial x \partial t$ and $\partial^2/\partial t \partial x$ as applied to v_{A} and v_{B} in Eq. (3.27) assumes that these partial derivatives are continuous for all (x,t).

[7]The telegrapher's equation governs the propagation and attenuation of electrical signals on telegraph lines.

undisturbed system; i.e., the initial conditions are

$$\Delta p(x,0) = f(x) \qquad \text{and} \qquad \frac{\partial \Delta p}{\partial t}(x,0) = 0. \tag{3.30a,b}$$

The solution to this initial-value problem is:

$$\begin{aligned}\Delta p(x,t) \;=\; & \frac{1}{2}\exp\!\left(-\frac{\beta_0 t}{2}\right)\left[f(x-c_0t)+f(x+c_0t)\right] \\ & +\frac{\beta_0 t}{4}\exp\!\left(-\frac{\beta_0 t}{2}\right)\int_{x-c_0t}^{x+c_0t}\frac{I_1\!\left[(\beta_0/2c_0)\sqrt{c_0^2t^2-(x-\xi)^2}\right]}{\sqrt{c_0^2t^2-(x-\xi)^2}}f(\xi)\,d\xi \\ & +\frac{\beta_0}{4c_0}\exp\!\left(-\frac{\beta_0 t}{2}\right)\int_{x-c_0t}^{x+c_0t} I_0\!\left[(\beta_0/2c_0)\sqrt{c_0^2t^2-(x-\xi)^2}\right]f(\xi)\,d\xi;\end{aligned} \tag{3.31}$$

I_0 and I_1 are zeroth and first order modified Bessel functions of the first kind, respectively. Other than choosing $f(x) = \delta(x)$, which does not correspond to any physical possibility, one must resort to quadrature to evaluate the two integral terms.

3.4.4 Model with a permeable spinal cord parenchyma

Here the flexible tube is returned to its impermeable state which gives the same continuity equations as employed by Berkouk *et al.* [2003; Eqs (2a,b)]; i.e.,

$$\frac{\partial \alpha}{\partial t} + \frac{\partial (v_{\rm A}\alpha)}{\partial x} = 0, \tag{3.32a}$$

$$\frac{\partial (1-\alpha)}{\partial t} + \frac{\partial (v_{\rm B}(1-\alpha))}{\partial x} = 0. \tag{3.32b}$$

Eq. (3.18a) still holds for the momentum balance for annular space A but the momentum equation for cylindrical space B is now given by Darcy's law,

$$v_{\rm B} = -\frac{\kappa_{\rm SC}}{\mu}\frac{\partial p_{\rm B}}{\partial x}. \tag{3.33}$$

The variable v_{B} now properly refers to a mean flux rather than a blunt velocity profile. Following much the same manipulation described in the previous section a damped wave equation is once again obtained,

$$\frac{\partial^2 \Delta p}{\partial t^2} - c_1^2 \frac{\partial^2 \Delta p}{\partial x^2} + \beta_1 \frac{\partial \Delta p}{\partial t} = 0, \tag{3.34}$$

where

$$c_1 = \sqrt{\frac{\alpha_0}{\rho D}} \qquad \text{and} \qquad \beta_1 = \frac{\mu}{\rho \kappa_{\mathrm{SC}}} \frac{\alpha_0}{(1-\alpha_0)}. \tag{3.35a,b}$$

3.4.5 Physiological parameters

The pial permeability κ_{pia} can be derived by consolidating Darcy's law with Poiseuille's law. The volumetric flow rate Q of a fluid of viscosity μ through a surface of area A having permeability κ due to a pressure gradient $-\partial p/\partial x$ is given by

$$Q = -A \frac{\kappa}{\mu} \frac{\partial p}{\partial x}. \tag{3.36}$$

If this permeability is due to n circular passages passing through the wall, each having radius r_i, then the total flow rate is given by

$$Q = \sum_{i=1}^{n} \left(\frac{\pi r_i^4}{8\mu} \frac{\partial p}{\partial x} \right). \tag{3.37}$$

In the pia mater these passages are in fact the annular perivascular spaces (PVS) surrounding fenestrating blood vessels. An annular space, defined by inner radius r_{inner} and outer radius r_{outer}, can be approximated by the equivalent circular space having radius $r_{\mathrm{PVS}} = r_{\mathrm{outer}} - r_{\mathrm{inner}}$ (i.e., twice the cross-sectional area divided by the wetted perimeter). Therefore, setting $r_i = r_{\mathrm{PVS}}$ and then equating (3.36) and (3.37) gives the pial permeability

$$\kappa_{\mathrm{pia}} = \frac{n_{\mathrm{PVS}}}{L_{\mathrm{SC}}} \frac{r_{\mathrm{PVS}}^4}{16\, r_{\mathrm{B0}}}; \tag{3.38}$$

Table 3.2: Parameter values used in permeable tissue models.

Parameter	Value	Parameter	Value
n_{SC}	225	κ_{pia}	3.1×10^{-15} m^2
L_{SC}	45 cm	κ_{SC}	5.6×10^{-15} m^2
r_{inner}	50 µm	c_0	4.6 m/s
r_{outer}	75 µm	c_1	8.4 m/s
r_{PVS}	25 µm	β_0	3.5×10^{-1} s^{-1}
t	150 µm	β_1	3.5×10^{8} s^{-1}

n_{PVS} is the total number of perivascular spaces over the length of the SC, which has surface area $A = 2\pi r_{\mathrm{B0}} L_{\mathrm{SC}}$. Using the parameter values from Table 3.1 together with empirical data from Bilston *et al.* (2003) the pial permeability is estimated at 3.1×10^{-15} m^2.

For the permeability of SC tissue to ISF flow a value of $\kappa_{\mathrm{SC}} = 5.6 \times 10^{-15}$ m^2 appears to be a best estimate, being the average of the values used by Smillie *et al.* (2005) for cranial grey (1.4×10^{-16} m^2) and white (1.1×10^{-14} m^2) matter in their poroelastic model of hydrocephalus. Finally, the two damping coefficients are calculated to be $\beta_0 = 3.5 \times 10^{-1}$ s^{-1} and $\beta_1 = 3.5 \times 10^{8}$ s^{-1}. The values of all the parameters introduced in this section are summarised in Table 3.2.

3.4.6 Results

Since the objective here is to assess the importance of attenuation in wave propagation, a simple square impulse of width a and amplitude 1 is chosen,

$$f(x) = H(x + a) - H(x - a), \tag{3.39}$$

constructed from Heaviside step functions; because the system is linear, positive and negative Δp attenuate in identical fashion, thus the polarity of $f(x)$ is unimportant. Eq. (3.31) is evaluated numerically using the adaptive Gauss-Kronrod algorithm (`quadgk` routine, MATLAB), which is able to handle the integration singularities. The wave is permitted to travel 0.3 m—two thirds of the length of the SC and the distance

from the cough excitation point to the hindbrain tonsil; i.e. the maximum distance a wave can travel before reaching the reflection site.

The results for the permeable pial membrane are shown in Fig. 3.5. Plotted is the amplitude of the impulse as it travels the length of the coaxial tube system [$\Delta p'_{c_0 t} = \Delta p(x = c_0 t)/\Delta p(x = 0)$]. Four values of attenuation coefficient are trialled, beginning with β_0 and then scaling by successive orders of magnitude. The impulse initially splits into two waves of half the original height, travelling in opposite directions; the right moving wave (shown), after travelling a distance of $a/2$, has an amplitude of 0.5. Evidently, for the value of β_0 calculated in Table 3.2, the propagation of the pressure pulse does not induce sufficient transpial flow for viscous losses to attenuate the pulse over its passage through the spinal canal. To effect significant attenuation β_0 must be around two orders of magnitude larger. Looking at the definitions of β_0 (3.24) and D (3.11) and reviewing the estimations for each of the parameters, the most likely candidates for such large-scale modifications are the permeability (κ_{pia}), elastic modulus (E) and thickness (t) of the pial membrane. Modified pial permeability could arise by disruption to the spinal blood supply, a common feature in SC pathologies, changing the resistance to perivascular flow. Scar tissue caused by arachnoiditis would tend to stiffen and thicken the pial membrane but this would increase the wave speed as well as the damping coefficient so the consequences for transpial flow and attenuation are not straightforward.[8]

The behaviour for the case of the permeable SC parenchyma, although not plotted, can be gleaned from Fig. 3.5. Since $\beta_1 \gg \beta_0$ the effect of adding viscous resistance to flow within the flexible tube is to damp the pressure pulse to zero almost instantly. This should be expected since, for the pulse to propagate, the continuity equations (3.32a,b) demand that fluid be displaced to accommodate the deformation of the flexible tube. It is interesting to note that tissue permeability plays opposing roles in the SC compared to the pial membrane; the propagation of a pressure wave is aided by a less-permeable pia but a more-permeable SC (compare (3.24) with (3.35)). However, it is known from

[8]The scale-dependent behaviour of Eq. (3.29) is demonstrated in §B.2.

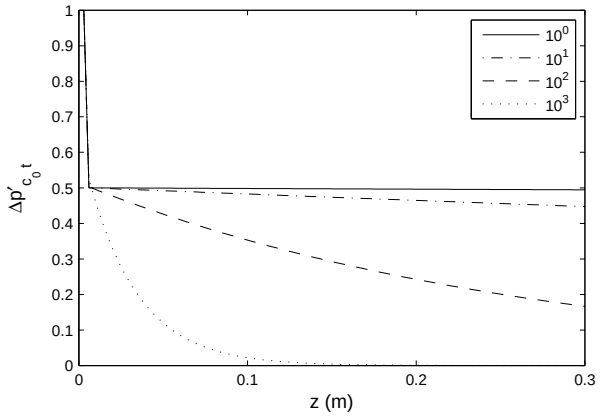

Fig. 3.5: The attenuation of a pressure pulse travelling two thirds of the length of the spinal cord, for the nondimensional damping ratios, β/β_0, indicated by the legend. The reference value β_0 is given in Table 3.2.

invasive pressure measurements that cough pulses manage to traverse the length of the SSS with only a moderate degree of attenuation (Lockey *et al.*, 1975). The other possibility for SC deformation, not accounted for by the simple nature of Darcy's law, is deformation of the SC tissue itself. This is the mechanism embraced by Bertram *et al.* (2005; 2008) in their model which approximated the SC as an elastic solid. In any case, Darcy's law does not adequately capture the poroelastic wave mechanics of the SC so a more detailed approach is required.

3.5 Summary

For a task as complex as a biomechanical model of syringomyelia all things cannot be resolved in one attempt. Analytical models such as that of Carpenter and colleagues are desirable as they give a deeper insight into the underlying mechanics. There is also a need for some systematic assumptions and approximations in order to make progress. The review of physiological parameters presented here establishes some guidelines for model design. In a one-dimensional model of the SSS the inviscid assumption is a reasonable one; as for the SC itself, a more realistic model is required taking into account the fluid-saturated poroelastic nature of the tissue. Transpial flow induced by pressure

wave propagation is a possible source for attenuation, which may be exacerbated by disruptions to the SC blood supply due to a spinal disease such as syringomyelia. The analysis presented here does not support the elastic-jump hypothesis and suggests that there must be some other localising factor more critical to providing the necessary conditions for syrinx formation than the magnitude of the transpial pressure differential. In the next chapter attention turns to the theory of poroelasticity.

Nomenclature

Latin symbols:

- A Cross-sectional area of tube;
- D Distensibility of the flexible tube;
- E Elastic modulus of the flexible tube;
- L Length;
- P The initial pressure generated by a cough (note that $\Delta P = P_{\mathrm{B}} - P_{\mathrm{A}}$);
- Q Volumetric flow rate;
- R The hydraulic radius of a tube, taken to be twice the cross-sectional area divided by the wetted perimeter;
- T Nondimensional number describing ratio of viscous-to-inertial forces in a pulsatile flow ($= \sqrt{\pi/2} \cdot 1/\mathrm{Wo}$);
- Wo Womersley number, describes the ratio of viscous-to-inertial forces in a pulsatile flow;
- n The number of (perivascular) spaces over the length of the spinal cord;
- p A pressure pertaining to a wave travelling in the coaxial tube system (note that $\Delta p = p_{\mathrm{B}} - p_{\mathrm{A}}$);

r A tube radius (also denotes the radial coordinate of a cylindrical coordinate system);

t Thickness of flexible tube;

x Axial coordinate of the cylindrical coordinate system.

Greek symbols:

α Cross-sectional area ratio ($= A_{\mathrm{A}}/A_{\mathrm{T}}$);

β Damping coefficient;

Δ_r Pressure amplification ratio ($= \Delta p_{\mathrm{r}}/\Delta p_{\mathrm{i}}$);

ε Small parameter used in weakly nonlinear theory ($= D\Delta P$);

κ Permeability;

μ Dynamic viscosity;

ν Kinematic viscosity;

ρ Density, both for fluids and solid tissues within the spinal canal;

τ Pressure pulse rise time, which is the time taken for pressure to reach its peak value from the beginning of a given pulse (for a cough this corresponds to a steep slope on the p-t trace);

ω Angular oscillation frequency.

Subscripts:

0 Refers to quantity at time $t = 0$ (quiescent state);

A Refers to quantity in annular cylindrical space A;

B Refers to quantity in circular cylindrical space B;

pia Refers to a property of the pial membrane;

PVS Refers to a property of the perivascular space;

SC Refers to a property of the spinal cord;

T Refers to quantity in total of space A and space B;

i Refers to a pulse incident on a stenosis;

r Refers to a pulse reflected from a stenosis;

x Refers to quantity varying in x direction;

τ Refers to a quantity associated with the pulse rise time.

CHAPTER 4

Poroelasticity in spinal cord tissue

"Every living membrane, of necessity, is permeable to fluid. The difference between a perforated and a permeable membrane is merely the size and number of its holes." — Gardner (1965; p.251).

4.1 Introduction

A complete model of the cerebrospinal system, taking into account the viscous and inertial effects of both the fluid and solid components of the porous SC tissue, is a substantial leap in complexity from what has been attempted to date. In the construction of any such model it is important to first understand the behaviour of each of the components before assembling them into the whole. Continuum models of the cerebrospinal system have been able to identify the dominant wave modes for approximations of the SC as either an inviscid fluid or an elastic solid but the simple Darcy's law approach to the porous problem is unsatisfactory. Therefore, in this chapter the wave-bearing properties are investigated for an infinite fluid-saturated poroelastic continuum having material properties representative of the human SC. A series of parametric sensitivity studies are reported which indicate the behaviour specific to the porous nature of the material.

For the study of wave propagation in a porous material there are two approaches

that are in present use: the *Theory of Poroelasticity* and the *Theory of Porous Media*. Both model a two-phase continuum consisting of a porous solid skeleton saturated with an interstitial pore fluid. Their main difference lies in the way the solid-fluid interaction is handled.

The framework for the Theory of Poroelasticity was first presented in 1941 by Biot, based on the earlier work of von Terzaghi (1923). This was a quasi-steady-state theory that was derived in an intuitive fashion and used to study the settlement of soils under load, a phenomenon called consolidation. Later Biot extended this theory to include anisotropy (Biot, 1955), viscoelasticity (Biot, 1956a), and eventually the full unsteady formulation for low-frequency (Biot, 1956b) and high-frequency waves (Biot, 1956c). One of the major findings in these latter two papers was the identification of three different plane wave types for a fluid-saturated porous continuum: a shear wave and two kinds of dilatational wave. The shear wave, transmitted by the solid, and the faster of the two dilatational waves, transmitted by the fluid and solid moving in phase, are analogous to the two wave types in classical linear elasticity theory. The additional dilatational wave, also known as the slow wave, corresponds to the solid and fluid moving out of phase with one another and has been confirmed experimentally (Plona, 1980).

In contrast to Biot's Theory of Poroelasticity, the Theory of Porous Media has been the incremental effort of a number of researchers and so has taken longer to develop. Inspired by the work of Fillunger (1913), this theory is based on the axioms of continuum theories of mixtures (Truesdell & Toupin, 1960; Bowen, 1976) extended by the concept of volume fractions (Bowen, 1980; 1982; Ehlers, 1993). Part of the motivation in developing this theory has been to rigorously define the pore-level micromechanics through tensor transformations, rather than keep to the more phenomenological approach of Biot. The same three wave types are predicted as described above.

In the case of incompressible constituents, the two theories are equivalent providing that the apparent mass density term is set to zero. On the other hand, if the constituents are compressible then each theory may predict a different outcome (Schanz

& Diebels, 2003). The different sets of governing equations and material parameters has made comparison of the two theories problematic. However, Biot's theory has been around longer and it has stood up to experimental validation, and so is the approach that is adopted here. For more details on the Theory of Porous Media, the interested reader is referred to the book by de Boer (2000). Next, the governing equations are given for the Theory of Poroelasticity, along with a description of the material parameters.

4.2 Governing equations

In a Lagrangian formulation the equations of motion for a fluid-saturated poroelastic solid are

$$N\nabla^2\boldsymbol{u} + \nabla[(A+N)\boldsymbol{e} + Q\boldsymbol{\epsilon}] = \frac{\partial^2}{\partial t^2}(\rho_{11}\boldsymbol{u} + \rho_{12}\boldsymbol{U}) + b\frac{\partial}{\partial t}(\boldsymbol{u} - \boldsymbol{U}), \qquad (4.1a)$$

$$\nabla[Q\boldsymbol{e} + R\boldsymbol{\epsilon}] = \frac{\partial^2}{\partial t^2}(\rho_{12}\boldsymbol{u} + \rho_{22}\boldsymbol{U}) - b\frac{\partial}{\partial t}(\boldsymbol{u} - \boldsymbol{U}), \qquad (4.1b)$$

where $\boldsymbol{u}$ and $\boldsymbol{U}$ are the average solid and fluid *displacement* vectors, and $\boldsymbol{e}$ and $\boldsymbol{\epsilon}$ are the corresponding dilatations, respectively. The constants A and N are the familiar Lamé coefficients from the theory of linear elasticity,[1]

$$A = \frac{E\nu}{(1+\nu)(1-\nu)}, \qquad N = \frac{E}{2(1+\nu)}, \qquad (4.2a,b)$$

with E being the elastic modulus and ν the Poisson's ratio; these quantities refer to *drained conditions* in which pore pressure is held fixed. The quantities Q and R are

[1] In non-porous solid mechanics these coefficients are more commonly denoted by the symbols λ and μ, respectively.

two of the three *compressibility constants*,

$$P = \frac{(1-\phi)[1-\phi-(K_\mathrm{b}/K_\mathrm{s})]K_\mathrm{s}+\phi(K_\mathrm{s}/K_\mathrm{f})K_\mathrm{b}}{1-\phi-(K_\mathrm{b}/K_\mathrm{s})+\phi(K_\mathrm{s}/K_\mathrm{f})}+\frac{4}{3}N, \tag{4.3a}$$

$$Q = \frac{[1-\phi-(K_\mathrm{b}/K_\mathrm{s})]\phi K_\mathrm{s}}{1-\phi-(K_\mathrm{b}/K_\mathrm{s})+\phi(K_\mathrm{s}/K_\mathrm{f})}, \tag{4.3b}$$

$$R = \frac{\phi^2 K_\mathrm{s}}{1-\phi-(K_\mathrm{b}/K_\mathrm{s})+\phi(K_\mathrm{s}/K_\mathrm{f})}, \tag{4.3c}$$

[Johnson, 2001; Eqs (5)] where ϕ is the porosity and K_s, K_b and K_f are the bulk moduli of the solid phase, the porous skeleton and the fluid phase, respectively. The *mass coefficients* are given by

$$\rho_{12} = (\alpha_\infty - 1)\phi\rho_\mathrm{f}, \tag{4.4a}$$

$$\rho_{11} = (1-\phi)\rho_\mathrm{s} - \rho_{12}, \tag{4.4b}$$

$$\rho_{22} = \phi\rho_\mathrm{f} - \rho_{12}, \tag{4.4c}$$

which relate the density of the solid (ρ_s) and fluid (ρ_f) phases to the tortuosity (α_∞) and porosity; ρ_{12} is also known as the *coupling coefficient* since it quantifies the additional mass imposed on one phase to move the other coupled phase. Kinetic energy dissipation occurs due to the relative motion between the fluid and the solid thus b is a *dissipation coefficient*,

$$b = \frac{\mu\phi^2}{\kappa}, \tag{4.5}$$

with μ being the dynamic viscosity and κ being Darcy's coefficient of permeability. A fluid-saturated poroelastic solid thus requires a number of additional parameters to characterize its physical nature over the usual set for either the fluid or solid in isolation. The porosity and tortuosity are purely geometric descriptors whereas the permeability is specific to a particular fluid flowing through a particular porous solid.

A shear wave is so-named because particle motion involves alternating movements normal to the direction of propagation thus producing a shearing motion. In contrast, dilatational waves involve alternating compressions and expansions that are directed

in the same direction as the wave is propagated; i.e., negative and positive dilatations. Here the SC material is assumed to be statistically isotropic so that the shear waves become uncoupled from the dilatational waves and obey independent equations of motion (Biot, 1956b). If the rotation of the solid ($\boldsymbol{\omega} = \nabla \times \boldsymbol{u}$) and fluid ($\boldsymbol{\Omega} = \nabla \times \boldsymbol{U}$) are harmonic, i.e.

$$\boldsymbol{\omega} = C_1 \exp[i(kx + \wp t)] \quad \text{and} \quad \boldsymbol{\Omega} = C_2 \exp[i(kx + \wp t)], \tag{4.6a,b}$$

then taking the curl of Equations (4.1a,b) gives the phase speed v_{r} and attenuation coefficient $1/x_{\mathrm{a}}$ of shear waves travelling in an infinite, fluid-filled poroelastic medium; C_1 and C_2 are amplitude constants and k and $\wp$ are the wave number and angular frequency, respectively. The shearing motion causes particle rotation and the dilatation vanishes from the governing equations so these waves are also referred to as *rotational* and *equivolumal* waves. The wave speed and attenuation coefficient can be nondimensionalised by introducing characteristic velocity and length scales,

$$V_{\mathrm{r}} = \sqrt{N/\rho} \quad \text{and} \quad L_{\mathrm{r}} = \frac{V_{\mathrm{r}}}{2\pi f_{\mathrm{c}}}, \tag{4.7a,b}$$

where $\rho = (1 - \phi)\rho_{\mathrm{s}} + \phi\rho_{\mathrm{f}}$ is the aggregate density, and

$$f_{\mathrm{c}} = \frac{b}{2\pi\phi\rho_{\mathrm{f}}} \tag{4.8}$$

is a characteristic frequency. Likewise, by taking the divergence of Equations (4.1a,b), with

$$\boldsymbol{e} = C_3 \exp[i(kx + \wp t)] \quad \text{and} \quad \boldsymbol{\epsilon} = C_4 \exp[i(kx + \wp t)], \tag{4.9a,b}$$

the phase speed and attenuation coefficient of fast (I) and slow (II) harmonic dilatational waves may be obtained. Since $\nabla \cdot (\nabla \times \boldsymbol{f}) \equiv 0$ for any vector field $\boldsymbol{f}$, dilatational

waves are also *irrotational* by nature. The appropriate velocity and length scales are

$$V_\mathrm{c} = \sqrt{H/\rho} \quad \text{and} \quad L_\mathrm{c} = \frac{V_\mathrm{c}}{2\pi f_\mathrm{c}}, \tag{4.10a,b}$$

where $H = P + 2Q + R$. Therefore the nondimensional properties of the three wave modes are

- shear (r, rotational): $v_\mathrm{r}/V_\mathrm{r}$ and $L_\mathrm{r}/x_\mathrm{a}$;
- fast dilatational (I): $v_\mathrm{I}/V_\mathrm{c}$ and $L_\mathrm{I}/x_\mathrm{I}$;
- slow dilatational (II): $v_\mathrm{II}/V_\mathrm{c}$ and $L_\mathrm{II}/x_\mathrm{II}$.

There is a considerable amount of manipulation required to solve for these wave speeds and attenuation coefficients (Biot, 1956b). Here, these wave properties were determined numerically using MATLAB and the additional equations are given in Appendix C.

4.3 Physiological parameters

Fluid exists in the SC within the tissue cells, in the spaces between the tissue cells (ISF), and in the plasma of the contained blood vessels. Only the ISF, though, is available for bulk flow. This fluid, like CSF, has similar physical properties to water (see Table 3.1 and referring text in §3.2.2), hence: $\rho_\mathrm{f} = 1000$ kg/m^3 (density), $\mu = 0.85$ mPa·s (dynamic viscosity) and $K_\mathrm{f} = 2.2$ GPa (bulk modulus). The solid phase of the SC is thus approximated as the aggregate of the non-ISF components, which is largely water by mass, hence $\rho_\mathrm{s} = 1000$ kg/m^3. For the remainder of the poroelastic properties of the SC the same problem is encountered as in the previous chapter (§3.2.2)—a lack of accurate empirical human data.

The volume fraction of ISF in the SC is likely to be similar to that in the brain as both are composed of the same tissue types, grey matter and white matter, and both are part of the same hydraulic system. In the human brain the ISF has been estimated to occupy about 20% of the total brain volume (Brodbelt & Stoodley, 2007; and references

therein). A number of studies of rat spinal cords place the volume fraction between 0.2 and 0.27 (Nicholson, 1999). Based on these values $\phi = 0.22$ is chosen for being closer to the lower end of the spectrum and perhaps more representative of the porosity of the human SC. The other geometric property of the SC tissue is the tortuosity (α_∞) which describes how long the average fluid pathway is compared to the straight-line distance between its ends. In adult mammals Syková (2004) stated that the tortuosity typically lies in the range 1.5–1.6 and so $\alpha_\infty = 1.6$ is chosen as a starting point. For the permeability of SC tissue to ISF flow the estimate is taken from the previous chapter ($\kappa = 5.6 \times 10^{-15}$ m^2; Table 3.2, p. 76). The same source for elastic modulus is used presently as for the EJH analysis (Ozawa *et al.*, 2004; rabbit SC), but in this case the appropriate value is $E = 5$ kPa since the present interest is in the SC parenchyma rather than the much stiffer pial membrane (§3.2.2). Due to the water content of the solid and fluid components of the SC tissue they are separately almost incompressible (i.e. $\nu \approx 0.5$), yet the ability of the fluid to be displaced through the pores gives the SC aggregate an effective compressibility (i.e. $\nu < 0.5$). Therefore, a value of $\nu = 0.49$ is chosen as an upper bound[2], thereby avoiding the singularities [e.g., see Eq. (4.2b)] and infinite wave speeds imposed by a value of 0.5, and lower values are investigated in a parametric study.

The shear and bulk moduli of the solid phase are computed from linear elasticity theory using the values of E and ν described above. From Eq. (4.2b), $N = 1.7$ kPa, and $K_\mathrm{s} = 83$ kPa is obtained from the following relation,

$$K_\mathrm{s} = \frac{E}{3(1-2\nu)}. \tag{4.11}$$

This just leaves the bulk modulus of the (empty) porous skeleton to compute—K_b—the compressibility measure that takes into account the geometry of the pores. It would seem reasonable that K_b should be a function of the porosity and the bulk modulus of the solid phase, since $K_\mathrm{b} \to K_\mathrm{s}$ must be true in the limit $\phi \to 0$. Heukamp *et al.*

[2]This is the value used by Bertram *et al.* (2005) for their linear elastic model of the SC.

(2001) established the following power law for cement pastes,

$$K_{\mathrm{b}} = (1-\phi)^n K_{\mathrm{s}}, \tag{4.12}$$

with an exponent of $n = 3$. As no equivalent information was found in the biological or biomechanical literature, Eq. (4.12) is used here for the SC tissue, and with $n = 3$ as a starting point $K_{\mathrm{b}} = 40$ kPa. In subsequent parametric studies n is restricted to positive values so that $K_{\mathrm{b}} \leq K_{\mathrm{s}}$. All of the above parameters are summarised in Table 4.1.

4.4 Results

The nondimensional wave speed and attenuation coefficient for each of the three wave modes are plotted in Fig. 4.1(a)–(f) for the parameter values from Table 4.1; these are the same wave properties that were plotted by Biot (1956b). The assumption of Poiseuille flow breaks down above a threshold frequency which corresponds to $f/f_{\mathrm{c}} \approx 0.15$ (Biot, 1956b), hence the abscissa range. The chief observation from these six plots is that the shear wave and the fast dilatational wave would appear to be quite insensitive to frequency in comparison to the slow dilatational wave. However, the physical significance of these wave properties for propagation in the SC becomes more evident when the plot axes are dimensional quantities, as follows.

In Fig. 4.2(a)–(f) the dimensional wave speed and the attenuation of a wave travelling the distance of one SC length are plotted for all three wave types. The vertical dashed lines in each plot bound the frequency range of interest, 1–10 Hz, which spans the lower cardiac frequencies through to the dominant modes of cough-induced pulsations (recall that Williams's invasive pressure measurements indicated a rise time of 0.1 s; §3.2.3). In the 1–10 Hz range the speeds of the three wave modes are $v_{\mathrm{r}} = 1.3$ m/s, $v_{\mathrm{I}} = 10.8$ m/s and $v_{\mathrm{II}} = 0.0$ m/s, which can be observed in panels (a), (c) and (e), respectively. For each of these waves travelling one SC length, the shear wave and fast dilatational wave do not attenuate at all, whereas the slow dilatational wave attenuates

Table 4.1: Parameter values used to calculate the poroelastic wave properties from Biot (1956b); solid is SC tissue, fluid is SC ISF.

Parameter	Value	Description	Notes/References
ϕ	0.22	Porosity	Average of SC in rat (0.2–0.27; Nicholson, 1999; Table 2, p.261, TMA+ method) and brain in humans (0.2; Brodbelt & Stoodley, 2007; p.510)
ρ_s	1000 kg/m^3	Density of solid	Taken to be equal to water
ρ_f	1000 kg/m^3	Density of fluid	CSF (Brodbelt & Stoodley, 2007; p.510)
μ	0.85 mPa·s	Dynamic viscosity of fluid	CSF (Table 3.1, p. 58)
κ	5.6×10^{-15} m^2	Permeability of solid to fluid	Average of 1.4×10^{-16} m^2 (grey matter) and 1.1×10^{-14} m^2 (white matter) for human brain (Smillie *et al.*, 2005; pp.430–431)
α_∞	1.6	Tortuosity of porous frame	Typical value for mammals (Syková, 2004; p.861)
K_f	2.2 GPa	Bulk modulus of fluid	Water
E	5 kPa	Elastic modulus of solid	Rabbit (Ozawa *et al.*, 2004)
ν	0.49	Poisson's ratio of solid	Rubber-like solid, nearly incompressible
n	3	Exponent for K_b power law	(Heukamp *et al.*, 2001; Eq. (7))
N	1.7 kPa	Shear modulus of solid	Theory of linear elasticity, Eq. (4.2b)
K_s	83 kPa	Bulk modulus of solid	Theory of linear elasticity, Eq. (4.11)
K_b	40 kPa	Bulk modulus of porous skeleton	Phenomelogical power law, Eq. (4.12)

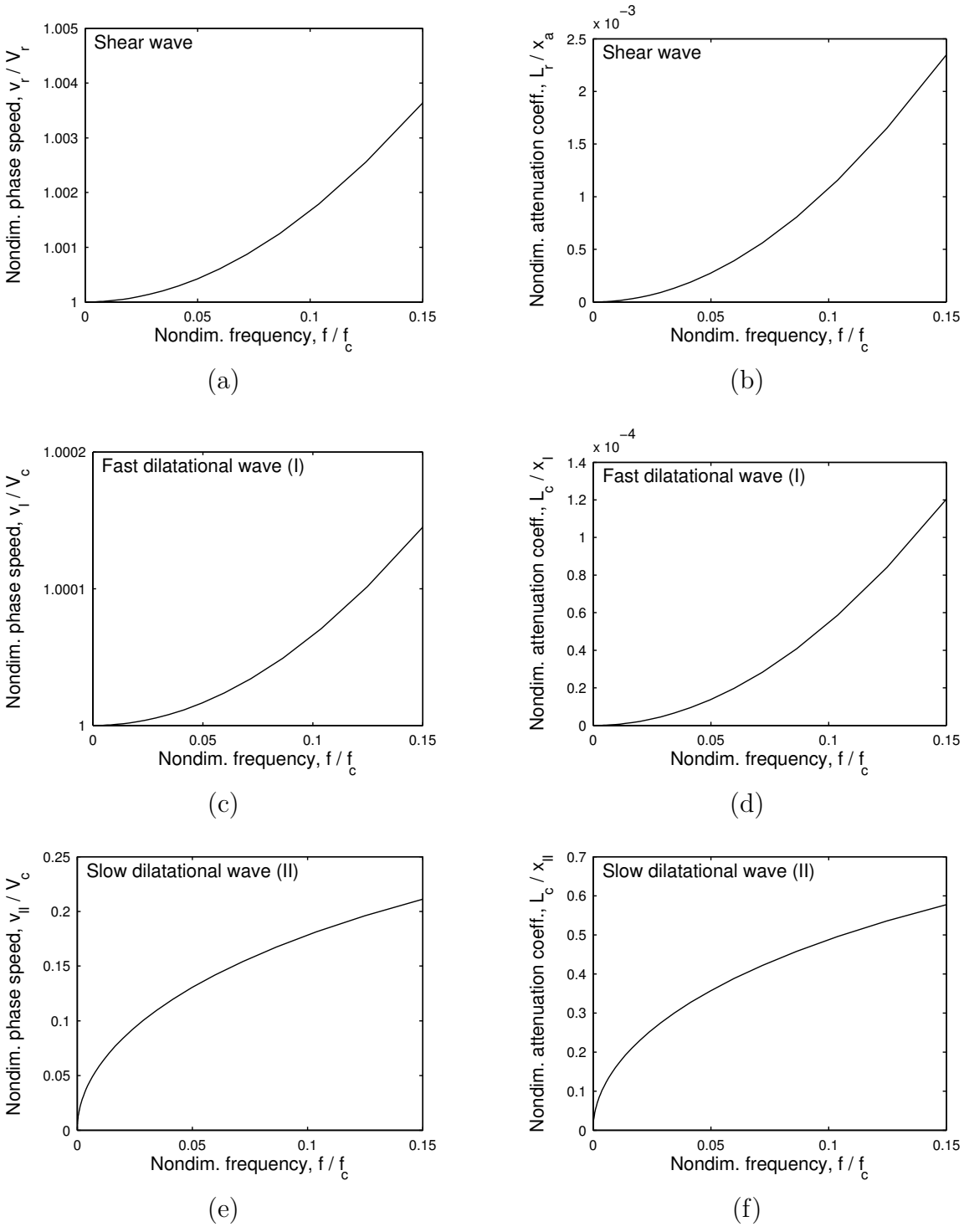

Fig. 4.1: The frequency dependence of phase speed and attenuation coefficient, in nondimensional form, for the three wave types supported by an infinite fluid-saturated porous continuum having the mechanical properties of SC tissue. The characteristic frequency, f_c, is given by Eq. (4.8) and the parameter values are taken from Table 4.1.

to zero [panels (b), (d) and (f), respectively]. This 'all or none' behaviour is due to the frequencies of interest being many orders of magnitude smaller than the characteristic frequency, $f_c = 5.6$ MHz. For comparison, in the nonporous case, i.e. a purely elastic solid with no dissipation, the speed of shear and dilatational waves are 1.3 m/s and 9.3 m/s, respectively.

The parameter values in Table 4.1 are a best estimate from the literature but there is much scope for variation owing to the dearth of empirical data. To assess the sensitivity of the wave properties to these parameters a parametric study has been carried out, the results of which are shown in Figures 4.3–4.6; in all figures the vertical dashed line in panel (a) and the solid curve in panel (b) corresponds to the parameter values in Table 4.1. Since f_c varies with μ, ϕ and κ the equivalent nondimensional frequency is different in each parametric study.

Figure 4.3 shows how the phase speed of the shear wave and fast dilatational wave are effected by changes in the parameters common between poroelastic and plain elastic materials; namely, (a) the elastic modulus and (b) Poisson's ratio. When the solid phase is made stiffer the wave speed increases across all frequencies for the shear and fast dilatational waves [Fig. 4.3(a)]. The same effect occurs in a nonporous linear-elastic solid as the wave speed is proportional to $\sqrt{E}$. The choice of ν for a fluid-saturated tissue such as the SC is not straightforward as published values for neural tissue often do not state whether measurement was made under drained or undrained conditions (e.g., see discussion in Smillie *et al.*, 2005). Over the range of 'likely' values (0.2–0.49) the speed of the shear wave varies slightly and that of the fast dilatational wave varies by up to a factor of four [Fig. 4.3(b)]. A similar effect occurs in the nonporous case. The phase speed of the slow dilatational wave is not affected by E or ν, nor is the attenuation behaviour of any of the three wave types.

The remaining three studies are for the parameters specific to poroelasticity: porosity, permeability and the power law for the bulk modulus of the porous skeleton. For porosity only the fast dilatational wave is affected, which is shown in Fig. 4.4. In panel (a) the phase speed is plotted for discrete values of ϕ and the vertical dashed line in-

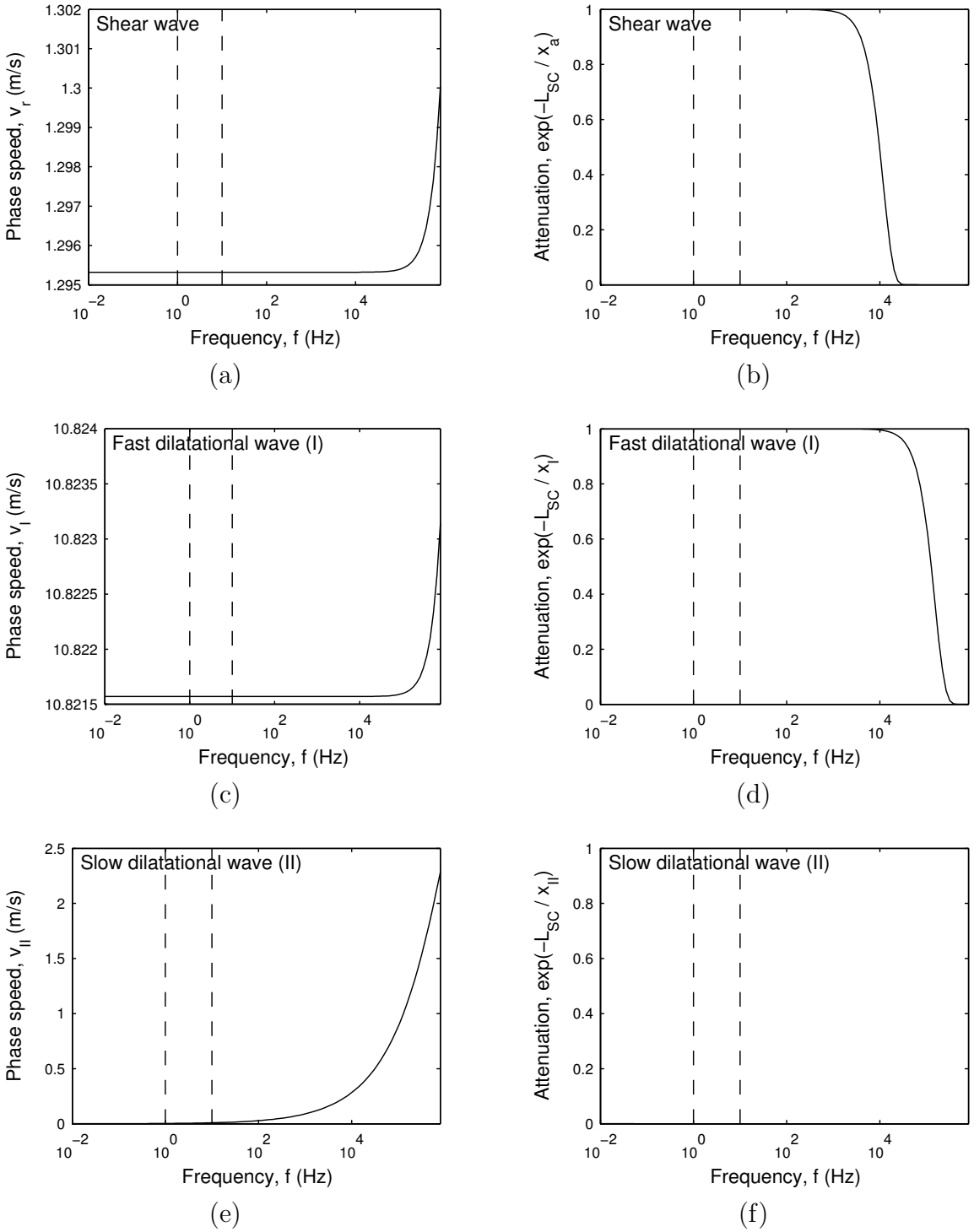

Fig. 4.2: The same wave properties as in Fig. 4.1 replotted here in dimensional form. The attenuation in panels (b), (d) and (e) refers to the scalar reduction in amplitude experienced by the respective wave types in travelling a distance equal to the length of the SC. Observe in panel (f) that the slow dilatational wave attenuates to zero almost instantly hence the empty-looking graph.

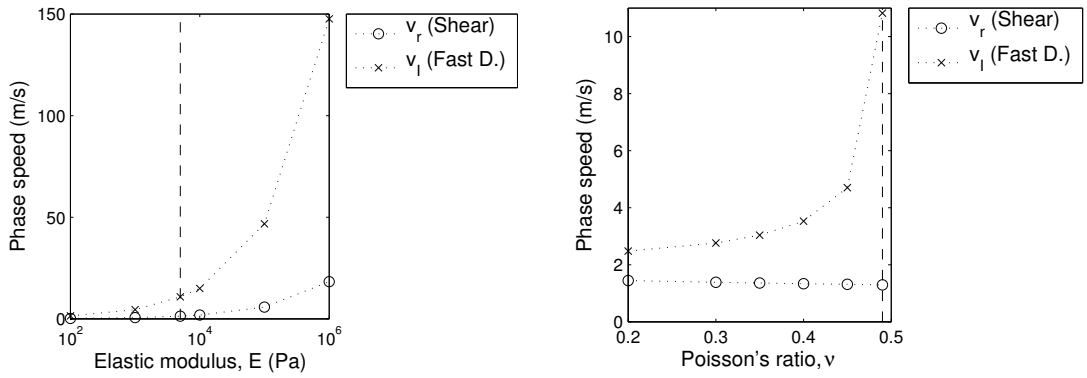

Fig. 4.3: The relationships between phase speed and (a) elastic modulus and (b) Poisson's ratio for shear waves and fast dilatational waves in an infinite fluid-saturated poroelastic continuum having the mechanical properties of SC tissue. Parameter values correspond to those in Table 4.1, and for E and ν this corresponds to the vertical dashed lines in each plot. There is no frequency dependence over the physiological range for any of the E or ν values investigated; here the frequency is 1 Hz.

dicates the reference value of 0.22 from Table 4.1. It can be seen that the speed of the fast dilatational wave is only sensitive to ϕ for values approaching 1; this behaviour is independent of frequency. The attenuation, on the other hand, occurs above some critical frequency, typically in the megaHertz range, as shown in panel (b). Note that the dash-dot curve in Fig. 4.4(b) for $\phi = 0.01$ is cut off at $f/f_c = 0.15$ due to the Poiseuille limit of the theory (Biot, 1956b). Neither of the other wave modes exhibit a sensitivity to porosity for physiological frequencies.

Figure 4.5 shows the frequency-dependent sensitivity of the slow dilatational wave to the permeability of the SC tissue. The vertical dashed lines once again delineate the 1–10 Hz frequency range and the solid curve in each panel corresponds to the reference value of κ from Table 4.1. Evidently, if κ is made relatively large (10^{-11} m^2) then the slow dilatational waves increase in speed to a measurable value (0.1 m/s) and are not entirely dissipated within one SC length; the other two wave types are unaffected in the 1–10 Hz range. Thus diffusion of fluid through the pores is, not surprisingly, most sensitive to changes in permeability.

Finally, the power law for the bulk modulus of the porous skeleton [Eq. (4.12)]

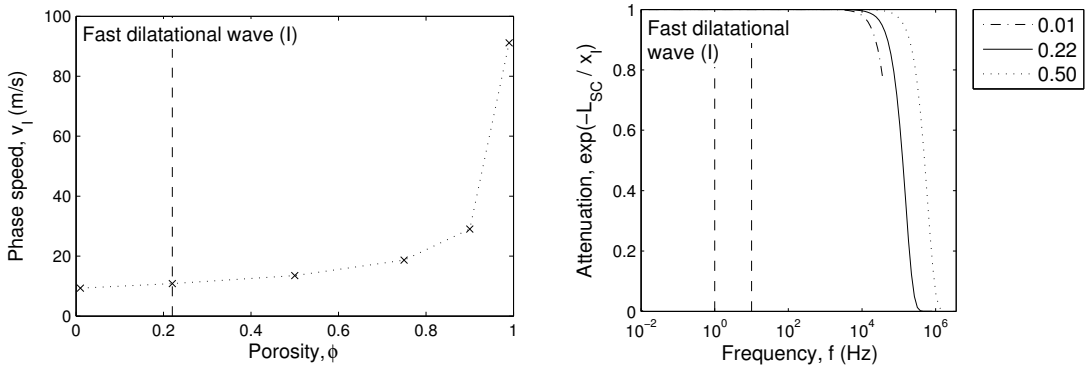

(a) (b)

Fig. 4.4: The sensitivity of the fast dilatational wave to porosity in an infinite fluid-saturated poroelastic continuum having the mechanical properties of SC tissue. The attenuation in panel (b) refers to the scalar reduction in amplitude over a propagation distance equal to the length of the SC. Parameter values correspond to those in Table 4.1, and for ϕ (= 0.22) this corresponds to the vertical dashed line in panel (a) and the solid line in panel (b). Neither the phase speed nor the attenuation have any frequency-dependent behaviour in the physiological range (1–10 Hz) but there is a pronounced dependence at higher frequencies, as shown by the attenuation in panel (b).

is examined in Fig. 4.6. The vertical dashed line corresponds to the reference value from Table 4.1. It can be seen that the phase speed of the fast dilatational wave is affected by the choice of exponent, asymptoting at $n = 1$; this result is independent of frequency. The attenuation is unaffected by changes in n, as are the propagation characteristics of the shear wave and slow dilatational wave.

4.5 Summary

The SC is a wave-bearing medium with poroelastic properties that have not been satisfactorily measured. However, if descriptions of the brain are anything to go by, e.g., "...its consistency is custardlike, firm enough to keep from puddling on the floor of the brain case, soft enough to be scooped out with a spoon" (Wilson, 1998; p. 106), then the water content of the SC likely renders it highly deformable. In fact, in laboratory experience with rats the SC has been observed to be even less firm than the

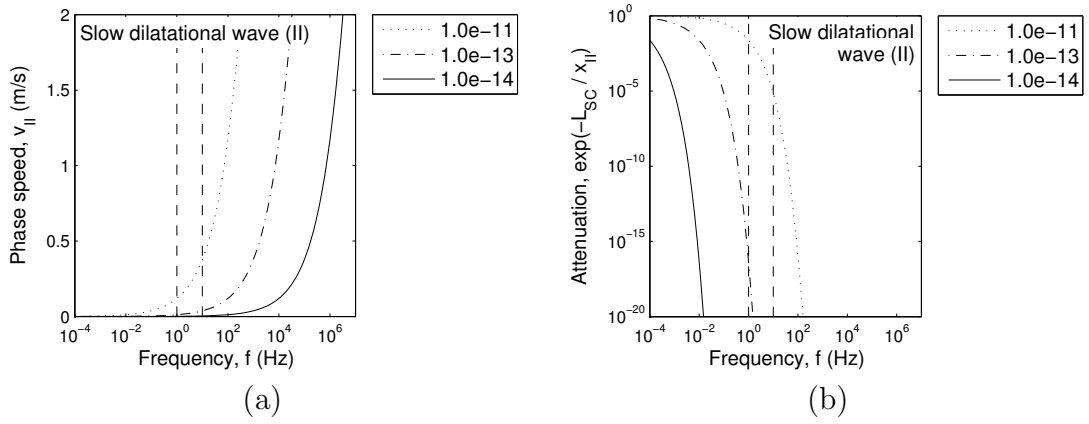

Fig. 4.5: The sensitivity of the slow dilatational wave to permeability (κ) in an infinite fluid-saturated poroelastic continuum having the mechanical properties of SC tissue. The attenuation in panel (b) refers to the scalar reduction in amplitude over a propagation distance equal to the length of the SC. Parameter values correspond to those in Table 4.1, which for κ corresponds to the solid line in each plot. The phase speed and attenuation show frequency-dependent behaviour in the physiological range (1–10 Hz, delineated by the vertical dashed lines) when κ is made large relative to the normal value.

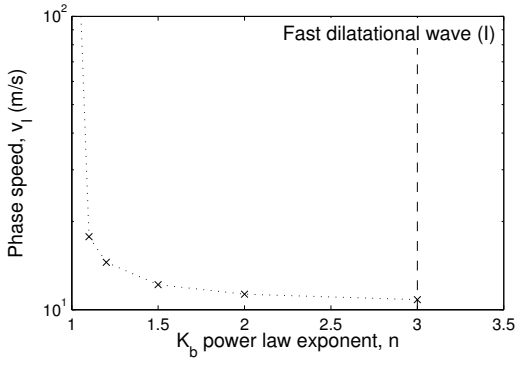

Fig. 4.6: The sensitivity of the fast dilatational wave to the exponent of the power law (for porous skeleton bulk modulus) in an infinite fluid-saturated poroelastic continuum having the mechanical properties of SC tissue. Parameter values correspond to those in Table 4.1, which for n is depicted by the vertical dashed line. The phase speed shows a strong dependence on n at low values approaching 1, which is independent of frequency.

brain (Brodbelt, 2009). Over the range of parameter values investigated here, which make allowance for uncertainties and inaccuracies in published measurements, it would seem that the physiological frequencies are too low for poroelastic dissipation to be of significance in such a soft and weak material. As in a nonporous linear-elastic solid, the speed of the shear and fast dilatational waves are sensitive to the elastic modulus and Poisson's ratio. Particular to the poroelasticity is the sensitivity of the speed of the fast dilatational wave to porosity, permeability, and the relation between the bulk moduli of the solid phase and its value in the form of the porous skeleton.

On short timescales of the order of fractions of a second the spinal canal operates as a wave guide, and for these transients the SC tissue may be functionally represented as an elastic solid. However, syringomyelia is a disease that develops over much longer timescales, typically months to years, and a solid SC cannot accumulate fluid. Therefore, to simulate syrinx formation in a model that can also be validated by clinical measurements of cough-based pressure waves, a full poroelastic representation of the SC is required. Before this can be done though better empirical measurements are needed for the poroelastic parameters. As the focus of the present investigation is on mathematical modelling, rather than experimental work, the next chapter introduces a lumped-parameter approach to simulating perivascular flow. By restricting the problem to the low-frequency domain qualitative predictions are made even without the complexity of poroelasticity.

Nomenclature

Latin symbols:

- $\boldsymbol{U}$ Average fluid displacement vector;
- $\boldsymbol{e}$ Solid dilatation vector;
- $\boldsymbol{u}$ Average solid displacement vector;
- A The first Lamé coefficient of elasticity;

E Elastic modulus;

K Bulk modulus;

L Characteristic length scale;

N The second Lamé coefficient of elasticity (shear modulus);

P The first poroelastic compressibility constant;

Q The second poroelastic compressibility constant;

R The third poroelastic compressibility constant;

V Characteristic velocity scale;

b Poroelastic dissipation coefficient;

f The (characteristic) frequency;

k Wave number;

n Exponent of the power law for K_{b}.

v Phase speed;

$1/x$ Attenuation coefficient.

Greek symbols:

$\boldsymbol{\epsilon}$ Fluid dilatation vector;

α_∞ Tortuosity;

ϕ Porosity;

κ Permeability;

μ Dynamic viscosity;

ν Poisson's ratio;

ρ Mass coefficient, or density (distinguished by subscript);

$\wp$ Angular frequency.

Subscripts:

11 Refers to a mass coefficient;

12 Refers to a mass coefficient known as the coupling coefficient;

22 Refers to a mass coefficient;

I Refers to a quantity of the fast dilatational wave;

II Refers to a quantity of the slow dilatational wave;

a Refers to a quantity of the shear (rotational) wave;

b Refers to a quantity of the porous skeleton structure;

c Refers to the characterisitc frequency, or characteristic velocity or length scale for dilatational waves;

f Refers to a quantity of the fluid phase;

r Refers to a quantity of the shear (rotational) wave;

s Refers to a quantity of the solid phase.

CHAPTER 5

Lumped-parameter model: Theory

5.1 Introduction

The work presented in the proceeding three chapters is motivated by the ideas of Stoodley and colleagues on the causes of syringomyelia (Stoodley *et al.*, 1997; 1999; Brodbelt, Stoodley, Watling, Tu & Jones, 2003; Bilston *et al.*, 2007). The aim is to develop a simple theoretical model that allows one to study pressure pulsation and fluid accumulation in the human cerebrospinal fluid system. It is believed that this work represents the first attempt at a closed model driven by the cardiac cycle over long time scales.

CSF pulsations result from changes in blood volume in the closed craniospinal cavity (Henry-Feugeas *et al.*, 2000); see Fig. 5.1. Although percussive events such as coughing and sneezing induce relatively large pressure fluctuations in the SSS through venous distension (50 mmHg; Lockey *et al.*, 1975), these events are isolated and do not suggest a mechanism for the maintenance of any raised intramedullary pressure. The cardiac cycle, on the other hand, provides the CSF with a source of continuous, albeit relatively small, pressure pulsations. If the dynamic equilibrium of this system were adversely perturbed then the progression of any ill effects may be slow but unrelenting. The cardiac cycle sets up a spinal CSF pulse wave, about 40% of which is generated by spinal arterial pulsations (originating from the descending aorta), an equal contribution

comes from spinal venous pulsations (originating from right atrial pressure) and the intracranial CSF pulse wave passing through the spinal canal from the brain contributes the remaining 20% (Urayama, 1994; Nakamura *et al.*, 1997; Brodbelt & Stoodley, 2007). The CSF in the spinal subarachnoid space (SSS) communicates with the fluid in the spinal cord (SC) via the perivascular spaces (PVS) that fenestrate the pial membrane (Fig. 5.2). Of these, the passage around central arteries has been suggested as the main route (Bilston *et al.*, 2007). In a healthy spinal canal, fluid is exchanged continuously between the SSS and SC but it never accumulates in either location. Syringomyelia is a situation involving localised build up of fluid in the SC—which might be due to a disruption in the mechanism that normally regulates flow between the regions on either side of the pial membrane. Stoodley *et al.* (1997) demonstrated in animal studies that perivascular flow from the SSS into the CC is abolished when the SC arterial pulsation is reduced while maintaining mean arterial pressure. The same CSF pathway was observed into extracanalicular syrinxes (Stoodley *et al.*, 1999), which was the preferential destination when accompanied with a subarachnoid block (Brodbelt, Stoodley, Watling, Tu & Jones, 2003).

The resistance to flow through a PVS is set by the level of inflation of the vessel passing through it. This, in turn, is set by the cardiac pulse—the same pressure source that provides the CSF with its pulsation. Bilston *et al.* (2007) proposed that phase differences between the SSS and arterial pulse waves enhance perivascular flow. This mechanism was demonstrated using a CFD model of flow through a PVS (developed in CFX, a commercial software package). The PVS was modelled as an annular cylinder with the inner surface deforming according to a simulated cardiac pulse. This pulse also featured in the form of an unsteady pressure boundary condition at the SSS end of the PVS; the other end of the PVS, corresponding to interior of the SC, was assigned a zero-pressure boundary condition. Bilston and colleagues found that when peak SSS pressure coincided with minimum cardiac pressure there was maximal perivascular inflow. Alterations to a normal phase difference might occur as a result of scar tissue, associated with syrinxes, interrupting the local blood supply.

Although Bilston *et al.*'s (2007) model was only intended to demonstrate the possibility of phase-dependent perivascular flow, its usefulness is limited by the fact that the greater part of the cerebrospinal system was omitted, all of which would normally be in direct hydraulic communication with the small section being modelled. Moreover, any fluid accumulated in the SC comes at the expense of displacement of other SC contents and/or distension of the cord itself. Therefore, there is a need for a 'complete' and thus closed model, rather than a partial model, of the cerebrospinal fluid system.

To address the above concerns here, a pair of lumped-parameter models of the complete cerebrospinal system are constructed. This systems modelling technique has long been popular in studying disorders of the intracranial CSF system, such as hydrocephalus (e.g., Agarwal *et al.*, 1969; Brown *et al.*, 1985; Drake & Sainte Rose, 1995; Ambarki *et al.*, 2007), but the intraspinal lumped-parameter models of Chang & Nakagawa (2003; 2004) appear to be amongst the few examples in the syringomyelia literature, and these did not include any route for transpial flow (such as the PVS). Bertram *et al.* (2005) developed a 2-d continuum model (using the software package ADINA) to investigate the wave-bearing properties of the spinal canal; both fluid and structural mechanics were resolved. They found that at cardiac frequencies the dynamic response was that of a *lumped system* with the pressure along the the length of the SSS rising and falling in synchrony. On this basis a lumped-parameter model is here deemed to be an appropriate choice for investigating cardiac-driven CSF flows in the SC. Pial *conductance* is allowed to vary periodically with a phase lag with respect to the SSS vascular pressure; conductance is the reciprocal of resistance, and is a more natural choice for the governing equations, as will be seen in §5.3. The governing equations are amenable to efficient numerical solution which permits long-timescale simulations to reach a periodic steady state. The sensitivity of SSS-cardiac phase differences to changes in local and system parameters are investigated, leading to the simulation of disease conditions and treatment options.

This chapter (the first of three on this topic) introduces the theoretical models and the equations which govern them. The procedure for estimating the values of the inter-

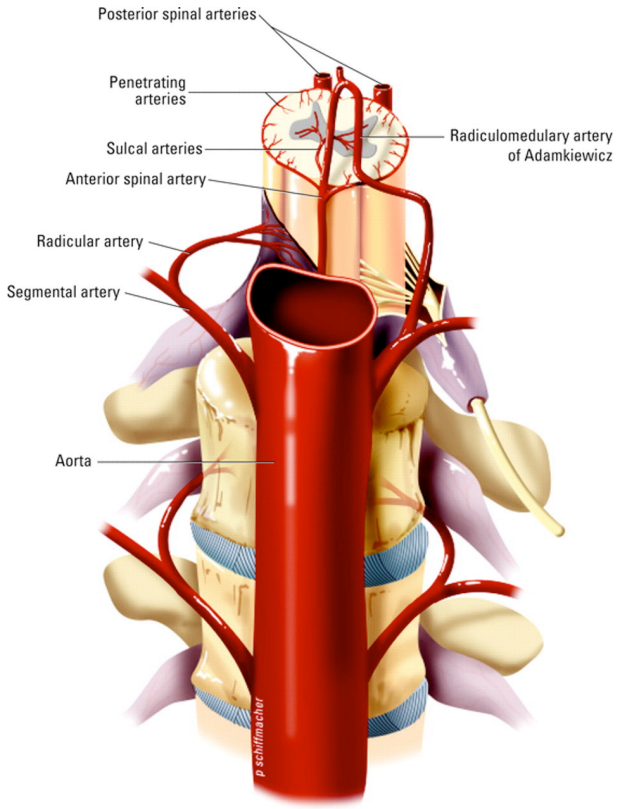

Fig. 5.1: A schematic illustration of the gross vasculature of the spinal cord and surrounding structures. Reproduced from Prasad *et al.* (2007), Fig. 4.

compartmental compliances and conductances is also given here, along with parameter values pertaining to the pressure source functions. In Chapter 6 simulation results are presented that elucidate the valvular mechanism for transpial flow. A number of parametric sensitivity studies are performed to determine the optimum physiological conditions for its operation. Having established an understanding of the system dynamics, simulations of syringomyelia and surgical treatment options are performed and are presented in Chapter 7.

5.2 Theoretical models

The CSF spaces to be modelled are shown schematically in Fig. 5.3. The interstitial fluid space of the SC is considered continuous with the CSF of the SSS, hence the dashed

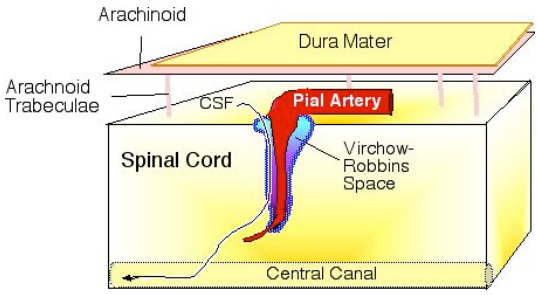

Fig. 5.2: An illustration showing how the Virchow-Robin spaces around pial arteries, also known as perivascular spaces (PVS in the text), are a possible route for cerebrospinal fluid (CSF) to enter the spinal cord.

boundary. The cerebral ventricles, on the other hand, are included for their CSF storage capacity only, enabled by the compliance of the brain, so no such perivascular flow is to be permitted within the head. This fluid system is to be excited by the cardiac pressure pulse therefore the vascular fluid spaces also have to be accounted for. To construct a lumped-parameter model the fluid spaces are divided into an appropriate set of compartments. The resistance to flow from one compartment to an adjacent one is *lumped* at the boundary between the two compartments. Likewise, the integrated change in volume of two adjacent compartments in response to a pressure difference acting across their common boundary, is represented as a mechanical compliance that is assigned to that boundary. Two lumped-parameter models are developed using these principles with the second model representing a finer level of detail than the first; these models are illustrated schematically in Figures 5.4 and 5.5, respectively.

Initially the head and the portion of the SSS that extends beyond the SC are ignored, and the SC and the main portion of the SSS are each represented as single compartments; this is illustrated in Fig. 5.4 as compartments 1 and 2, respectively. CSF may be exchanged between the SC and SSS via the PVS, which has an associated conductance ($z_{\mathrm{PVS}} = z_{1,2}$, physically representative of the ease in which CSF overcomes viscous resistance in the PVS), and this change in volume of CSF is accommodated by the compliance of the pial membrane ($c_{\mathrm{PVS}} = c_{1,2}$). The CSF volume of the SC may also be expanded by compression of the venous bed within, and subsequent ejection of

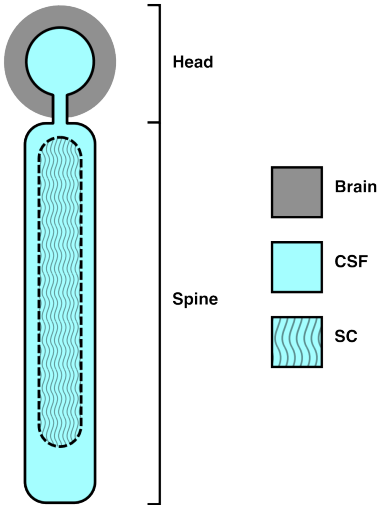

Fig. 5.3: A schematic diagram of the CSF compartments in the lumped-parameter model.

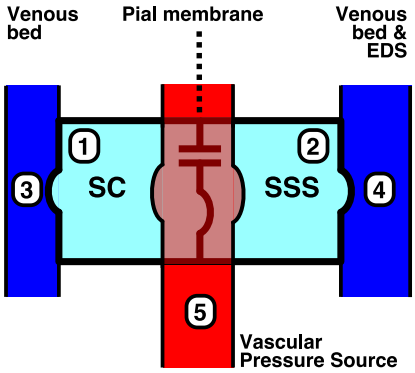

Fig. 5.4: A schematic diagram of the single-segment model of the cerebrospinal system. The spinal canal is functionally divided into five compartments: the spinal cord (SC, 1), the spinal subarachnoid space (SSS, 2), the venous bed of the spinal cord (3), the combined SSS venous bed and extradural space (4), and the vascular pressure source (5). The pial membrane separates the SC and SSS compartments.

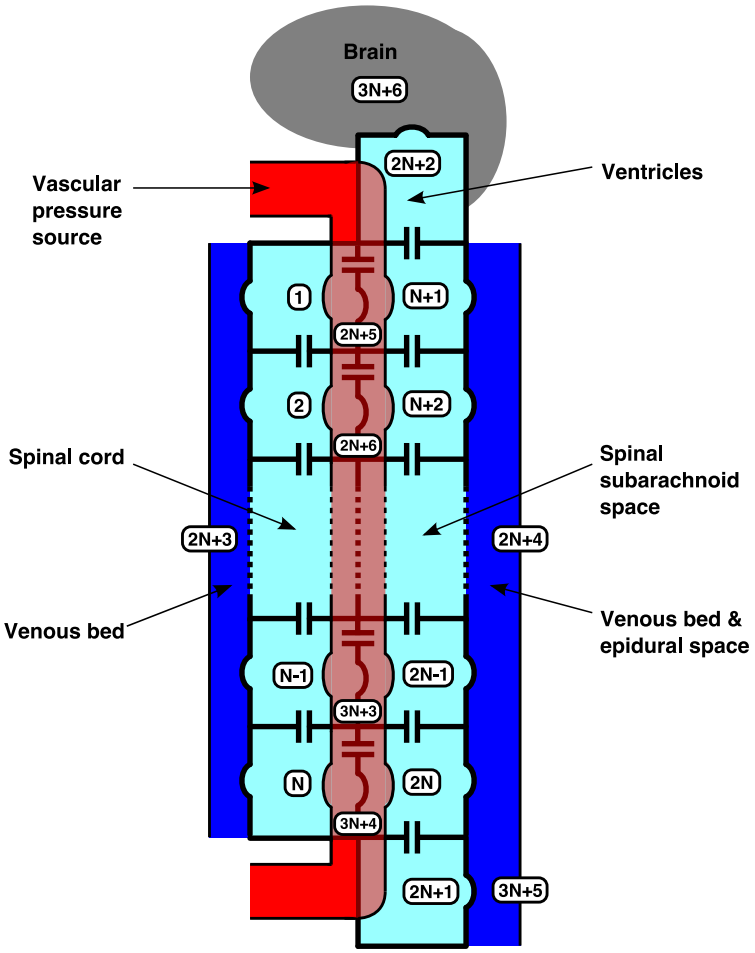

Fig. 5.5: A schematic diagram of the multiple-segment model of the cerebrospinal system.

blood towards the heart, hence the addition of compartment 3. The same is true in the SSS but there is the additional possibility of fluid displacement in the epidural space (EDS); both the venous bed of the SSS and the EDS are combined into compartment 4. In reality there are arterial and venous components to the cardiac pulse and these will be different in the SC and SSS. However, such complexity is not warranted in a simple lumped-parameter model so instead the venous and arterial components were combined into a generic 'vascular pressure source' and designated as compartment 5. The model thus describes two incompressible fluids that are coupled through the elasticity of nervous and vascular tissues.

In the second, more detailed model the head (ventricles and brain) and lower extent of the SSS (lumbar cistern) are included. The 'brain' includes not just the organ itself but also all cerebral blood vessels—which give this compartment much of its compliance. Furthermore, the SC and surrounding SSS are discretized into N segments. This *multiple-segment model*, as opposed to the original *single-segment model*, is depicted in Fig. 5.5. Compartments 1 to N represent the SC, $N+1$ to $2N$ represent the SSS proper, $2N+1$ represents the SSS containing the filum terminale (FT; i.e., the lumbar cistern), and $2N+2$ is the ventricles, making up the CSF-bearing compartments. The remaining $N+4$ compartments correspond to the venous beds of the SC ($2N+3$) and SSS ($2N+4, 3N+5$, including the EDS), their vascular sources ($2N+5$ to $2N+4+N=3N+4$), and the brain ($3N+6$).

Rather than keep track of the first model having 5 compartments and the second having $3N+6$, it is simpler to refer to the single-segment model ($N=1$) and the multiple-segment model. For the latter, various values of N are utilised to investigate the dynamic system response. Values for the compliance and conductance parameters intrinsic to the compartmental subdivision of these models are derived in Section §5.6 but next—the governing equations.

5.3 Governing equations

In a lumped-parameter model each compartment is represented by a single value of pressure and by values of volume flux exchanged with adjacent compartments. Since compartment pressures may be time dependent but do not vary in space, such a model may be described as *zero dimensional*. For an individual compartment i in a system of n compartments, conservation of mass dictates

$$\frac{\mathrm{d}V_i}{\mathrm{d}t} + Q_i = q_i, \tag{5.1}$$

where V_i is the compartment volume, Q_i is the net outflow rate to connecting compartments and q_i is a flux source term. The equations of state relating the compartment pressure and volume are as follows,

$$V_i = V_{i(0)} + \sum_{j=1}^{n} c_{i,j}\,(p_i - p_j), \tag{5.2a}$$

$$Q_i = \sum_{j=1}^{n} z_{i,j}\,(p_i - p_j); \tag{5.2b}$$

$z_{i,j}$ and $c_{i,j}$ are respectively the flow conductance and wall compliance assigned to the boundary between compartments i and j, across which acts the pressure differential $p_i - p_j$. For a pair of compartments i and j that are not adjacent or do not have a compliant interface, $c_{i,j} \equiv 0$; likewise if there is no flow connection between a given pair of compartments then $z_{i,j} \equiv 0$. The constant $V_{i(0)}$ is the notional reference volume when all the relevant pressure differences are zero. Equation (5.2a) is akin to the tube law from the 1-d theory [(3.3a), p. 59], except that it is a pressure-volume relation rather than a pressure-area relation; i.e., no inertia associated with the rate of dilatation of a compartment, either fluid or structural, is included. The second equation of state, (5.2b), is analogous to Poiseuille's law and can thus be derived from the Navier-Stokes equations.[1] Substituting (5.2a,b) into (5.1) gives the governing equation for

[1] Since there is no unsteady term this equation is simply a sum of forces rather than a true momentum equation.

compartment i,

$$\sum_{j=1}^{n}\left[c_{i,j}\frac{\mathrm{d}(p_i-p_j)}{\mathrm{d}t}+z_{i,j}(p_i-p_j)\right]=q_i. \tag{5.3}$$

The compartment reference volume $V_{i(0)}$ does not appear in the governing equation. This is the hydraulic analogue of an electric circuit or a mass-spring-dashpot system, as elucidated in Table 5.1. The lack of a second-order term here is due to the assumption of no inertia in the pressure-volume relation (3.3a).

Equation (5.3) can be written for compartment 1 as

$$\begin{aligned} c_{1,2}\frac{\mathrm{d}(p_1-p_2)}{\mathrm{d}t}+c_{1,3}\frac{\mathrm{d}(p_1-p_3)}{\mathrm{d}t}+\cdots+c_{1,n}\frac{\mathrm{d}(p_1-p_n)}{\mathrm{d}t} & \\ +z_{1,2}(p_1-p_2)+z_{1,3}(p_1-p_3)+\cdots+z_{1,n}(p_1-p_n) &= q_1, \end{aligned} \tag{5.4}$$

and then rearranged into the following form

$$\begin{aligned} (c_{1,2}+c_{1,3}+\cdots c_{1,n})\frac{\mathrm{d}p_1}{\mathrm{d}t}+(-c_{1,2})\frac{\mathrm{d}p_2}{\mathrm{d}t}+\cdots+(-c_{1,n})\frac{\mathrm{d}p_n}{\mathrm{d}t} & \\ +(z_{1,2}+z_{1,3}+\cdots z_{1,n})p_1+(-z_{1,2})p_2+\cdots+(-z_{1,n})p_n &= q_1. \end{aligned} \tag{5.5}$$

Repeating this procedure for compartments 2 to n yields a system of n first-order linear ordinary differential equations in n dependent pressure variables,

$$\mathbf{C}\,\dot{\mathbf{p}}(t)+\mathbf{Z}\,\mathbf{p}(t)=\mathbf{q}(t); \tag{5.6}$$

the vectors $\mathbf{p}=\{p_1,p_2\ldots,p_n\}$ and $\mathbf{q}=\{q_1,q_2\ldots,q_n\}$, and the matrices $\mathbf{C}$ and $\mathbf{Z}$ have elements

$$C_{ij}=\begin{cases}\sum_{k=1}^{n}c_{i,k}, & i=j\\ -c_{i,j}, & i\neq j\end{cases}, \tag{5.7a}$$

$$Z_{ij}=\begin{cases}\sum_{k=1}^{n}z_{i,k}, & i=j\\ -z_{i,j}, & i\neq j\end{cases}, \tag{5.7b}$$

for $i,j=1$ to n. In terms of notation, the more traditional 'ij'-style indices with

Table 5.1: Second-order system modelling analogies; spring extensibility is the reciprocal of spring stiffness, k. Adapted from Alciatore & Histand (2002; Table 4.1, p.130).

Generic quantity	Hydraulic	Electrical	Mechanical
Potential	Pressure (p)	Voltage (V)	Force (F)
Flow	Volumetric flow rate (Q)	Current (i)	Speed (v)
Displacement	Volume (V)	Charge (q)	Displacement (x)
Resistance	Viscous resistance (R)	Electrical resistance (R)	Damping, dashpot (b)
Storage	Compliance (C)	Capacitance (C)	Extensibility, spring ($1/k$)
Inertia	Inertance (I)	Inductance (L)	Inertia, mass (m)
Energy storage	$p = (1/C)\,V$	$V = (1/C)\,q$	$F = k\,x$
Energy dissipation	$p = R\,Q$	$V = R\,i$	$F = b\,v$
Governing equation:			
(Potential)	$\frac{IC}{R}\ddot{p} + C\dot{p} + \frac{1}{R}p = Q$	$\frac{LC}{R}\ddot{V} + C\dot{V} + \frac{1}{R}V = i$	$\frac{m}{bk}\ddot{F} + \frac{1}{k}\dot{F} + \frac{1}{b}F = v$
(Flow)	$I\ddot{Q} + R\dot{Q} + \frac{1}{C}Q = \dot{p}$	$L\ddot{i} + R\dot{i} + \frac{1}{C}i = \dot{V}$	$m\ddot{v} + b\dot{v} + kv = \dot{F}$
(Displacement)	$I\ddot{V} + R\dot{V} + \frac{1}{C}V = p$	$L\ddot{q} + R\dot{q} + \frac{1}{C}q = V$	$m\ddot{x} + b\dot{x} + kx = F$

uppercase letters are used to indicate a coefficient matrix that appears directly in the governing equations, which themselves are element-wise summations of matrices of physical quantities that are denoted by lowercase letters and indices with a comma, 'i, j'.

However, those compartments filled with CSF—the first m compartments—will have dependent pressure variables. For the single-segment model $m = 2N$ (= 2, one compartment for each of the SC and SSS) and for the multiple-segment model $m = 2N + 2$ (N compartments for each of the SC and SSS, one compartment for the extension of the SSS to the lower extent of the FT, and one compartment for the ventricles). The lumped-parameter model is driven by the cardiac pulse so arterial compartments will have a prescribed pressure function; i.e., *pressure source terms*. And the venous and brain compartments are considered to be sufficiently accommodating for their pressure to remain *constant* in response to changes in volume; i.e., these compartments are not closed and so maintain their pressure by the displacement of venous fluid to or from connecting vessels which lie outside the bounds of the lumped-parameter model (as opposed to an infinite compliance). Therefore, Eq. (5.5) reduces to the $m \times m$ system

$$\begin{aligned}
& (c_{1,2} + c_{1,3} + \cdots c_{1,n})\frac{\mathrm{d}p_1}{\mathrm{d}t} + (-c_{1,2})\frac{\mathrm{d}p_2}{\mathrm{d}t} + \cdots + (-c_{1,m})\frac{\mathrm{d}p_m}{\mathrm{d}t} \\
& +(z_{1,2} + z_{1,3} + \cdots z_{1,n})p_1 + (-z_{1,2})p_2 + \cdots + (-z_{1,m})p_m \\
= \; & q_1 \\
& -(-c_{1,m+1})\frac{\mathrm{d}p_{m+1}}{\mathrm{d}t} - (-c_{1,m+2})\frac{\mathrm{d}p_{m+2}}{\mathrm{d}t} - \cdots - (-c_{1,n})\frac{\mathrm{d}p_n}{\mathrm{d}t} \\
& -(-z_{1,m+1})p_{m+1} - (-z_{1,m+2})p_{m+2} - \cdots - (-z_{1,n})p_n,
\end{aligned} \tag{5.8}$$

which may be written in matrix form as

$$\mathbf{C}\,\dot{\mathbf{p}}(t) + \mathbf{Z}\,\mathbf{p}(t) = \mathbf{s}(t); \tag{5.9}$$

the vector $\mathbf{p} = \{p_1, p_2 \ldots, p_m\}$, the elements of the source vector $\mathbf{s}$ are

$$s_i = q_i + \sum_{k=m+1}^{n} \left(c_{i,k} \frac{\mathrm{d}p_k}{\mathrm{d}t} + z_{i,k}\, p_k \right), \tag{5.10}$$

and the matrices $\mathbf{C}$ and $\mathbf{Z}$ have elements

$$C_{ij} = \begin{cases} \sum_{k=1}^{n} c_{i,k}, & i = j \\ -c_{i,j}, & i \neq j \end{cases}, \tag{5.11a}$$

$$Z_{ij} = \begin{cases} \sum_{k=1}^{n} z_{i,k}, & i = j \\ -z_{i,j}, & i \neq j \end{cases}, \tag{5.11b}$$

for $i, j = 1$ to m. Equations (5.9), (5.10) and (5.11a,b), together with an initial condition $\mathbf{p}(0)$, describe the initial value problem for the single- and multiple-segment lumped-parameter models.

5.4 Source terms

The source terms given by Eq. (5.10) contain flux and pressure components. Neither the production nor absorption of CSF are included in the models presented here so $q_i \equiv 0$. The brain, the venous bed of the SC, and the venous bed of the SSS combined with the epidural space are all considered to be connected to sufficient compliance for a change in volume to produce a negligible change in pressure. Since none of these compartments have a flow connection with the CSF compartments they will not make a contribution to $\mathbf{s}$; i.e., $\mathrm{d}p/\mathrm{d}t \approx 0$ and $z \equiv 0$.

Blood pressure in the human body varies in response to the rhythmic contractions of the heart and opening and closing of the one-way valves that maintain unidirectional blood flow. The relationship between arterial pressure (aorta) and that of the two chambers of the left side of the heart (atrium and ventricle) over the cardiac cycle is shown schematically in Fig. 5.6. Since the vascular source pressure in the lumped-parameter models does not correspond to a specific vessel, prescribing a 'realistic'

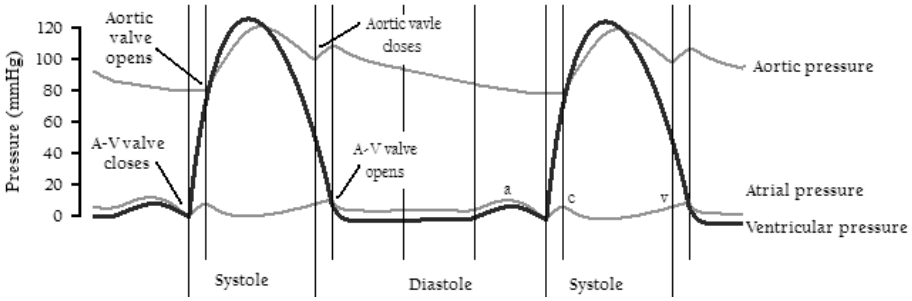

Fig. 5.6: Blood pressure in the cardiac cycle.

waveform is neither straightforward nor warranted. Therefore, in keeping with the level of detail of the modelling, the vascular source pressure was defined to be a sinusoidal function; for segment g of N this is given by

$$p_g(t) = \bar{p}_{\text{Vasc}} + \hat{p}_{\text{Vasc}} \times \sin\{\omega_{\text{HR}}[t - (g-1)\tau_{\text{seg}}]\}, \tag{5.12}$$

where $\bar{p}_{\text{Vasc}}$ is the mean vascular pressure, $\hat{p}_{\text{Vasc}}$ is the vascular pressure amplitude (half of the peak-to-peak value), ω_{HR} is the oscillation frequency, and τ_{seg} is the time required for the pulse wave to travel the length of one segment. To express Eq. (5.12) in terms of compartment number k, in the single-segment model $k = g + 4$ and in the multiple-segment model $k = g + 2N + 4$ (for $g = 1$ to N).

The cardiac cycle will also cause the central arteries in the PVS to pulsate and thus the conductance of the pial membrane to vary periodically. To determine how the PVS conductance is related to the central arterial pressure the coaxial tube analogy from Chapter 3 is used. In this instance the inner flexible tube represents the central artery and the outer rigid tube represents the wall of the PVS; for simplicity the same notation used in Chapter 3 is used here. The conductance through the annular space A is given by

$$z_{\text{A}} = \frac{\pi r_{\text{A}}^4}{8\mu L}, \tag{5.13}$$

where r_{A} is the hydraulic radius, L is the tube length and μ is the dynamic viscosity

of the fluid. Using the tube law the hydraulic radius can be expressed as

$$r_{\mathrm{A}} = r_{\mathrm{T}} - r_{\mathrm{B}} = [r_{\mathrm{T}}^2(\alpha_0 - D\Delta p)]^{1/2}; \tag{5.14a,b}$$

the variables D and Δp are the flexible tube distensibility and the pressure difference between the two fluid spaces. By raising Eq. (5.14b) to the fourth power and taking a leading-order approximation in $D\Delta p$ (a small parameter, $\ll 1$), the conductance may be expressed as

$$z_{\mathrm{A}} \approx \frac{\pi r_{\mathrm{T}}^4}{8\mu L}\,(\alpha_0^2 - 2\alpha_0 D\Delta p). \tag{5.15}$$

From Eq. (3.13a) [p. 65] the pressure differential Δp is related to the pressure in the inner fluid space B as $\Delta p = p_{\mathrm{B}}/\alpha_0$, therefore

$$z_{\mathrm{A}} \propto -p_B. \tag{5.16}$$

Admittedly the assumptions of an artery as a thin-walled tube and the wall of the PVS as a rigid tube are quite crude, but this simple analysis is useful nonetheless in capturing the time-dependent features of the pial conductance. For a given compartment pair in segment i of N, the transpial conductance is defined as

$$z_{i,N+i}(t) = \bar{z}_{i,N+i} + \hat{z}_{i,N+i}\,\sin\{\omega_{\mathrm{HR}}[t - (i-1)\tau_{\mathrm{seg}}] + \pi - \theta_i\}, \tag{5.17}$$

where $\bar{z}_{i,j}$ is the mean value and $\hat{z}_{i,N+i}$ the amplitude. The parameter θ is a phase lag with respect to the vascular source pressure given by Eq. (5.12). The additional phase offset π is required since inflation of the central artery corresponds to increasing vascular pressure (and perivascular resistance) but decreasing perivascular conductance, as per Eq. (5.16).

5.5 Solution method

Equations of the form (5.9) with constant coefficients can be solved analytically using matrix methods (e.g., Bronson, 1973; Ch. 22). However, to simulate the pulsation of the central arteries in the PVS, the conductance between the SSS and the SC (i.e., the pial membrane) must vary in time. Moreover, in the multiple compartment model it is desirable to obtain a solution for an arbitrary number of segments to ensure that the system response is independent of the level of discretization. For these reasons, Eq. (5.9) was reformulated as

$$\dot{\mathbf{p}}(t) = \mathbf{A}(t)\,\mathbf{p}(t) + \mathbf{f}(t), \tag{5.18}$$

where $\mathbf{A}(t) = -\mathbf{C}^{-1}\mathbf{Z}(t)$ and $\mathbf{f}(t) = \mathbf{C}^{-1}\mathbf{s}(t)$, and solved numerically using a code written in MATLAB. An explicit Runge-Kutta ODE solver was chosen (routine `ode45`) and the maximum timestep size was set to ensure at least 40 timesteps per oscillation cycle. Leaving other solver settings at default values, this algorithm was numerically stable. Although the solution always contained two different timescales (as will be seen in the following chapter) the numerical method was sufficiently robust and the discretization sufficiently fine to overcome any potential problems associated with a stiff system (Shampine & Gear, 1979). The choice of appropriate initial conditions $\mathbf{p}(0)$ is the subject of several numerical experiments in Chapter 6.

5.6 Physiological parameters

The physiological basis for the models developed in this chapter lies in the inter-compartmental compliances and conductances, and the source terms. The values of these parameters are estimated from other cerebrospinal lumped-parameter models, where available, as well as simple calculations from anatomical measurements. Although the lack of empirical data is somewhat restrictive, only order-of-magnitude estimates are required in the first instance as the sensitivity of the solution to these

values is subsequently analysed through a number of parametric studies (Chapter 6). Parameter values are initially obtained for the 'whole' fluid spaces, which mostly coincide with the compartments of the single-segment model, and then scaled appropriately for a spinal canal discretized into N segments (details given in §5.6.3). In all cases it is assumed that $c_{i,j} = c_{j,i}$ and $z_{i,j} = z_{j,i}$. These parameter values are summarised in Table 5.2 and the details of the estimation procedure now follows.

5.6.1 Compliances

The compliance between the SSS and the volumes containing the venous bed and spinal epidural space is described by the parameter c_{SSS}. Wallace (1999; p. 358) reported the compliance of the epidural space with surrounding structures as 0.39 ml/mmHg. There are no reports of the compliance of the SSS with the spinal venous bed, and as there is no simple way of calculating it, the value for the epidural space is taken as representative of the combined compliance with both volumes; in SI units $c_{\mathrm{SSS}} = 2.9 \times 10^{-9}$ m^3/Pa. The intrinsic compliance of the SC, c_{SC}, would be lower than that of the SSS. The volume of the venous bed is smaller in the SC (being deeper in the vascular tree) and the SC has no equivalent to the epidural space; i.e., $c_{\mathrm{SC}} < c_{\mathrm{SSS}}$. As there are no reported values for this property $c_{\mathrm{SC}} = 1 \times 10^{-10}$ m^3/Pa is chosen as an order-of-magnitude estimate (the sensitivity of the system to changes in this value are investigated in Chapter 6).

If all of the venous blood has been ejected from the SC, a volume of extracellular fluid entering the SC can still be accommodated by the distensible nature of the pial membrane, which will be associated with a rise in SC fluid pressure. This compliance, c_{Pia}, can be calculated from the distensibility relation that was used in the coaxial tube model [Eq. (3.3b), p. 59]; i.e.,

$$D = \frac{1}{A_{\mathrm{rigid}}} \left. \frac{\mathrm{d}A_{\mathrm{flexible}}}{\mathrm{d}\Delta p} \right|_{\Delta p=0} \quad \Rightarrow \quad c = \frac{\mathrm{d}V}{\mathrm{d}\Delta p} \approx V_{\mathrm{rigid}} \times D, \tag{5.19a,b}$$

with the flexible tube representing the pia and the rigid tube the dura. The volume $V_{\mathrm{rigid}} = \pi r_{\mathrm{T}}^2 \, L_{\mathrm{SC}}$, so for a SC length of half a metre and parameter values from Table 3.1

($r_{\mathrm{T}} = 7.5$ mm, $D = 1{\times}10^{-5}$ Pa^{-1}; p. 58), the pial compliance becomes $8{\times}10^{-10}$ m^3/Pa. However, this value is an overestimate since Eq. (5.19a) assumes an infinite tube filled with fluid thereby ignoring the elastic contribution of the attached SC tissue and ends of the pial membrane. Bertram *et al.* (2005) asserted that the SSS holds the main source of volume compliance so conservatively the value 2×10^{-10} m^3/Pa is chosen to ensure $c_{\mathrm{Pia}} \ll c_{\mathrm{SSS}}$.

There are two compliance parameters that are specific to the multiple segment model: c_{FT} and c_{V}. The first is the compliance between the portion of the SSS containing the FT and the volume containing the venous bed and epidural space. For this parameter the same value is chosen as for the main part of the SSS ($2.9{\times}10^{-9}$ m^3/Pa). The second parameter represents the compliance between the ventricles and the brain. Compartment models have been popular for studying the intracranial hydrodynamics in hydrocephalus, so the value used by Sorek *et al.* ($C_{\mathrm{FB}} = 0.2093$ ml/mmHg; 1989; p. 9) is also used here; in SI units $c_{\mathrm{V}} = 1.6 \times 10^{-9}$ m^3/Pa.

The compliance between the SSS and the vascular pressure source (arterial and venous combined) is denoted by $c_{\mathrm{Vasc,SSS}}$. This parameter determines what proportion of the prescribed vascular pressure is transmitted to the CSF in the SSS. The value 1×10^{-9} m^3/Pa is chosen, that being the order of magnitude of c_{SSS}. For most of the work presented in the following two chapters only the SSS is excited by the vascular source, thus in the SC $c_{\mathrm{Vasc,SC}} = 0$. However, a systematic study is performed of the effect of having both the SSS and the SC receive pressure input for which $c_{\mathrm{Vasc,SC}}$ is varied between 0 and $c_{\mathrm{Vasc,SSS}}$.

5.6.2 Conductances

Flux between the SC and SSS compartments is permitted by the perivascular passages that perforate the pial membrane. This conductance, lumped at the pial boundary,

can be estimated by Poiseuille's law

$$z_{\mathrm{Pia}} = \frac{\pi\, r_{\mathrm{PVS}}^4}{8\mu_{\mathrm{CSF}} r_{\mathrm{B0}}} \times n_{\mathrm{SC}}; \tag{5.20}$$

values for the dynamic viscosity of the CSF and radius of the SC are listed in Table 3.1 (μ and r_{B0}, respectively; p. 58), and those for the effective radius of the PVS and the number of PVS over the length of the SC are listed in Table 3.2 (r_{PVS} and n_{SC}, respectively; p. 76). With the aforementioned inputs Eq. (5.20) yields a value of 1.0×10^{-11} m^3/Pa·s. This calculation is based on the same rationale as for the pial permeability [z_{Pia}; Eq. (3.38), p. 75].

The anatomical survey of the spinal canal illustrated in Fig. 3.2 (p. 60) established the gross dimensions of the SSS. The conductance of this fluid conduit, restricted to that portion surrounding the SC, can be estimated from Poiseuille's law

$$z_{\mathrm{SSS}} = \frac{\pi r_{\mathrm{SSS}}^4}{8\mu L_{\mathrm{SC}}} \tag{5.21}$$

where $r_{\mathrm{SSS}} = r_{\mathrm{T}} - r_{\mathrm{B0}}$ is the effective radius of the SSS (twice the cross-sectional area divided by the wetted perimeter). This gives a value of 1.6×10^{-7} m^3/Pa·s. However, this is likely to be an overestimate since changes in cross-sectional area and any impediment to flow, such as trabeculae interconnecting the meninges, have been neglected. Bozanovic-Sosic *et al.* (2001) measured the resistance in the SSS to be 380.3 ± 26.1 cmH$_2$O·min/ml, which translates to a conductance of 4.3×10^{-9} m^3/Pa·s. Therefore this latter empirical value, being a lower estimate, is used for z_{SSS}.

The conductance within the SC itself along the rostrocaudal axis, z_{SC}, is calculated using Darcy's law [Eq. (3.16); p. 70]; i.e.,

$$z_{\mathrm{SC}} = \frac{Q}{\Delta p} = k_{\mathrm{SC}} \frac{\pi\, r_{\mathrm{B0}}^2}{L_{\mathrm{SC}}}, \tag{5.22a,b}$$

where $k_{\mathrm{SC}} = \kappa_{\mathrm{SC}}/\mu$ is the hydraulic conductivity of the SC to CSF. On the assumption that the brain and SC will have similar hydraulic properties, the empirical values

reported by Smillie *et al.* (2005; discussed here earlier in §3.4.5) and Smith & Humphrey (hydraulic conductivity of 2×10^{-9} cm^4/dyn·s; 2007; p. 61) are averaged to derive a conductance estimate of $z_{\mathrm{SC}} = 4.9 \times 10^{-16}$ m^3/Pa·s. The remaining portion of the SSS contains the FT and is about one third the length of the SC. Therefore the conductance of this passageway (in the multiple segment model only) is simply the value for the main part of the spinal canal multiplied by a factor of three; i.e., $z_{\mathrm{FT}} = 1.3 \times 10^{-8}$ m^3/Pa·s.

Finally, a value is required for the conductance between the SSS and the cavity formed by the cranial ventricles, z_{V}. Ambarki *et al.* (2007) estimated the conductance of the cerebral aqueduct at 5.0 ml/mmHg·s (G_8, p. 486) from a lumped-parameter model by matching CSF pressure amplitudes and signal delays during the cardiac cycle. Since the cerebral aqueduct is the narrowest part of this cerebral conduit it will provide the major source of flow resistance. Therefore this empirical value for the cerebral aqueduct is used as a representative conductance between the SSS and ventricular compartments; in SI units $z_{\mathrm{V}} = 3.8 \times 10^{-8}$ m^3/Pa·s.

5.6.3 Scaling parameters for multiple segments

When the spinal canal is discretized into a number of segments, the compliances and conductances must be scaled accordingly. Compliance is proportional to compartment volume, so the parameters c_{Pia}, c_{SSS}, c_{SC}, $c_{\mathrm{Vasc,SSS}}$ and $c_{\mathrm{Vasc,SC}}$ for the single-segment model will be reduced by a factor of N in a model having N segments. Likewise, conductance is proportional to cross-sectional area and inversely proportional to length, so z_{Pia} reduces by a factor of N and z_{SSS} and z_{SC} increase by a factor of N. The conductance between the first SSS compartment $(N+1)$ and the ventricular compartment $(2N+2)$, also varies with the level of discretization because it must account for the flux to the *centres* of these two compartments. Therefore, adding the component conductances in series,

$$z_{N+1,2N+2} = \frac{(2N\, z_{\mathrm{SSS}}) z_{\mathrm{V}}}{(2N\, z_{\mathrm{SSS}}) + z_{\mathrm{V}}}. \tag{5.23}$$

Table 5.2: Compliance and conductance values used in the lumped-parameter models. For an N-segment model those parameters lumped between compartments in the same segment contain the subscript i (1 to N) and those between adjacent segments are denoted by the subscript j ($= 1$ to $N-1$).

Parameter			Value	Description
Generic	1-seg.	N-seg.		
c_{Pia}	$c_{1,2}$	$c_{i,N+i} \times N$	2×10^{-10} m^3/Pa	Compliance between the SC and SSS due to pial membrane.
c_{SSS}	$c_{2,4}$	$c_{N+i,2N+3} \times N$	2.9×10^{-9} m^3/Pa	Compliance between the SSS and the volume containing the venous bed and spinal epidural space.
c_{SC}	$c_{1,3}$	$c_{i,2N+3} \times N$	1.0×10^{-10} m^3/Pa	Compliance between the SC proper and the SC volume containing the venous bed.
c_{FT}	-	$c_{2N+1,3N+5}$	2.9×10^{-9} m^3/Pa	Compliance between the portion of the SSS containing the FT and the volume containing the venous bed and epidural space.
c_{V}	-	$c_{2N+2,3N+6}$	1.6×10^{-9} m^3/Pa	Compliance between the ventricles and the brain.
$c_{\mathrm{Vasc,SSS}}$	$c_{2,5}$	$c_{N+i,2N+4+i} \times N$	1×10^{-9} m^3/Pa	Compliance between the SSS and the vascular pressure source (arterial and venous combined).
$c_{\mathrm{Vasc,SC}}$	$c_{1,5}$	$c_{i,2N+4+i} \times N$	0 m^3/Pa	Compliance between the SC and the vascular pressure source (arterial and venous combined).
z_{Pia}	$\bar{z}_{1,2}$	$\bar{z}_{i,N+i} \times N$	1.0×10^{-11} m^3/Pa·s	Conductance between the SC and SSS via pial membrane.
z_{SSS}	-	$z_{N+j,N+j+1}/N$	4.3×10^{-9} m^3/Pa·s	Conductance within the portion of the SSS that surrounds the SC, along the rostrocaudal axis.
z_{SC}	-	$z_{j,j+1}/N$	4.9×10^{-16} m^3/Pa·s	Conductance within the SC, along the rostrocaudal axis.
z_{FT}	-	$\frac{2N z_{\mathrm{SSS}}\, z_{2N,2N+1}}{2N z_{\mathrm{SSS}} - z_{2N,2N+1}}$	1.3×10^{-8} m^3/Pa·s	Conductance within the portion of the SSS containing the FT.
z_{V}	-	$\frac{2N z_{\mathrm{SSS}}\, z_{N+1,2N+2}}{2N z_{\mathrm{SSS}} - z_{N+1,2N+2}}$	3.8×10^{-8} m^3/Pa·s	Conductance between the SSS and the ventricles.

Table 5.3: Parameter values for source terms.

Parameter	Value	
$\bar{p}_{\text{Vasc}}$	1.33 kPa	(10 mmHg)
$\hat{p}_{\text{Vasc}}$	133 Pa	(1 mmHg)
v_{PW}	5 m/s	
f_{HR}	1 Hz	(60 bpm)

The same is true at the opposite end of the SSS with the FT compartment. All of these parameter scalings are summarised in Table 5.2, expressed in terms of equivalent parameter value.

5.6.4 Source terms

The vascular pressure in the lumped-parameter models doesn't correspond to a specific blood vessel and, since spinal blood pressure is not normally measured, one might reasonably choose intracranial pressure (ICP) to obtain representative magnitudes for the mean and amplitude. When lying face upward a healthy adult has a mean ICP in the range 7–15 mmHg but this will fall to around −10 mmHg when standing (Steiner & Andrews, 2006). The ICP pulse amplitude is around 2.5 mmHg (Eide & Sorteberg, 2007). However, as the governing differential equations are linear (with variable coefficients) the magnitude of the vascular pressure will simply scale the system response. For this reason the whole-number values $\bar{p}_{\text{Vasc}} = 10$ mmHg (1.33 kPa) and $\hat{p}_{\text{Vasc}} = 1$ mmHg (133 Pa) are chosen as a starting point for subsequent parametric studies. The oscillation frequency is the heart rate, which ranges around 70–75 bpm for adults at rest. Thus a frequency of $f_{\text{HR}} = 1$ Hz is chosen giving $\omega_{\text{HR}} = 2\pi$. The time taken for the pulse wave to travel one segment in a model containing N segments is $\tau_{\text{seg}} = L_{\text{SC}}/(N\, v_{\text{PW}})$, where v_{PW} is the arterial pulse wave velocity. Since a blood-filled artery is simply a thin elastic tube filled with an incompressible fluid, the wave speed calculated for the SC in Chapter 3 should give a reasonable estimate for the arterial pulse wave velocity; i.e., $v_{\text{PW}} = 5$ m/s. These parameter values are summarised in Table 5.3.

The expression for pial conductance given by Eq. (5.17) is based on a mean, $\bar{z}_{i,N+i}$, and an amplitude $\bar{z}_{i,N+i}$, where $i = 1$ to N. The mean is set at the value given in Table 5.2, i.e. $\bar{z}_{i,N+i} = z_{\text{Pia}}$, and the amplitude is initially chosen to be half of the mean, $\hat{z}_{i,N+i} = \bar{z}_{i,N+i}/2$.

5.7 Summary

In this chapter two lumped-parameter models have been introduced. The first model has five compartments in total with each spanning the length of the spinal canal; in the second model the spinal canal was discretized into N possible segments and additional compartments above and below the SSS were included. The governing equations were derived from a mechanical standpoint and the values of the physiological parameters were estimated for models having an arbitrary number of spinal segments. The intention is to capture and investigate broad qualitative behaviour using these somewhat rough parameter estimates. In the next chapter the steady-state response of these models is analysed through a series of parametric sensitivity studies.

Nomenclature

Latin symbols:

- $\boldsymbol{C}$ Compliance coefficient matrix (vector notation);
- $\boldsymbol{Z}$ Conductance coefficient matrix (vector notation);
- $\boldsymbol{q}$ Source term vector (vector notation);
- C Compliance coefficient matrix (index notation);
- N The number of spinal segments in a multiple-segment model;
- Z Conductance coefficient matrix (index notation);
- c Intercompartmental compliance;

p Compartment pressure;

q Source term vector (index notation);

t Time;

z Intercompartmental conductance.

Greek symbols:

μ Dynamic viscosity;

ω Angular frequency;

τ Time for a pulse wave to travel the length of one spinal segment.

Subscripts:

FT Refers to a property of the lower enlargement of the spinal subarachnoid space containing the filum terminale (i.e., the lumbar cistern);

HR Refers to a property associated with the heart rate;

Pia Refers to a property of the pial membrane;

PVS Refers to a property of the perivascular space;

PW Refers to a property of the pulse wave;

SC Refers to a property of the spinal cord;

SSS Refers to a property of the spinal subarachnoid space;

V Refers to a property of the cerebral ventricles;

Vasc Refers to a property of the vascular pressure source;

VSSSFT Refers to a property spanning the ventricular (V), spinal subarachnoid space (SSS) and filum terminale (FT) compartments;

i, j Refers to a compliance or conductance lumped between compartments i and j;

ij Refers to element ij of a coefficient matrix;

seg Refers to a property of a spinal segment.

CHAPTER 6

Lumped-parameter model: Sensitivity analysis

6.1 Introduction

The pair of lumped-parameter models developed in the previous chapter contain a number of physiological parameters. The measurement of these quantities is a non-trivial problem in biomechanics since standard engineering tests are often difficult to apply to soft biological tissues. *In vitro* measurements can be more practical than those made *in vivo* (which are often ethically problematic) but material behaviour can differ significantly. Consequently, the parameter values summarised in Tables 5.2 and 5.3 are likely to be rough estimates. This being the case, the strategy employed in this chapter is to explore the system behaviour through a series of parametric sensitivity studies. Parameters are scaled from the values in Tables 5.2 and 5.3 on an order-of-magnitude basis, and the effect this has on the steady-state solution is evaluated in terms of the mean and amplitude of the compartment pressure pulsations. The analysis begins with the single-segment model, demonstrating the role of cardiac-PVS phase lag in transpial flow and the sensitivity of this mechanism to the values of the various conductances and compliances. Next the multiple-segment model is used to determine the function of the ventricles and lower extent of SSS, and to observe how the system response varies

along the length of the SC. Although the results are presented in dimensioned units of pressure the emphasis is on qualitative behaviour rather than quantitative predictions.

6.2 Single-segment model

6.2.1 Basic concept

To analyse the dynamic response of this lumped-parameter model it is instructive to first consider the simplest situation of a fixed pial conductance; i.e., zero conductance amplitude, $\hat{z}_{\mathrm{Pia}} = \hat{z}_{1,2} \equiv 0$, so that $z_{\mathrm{Pia}} \equiv \bar{z}_{\mathrm{Pia}}$. The vascular source pressure, p_{Vasc}, is plotted in Fig. 6.1(a) against a timescale that has been nondimensionalised by the frequency; i.e., $t' = f\,t$, although since $f = 1$ Hz here the scale could equally be interpreted in dimensional units (seconds). The mean of the source pressure ($\bar{p}_{\mathrm{Vasc}}$) was computed by a moving-quadrature technique (based on Simpson's rule; Getreuer, 2008) and is plotted as the thick line, indicating a constant value of 1.33 kPa (10 mmHg); the amplitude is easily reckoned at 133 Pa (1 mmHg). The response of the SC and SSS compartments to this sinusoidal driver are plotted in Fig. 6.1(b). Both of these compartments begin with a zero initial pressure [$p_{\mathrm{SC}}(0) = p_{\mathrm{SSS}}(0) = 0$] that subsequently become the mean value about which their pressures oscillate. Comparing these plots with panel (a), it is evident that the SC and SSS are also in phase with the source pressure, which would be expected since fluid inertia has not been included. For this base set of compliance values the SSS compartment oscillates with a greater amplitude than the SC, causing the pressure differential Δp ($= p_{\mathrm{SC}} - p_{\mathrm{SSS}}$) to be half a cycle out of phase. The amplitude of the Δp pulsations is equal to the difference in amplitude of the SC and SSS signals.

Figure 6.2 demonstrates what happens if the initial conditions are changed, giving the SC compartment a higher starting pressure (100 Pa) than the SSS (0 Pa). Over the course of about 150 oscillations the two compartments equilibrate ($\Delta p \to 0$). However, the periodic steady state is not midway between the initial conditions, instead the

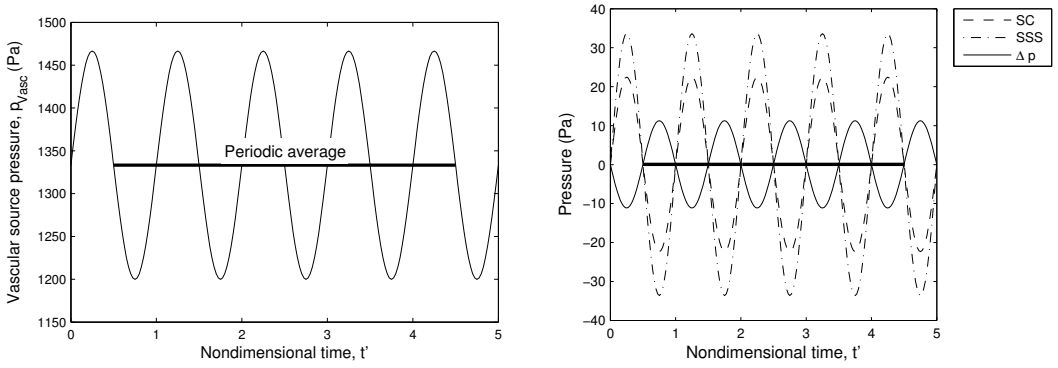

(a) (b)

Fig. 6.1: The single-segment model operating with fixed pial conductance and zero starting pressure in both compartments. The sinusoidal driver, shown in (a), effects the response in the spinal cord (SC) and spinal subarachnoid space (SSS) compartments, shown in (b). Parameter values as per Tables 5.2 (p. 120) and 5.3 (p. 121).

SC pressure is made to adapt to the SSS which receives a more direct input from the adjacent vascular source. If the starting pressures were swapped then the mean equilibrium pressure would be closer to 100 Pa than 0 Pa (not shown). The SC normally holds its shape suggesting that the pressure within the SC is at least slightly greater than the pressure in the surrounding SSS. When a syrinx is present, raised SC pressure may significantly distend the cord. If the pial conductance is fixed then the lumped-parameter model offers no mechanism to maintain a mean pressure difference between the SC and SSS compartments.

The dynamic pial conductance described by Eq. (5.17) [p. 114] is introduced in Fig. 6.3. The initial conditions are zero pressure in both compartments and the conductance lags the source pressure by half a cycle (i.e. $\theta = 180°$). The pressure in the SC compartment is seen to gradually rise over about 100 oscillations [corresponding to an increase in CSF volume, panel (a)] while the SSS pressure appears to stay constant [panel (b)], resulting in a non-zero mean pressure difference at steady state [$\overline{\Delta p} = 2.8$ Pa, panel (c)]. The mechanism by which this occurs can be explained with the aid of Fig. 6.3(d) and (e) where the pressure difference Δp and the pial conductance z_{Pia} have been plotted, respectively, during the last cycle of the simulation. Fluid will

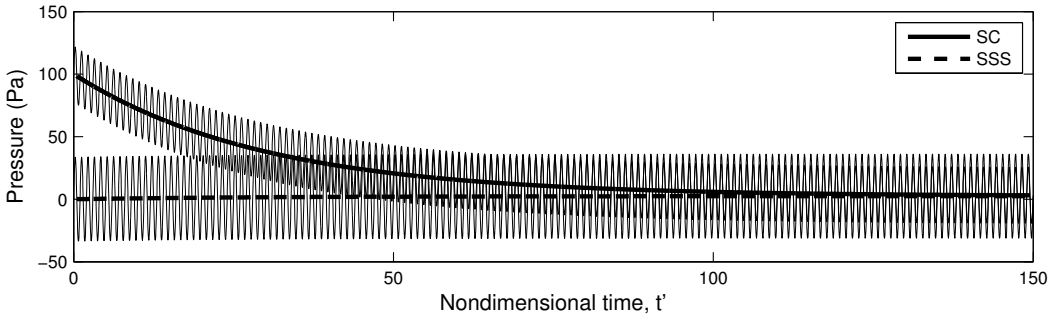

Fig. 6.2: The response of the single-segment model with the same setup as for Fig. 6.1 except with different initial conditions; the spinal cord (SC) compartment begins with a higher pressure (100 Pa) than the spinal subarachnoid space (SSS) compartment (0 Pa). The bold lines denote the periodic average of each pressure signal.

tend to flow into the SC when Δp is negative and back out again when Δp is positive. Since the conductance has been set out of phase with Δp, inflow to the SC will be encouraged by large z but outflow will be met with reduced conductance (i.e., higher resistance). Thus the pial membrane acts as a dynamic valve, driven by but lagging behind the cardiac pressure, allowing a volume of fluid to accumulate in the SC with a concomitant increase in SC mean pressure. The question is—what might affect the phase lag?

Although local disruptions to the SC blood supply are likely to produce changes in the relative timing of the cardiac and PVS pulsations, it would be difficult to measure this phase difference *in situ*. Therefore, the full range of θ are explored. In Fig. 6.4 the (a) mean pressure and (b) pressure amplitude are plotted for the steady state (achieved after 250 oscillations) at a number of θ spanning 0 to 180°. The mean pressure of both compartments varies with phase lag such that there exists an optimal condition for fluid accumulation in one compartment over the other; $\theta = 180°$ favours accumulation into the SC compartment, $\theta = -180°$ favours accumulation into the SSS, and $\theta = 90°$ gives zero net accumulation. The results for negative θ are a mirror image about the $\theta = 0°$ axis. Pressure fluctuation amplitude, on the other hand, is independent of θ, as shown in Fig. 6.4(b). Since the SC and SSS pulsations are in phase with each other, the amplitude of the transpial pressure difference, $\widehat{\Delta p}$, can be calculated to be 11.2 Pa

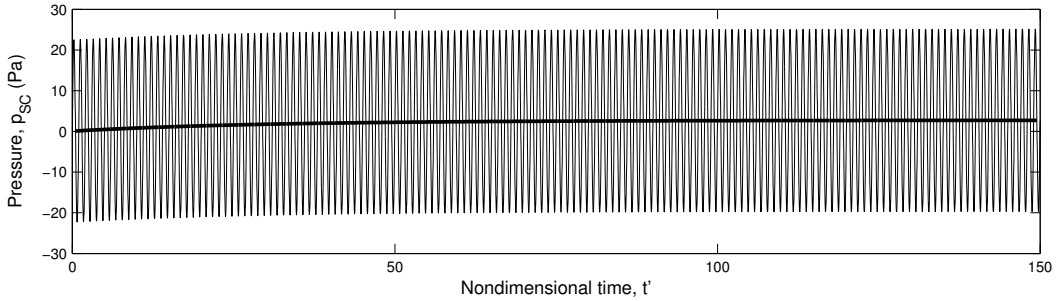

(a)

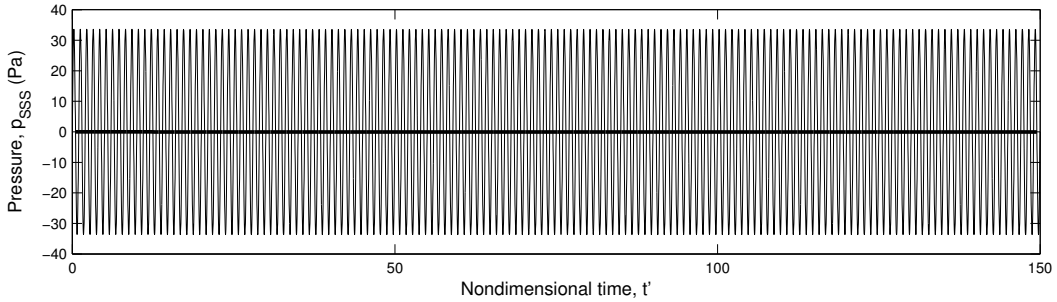

(b)

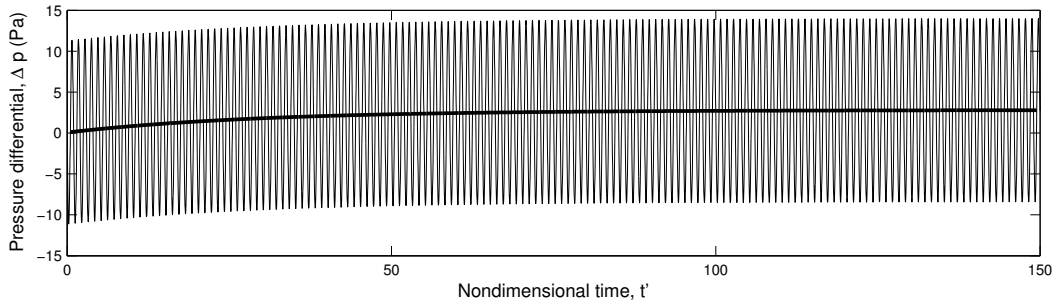

(c)

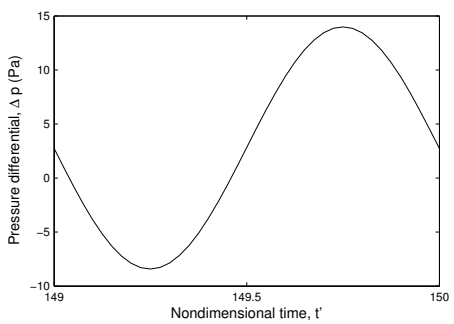

(d)

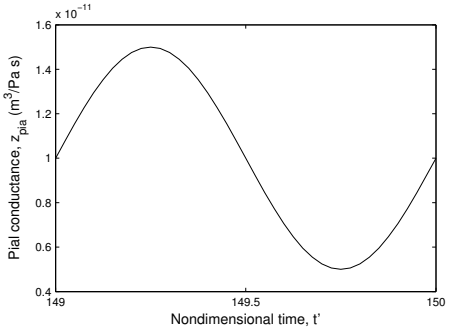

(e)

Fig. 6.3: The effect of a dynamic pial conductance in the single-segment model offset by a phase lag ($\theta = 180°$) with respect to the vascular pressure source. The pressures of the spinal cord (SC), spinal subarachnoid space (SSS) and their difference are plotted in (a), (b) and (c), respectively; bold lines denote the periodic average of each pressure signal, and values of other parameters are as per Tables 5.2 (p. 120) and 5.3 (p. 121). The phase lag, observed between (d) and (e), causes net inflow to the SC and a corresponding increase in SC mean pressure with respect to that of the SSS, hence $\overline{\Delta p} > 0$ at steady state.

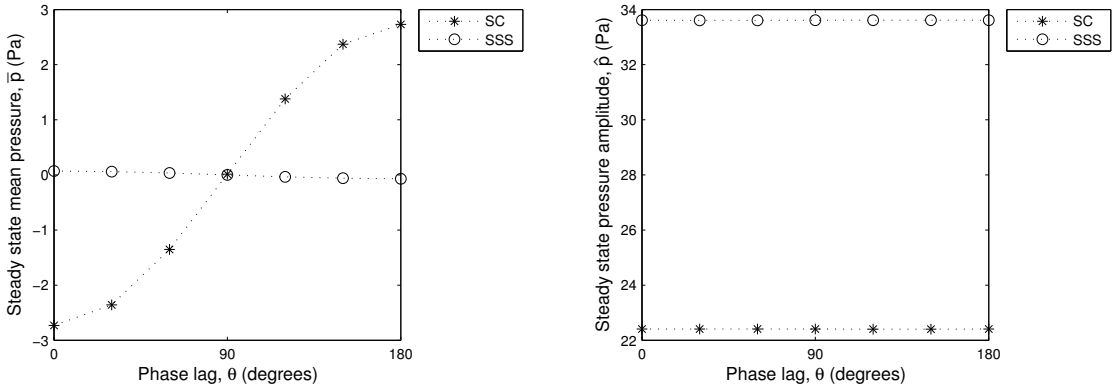

(a) (b)

Fig. 6.4: The steady state response of the single-segment model to variations in phase lag. Plotted are the (a) mean and (b) amplitude of the pressure in the spinal cord (SC) and spinal subarachnoid space (SSS) compartments. Parameter values as per Tables 5.2 (p. 120) and 5.3 (p. 121). At $\theta = 180°$ the mean transpial pressure differential, $\overline{\Delta p}$ $(= \bar{p}_{\mathrm{SC}} - \bar{p}_{\mathrm{SSS}})$, is maximal.

by inspection for all θ.

6.2.2 Source terms

The mean vascular pressure is influenced by changes in pumping rate (cardiac output), vessel resistance (systemic vascular resistance) and fluid volume (especially in the venous reservoir). Most spinal pathologies will perturb the healthy equilibrium state. In the present lumped-parameter approximation of the cerebrospinal system the mean value of the source pressure plays no role in the dynamic response. This is in the nature of the modelling technique—compliances connect adjacent compartments directly rather than each to some general reference pressure—described precisely by the equation of state (5.2b) [p. 108]. However, the *amplitude* of the source pressure plays a role, as demonstrated in Fig. 6.5. The diamond-shaped markers correspond to the amplitude listed in Table 5.3 (p. 121) and the legend indicates a scaling of this value. The mean and amplitude of the SC and SSS compartment pressures all scale linearly with $\widehat{p_{\mathrm{Vasc}}}$, as would be expected for a linear system. These compartments respond in opposition to one another so while the mean pressure of the SC rises with θ the mean

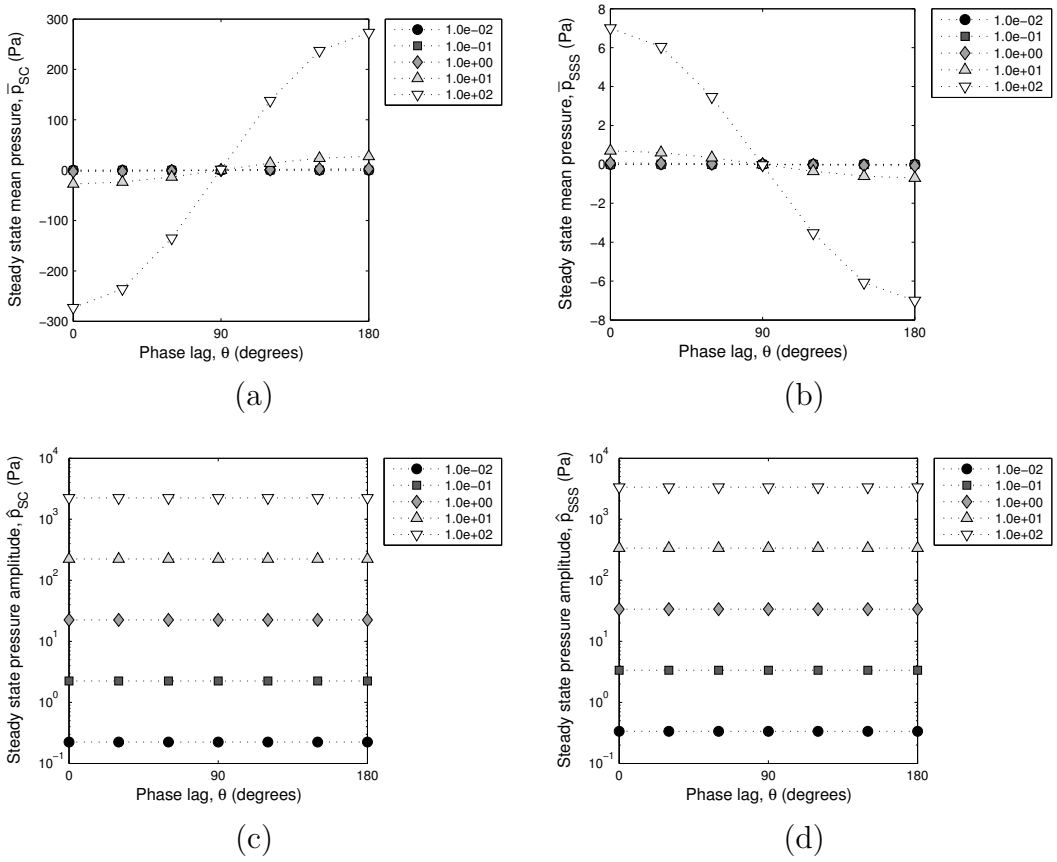

Fig. 6.5: The influence of source pressure amplitude on the steady-state response to phase lag in the single-segment model. The legend indicates the scaling of the source amplitude with respect to the reference value given in Table 5.3 (p. 121); values of the other parameters are given in the same Table and also in 5.2 (p. 120).

pressure of the SSS falls, although to a lesser magnitude [panels (a) and (b)]. The response of the compartment amplitudes is opposite to that of their respective means with the SSS amplifying more strongly than the SC [panels (c) and (d)].

Since the frequency is held constant in Fig. 6.5 one might be tempted to think that the rate of change of the source pressure is important in determining the magnitude of the system response. However, this notion is quashed by performing the reverse experiment—varying the frequency whilst fixing the source amplitude. Figure 6.6 plots the system response for five different frequency values (indicated by the legend). The only significant effect of the driving frequency is the number of oscillations taken for the system to respond to a perturbation and settle into an equilibrium state; the amount of

time does not change though since the number of oscillations is inversely proportional to the frequency. Mathematically this makes sense as the viscous damping described by Eq. (5.2b) has no temporal dependence.

6.2.3 Conductance

When the conductance of the pial membrane is prescribed by a periodic function it approximates the effect of the arterial pressure on the geometry of the perivascular spaces. Changing the mean value of this pial conductance has just one effect—to alter system responsiveness. Lower values of $\bar{z}_{Pia}$ require more oscillations (at the same frequency) to respond to changes in phase lag; compare panels (a) and (b) of Fig. 6.7. The amplitude of pial conductance pulsations, on the other hand, has a linear scaling effect on $\overline{\Delta p}$. Figure 6.8 illustrates this over three orders of magnitude for the case of $\theta = 180°$, where the ◯ marker corresponds to the base value of half the mean listed in Table 5.2. The amplitude of transpial pulsations remains invariant to $\hat{z}_{Pia}$.

6.2.4 Compliances

Compliance quantifies the change in compartment pressure for a given change in fluid volume. The compliance between the vascular source and the SSS compartments determines what proportion of the source pressure will be transmitted to the SSS. This is straightforward from the governing equations. For compliances between non-source compartments, of which there are three, the behaviour is perhaps less intuitive. In panel (a) of each of the next three figures (6.9, 6.10 and 6.11), the diamond-shaped markers correspond to the appropriate compliance value from Table 5.2 (p. 120) and the legend indicates a scaling of this value. These same parameter ranges are covered on the abscissas of panel (b) of the respective figures.

The effect of altering the pial compliance is demonstrated in Fig. 6.9 over the now standard range of phase lag values (θ). The mean SC and SSS pressures each scale in the opposite sense to Fig. 6.5(a,b), which is summarised here by a single plot of

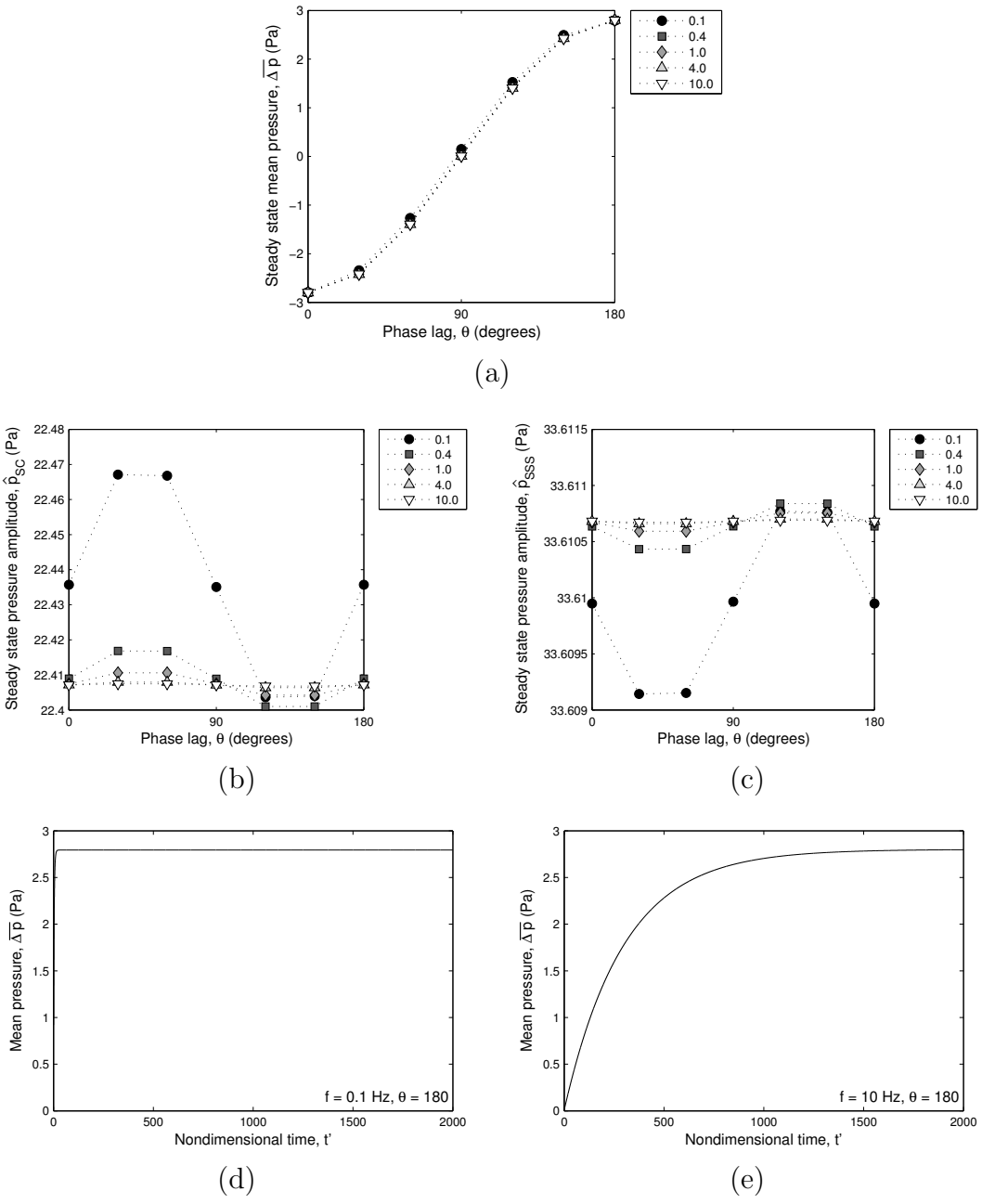

Fig. 6.6: The influence of driving frequency on the steady-state response to phase lag in the single-segment model. The legends in panels (a), (b) and (c) indicate the frequency in Hertz, where the standard reference value is 1 Hz, as per Table 5.3 (p. 121); values of the other parameters are given in the same Table and also in 5.2 (p. 120).

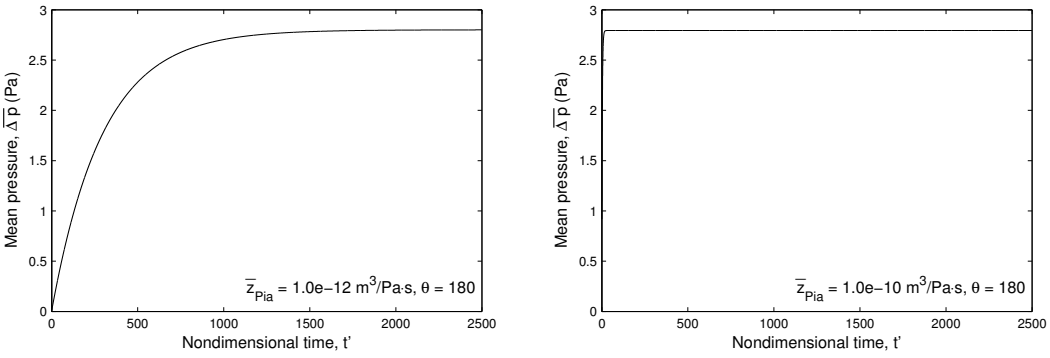

(a) (b)

Fig. 6.7: The influence of mean pial conductance ($\bar{z}_{Pia}$) on system responsiveness in the single segment model. The mean transpial pressure ($\overline{\Delta p}$) takes longer to reach a steady state in (a) compared to (b) due to the lower $\bar{z}_{Pia}$ value. Other parameters have the values listed in Tables 5.2 (p. 120) and 5.3 (p. 121).

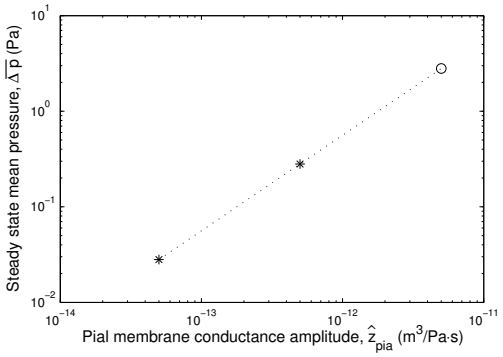

Fig. 6.8: The linear dependence of mean transpial pressure ($\overline{\Delta p}$) on the amplitude of pial conductance pulsations ($\hat{z}_{Pia}$) in the single-segment model. This result is independent of phase lag (θ). The ◯ marker corresponds to half the value listed in Table 5.2 (p. 120), other parameters have values from the same table and also from Table 5.3 (p. 121).

$\overline{\Delta p}$ [Fig. 6.9(a)]. Evidently, for a stiffer pial membrane (lower c_{Pia}) the mean transpial pressure differential becomes amplified. In fact, from panel (b), the amplitude of transpial pulsations (for all θ) are also observed to amplify as the pial membrane is made stiffer, which is associated with slower convergence times [compare panels (c) and (d)].

The intrinsic compliances of the SC and SSS compartments allow a volume of CSF to be accommodated by the expulsion of venous blood and in the case of the SSS, the displacement of epidural fluid. The compliance values are set by the stiffness of the vessel walls, the volume of contained fluid and the ease with which this fluid can be displaced. Figure 6.10 shows the situation for the SC. It can be seen that reducing c_{SC} attenuates Δp, both in (a) mean value and (b) amplitude, the opposite effect to that of the pial compliance described earlier. In fact, Δp approaches zero in the limit of $c_{\mathrm{SC}} = 0$. This is a significant finding as it means that the intrinsic compliance of the SC must be *non-zero* for the cardiac-PVS phase difference mechanism to operate. Mechanically this makes sense as fluid will not accumulate in the SC compartment by the displacement of the pia membrane alone—the pressure gradient driving such a flow will be opposed by the elastic forces induced by the stretching of the membrane. The intrinsic compliance on the opposite side of the pial membrane, c_{SSS}, has the reverse effect on Δp, as demonstrated in Fig. 6.11.

6.2.5 Dual excitation

Up until this point all simulations have been driven by the vascular pressure oscillations, transmitted solely to the SSS by the direct mechanical connection of the intervening flexible compartment wall. The anatomical reality is, of course, more complicated. The spinal arteries track along the surface of the SC so their pulsation will be felt in the SC as well as the SSS. Therefore a vascular pulse is introduced in the SC by allowing the compliance with the pressure source ($c_{\mathrm{Vasc,SC}}$) to become non-zero. The effect of this modification is shown in Fig. 6.12. The legend indicates the magnitude

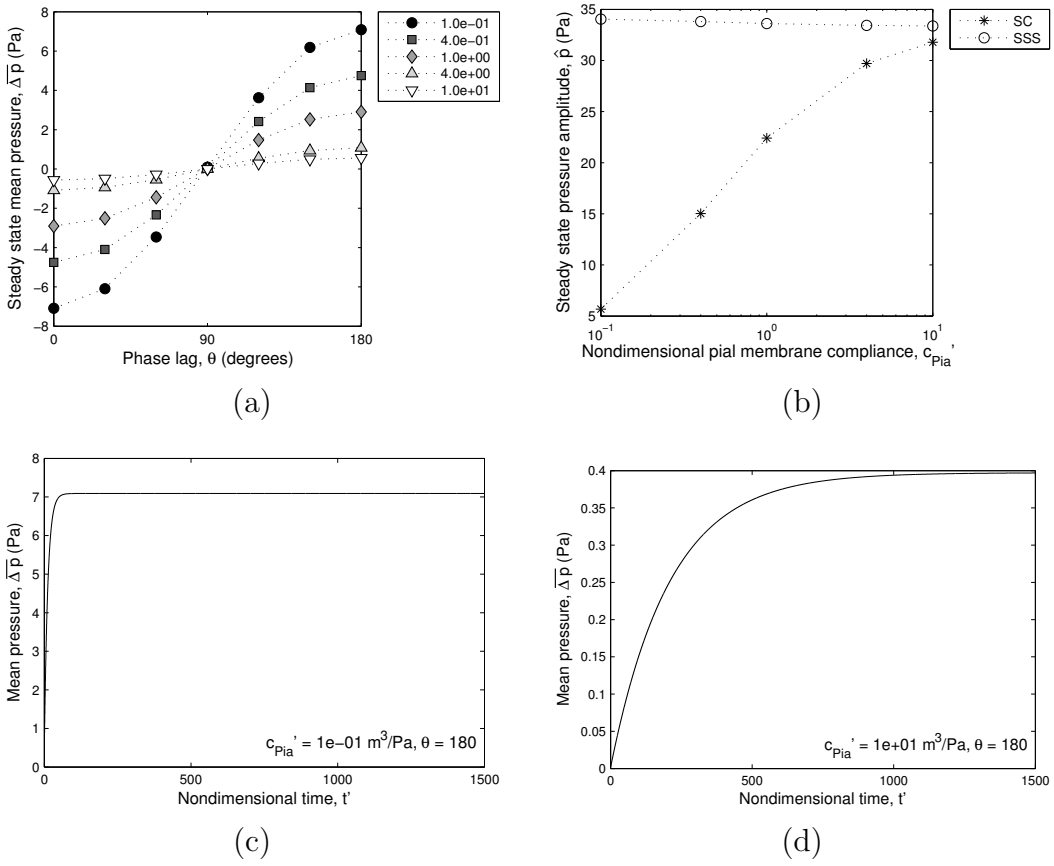

Fig. 6.9: The effect of altering the pial compliance on the pressure in the spinal cord (SC) and spinal subarachnoid space (SSS) compartments in the single-segment model. The diamond-shaped markers in (a) correspond to the pial compliance value from Table 5.2 (p. 120) and the legend indicates a scaling of this value; this nondimensional pial membrane compliance ($c_{\mathrm{Pia}}\prime$) is the abscissa coordinate in (b). Other parameters have the values listed in the same table and in Table 5.3 (p. 121). A stiffer pial membrane (lower $c_{\mathrm{Pia}}\prime$) amplifies the (a) mean and (b) amplitude of transpial pulsations ($\Delta p = p_{\mathrm{SC}} - p_{\mathrm{SSS}}$), which is associated with slower convergence times [cf. (c) and (d)]. The result in (b) is independent of phase lag (θ).

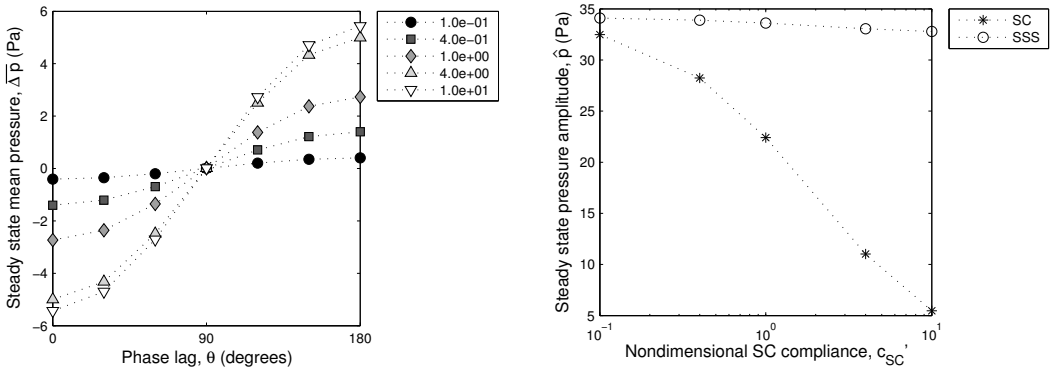

(a) (b)

Fig. 6.10: The effect of altering the spinal cord (SC) compliance on the pressure within the SC and spinal subarachnoid space (SSS) compartments in the single-segment model. The diamond-shaped markers in (a) correspond to the SC compliance value from Table 5.2 (p. 120) and the legend indicates a scaling of this value; this nondimensional SC compliance ($c_{\mathrm{SC}}\prime$) is the abscissa coordinate in (b). Other parameters have the values listed in the same table and in Table 5.3 (p. 121). Reducing $c_{\mathrm{SC}}\prime$ attenuates Δp ($= p_{\mathrm{SC}} - p_{\mathrm{SSS}}$), both in (a) mean value and (b) amplitude. The result in (b) is independent of phase lag (θ).

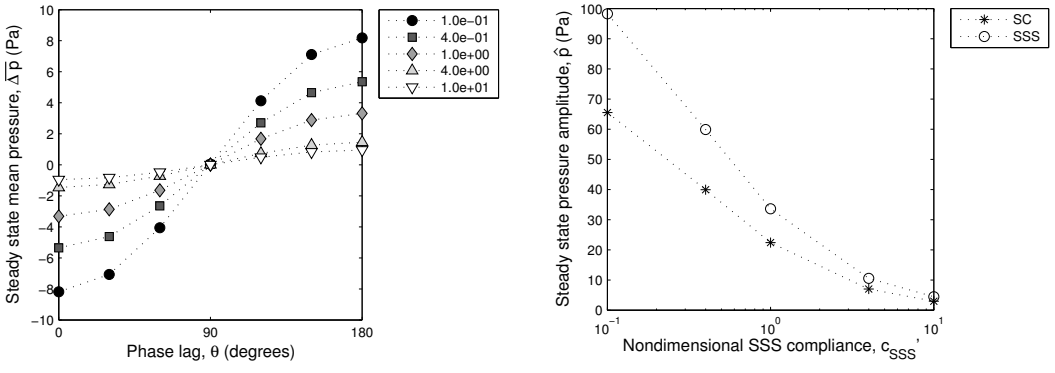

(a) (b)

Fig. 6.11: The effect of altering the spinal subarachnoid space (SSS) compliance on the pressure within the spinal cord (SC) and SSS compartments in the single-segment model. The diamond-shaped markers in (a) correspond to the SC compliance value from Table 5.2 (p. 120) and the legend indicates a scaling of this value; this nondimensional SC compliance ($c_{\mathrm{SSS}}\prime$) is the abscissa coordinate in (b). Other parameters have the values listed in the same table and in Table 5.3 (p. 121). Reducing $c_{\mathrm{SSS}}\prime$ amplifies Δp ($= p_{\mathrm{SC}} - p_{\mathrm{SSS}}$), both in (a) mean value and (b) amplitude. The result in (b) is independent of phase lag (θ).

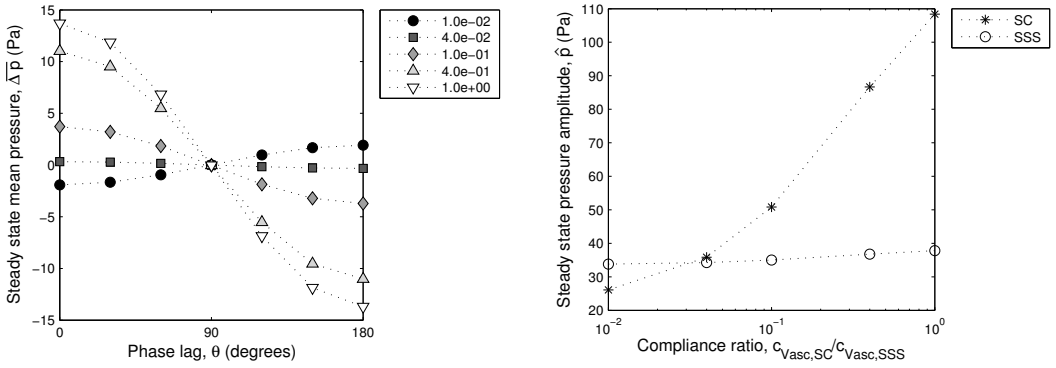

(a) (b)

Fig. 6.12: The effect of the vascular pulse driving both the spinal subarachnoid space (SSS) and spinal cord (SC) compartments in the single-segment model. The compliance between the SC compartment and the vascular source ($c_{\mathrm{Vasc,SC}}$, set to zero in previous figures) was varied with respect to the compliance of the SSS with the same source ($c_{\mathrm{Vasc,SSS}}$). The legend in (a) indicates this nondimensional ratio, which is the abscissa coordinate in (b); $c_{\mathrm{Vasc,SSS}}$ has the value from Table 5.2 (p. 120), and other parameters have the values listed in the same table and also in Table 5.2 (p. 120). (a) The polarity of $\overline{\Delta p}$ tends to reverse as the SC and SSS compartments receive more comparable inputs and (b) the pressure amplitude in both compartments rises with increasing $c_{\mathrm{Vasc,SC}}/c_{\mathrm{Vasc,SSS}}$.

of this compliance as compared to the compliance between the SSS compartment and the vascular source ($c_{\mathrm{Vasc,SSS}}$, value from Table 5.2). From panel (a) it is evident that the polarity of $\overline{\Delta p}$ tends to reverse as the SC and SSS compartments receive more comparable inputs. One also notices from panel (b) that the pressure amplitude in both compartments rises with increasing $c_{\mathrm{Vasc,SC}}/c_{\mathrm{Vasc,SSS}}$, and only small ratios are required for the pulse amplitude of the SC compartment to overtake that of the SSS.

6.2.6 Analysis

The findings up until this point are summarised in Table 6.1, which reads as follows. At the intersection of a parameter from the left-hand column and a steady-state quantity from the first row is a symbol denoting the relationship between the two: '+', '−' or '0'. For example, increasing the amplitude of the vascular source pressure, $\hat{p}_{\mathrm{Vasc}}$, will increase ('+') the magnitude of the mean SC pressure, $|p_{\mathrm{SC}}|$, decrease ('−') the transpial

Table 6.1: Summary of results for the single-segment model.

Parameter	$\lvert\bar{p}_{\mathrm{SC}}\rvert$	$\lvert\bar{p}_{\mathrm{SSS}}\rvert$	$\hat{p}_{\mathrm{SC}}$	$\hat{p}_{\mathrm{SSS}}$	$\lvert\overline{\Delta p}\rvert$	$\widehat{\Delta p}$	T	Figure
$\bar{p}_{\mathrm{Vasc}}$	0	0	0	0	0	0	0	N/A
$\hat{p}_{\mathrm{Vasc}}$	+	+	+	+	+	−	0	6.5
ω_{HR}	0	0	0	0	0	0	0	6.6
$\bar{z}_{\mathrm{Pia}}$	0	0	0	0	0	0	−	6.7
$\hat{z}_{\mathrm{Pia}}$	+	+	0	0	+	0	0	6.8
c_{Pia}	−	−	+	−	−	−	−	6.9
c_{SC}	+	+	−	−	+	+	−	6.10
c_{SSS}	−	−	−	−	−	−	0	6.11
$c_{\mathrm{Vasc,SC}}/c_{\mathrm{Vasc,SSS}}$	∓	∓	+	+	∓	∓	−	6.12

pulsation amplitude, $\widehat{\Delta p}$, and make no difference to the time taken to converge to the steady state, T. The '∓' symbol in the last row refers to a change in behaviour from '−' to '+' as the compliance ratio $c_{\mathrm{Vasc,SC}}/c_{\mathrm{Vasc,SSS}}$ increases for the respective steady-state quantities. A syrinx distends the SC due to the pressure within it being greater than that outside. In the single-segment model this is equivalent to a raised $\overline{\Delta p}$, which is indicated in Table 6.1 (column 6 of 9) by an increased pulse amplitude of the vascular source pressure or PVS conductance, an increase in SC intrinsic compliance, a decrease in either pial or intrinsic SSS compliance, or some alteration of the relative compliance of the vascular source pressure to the SC and SSS compartments.

6.3 Multiple-segment model

6.3.1 Basic concept

The SC is discretized along the rostrocaudal axis into five compartments which are paired with adjacent SSS compartments to form five spinal canal segments ($N = 5$). The SSS is extended downwards to include the region of the filum terminale (FT) and upward to connect with the ventricular cavities within the brain (V). These CSF-filled compartments are excited, as before, by vascular pressure pulsations transmitted to the SSS, which are also the basis of the time-varying pial conductance. Intercompartmental compliances account for the flexibility of the pial membrane, the collapsibility of venous

reservoirs and the displacement of epidural fluid, as illustrated schematically in Fig. 5.5 (p. 106). Beginning with a zero-pressure initial condition, a simulation was run for 150 oscillations for the case when $\theta = 180°$, which is shown in Fig. 6.13 (all other parameters were as per Tables 5.2 and 5.3). This is the equivalent simulation to that plotted in Fig. 6.3 for the single-segment model, except here a pressure of a given segment is plotted as a band rather than a simple line since having multiple segments adds an extra dimension to the data; collectively the bands form an image plot. Bands have the same width in the x direction (0.2, giving a nondimensionalised SC length of 1 for the 5-segment model; the ventricular and FT compartments are plotted as bands of the same width having effective x coordinates < 0 and > 1, respectively) and pressure values are constant across the width of each band as the pressure throughout a given compartment is uniform at each instant in time.

The vascular source pressure is plotted on axes of nondimensionalised time (t) versus normalised rostrocaudal position in Fig. 6.13(a); $x = 0$ corresponds to the head end of the SC and $x = 1$ to the tail end. For a wave speed of 5 m/s and a driving frequency of 1 Hz the wavelength is long with respect to the length of the SC, which gives rise to the striped appearance of the plot as the sinusoidal waveform in each of the segments are in-phase. The source pressure is thus almost independent of x, as expected.

A similar long-wave response can be seen in the CSF compartments outside the SC in panel (b); the annotations 'V' and 'FT' indicate the compartments for the ventricles and the portion of the SSS occupied by the filum terminale. Panels (c) and (d) demonstrate that the phase lag mechanism for trans-pial pressure build-up still operates in the multiple-segment model, but Δp now varies with x. To complete this preliminary description panels (e) and (f) show that the pressure amplitude tends to taper off in the V and FT compartments which is probably a result of them not being driven directly by the source.

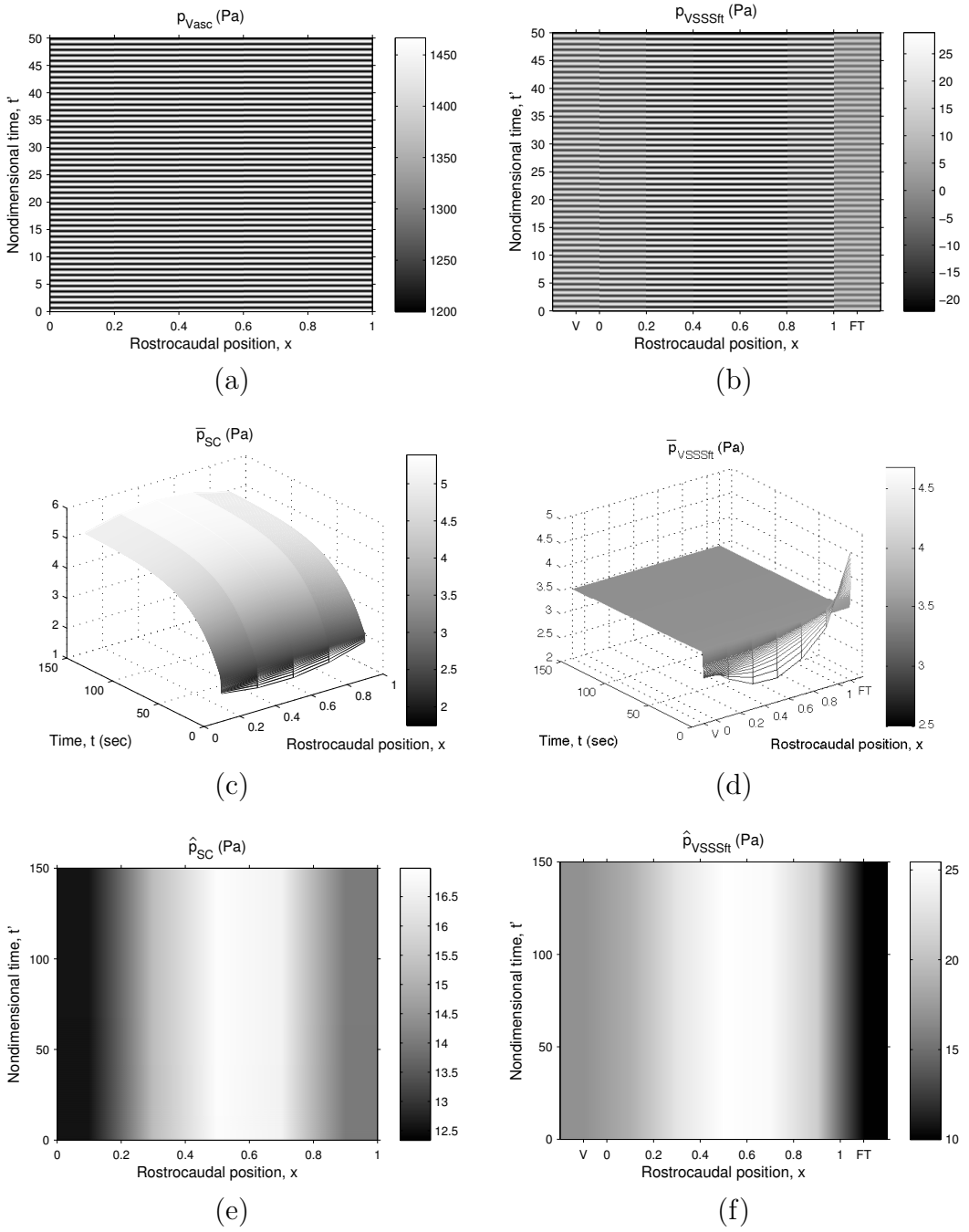

Fig. 6.13: The effect of a dynamic pial conductance in a 5-segment model. This is the equivalent simulation to that plotted in Fig. 6.3 (p. 129) for the single-segment model; the phase lag $\theta = 180°$ and all other parameters were as per Tables 5.2 (p. 120) and 5.3 (p. 121).

6.3.2 Discretization study

When solving continuum equations numerically, for the resulting solution to be physically meaningful it must be independent of the level of discretization of the solution domain. To demonstrate this, one typically performs a grid-independence study. Since a lumped-parameter model has zero spatial dimensions the concept of grid independence does not apply. However, to demonstrate that the equations are being solved correctly the same solution should be found independent of the number of compartments involved. In this model one expects the SC and SSS pressure profiles to be the same along the rostrocaudal axis regardless of the number segments in the model. Therefore, the number of segments is varied from 3 to 21 and the system response is compared for a range of phase lag values. To ensure that the excitation is the same in both models the pulse wave speed is made very large so that all SSS compartments are excited by the same phase of the cardiac cycle. The conductances at either end of the SSS (to the ventricles and filum terminale compartments) are reduced to a sufficiently small value so that end effects from these compartments do not play a role.

In Fig. 6.14(a) the SC mean pressure ($\bar{p}_{\mathrm{SC}}$) at position $x = 0.5$ is plotted against number of segments (N) for the case of $\theta = 180°$. The variation in pressure amplitude is about one per cent and even less for the mean pressures, and with no obvious trend in N, which is deemed acceptable. Analogous plots are given in panels (b), (c) and (d) for the mean SSS pressure, and the amplitudes of the SC and SSS pressures, respectively, from which similar conclusions may be drawn. To ensure that any phase-dependent behaviour is preserved at different discretizations, the results from the 5-segment and 11-segment models are plotted in Fig. 6.15 over the full range of θ. By comparing consecutive pairs of plots it is clear that the number of segments does not influence the converged solution. This being the case, it was decided to perform the remaining suite of parametric studies using the 5-segment model since this required minimal computational effort.

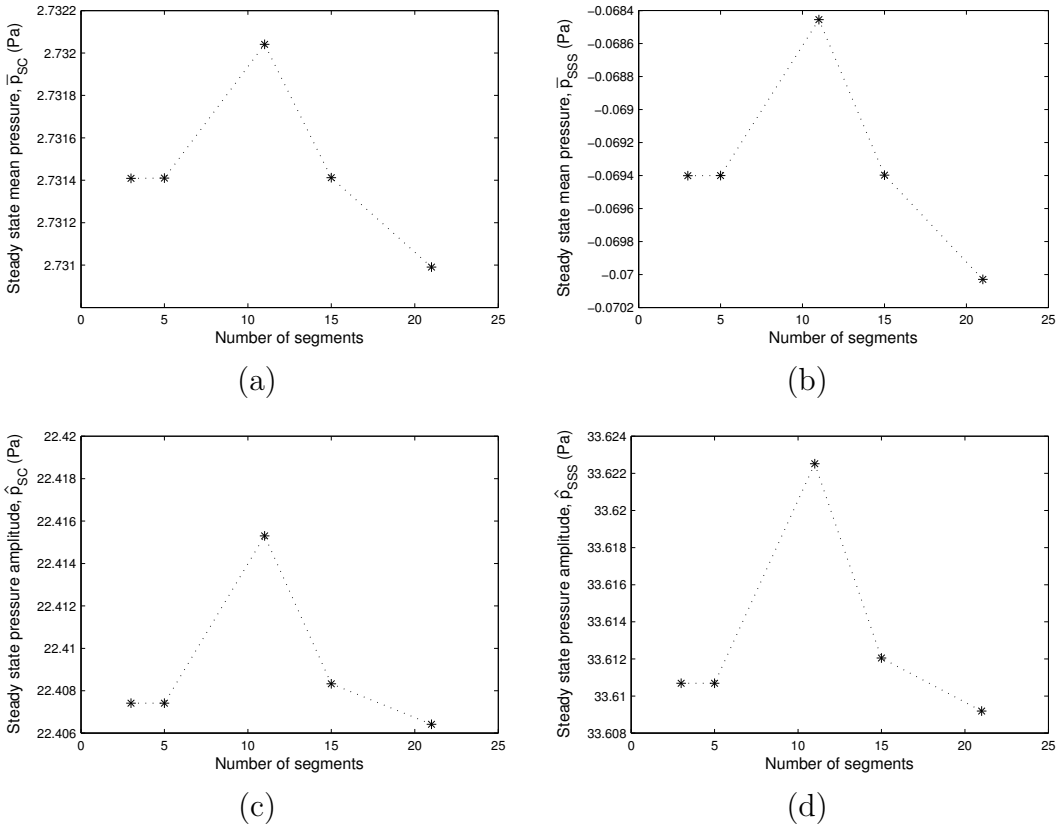

Fig. 6.14: Discretization study for the multiple-segment model at location $x = 0.5$ and with phase lag $\theta = 180°$. The same simulation was repeated for models having different numbers of segments. The pulse wave speed was made very large so that all SSS compartments were excited by the same phase of the cardiac cycle, and the conductance between the spinal subarachnoid space and the ventricular (V) and filum terminale (FT) compartments was made sufficiently small to make end effects negligible. Parameter values were as per Tables 5.2 (p. 120) and 5.3 (p. 121). To an acceptable degree of accuracy the solution is independent of the number of compartments.

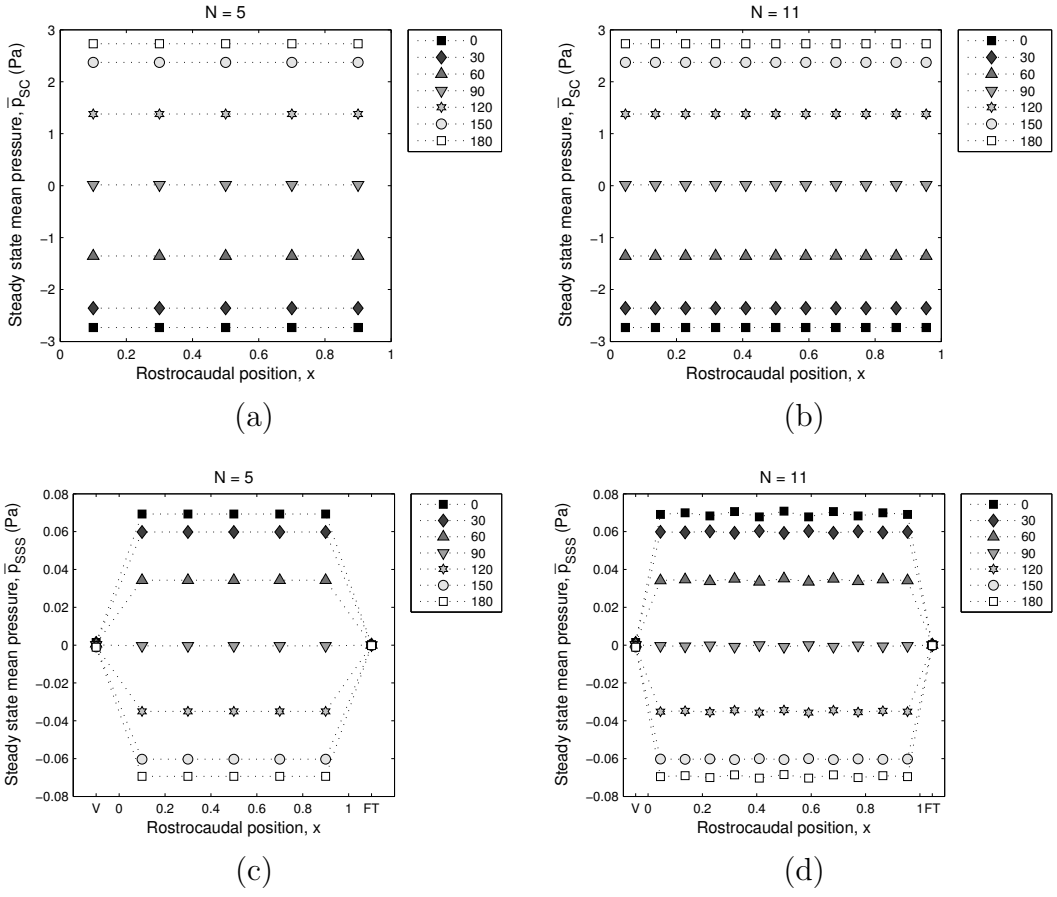

Fig. 6.15: The 5-segment and 11-segment models of Fig. 6.14 were rerun over the range of θ indicated in the legend. The phase-dependent behaviour is preserved at different discretizations. Continued on page 145.

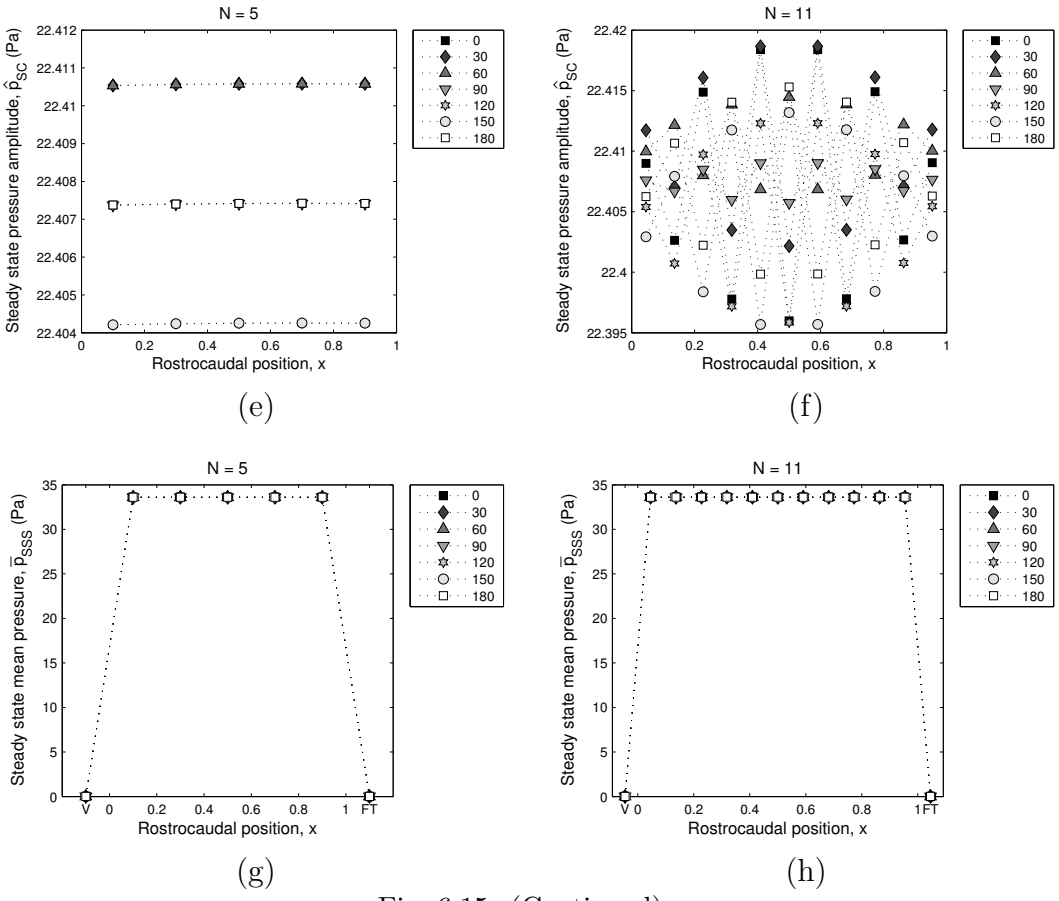

Fig. 6.15: (Continued).

6.3.3 End effects

The multiple-segment model offers two main refinements over its single-segment counterpart. Firstly, it includes the cerebral ventricles and the portion of the SSS that extends beyond the termination level of the SC. Secondly, the SC and surrounding SSS are discretized into a number of segments, which allows for spatial resolution of pressure along the spinal axis. The end effects associated with the additional two compartments will be dealt with here, leaving the spatial effects for §6.3.4.

Fig. 6.16 shows the effect of obstructing flow between the SSS and the ventricular compartment by reducing the conductance z_{V} by three orders of magnitude. In terms of mean pressure values the outcome is subtle. There is a slight increase in ventricular pressure when the conductance is reduced, evident when comparing panels (a) and (b), which tends to 'straighten out' the rounded $\overline{\Delta p}$ profiles typical of the multiple-compartment model [panels (c) and (d)]. The ventricular conductance has a more pronounced effect on pulsation amplitude, with lower values tending to damp out pulsations in the ventricles [panels (e) and (f)]. Similar observations are made at the opposite end of the spinal canal for flow obstructions to the SSS-FT compartment.

6.3.4 Spatial effects

Subdividing one fluid space into a series of interconnecting compartments introduces a conductance lumped at each of the intercompartmental boundaries. The conductance value listed in Table 5.2 for flow within the SC (z_{SC}) is likely to be a lower bound since any fluid accumulated in the cord will tend to raise the porosity and the conductance along with it. However, raising z_{SC} in the whole SC by some five orders of magnitude has no observable effect on either the mean or amplitude of any of the compartment pressures. The conductance within the SSS, on the other hand, proves to be a more sensitive parameter. The SSS is susceptible to blockages so the value of z_{SSS} between each of the SSS compartments is reduced by first one and then three orders of magnitude, as shown in Fig. 6.17 (left and right columns, respectively). Compar-

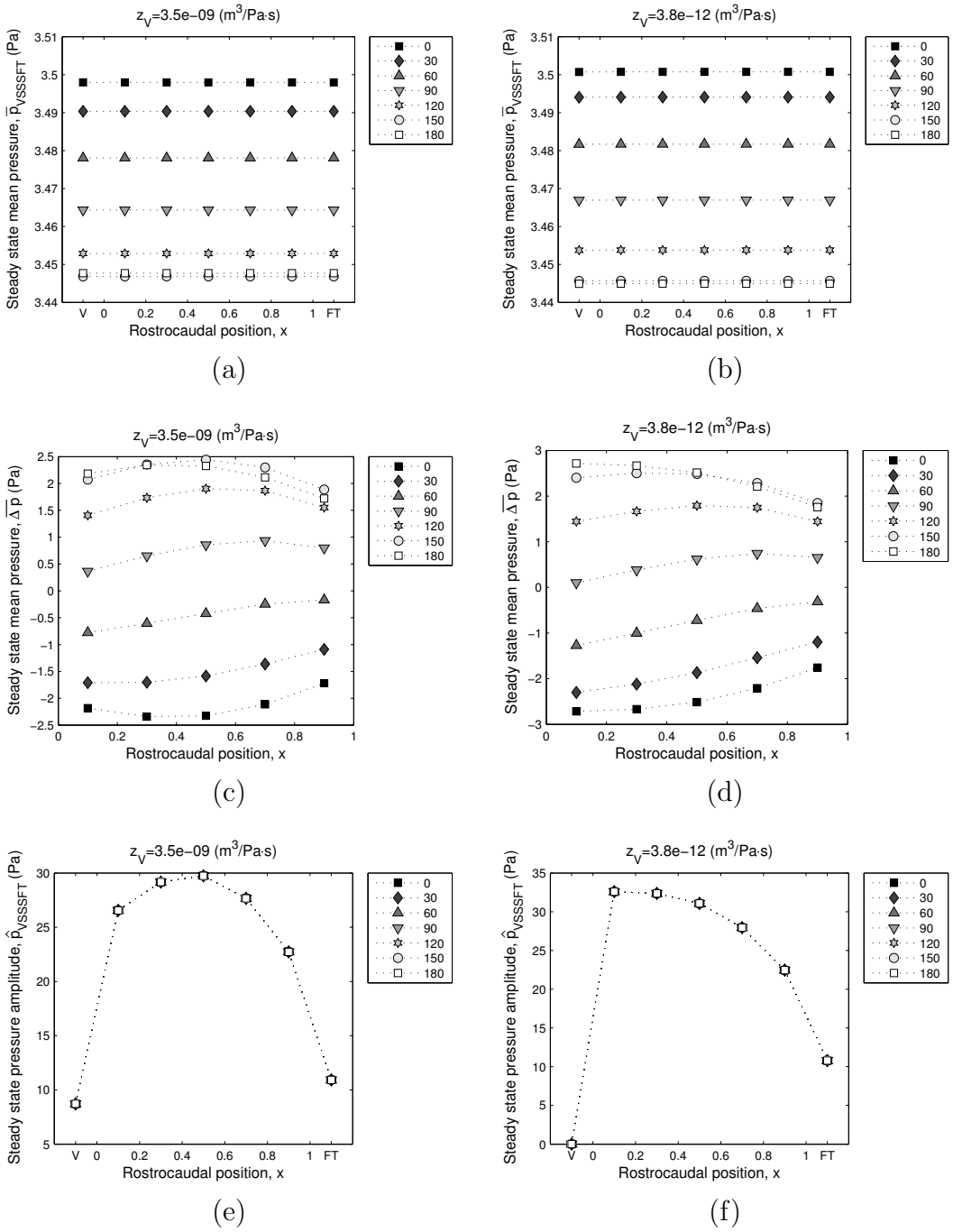

Fig. 6.16: The effect of altering the ventricular conductance (z_{V}) in a 5-segment model. The legend indicates the phase lag value (θ) and all other parameters were as per Tables 5.2 (p. 120) and 5.3 (p. 121). Reducing z_{V} increases mean ventricular pressure slightly [(a), (b)], straightens out the $\overline{\Delta p}$ profile [(c), (d)], and damps out pulsations in the ventricles [(e), (f)].

ing Fig. 6.17(a) and (c) with Fig. 6.15(a) and (c) it would appear that reducing the conductance within the SSS tends to uniformly raise the mean pressure in both the SC and SSS (the pressure of the FT and V are also of course no longer constrained to be zero). Reducing the conductance by a further two orders of magnitude mainly tends to raise the mean SC pressure towards the ends, flattening the $\bar{p}_{\mathrm{SC}}$ and $\overline{\Delta p}$ profiles, as shown in Fig. 6.17(b) and (f). Lowering conductance along the SSS causes the amplitude of pulsations in the ventricle and FT compartments to subside with a concomitant increase of the amplitude in neighbouring compartments in the SSS and SC [Fig. 6.17(g) to (j)].

The purpose of discretizing the SC and SSS into a number of segments is to allow alterations of physiological parameters to be *localised*. This is in some sense a '1-d approximation', with a finer discretization approaching the continuum limit. In Fig. 6.18 the phase lag is fixed at $\theta = 90°$ for all segments except the central segment, where it varies according to the legend. The response of the SC compartments is localised like the phase lag whereas the SSS exhibits a uniform response across the whole spinal axis, as shown in panels (a) and (b), respectively. This allows for a non-zero $\overline{\Delta p}$ across the pial membrane to persist locally, despite the surrounding compartments maintaining a near-zero value [panel (c)]. In other words, the pressure is equilibrated within the SSS but not within the SC. This result resembles the situation of a syrinx. None of the pressure amplitudes are affected by the localised phase lag disturbance for the parameter values chosen here.

6.3.5 Analysis

The spinal canal from the single-segment model was subdivided into multiple segments, and the contained SSS was also extended downward to the insertion of the filum terminale (FT) and upward to connect with the ventricular cavities (V) by the inclusion of two extra compartments, respectively. The implementation of the segmental discretization was demonstrated to be consistent with the single segment case. The end

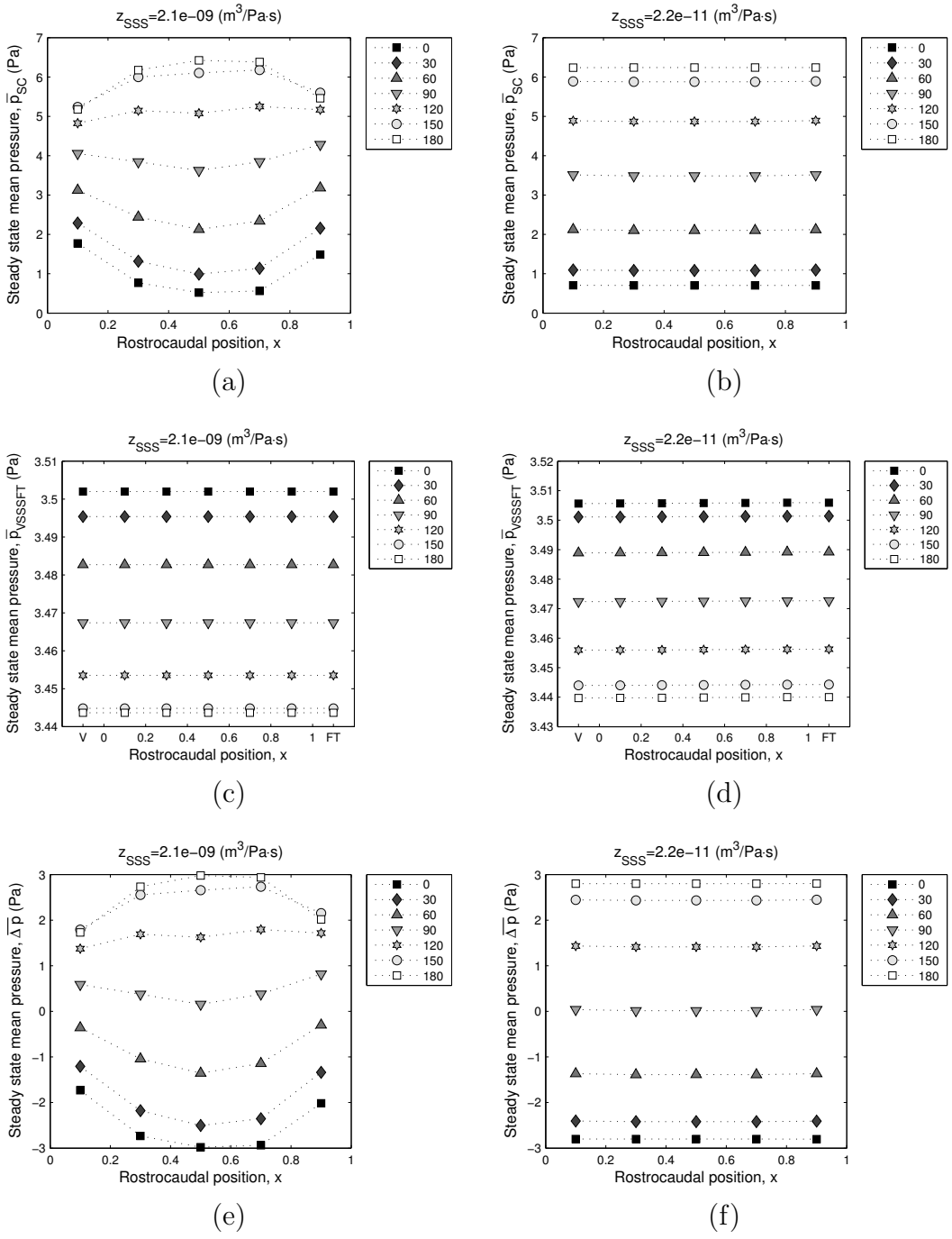

Fig. 6.17: The effect of altering the spinal subarachnoid conductance (z_{SSS}) in the entire spinal canal of a 5-segment model. The legend indicates the phase lag value (θ) and all other parameters were as per Tables 5.2 (p. 120) and 5.3 (p. 121). Reducing z_{SSS} raises the mean pressure in the SC and SSS [(a) to (d)], especially towards the ends in the case of the SC where the amplitude of pulsations are damped [(i), (j)]. Continued on page 150.

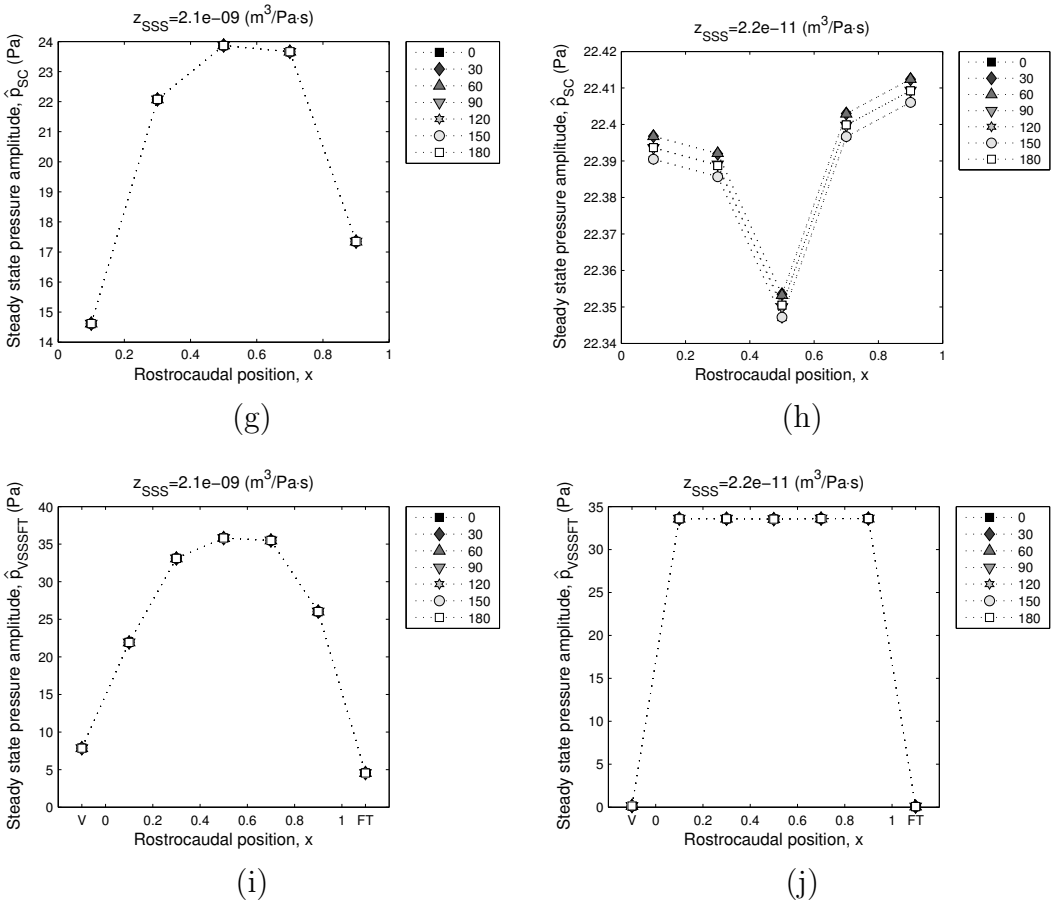

Fig. 6.17: (Continued).

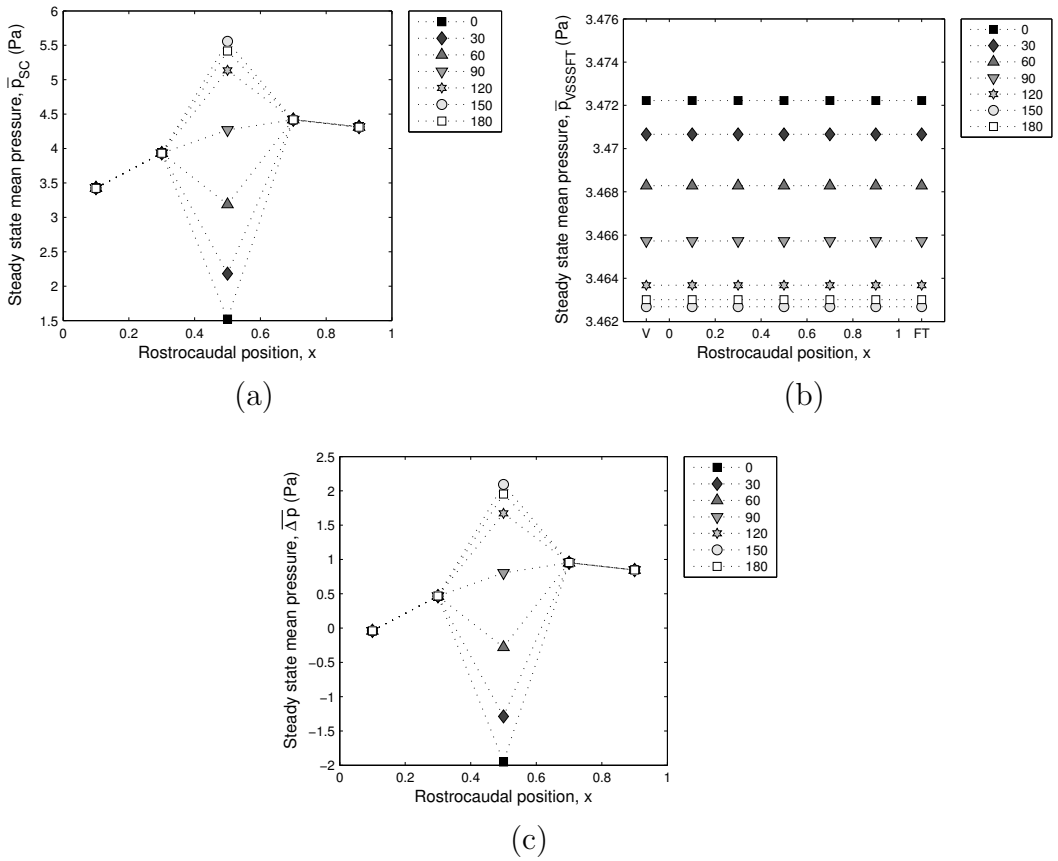

Fig. 6.18: The effect of a localised phase-lag perturbation in a 5-segment model. The phase lag is $\theta = 90°$ for all segments except the central segment, where it varies according to the legend. All other parameters were as per Tables 5.2 (p. 120) and 5.3 (p. 121). The response of the (a) SC compartments follows θ whereas the (b) SSS exhibits a uniform response across the whole spinal axis.

compartments (V and FT) functioned to reduce the mean pressure in the SC and SSS and of their difference $\overline{\Delta p}$. Changing the conductance of the entire SC had no noticeable effect but the same modification to the SSS introduced a positive pressure gradient in the x direction and flattened out the $\overline{\Delta p}$ profile. Varying the phase lag θ locally was able to achieve a local change in $\overline{\Delta p}$; i.e., it was not equilibrated along the length of the SC.

6.4 Summary

The lumped-parameter models developed in Chapter 5 have been used presently to investigate Bilston *et al.*'s (2007) phase-lag mechanism for perivascular flow, and its possible role in syrinx formation. Since flux itself did not feature in the final governing equations perivascular flow was determined by its resultant effect—altering the pressure differential between the SC and the SSS. A syrinx is an accumulation of fluid at high pressure in the SC. In the lumped-parameter models this corresponded to a sustained positive value for the mean transpial pressure differential, $\overline{\Delta p}$ (i.e., $\overline{p}_{\mathrm{SC}} > \overline{p}_{\mathrm{SSS}}$), which was proportional to a change in SC fluid volume. The amplitude of transpial pulsations, $\widehat{\Delta p}$, was also affected by the system parameters, and it was put forth that the magnitude of this quantity may be proportional to the rate of fluid exchanged across the pial membrane.

In the single-segment model it was demonstrated here that a dynamic pial conductance that differs in phase to a vascular driving pressure can raise pressure in the SC above the level of the SSS. However, this was only possible when the intrinsic compliance of the SC, representing the collapsibility of the contained vascular bed, was not zero. The values of the physiological parameters that were estimated to order of magnitude in the previous chapter were used here as a starting point for a parametric sensitivity study. It was found that $\overline{\Delta p}$ may be amplified by an increased pulse amplitude of the vascular source pressure or of the PVS conductance, an increase in the intrinsic compliance of the SC, a decrease in either pial or intrinsic SSS compliance,

or some alteration of the relative compliance of the vascular source pressure to the SC and SSS compartments.

The main purpose of the multiple-segment model was in demonstrating that the phase-lag mechanism can be localised. Due to the comparatively lower conductance in the SC compared to the SSS, an elevated cord pressure could persist at an isolated location. The additional compartments at the ends of the SSS, representing the ventricles and the extension of the SSS to the level of the filum terminale, functioned to reduce the mean pressure in the SC, SSS and the difference between the two. In the next chapter the results of simulations of pathologies and surgical treatment options are presented, using the present findings as a point of reference.

CHAPTER 7

Lumped-parameter model: Pathology & treatment simulations

7.1 Introduction

The ultimate aim of any model of syringomyelia is to provide insight into the disease process that will assist neurosurgeons in devising treatment strategies. However, as syringomyelia occurs in conjunction with many other diseases it is difficult to determine whether specific pathological features are the cause or effect of syringomyelia. Therefore, in this chapter two diseases commonly associated with syringomyelia—Chiari malformation and arachnoiditis—as well as a syrinx, are simulated; the Chiari and a cervical syrinx are each examined in isolation before simulating the combined pathology, likewise with the arachnoiditis and a mid-thoracic syrinx. Most surgeons today advocate that CSF flow obstructions and abnormal cord tethers should be removed; i.e., the fluid and solid mechanics should be returned to normal. Three current surgical treatments of syringomyelia based on this principle are simulated here: a syringo-subarachnoid shunt, a subarachnoid bypass and a foramen magnum decompression. Details of these treatments are given where their respective implementations in the lumped-parameter model are described. Up until this point, though, the lumped-parameter models have only been the subject of functional testing. Before applying

them to the simulation of more physiological problems these lumped-parameter models are assessed for their suitability as a theoretical description of the cerebrospinal system.

7.2 Assessment of the craniospinal model

In developing the pair of cerebrospinal models presented in Chapters 5 and 6 a number of assumptions were made. These were chiefly reasoned to reconcile physical representation with mathematical tractability, the basis of which will now be assessed. The various fluid spaces within the spinal canal and cranium were divided into compartments and the pressure within each of these was made uniform. Resistance to flow was lumped at the boundaries of communicating compartments. The deformable nature of the biological tissues was represented by elastic compartment walls whose behaviour was defined by a value of compliance, also lumped at the intercompartmental boundary. A pressure change will thus induce flow between compartments and change compartment volume. This is the lumped-parameter modelling approach and has long been used for studying hydraulic disorders of the central nervous system.

In formulating the governing equations for the lumped-parameter models, inertia, analogous to inductance in the equivalent electrical circuit, was not included. This is the inertia associated with the rate of dilatation of a compartment and will be small for the cerebrospinal system as the tissue and fluid masses and the cardiac pulsation frequency are all small quantities. The inertia referred to above should not be confused with the inertia associated with the transfer of momentum between adjacent compartments, predominantly in the axial direction, which is implicitly omitted in lumped-parameter models by their compartmental nature. Since the present lumped-parameter model is driven by the cardiac cycle, the dominant frequencies are an order of magnitude lower than for the cough-based pressure waves studied in Chapter 3, and the Womersley numbers for the cerebrospinal fluid conduits (including the PVS) will tend to lie in the viscous-dominated range (0–10), making the contribution of axial fluid inertia marginal. Moreover, at the low cardiac frequencies studied here, Bertram *et al.* (2005) found that

the spinal fluid-structure system exhibited a lumped response. Although axial fluid inertia will affect the phase difference between CSF and blood, which is the basis for fluid accumulation in the present models, this is accounted for by prescribing phase lag values.

In order to make the governing equations closed the source vector described by Eq. (5.10) [p. 112] is required. Neither the production nor absorption of CSF have been considered as the focus here is on a mechanism for syringomyelia not reliant upon the presence of a hydrocephalus, hence no flux source terms have been included. Pressure terms in the source vector take two forms: (i) a source of excitation or (ii) a boundary condition. The implementation of the blood vessels makes use of both. The spinal CSF pulse pressure is generated by the spinal arterial pulsations (40%), the spinal venous pulsations (40%) and intracranial CSF pulsations propagating through the spinal canal. The vessels of the arterial system are normally distended and operate at a higher mean pressure than the venules and veins downstream, which often collapse due to their relatively thinner walls thereby ejecting venous blood towards the heart. A decrease in venous volume makes extra room for the surrounding tissues and fluids and so for the SC and SSS compartments this equates to volume compliance. Rather than attempt an anatomically correct vascular system, which the simple nature of a lumped-parameter model precludes, a functional approach was taken whereby a generic vascular pressure provided the excitation source and the SC and SSS each contained an intrinsic compliance with a constant-pressure compartment; i.e., the venous vessels were considered to be sufficiently collapsible for their pressure to remain approximately constant. In the SSS this source of compliance was also assumed to include the epidural space. Another way of thinking about these highly compliant compartments are as constant-pressure boundary conditions. The other boundary condition possible is one having constant volume, which is implemented by setting the relevant compliances to be zero in order to make the outermost compartment(s) rigid. This is the so-called Monro-Kellie doctrine and is a reasonable approximation in a cranial model as the bounding dural membrane is firmly adherent to the skull (Agarwal *et al.*, 1969). However, in

the spinal canal the dura mater is surrounded by the epidural space which contains fluid and fatty tissue necessary for the mobility of the spine. Therefore in the spinal canal a constant-pressure boundary condition was prescribed. To limit the dependent pressure variables in the cranium to one, the ventricular pressure, a constant-pressure boundary condition was also assigned to the brain. This is the same approach adopted by Carpenter *et al.* (2003) and effectively renders the ventricles as a CSF storage device, with the change in brain volume made possible by displacement of cerebral blood. The source terms and boundary conditions described above are here submitted to be a reasonable approximation of the cerebrospinal system.

The function ascribed to the vascular pressure varies sinusoidally in time. Although this is a simplification of the physiology, as indicated by Fig. 5.6 (p. 113), more realistic signals are arguably beyond the level of detail of the modelling. Using a trigonometric function also has the advantage of having an exact derivative which avoids introducing a numerical approximation in the source vector and an associated error. To be mechanically consistent the pial conductance was also given a sinusoidal function.

A limitation of the lumped-parameter models is that the phase lag between the vascular source and the pial conductance is prescribed rather than the consequence of a direct physical perturbation to the system. Disruption to the vascular supply of the spinal cord due to constricted and distorted vessels will cause partial pressure wave reflection, tending to increase upstream vascular pressure and decrease downstream pressure and also change the arrival time of a pulse due to the augmented wave speed effected by the change in composition of the vessel wall (more collagen). Ischaemia will also lead to necrosis further modifying the mechanical environment. Without physical measurements (in animals) one can only speculate as to the quantitative effects of vascular disruption due to a given pathology which is why the parametric studies of Chapter 6 were carried out on a range of phase lag values in order to determine the possible role of this mechanism in syringomyelia.

One of the main strengths of a lumped-parameter model is its mathematical simplicity. It is relatively straightforward to solve a large-dimension system numerically

using standard matrix libraries. However, this comes at a price. Approximating the contents of the human body as a discrete set of compartments introduces the problem of determining appropriate parameter values. The various compliances and conductances derived in §5.6 are necessarily order-of-magnitude estimates. Nevertheless, since the objective is to demonstrate qualitative rather than quantitative behaviour, it is submitted that the scope of predictions from these simulations are within the bounds dictated by the assumptions upon which they are based. Having established the suitability of the lumped-parameter model for studying cerebrospinal physiology, the presentation of pathological simulations now follows.

7.3 Healthy system

To simulate a spinal disease a nominal 'healthy state' must be defined from which various perturbations are applied. And to determine this quiescent baseline the steady-state response of a 10-segment cerebrospinal model excited by a 1 Hz vascular source is plotted in Fig. 7.1. The parameter values correspond to those listed in Tables 5.2 and 5.3 (p. 120 and 121, respectively) and simulations were run over a range of prescribed phase lags (τ) between 0° and 180°. It can be seen in panels (a) and (b) that the mean pressure in the SC and SSS generally scales monotonically with phase lag across all segments, except around $\theta = 180°$ where the curves cross over; the SC clearly displays a greater sensitivity to θ than the SSS. There is a trend for $\bar{p}_{\mathrm{SC}}$ increasing with x (tailward) at intermediate vales of θ, observable in panel (a), which is probably related to the caudal propagation of the vascular pulse. The combined result of the above mean-pressure features is that in the cervical and thoracic regions the minimum and maximum $|\overline{\Delta p}|$ correspond to $\theta = 90°$ and 180°, respectively [panel (e)]. In terms of the pressure amplitude, the SSS exhibits a stronger pulse than the SC but neither demonstrate any sensitivity to θ [panels (c) and (d)], and the amplitude of Δp pulsations is maximal in the centre of the spinal axis [panel (f)]. For the healthy state the $\theta = 90°$ solution is chosen for having a small and mostly positive $\overline{\Delta p}$ as representative

of the intraspinal system. Two disease situations are then simulated: (i) a Chiari malformation and (ii) arachnoiditis. These pathologies are presumed to be associated with a disturbed SC blood supply in the affected region, manifested as a local change in θ from the otherwise healthy value (90°). The choice of θ for the disturbed blood supply is somewhat arbitrary but the value 180° is chosen to maximise pathological effects in the cervical and mid-thoracic regions.

7.4 Chiari Malformation

The pathological site is the craniocervical junction which is located at segment 1 in the 10-segment model ($0 < x < 0.1$). At this location θ is set to 180° and the remaining nine segments are left at the healthy value of 90°. The Chiari malformation is simulated by two further mechanical disturbances. Firstly, the flow between the ventricular compartment and the SSS is occluded by scaling the conductance z_{V} by a factor of 10^{-6}. This is to simulate the effect of the hindbrain tonsil protruding through and obstructing the foramen magnum. Next, the pial membrane is stiffened in segment 1 to account for the compressive force of the hindbrain on the SC ($c_{\mathrm{Pia}} \times 10^{-4}$). These two effects are first simulated individually and then both together, corresponding to markers $\bigcirc$, $\triangle$ and $*$, respectively, in Fig. 7.2. For reference the curves from Fig. 7.1 corresponding to the healthy state ($\theta = 90°$) and a state of disturbed blood supply ($\theta = 180°$, with mechanical parameters intact as for the healthy state) are plotted here as dashed ($- -$) and dash-dot ($- \cdot -$) lines, respectively.

The flow blockage at the craniocervical junction effectively disconnects the ventricles from the hydraulic system, and their contribution to cerebrospinal compliance. This causes the ventricular pressure to attenuate to zero [panels (b) and (d)] with a concomitant increase in mean and amplitude of the pressure in the SC and SSS [panels (a) to (d)]. In terms of the transpial pressure differential, the mean ($\overline{\Delta p}$) is only elevated at the pathological site ($0 < x < 0.1$) while the pulsation amplitude ($\widehat{\Delta p}$) is elevated across the length of the spinal axis, although to a lesser degree at lower

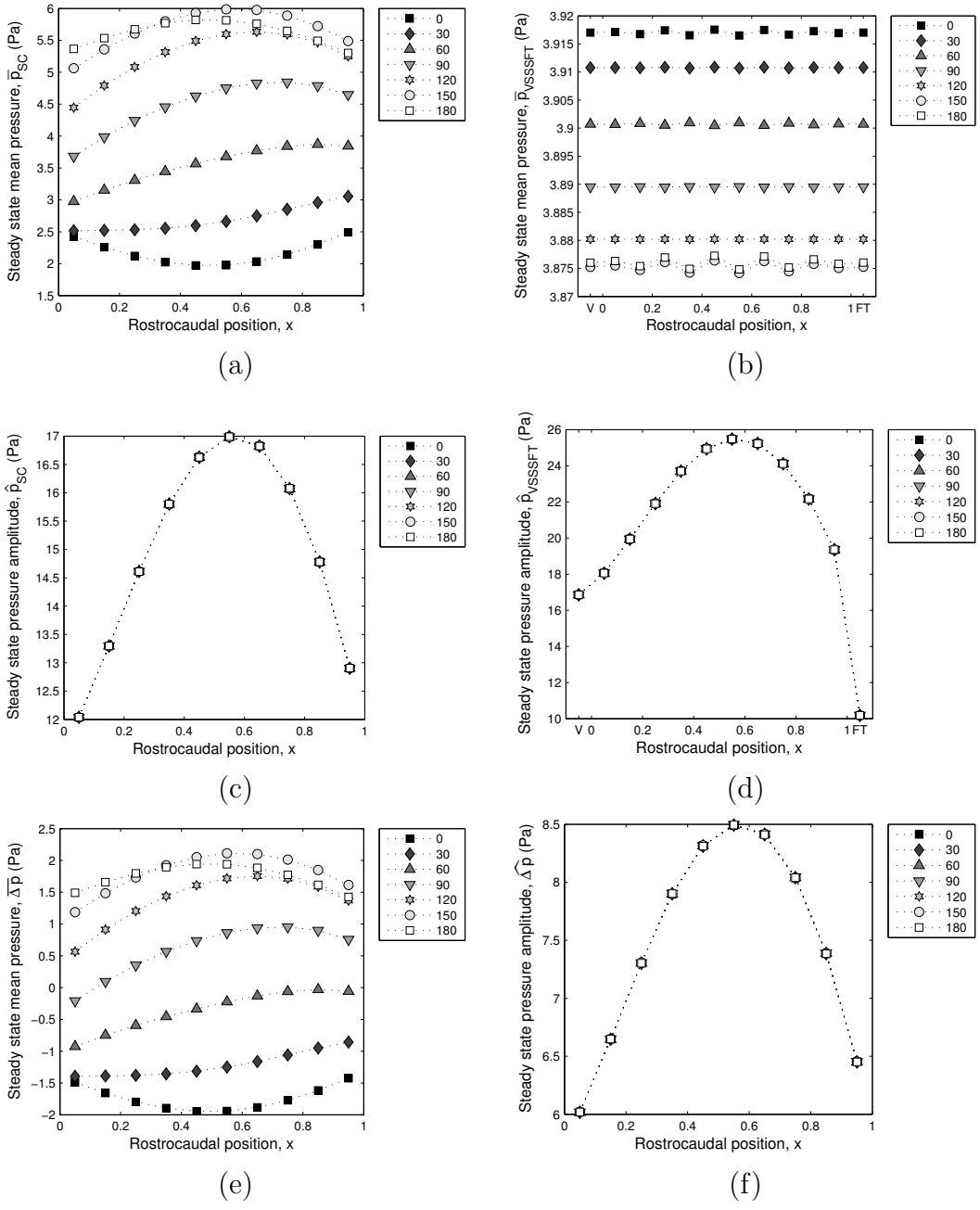

Fig. 7.1: The steady-state response of a 10-segment cerebrospinal model excited by a 1 Hz vascular source for a range of phase lag values (θ), which are indicated by the legend. The values of all other parameters correspond to those listed in Tables 5.2 and 5.3 (p. 120 and 121, respectively). The $\theta = 90°$ solution is chosen for the healthy state and $\theta = 180°$ for the condition of a disturbed blood supply.

locations [panels (e) and (f)]. Stiffening the pia only affects SC and this is limited to the pathological site, with a resultant increase in $\overline{\Delta p}$ and $\widehat{\Delta p}$. The superposition of these two Chiari-like disturbances is essentially a summation of the individual pressure perturbations, as observed by the asterisk markers in each of the panels.

The Chiari malformation is commonly associated with syrinxes in the upper cervical region of the SC. As a syrinx is effectively an elevation in porosity of the cord tissue it can be simulated by increasing the conductance between participating SC compartments. To this end, z_{SC} was scaled up by 10^6 at the interface between the first and second SC compartments ($x = 0.1$). In contrast to the Chiari disturbances, the syrinx spreads the raised $\overline{\Delta p}$ across two segments, giving a value around half that of the $\theta = 180°$ curve, and the amplitude of the transpial pulsations, $\widehat{\Delta p}$, reduces slightly at the pathological site [Fig. 7.2(e) and (f), □ markers].

One surgical treatment for SC syrinxes is a *syringo-subarachnoid shunt*. This procedure involves implanting a short plastic tube that perforates the syrinx so as to provide permanent drainage into the SSS. The shunt is implemented by increasing the pial conductance and setting it to be constant in the segment below the blockage (segment 2, $0.1 < x < 0.2$), thereby communicating the syrinx directly with the SSS. Figure 7.3 shows the effect of this surgical treatment on a simulated syrinx occurring in conjunction with a Chiari malformation; i.e., all three pathological conditions demonstrated in Fig. 7.2 have been combined into a state typically referred for surgery. As shown in panels (a) and (b), the shunt had the effect of reducing, respectively, both the mean and the amplitude of Δp pulsations in segments 1 and 2; in fact, in these segments $\overline{\Delta p} \equiv 0$. Over the lower portion of the spinal canal the shunt did not alter the reduced mean and elevated amplitude of Δp set up by the Chiari and associated syrinx. Whether these results favour a syringo-subarachnoid shunt as a treatment for syringomyelia is a matter of interpretation. Compared to the pre-treatment case, the reduction in mean transpial pressure at the pathological site indicates shunted drainage of the syrinx. However, the persistently high downstream pressure swings, despite the presence of the shunt, are suggestive of a more vigorous transpial flow, which may have

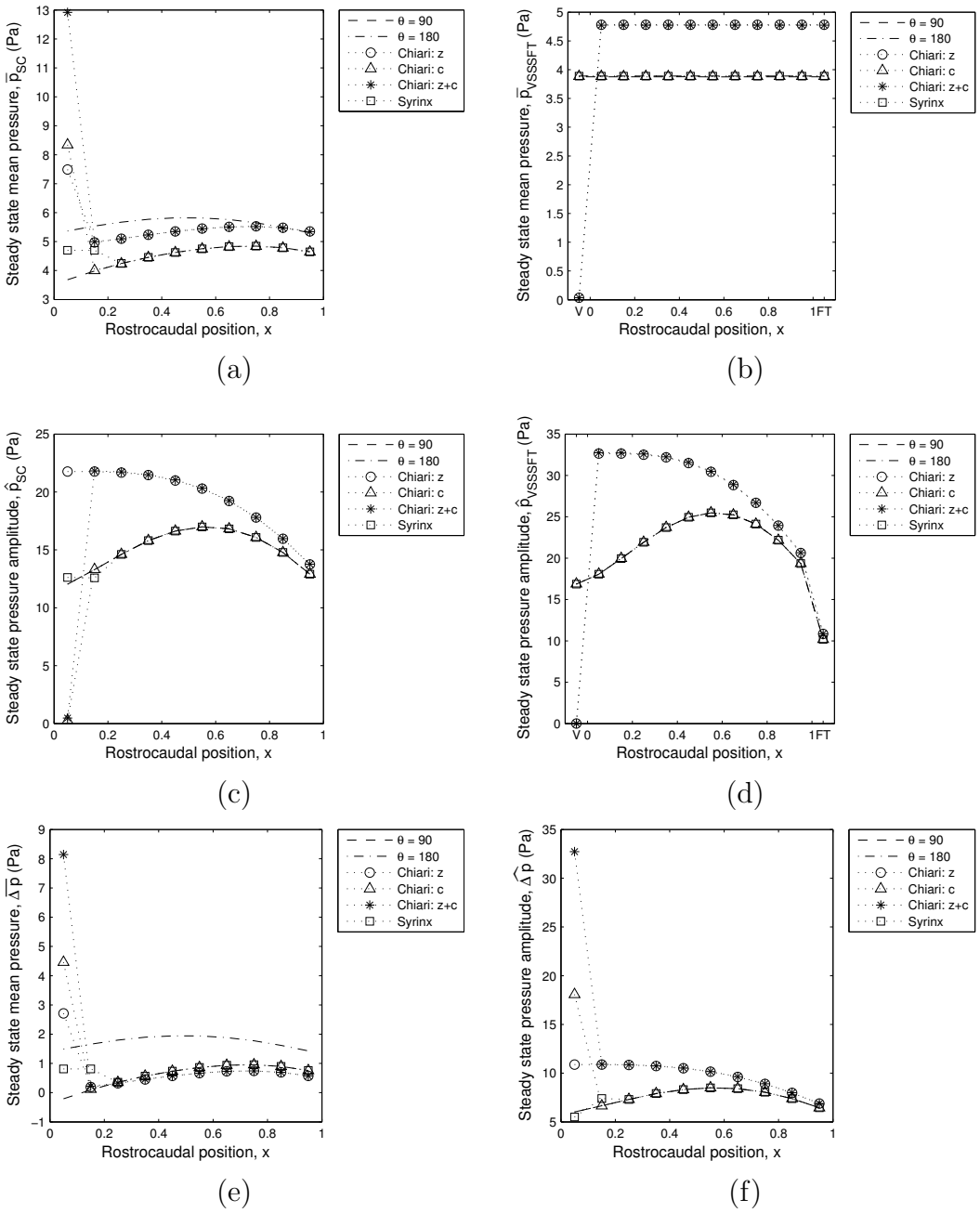

Fig. 7.2: The steady-state response of a 10-segment model with simulated pathological features of a Chiari malformation and a cervical syrinx. The base set of parameter values is as per Tables 5.2 and 5.3 (p. 120 and 121, respectively) and the legend indicates specific changes. Plotted are the healthy state ('$\theta = 90$') and the condition of disturbed blood supply ('$\theta = 180$') defined in Fig. 7.1, an occlusion between the ventricles and the SSS ('Chiari: z'), a stiffened pial membrane in the cervical region ('Chiari: c'), the occlusion and stiffened pial membrane together ('Chiari: z+c'), and a cervical syrinx ('Syrinx'). See text for details of how these were implemented in the model.

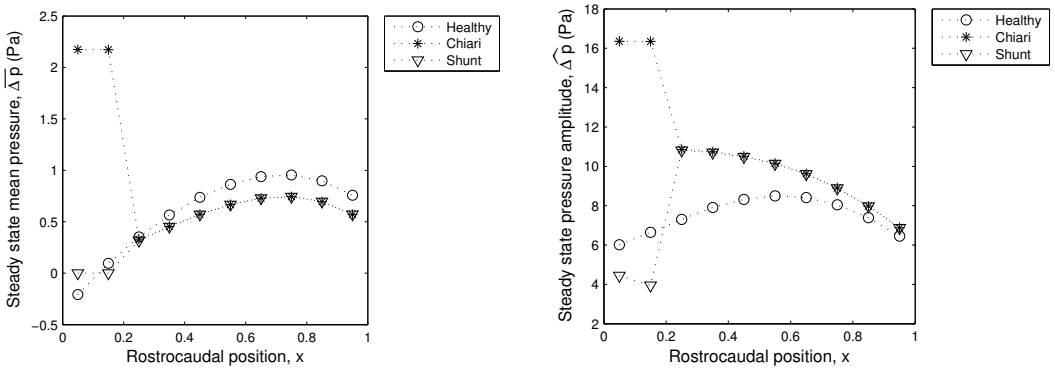

(a) (b)

Fig. 7.3: The steady-state response of a 10-segment model with simulated treatment of a Chiari malformation and associated cervical syrinx. The base set of parameter values is as per Tables 5.2 and 5.3 (p. 120 and 121, respectively) and the legend indicates specific changes. Plotted are the healthy state ('Healthy') defined in Fig. 7.1, a Chiari malformation with associated cervical syrinx ('Chiari'), and the Chiari treated with a syringosubarachnoid shunt ('Shunt'). See text for details of how these were implemented in the model.

a damaging effect.

7.5 Arachnoiditis

Arachnoiditis is characterised by scar tissue formation on the SC surface which tends to obstruct flow through the SSS and stiffen the pial membrane. The site of arachnoiditis is chosen to be the mid-thoracic region of the SSS and SC which corresponds to segments 5 and 6 in the 10-segment model ($0.4 < x < 0.6$). As with the Chiari malformation, it is assumed that the pathological condition has disturbed the SC blood supply and effected a local cardiac-PVS phase difference, so $\theta = 180°$ in segments 5 and 6 and $\theta = 90°$ in the remaining eight segments. To simulate a scar-induced blockage the SSS conductance is reduced between segments 5 and 6 ($z_{\mathrm{SSS}} \times 10^{-6}$). The attachment of the scar tissue to the pia is simulated by reducing the pial compliance ($c_{\mathrm{Pia}} \times 10^{-4}$). These are, of course, analogous to the simulation of the Chiari malformation except that the modifications are made equidistant from the capacitive end compartments. Two different syrinx types are also simulated. The first is confined within the boundaries of

the arachnoiditis, setting the SC conductance between segments 5 and 6 to 10^6 times the nominal healthy value. The second type of syrinx extends below the lower boundary and into segment 7 ($0.4 < x < 0.7$). The effects of all these mechanical disturbances are shown in Fig. 7.4, along with the same reference curves (dashed, dash-dot) as plotted in Fig. 7.2.

The blockage has an interesting effect on the mean compartment pressures. Referring to Fig. 7.4 ($\triangle$ markers), the (a) SC and (b) SSS have a reduced mean pressure above the level of the blockage and a correspondingly increased value below it; the amplitude of these pulsations alters in the same manner [panels (c) and (d)]. The mean pressure changes cancel though so the the effect of the blockage on $\overline{\Delta p}$ is no worse than the disturbed blood supply alone [panel (e), dash-dot line]. The stiffened pial membrane has no effect above and below the arachnoiditis but does serve to raise the mean and lower the amplitude of SC pulsations within [panels (a) and (c), $\bigtriangledown$ markers]. Ultimately the stiffened pial membrane raises the $\overline{\Delta p}$ value within the disease-affected region and produces a corresponding amplification of $\widehat{\Delta p}$ [panels (e) and (f)].

The syrinxes differ only by their length but exhibit quite different effects, as seen in Fig. 7.4. The shorter syrinx, spanning segments 5 and 6, scarcely changes the system response from the applied phase lag alone (dash-dot line) in the region of the arachnoiditis. However, the longer syrinx, extending below the level of the phase-affected region, reduces the peak value of the $\overline{\Delta p}$ with respect to the aforementioned $\theta = 180^\circ$ reference. As syringomyelia progresses, syrinxes tend to elongate and when post-traumatic arachnoiditis is present the syrinx may extend beyond the level of the trauma site. The results in Fig. 7.4 suggest that syrinx elongation could be a physiological process for lowering the mean transpial pressure differential.

Three surgical treatment options were simulated for syrinxes occurring in conjunction with arachnoiditis: (i) syringo-subarachnoid shunt, (ii) subarachnoid-bypass and (iii) foramen magnum decompression. The results of these simulations are shown in Fig. 7.5 in terms of (a) $\overline{\Delta p}$ and (b) $\widehat{\Delta p}$. The arachnoiditis condition, denoted by the '$*$' markers, is the combination of a SSS blockage and stiffened pia in segments 5 and

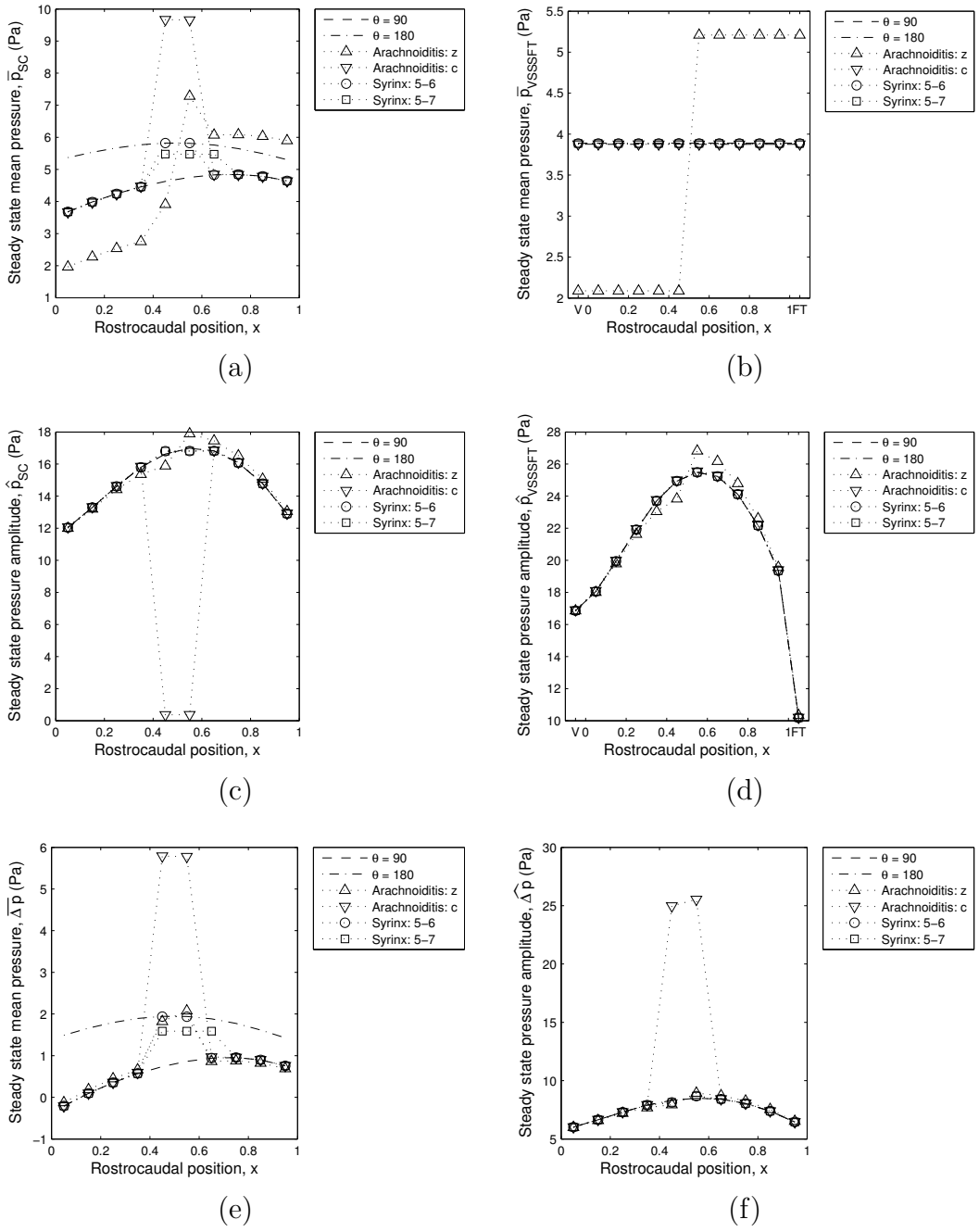

Fig. 7.4: The steady-state response of a 10-segment model with simulated pathological features of arachnoiditis and a syrinx at mid-thoracic level. The base set of parameter values is as per Tables 5.2 and 5.3 (p. 120 and 121, respectively) and the legend indicates specific changes. Plotted are the healthy state ('$\theta = 90$') and the condition of disturbed blood supply ('$\theta = 180$') defined in Fig. 7.1, a scar-induced blockage of the SSS ('Arachnoiditis: z'), scar attachment to the pial membrane ('Arachnoiditis: c'), the blockage and attachment together ('Arachnoiditis: z+c'), a short syrinx ('Syrinx: 5–6') and a longer syrinx ('Syrinx: 5–7'). See text for details of how these were implemented in the model.

6, together with an associated syrinx spanning segments 5 to 7 (i.e., the points with $\triangle$, $\triangledown$ and $\square$ markers in Fig. 7.4, respectively). This disease state corresponds to a locally elevated mean and amplitude of transpial pressure pulsations with respect to the healthy state, which is denoted by the $\bigcirc$ markers.

The shunt is implemented by increasing the pial conductance and setting it to be constant in the segment below the blockage ($0.6 < x < 0.7$), thereby communicating the syrinx directly with the SSS. This has the effect of reducing $\overline{\Delta p}$ across the level of the syrinx, to zero in the caudal and mid regions and to a negative value at the rostral end; i.e., below even the nominal healthy values. Likewise the shunt acts to attenuate the amplitude of transpial pulsations in the region of the disease to values at or below the healthy state. If a cardiac-PVS phase-lag mechanism—operating in the regime in which the cerebrospinal system has a lumped dynamic response—underlies syrinx formation in the SC, then, on mechanical grounds, these results favour the syringo-subarachnoid shunt as a treatment for syringomyelia in association with arachnoiditis.

The subarachnoid-bypass procedure involves forming an alternative CSF pathway between opposite sides of a SSS blockage. Some surgeons do not 'patch' this artificial conduit, making it also large enough to serve as a CSF reservoir (i.e., effectively a pseudomeningocele). As the volume of the bypass cannot be accounted for in a lumped-parameter model and the compliance of such a conduit would be difficult to estimate, a 'pure' bypass is implemented as a conductance between the SSS compartments in segments 4 and 7, with a value proportional to the normal SSS conductance (Table 5.2) for a pathway 3 segments long; i.e., only the flux function of the bypass is modelled. As shown in Fig. 7.5(a), the simulated bypass tends to equalise $\overline{\Delta p}$ across the span of the syrinx (segment 5 to 7) but the magnitude remains approximately the same as for the diseased state. The amplitude of transpial pulsations is also largely unaffected by the bypass [panel (b)]. These results suggest that, based on lumped-parameter mechanics, the flux function of the bypass procedure does little to alleviate the pressure differential acting across the pial membrane that may be set up by a cardiac-PVS phase-lag mechanism.

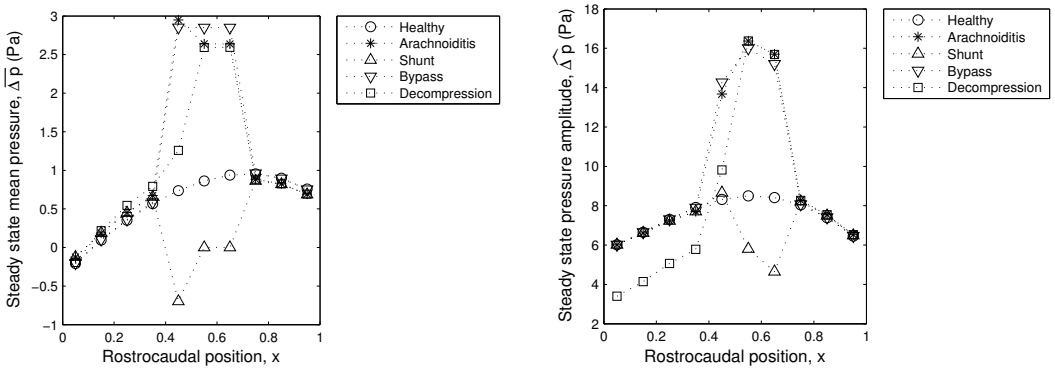

(a) (b)

Fig. 7.5: The steady-state response of a 10-segment model with three simulated treatments of arachnoiditis and associated mid-thoracic syrinx. The base set of parameter values is as per Tables 5.2 and 5.3 (p. 120 and 121, respectively) and the legend indicates specific changes. Plotted are the healthy state ('Healthy') defined in Fig. 7.1, arachnoiditis with associated mid-thoracic syrinx ('Arachnoiditis'), and the arachnoiditis treated with a syringosubarachnoid shunt ('Shunt'), treated by subarachnoid bypass ('Bypass') and treated by foramen magnum decompression ('Decompression'). See text for details of how these were implemented in the model.

A foramen magnum decompression is typically used to treat a Chiari malformation. This procedure involves removing some of the base of the skull and expanding the dura to accommodate an enlarged hindbrain. It was suggested by Chang & Nakagawa (2004) that a decompression might be a viable treatment for syringomyelia associated with adhesive arachnoiditis. This unorthodox proposal was made on the basis that syrinxes are formed by fluid driven into the central canal by pulsations of the hindbrain, which arise when the hindbrain has insufficient compliance with its surroundings. Since the cranial end of this model is already in the healthy state, to effect a decompression in the model the only change imposed is an increase in the SSS compliance at the rostral end (segment 1, $c_{\mathrm{SSS}} \times 10$). As can be seen in Fig. 7.5, this treatment mainly affects the cord levels above the syrinx where $\widehat{\Delta p}$ is attenuated. The value of Δp at the rostral end of the syrinx (segment 5) appears to be an average of the segments either side which represents an improvement over the disease state. Overall though the results of the 10-segment model do not support a foramen magnum decompression as a treatment for syrinxes in association with arachnoiditis.

7.6 Summary

The results from the disease and treatment simulations have been summarized in Table 7.1. The symbols '+', '−' and '0' denote the effect of the respective disease conditions on $\overline{\Delta p}$ and $\widehat{\Delta p}$ with respect to the nominal healthy state. The symbols '$\surd$' and '$\times$' are respectively a vote for or against a particular treatment, although it is acknowledged that the evidence presented here is purely mechanical in nature and does not account for practical considerations in carrying out these procedures or subsequent pathological complications. Taken together with the results from the previous chapter the major findings of the lumped-parameter modelling are described as follows.

1. A dynamic pial conductance that differs in phase from the vascular source pressure acts as a valve that allows for a net flow of CSF into the SC. This is the conclusion of the original work by Bilston *et al.* (2007). However, for fluid to accumulate in the SC and thereby raise the mean pressure within, as in the case of a syrinx, the SC must have a non-zero intrinsic compliance with the contained vascular bed. In other words, the SC cannot store extra fluid by the distension of the pial membrane alone—the induced tensile forces will counter the pressure gradient of the fluid. In contrast to this, the SC is often assumed to be incompressible hence an intrinsic compliance of zero, though this has never been measured.

2. A blockage of the SSS, as occurs at the craniocervical junction by the hindbrain or by scar tissue build-up at a trauma site, tends to aggravate the condition set up by the cardiac-PVS phase difference. The mean transpial pressure differential increases suggesting more fluid influx to the SC.

3. The impingement of the hindbrain on the SC in a Chiari malformation or scar tissue adherent to the pia may reduce the pial compliance. A stiffer pia will have a similar effect to a SSS blockage, except that the amplitude of transpial pulsations will also be amplified at the disease location.

Table 7.1: Summary of disease simulation outcomes.

Condition	$\overline{\Delta p}$	$\widehat{\Delta p}$	Condition	$\overline{\Delta p}$	$\widehat{\Delta p}$
Chiari: foramen magnum blockage	+	+	Arachnoiditis: SSS blockage	+	0
Chiari: SC compression	+	+	Arachnoiditis: stiffened pia	+	+
Cervical syrinx	+	−	Mid-thoracic syrinx	+	0
Combined pathology	+	+	Combined pathology	+	+
Syringo-subarachnoid shunt	√	√	Syringo-subarachnoid shunt	√	√
			Subarachnoid bypass	×	×
			Craniocervical decompression	×	×

4. A syrinx, modelled here as a local increase in the conductance within the SC, reduces the mean transpial pressure set up by the phase-lag mechanism alone. Therefore, when a syrinx was simulated in conjunction with conditions typical of a Chiari or arachnoiditis, the resulting disease state was not as severe as without the syrinx present. This was particularly so when the syrinx was elongated to the otherwise unaffected segment below. The elongation of a syrinx may thus be a homeostatic mechanism for alleviating symptoms associated with high syrinx pressures.

5. Three treatments were simulated: a syringo-subarachnoid shunt, a subarachnoid bypass and a foramen magnum decompression. The shunt was effective in equilibrating the mean pressure between the SC and SSS for both the Chiari and arachnoiditis cases. This would appear to be a favourable outcome in terms of fluid distribution in the spinal canal but the amplitude of transpial pulsations should also be considered. When shunting the Chiari-associated syrinx the pulsation amplitude rose in the greater part of the spinal canal suggesting a more vigorous fluid exchange between the SC and SSS. The implications of this are unknown. For the arachnoiditis-associated syrinx the bypass and decompression treatments were not as effective as the shunt in alleviating the perturbed pressure state.

In Part II a large number of concepts have been presented which draw upon many different mechanical theories. In the next Part of this thesis the accumulated set of

results will be consolidated and discussed with respect to the pathogenesis hypotheses introduced in Part I.

Part III

Discussion & conclusions

Synopsis

This Part consolidates the different modelling strategies that have been employed in this thesis and makes clear the significance of the results to the pathogenesis of syringomyelia. The results that have been presented in Part II are discussed here (Chapter 8) in relation to the models and medical evidence that were reviewed in Part I. Conclusions and recommendations for further work complete the substantive part of this thesis (Chapter 9).

CHAPTER 8

Discussion

8.1 The clinical problem

Syringomyelia is a disease that occurs in combination with a wide spectrum of disorders affecting the spine and craniocervical junction, with the end result being the formation of fluid-filled syrinxes within the SC. Syrinxes can form either as a dilatation of the CC or directly within the SC parenchyma. Canalicular syrinxes are often associated with craniocervical junction abnormalities, and SC injury is a typical precursor to extracanalicular syrinxes. While the pathogenesis mechanism for each combination of syrinx type and associated pathologies may be different, some hypotheses have been largely ruled out based on accumulated clinical and laboratory evidence.

Syringomyelia may occur without gross deformities such as spina bifida which makes a dysraphic mechanism unlikely. The similar appearance of spinal tumours and syrinxes led many to the belief that the two were of the same neoplastic origin (e.g., Virchow, 1863; Simon, 1875; Hassin, 1920; Riley, 1930). However, retrospective studies have shown that radiotherapy makes no difference to the long-term course of syringomyelia which strongly suggests that syrinx formation is not reliant on a neoplastic mechanism (Boman & Iivanainen, 1967). An alternative explanation for the situation of tumours and syrinxes coexisting is that fluid from the tumour transudes into the syrinx (Holmes, 1915; Gardner, 1965; Williams, 1970; Lohle *et al.*, 1994) but this does not explain

why syringomyelia is more frequently associated with tumours at the cervical level than those at lower levels of the same histology (Samii & Klekamp, 1994). It is now generally accepted that the human CC gradually occludes with age in otherwise healthy individuals (Kasantikul *et al.*, 1979; Milhorat *et al.*, 1994). This finding refutes the notion that syrinxes form in stenosed segments of the CC due to the buildup of CSF secreted from within. If this hypothesis were valid then syringomyelia would be one of the most common neurological diseases.

No matter what the associated pathology, most cases of syringomyelia are likely to have a disrupted blood supply at some point in the disease progression (Klekamp, 2002). This may be a precursor to the disease due to arterial compression, resulting from an impinging hindbrain or constricting scar tissue, or, blood supply may be disrupted as an effect of the disease, whereby expanding syrinxes compress the surrounding spinal arteries. Whichever version of events applies, although any induced ischaemia will cause tissue damage, this does not account for the progressive expansion of syrinxes over years—syringomyelia must be distinguished from myelomalacia (Klekamp, 2002). Likewise, blood clotting following a traumatic event is more consistent with necrosis than cavitation of the SC, which discounts the haematomyelic hypothesis for syrinx formation. So, with the biological-based mechanisms relegated to a secondary role, the research focus has recently turned to more mechanical-based hypotheses.

The syringomyelia community has long had an interest in biomechanics. Neurosurgeons make judgements involving the mechanical properties of the SC and brain as part of standard routine. When examining CT and static MRI images of a Chiari malformation, some estimate is made of the pressure and deformation of the impinging hindbrain. The opening pressure of CSF may be taken during lumbar puncture by using a column manometer, and the protein concentration of the CSF subsequently collected gives an indication of viscosity. During a spinal procedure the surgeon may palpate the exposed SC, thereby estimating compliance, to determine the degree of scar tissue buildup and the size and location of cord syrinxes or tumours. Dynamic MR imaging is used to identify CSF flow obstructions which are areas of high resistance,

and the wave-bearing properties of the cerebrospinal system can also be appreciated from this imaging modality.

The poor surgical prognosis for syringomyelia and difficulty of experimental work make mathematical models of the biomechanics very attractive for research. However, such models rely upon accurate measurement of mechanical quantities that are problematic to obtain due to the delicate nature of neurological tissues, the inaccessibility of *in situ* locations, and the inherent ethical concerns. Furthermore, the degree of mathematical complexity increases dramatically with attempts to more realistically represent the cerebrospinal system, making it difficult for surgeons to provide critical evaluation. For these reasons, mathematical models of syringomyelia have been slow to evolve. Nonetheless, useful insights are now being made by models that are consistent with the pathology and adhere to the laws of mechanics. The fundamental requirements for modelling syrinx formation are:

1. a mechanism for raising pressure within the SC above the level of the SSS;
2. a fluid pathway into the syrinx;
3. a pressure source providing either a favourable passive pressure gradient to a potential syrinx location, or a means of overcoming an unfavourable pressure gradient;
4. a means of retaining any fluid accumulated;
5. a means localising the above features.

8.2 Previous mathematical approaches to the problem

The body of work to date constituting the mathematical contribution to syringomyelia research can be synthesized into two modelling strategies—the continuum approach and the lumped-parameter approach. Their main difference is that a continuum model includes spatial variation of momentum while a lumped-parameter model does not.

Consequently, continuum models are better suited to problems involving wave propagation.

8.2.1 Continuum models

A number of researchers have constructed continuum models based upon idealising the contents of the spinal canal as a pair of coaxial tubes (Lockey *et al.*, 1975; Loth *et al.*, 2001; Berkouk *et al.*, 2003; Carpenter *et al.*, 2003; Bertram *et al.*, 2005; 2008; Cirovic, 2009). The outer tube represents the dura and supporting bone and fat and the annular space between the tube pair represents the SSS, which is filled with fluid representing the CSF. The inner tube itself and the cylindrical space within may have various interpretations depending on the thickness and stiffness of the inner tube. Lockey *et al.* (1975) and Loth *et al.* (2001) set the inner tube to be rigid, making the SC rigid and thus not distinguishing between the cord parenchyma and the surrounding pial membrane. Berkouk *et al.* (2003) set the inner tube to be thin and flexible in order to represent the pial membrane, and the cord parenchyma was approximated as inviscid fluid. Bertram and colleagues constructed models with a solid central cylinder, effectively making the inner tube and its contents of uniform composition; their first model had a plain elastic cord (Bertram *et al.*, 2005) and in the follow-up model this was replaced with a viscoelastic cord (Bertram *et al.*, 2008). Cirovic (2009) interpreted a flexible inner tube as the combined SC parenchyma and pial membrane but the identity of the contained fluid depended on the wall thickness of this tube; a thick wall left a narrow cavity which was deemed the CC, while a large cavity representing a syrinx corresponded to a thin-walled tube. Each of these tube configurations have been used to study wave propagation in the spinal canal, the matter of which tube configuration is most appropriate to syringomyelia though will be discussed in the sections to follow.

Greitz (1995) introduced a theory for syrinx formation based around the notion that the partial transmission and reflection of pressure waves near a spinal block may distend the cord at adjacent sites, making favourable conditions for plasma in high-pressure

intramedullary arteries to filter into the interstitial spaces and accumulate to form a syrinx. This so-called intramedullary pulse pressure hypothesis, based on a coaxial-tube idealisation of the spinal system, has not been the subject of much scrutiny from the engineering community, despite amassing a following in the medical literature through continuing publications (Greitz *et al.*, 1999; Josephson *et al.*, 2001; Greitz & Flodmark, 2004; Greitz, 2006). This may, in part, be due to the ambiguity in the nature of the proposed SC pressure wave and therefore how it can become uncoupled from the SSS wave. Carpenter *et al.* (2003) showed that a wave of differential pressure acting across the SC surface reflected in its entirety at a complete SSS obstruction; from this finding they concluded that in the case of hind-brain-related syringomyelia, at least, "our model does not support the differential-pressure-propagation mechanism proposed by Greitz *et al.* (1999)". The fact that Greitz (2006) cites Carpenter *et al.* (2003) in support of his theory sheds little light on the matter. While the hypothesis is argued using mechanical terminology, there is no mathematical modelling supporting the predictions. This is not a flaw *per se*, but seems wanted given the lack of empirical evidence. Dynamic MRI measurements in humans showed that CSF velocity increases through a partial obstruction in the SSS (Greitz *et al.*, 1999). These velocity measurements do little more than demonstrate conservation of mass—with such small velocities involved the induced pressure drop over the throat of the obstruction would be on the order of a few Pascals, hardly enough to distend the SC. Finally, Greitz and colleagues did not take any pressure recordings at all in their experiments, so it is difficult to assess the likelihood that such an intramedullary-pulse-pressure mechanism might operate in the formation of a syrinx.

The continuum models of Bilston *et al.* (2003; 2007), used computational methods to solve the flow in a geometry representing a perivascular space interfacing with the SSS. This is a shift in focus from the coaxial tube models cited above that sought to understand the wave propagation characteristics of the spinal canal as whole. Instead, Bilston and colleagues attempted to demonstrate mechanisms for active pumping of CSF from the SSS into the SC.

8.2.2 Lumped-parameter models

Although lumped-parameter models have been popular in hydrocephalus research, the pair of models by Chang & Nakagawa (2003; 2004) are the only previous attempts at modelling syringomyelia. In the first of these models the SC and surrounding structures were represented by an electrical circuit of nine capacitive-resistive segments, with additional resistors connecting cranial chamber voltages (pressures) via the obex and additional capacitors representing the lumbar thecal sac and cisterna magna (Fig. 2.3, p.27). Chang and Nakagawa suggested the cisterna magna has a shock-absorbing capacity and if this were diminished due to crowding of the base of the skull (Chiari) then pulsatile CSF waves from the cranium would generate an increase in CC pressure, leading to syringomyelia. Aside from the reliance on a patent CC, which could perhaps be reinterpreted as the spinal extracellular space, the model has a number of shortcomings. It provides no mechanism to localise the simulated pressure buildup, and is there is no facility for raised intramedullary pressure to be maintained. The spinal PVS were not included in the model so there was no transpial flow, despite this pathway being well-established through tracer studies (e.g., Ball & Dayan, 1972; Stoodley *et al.*, 1996). Finally, Chang & Nakagawa (2003) gave no justification for the physiological parameter values used. Although the authors defend this last criticism on the grounds that they are only interested in qualitative behaviour, such a model still requires an explanation for the relative scales chosen between the various parameters in order to assess the applicability to the cerebrospinal system, especially since the parameter values span some ten orders of magnitude. The same criticisms apply in the second model (Chang & Nakagawa, 2004), which was modified to simulate flow obstruction in the SSS.

8.3 Limitations of the current models

The work presented in this thesis uses mathematical methods for modelling aspects of cerebrospinal mechanics that are relevant to syringomyelia. These models are based on certain idealisations of the phenomena being studied and as such are subject to limitations. Foremost, in all of the models in Part II, the equations were derived from a purely biomechanical standpoint and so do not include biochemical or bioelectrical inputs. This was a deliberate attempt to simplify the problem in order to make useful predictions—at present there is insufficient understanding of the mechanics to justify adding the complications of chemical and electrical interactions. The mechanics are also limited to the tissue scale and so do not take into account any effects at the cellular or molecular scale. This is mostly a consequence of omitting the non-mechanical phenomena as cellular mechanics are intimately related to ionic concentration levels which confer an electrochemical gradient across the cell membrane. The tissue deformations simulated in the coaxial tube model (Ch. 3) and the poroelasticity investigation (Ch. 4) are limited to being 'small' with respect to the gross geometry in order to satisfy linearity constraints in the governing equations. Although a syringomyelic cord may be quite distended, an initial syrinx typically forms in an otherwise normal sized cord, so even linear deformations will be sufficient to capture the disease origins. The predictions about SC tissue poroelasticity were made from analysis of an infinite continuum rather than from a finite geometrical representation of the cerebrospinal system. This chiefly ignores a mechanism for wave dispersion through the interaction of wavefronts at a surface, which will tend to attenuate high-frequency components (Kolsky, 1953). The poroelastic analysis presented here establishes some guidelines for the construction of such a model with finite geometry. Finally, the lumped-parameter models presented in Chapters 5 to 7, due to the implicit omission of momentum transport, cannot reproduce cough-based pressure waves that are often used for model validation. These models were used for investigating qualitative behaviour rather than making quantitative predictions, and were restricted to the low-frequency domain, which is in keeping

with the limits of their physical realism.

8.4 Implications of the present findings

8.4.1 Parameter surveys

In this thesis a number of surveys have been made of the mechanical and geometrical properties of the cerebrospinal system. Initially the cross-sectional dimensions of the SC and the elastic properties of the pial membrane were reviewed to establish the appropriate values for evaluating the elastic jump hypothesis (Table 3.1, p. 58). In addition to the original aim, this drew to attention the lack of agreement between parameter values for existing coaxial tube models. For the cross-sectional dimensions of the cord, the theoretical model of Lockey *et al.* (1975) did much better than that of Carpenter *et al.* (2003). The numerical experiments of Bertram *et al.* (2005; 2008), while methodically rigorous, omit the pial membrane in the construction of the computational model. However, it has been shown here that the pia mater and subpial collagen layer have a non-negligible thickness and are significantly stiffer than the SC parenchyma contained within. Therefore the pial membrane should be included as a distinct component of any model seeking to capture the wave-bearing characteristics of the spinal canal. The permeable nature of the spinal tissues can be modelled to various levels of sophistication, from the simple approach of Darcy's law, an expression of conservation of momentum for creeping flow through a porous matrix, to the more complete theory of linear poroelasticity of Biot, which accounts for momentum of the solid phase and its interaction with the fluid. As no porous models of syringomyelia have been attempted previously, the parameter values in Tables 3.2 (Darcy's law, p. 76) and 4.1 (Biot's theory, p. 90) have novel value. The parameter surveys mentioned above are relevant to continuum models of one or more spatial dimension. Table 5.2 (p. 120) lists the compliances and conductances for the lumped-parameter models developed in Chapters 5–7; i.e., models having zero spatial dimensions. Although in reality these

won't be constant, particularly for the compliances that are a function of pressure and filling volume (Tenti *et al.*, 2000), these values at least indicate the relative order of magnitude of the various components of the central nervous system. Since obtaining accurate values of physiological properties is problematic, it is important that estimates be based on all available data. For this reason the parameter surveys presented throughout this thesis serve as a physical basis for the construction of mathematical models of syringomyelia.

8.4.2 Elastic jump mechanism

The elastic jump hypothesis for syrinx formation was developed using asymptotic analysis of the equations governing flow through collapsible tubes. Although one of the merits of this work was in its assessment of some of the more intuitively conceived theories (e.g., hydrodynamic and piston hypotheses), the level of mathematics involved largely excluded the medical audience from providing critical feedback. The paper by Bertram *et al.* (2005) is the only previous attempt to scrutinize the predictions of the elastic jump hypothesis. By exciting the spinal system with pressure impulses containing a spectrum of physiological frequencies, it was demonstrated that, taking dispersion into account, the SC is much less than one wavelength long. This suggested to the authors that a pressure wave will not have time to steepen sufficiently for elastic jumps to be significant in syringomyelia. However, Bertram *et al.*'s (2005) model differed qualitatively from Carpenter *et al.*'s (2003) and also from the real spinal system. The SC was represented as a linear elastic solid rather than an inviscid fluid as per Carpenter *et al.* (2003), still a significant deviation from fluid-saturated poroelastic tissue, and the pial membrane was not included in the model. Therefore the elastic jump hypothesis was re-evaluated here on its own terms; i.e., testing the assumptions upon which it was based and the predictions made from these assumptions. Using appropriate values for the cross-sectional geometry it was found that the CSF flow in the SSS is inertia-dominated, making the inviscid assumption reasonable. However, it is precisely

these conditions that make the weakly-nonlinear pressure amplification minimal—a significant amplification will only occur under conditions for which an inviscid fluid no longer applies. Moreover, it was shown here using asymptotics that the pressure wave is unlikely to have time to steepen fully within the length of the spinal canal, further reducing the hydrodynamic potential of the elastic jump. Therefore, with this marginal nonlinear effect, the maximum pressure differential at the reflection site will not overcome typical levels of attenuation measured clinically (Lockey *et al.*, 1975) and thus will not exceed the unattenuated pressure differential at the site of the cough pulse generation. Since this is not consistent with the pathology, it is submitted that there must be some other localising factor more critical to providing the necessary conditions for syrinx formation than the magnitude of the transpial pressure differential.

8.4.3 Transpial flux mechanism for pressure wave attenuation

In healthy individuals a CSF pressure wave generated by a cough will attenuate as it propagates through the SSS in the cranial direction. This may be due to the compliance of the veins of the upper thorax and neck, as suggested by Williams (1976), or viscous losses associated with fluid displacement. The latter might not be significant within the SSS, based on a Womersley number argument, but there also exists the possibility of viscous losses associated with transpial flux. Therefore, the governing equations from the coaxial tube model (Carpenter *et al.*, 2003) were here modified using Darcy's law to make the flexible tube permeable, which represented the pial membrane with perforating PVS; linearisation yielded a damped wave equation. For the healthy pia it was predicted that there will not be sufficient transpial flow induced for viscous losses to attenuate a pressure pulse over its passage through the spinal canal. However, the analytical expressions obtained for the damping coefficient and wave speed indicate that increasing the permeability or stiffness of the pial membrane will favour transpial flow. A disruption to the spinal blood supply, a common feature in SC pathologies, may affect the resistance of perivascular flow hence pial permeability. Scar tissue caused

by arachnoiditis would tend to stiffen and thicken the pial membrane but this would increase the wave speed as well as the damping coefficient, reducing the time available for transpial flow, so the consequences for attenuation are not so well defined.

8.4.4 Poroelasticity of the SC and wave propagation

The SC is a long tubular bundle of nervous tissue contained within the pial sheath. The nerve fibres are arranged in a longitudinal direction and between these exists extracellular fluid and various support cells. The cells themselves are largely water by mass, yet only about 20% of the tissue volume—the extracellular space— is available for the free passage of fluid. A reasonable mechanical description of the SC would be a fluid-saturated, anisotropic, poro-visco-elastic solid. Due to the difficulties in load testing the SC an accurate nonlinear constitutive relation has not yet been conceived, what's more, the complexity of a model incorporating such a relation would inhibit an analytical treatment. For these reasons researchers have employed a number of approximations when modelling the mechanics of the SC. Lockey *et al.* (1975) took the simplest approach and set the SC to be rigid. This doesn't allow pressure within the SC to be modelled and so holds little value for studying syrinx formation. Carpenter and colleagues chose the opposite extreme in their representation of the SC as inviscid fluid, contained within an inertialess flexible tube representing the pia. This approach had no source of dissipation and the compliance between the SC and SSS fluids supported a radial distension wave of the flexible tube. Although such an approximation may appear to be too crude to be useful, it fares better than using Darcy's law to model SC permeability in the context of wave propagation. The coaxial tube model of Berkouk *et al.* (2003) was modified here a second time, swapping the inviscid fluid within the inner tube for fluid with viscous resistance proportional to Darcy filtration through the permeable SC tissue. For a pressure wave travelling up the spinal canal this had the effect of damping the amplitude to zero almost instantaneously, which is not realistic. Darcy's law does not account for the momentum of the solid, which is likely what

carries the waves. It is interesting to note that tissue permeability plays opposing roles in the SC compared to the pial membrane; the propagation of a pressure wave is aided by a less-permeable pia but a more-permeable SC, as demonstrated by the pair of models presented in §3.4.3 and §3.4.4.

To account for the permeability and inertia of the SC tissue Biot's linear theory of poroelasticity was trialled here. The governing equations support three wave types: a shear wave in the solid phase, and fast and slow dilatational waves that correspond to in-phase and out-of-phase interactions between the solid matrix and saturating fluid, respectively. Over the range of parameter values investigated in Chapter 4, which make allowance for uncertainties and inaccuracies in published measurements, it would seem that the physiological frequencies are too low for poroelastic dissipation to be of significance in such a soft and weak material. The speed of the shear and first dilatational waves are sensitive to the elastic modulus and Poisson's ratio, as in a nonporous linear-elastic solid (Bertram *et al.*, 2005). Particular to the poroelasticity, though, is the sensitivity of the speed of the first dilatational wave to porosity, permeability, and the relation between the bulk moduli of the solid phase and its value in the form of the porous skeleton. The choice of how best to model the SC for pressure wave propagation thus depends upon what questions are being asked. If one only requires the dominant wave speed to be functionally correct then either an inviscid fluid or a linear elastic solid may be adequate. However, if one additionally seeks to investigate the transport of fluid across the pia and within the SC for syrinx formation, then a poroelastic approach is required and Biot's theory is a reasonable starting point, although more work needs to be done experimentally to establish appropriate values for the porous parameters.

8.4.5 The phase-lag mechanism for net perivascular flow

The wave-bearing properties of the cerebrospinal system described above are most likely to pertain to the higher frequencies of cough-based excitation. For the lower frequencies

of the cardiac cycle the dynamics will be closer to that of a lumped system (Bertram *et al.*, 2005). Bilston *et al.* (2007) recently proposed that phase differences between the SSS and arterial pulse waves may enhance perivascular inflow; alterations to a normal phase difference might occur, for example, as a result of scar tissue, associated with syrinxes, interrupting the local blood supply. This phase-lag mechanism for fluid accumulation in the SC was corroborated here with one caveat—*the SC must have a non-zero intrinsic compliance with the contained vascular bed.* This is an important requirement as the SC is often assumed to be incompressible (e.g., Bertram *et al.*, 2005) hence an intrinsic compliance of zero, though this has never been measured. The hypothesis of Bilston and colleagues was based on a CFD model of an isolated PVS and so could not predict the response of the rest of the cerebrospinal system to the perivascular pumping. For this reason a lumped-parameter model was developed in the present investigation, which allowed a closed and more complete representation of the cerebrospinal system to be simulated for relatively little computational expense. The matter of tissue permeability was dealt with using Darcy flow lumped at the boundary between relevant compartments, deemed an appropriate approximation for low-frequency pulsations. A dynamic pial conductance was prescribed that differed in phase from a vascular source pressure, which acted as a valve allowing a net flow of CSF into the SC. However, for fluid to accumulate in the SC and thereby raise the mean pressure within, as in the case of a syrinx, an equal volume of blood had to be ejected from the vascular compartment inside the SC. In other words, the SC cannot store extra fluid by the distension of the pial membrane alone—the induced tensile forces will counter the pressure gradient of the fluid. This can also be predicted from the coaxial tube model. When the pial membrane was impermeable, as in Carpenter's formulation, a negative SSS-SC pressure differential, although favouring SC inflow, could only act to constrict the pial membrane and so the pressure pulse would propagate unattenuated. By making the pial membrane permeable, the force of the pressure differential was shared between constricting the membrane and driving fluid across it, the latter introducing viscous dissipation which would attenuate the pressure pulse.

However, the movement of fluid across the pial membrane can only be considered inward in the moving reference frame of the pial membrane; it will lessen the degree of constriction, to zero in the theoretical limit of infinite permeability, but cannot lead to pial distension.

The pathology of syringomyelia was found to be consistent with the optimum conditions for the phase-lag mechanism to operate. A blockage of the SSS, as occurs at the craniocervical junction by the hindbrain or by scar tissue build-up at a trauma site, tends to aggravate the condition set up by the cardiac-PVS phase difference; the mean transpial pressure differential increases suggesting a more favourable environment for fluid influx to the SC. The impingement of the hindbrain on the SC in a Chiari malformation or scar tissue adherent to the pia may reduce the pial compliance. A stiffer pia had a similar effect to a SSS blockage, except that the amplitude of transpial pulsations was also amplified at the disease location.

8.4.6 Syrinx formation as a mechanism for homeostasis

A high-pressure syrinx compresses the surrounding nerve fibres and blood vessels, which is associated with neurological damage that manifests as symptoms such as pain, loss of temperature sensation and paralysis. So what is the best way to alleviate these symptoms? The nature of the disease progression itself may provide some insight. A syrinx, represented in the lumped-parameter model here as a local increase in the conductance within the SC, reduced the mean transpial pressure set up by the phase-lag mechanism alone. When a syrinx was simulated in conjunction with conditions typical of a Chiari or arachnoiditis, the resulting disease state was not as severe as without the syrinx present. This was particularly so when the syrinx was elongated to the otherwise unaffected segment below. These results suggest that high pressure in the SC may be the precursor to, rather than the result of, syrinx formation, and that syrinx formation and elongation may act to lower the pressure inside the SC. If this were the case then syrinx progression could be viewed as a homeostatic mechanism for

alleviating symptoms associated with high pressure within the SC. However, the fact that syrinxes continue to grow over the lifetime of the disease, in size and number, means that, whatever the reason for their existence, an interventional treatment is required.

Three surgical treatments were simulated using the lumped-parameter model: a syringo-subarachnoid shunt, a subarachnoid bypass and a foramen magnum decompression. The shunt was effective in equilibrating the mean pressure between the SC and SSS for both the Chiari and arachnoiditis cases. This would appear to be a favourable outcome in terms of fluid distribution in the spinal canal but the amplitude of transpial pulsations should also be considered. When shunting the Chiari-associated syrinx the pulsation amplitude rose in the greater part of the spinal canal. This suggests a more vigorous fluid exchange between the SC and SSS, the implications of which are yet to be determined. For the arachnoiditis-associated syrinx the bypass and decompression treatments were not as effective as the shunt in alleviating the perturbed pressure state. However, in practice most shunts block, become infected or move and this affects the clinical outcome, which begs the question—should we be working on a better shunting mechanism or a better shunt material? Furthermore, a syringosubarachnoid bypass is not simply a short-circuit flux connection as modelled, it is a passageway with finite dimensions and an associated compliance which may also play a role in alleviating the effects of intraspinal syrinxes.

CHAPTER 9

Conclusions and recommendations for future work

9.1 Conclusions

This project was an investigation of the pathogenesis of syringomyelia based upon mathematical modelling and analysis of human cerebrospinal mechanics. The methods involved classical theory of flow through collapsible tubes, the theory of poroelasticity and lumped-parameter hydraulics. While being aware of the assailability of deductions drawn from an experience lacking in biological contact, nevertheless the following conclusions seem inescapable.

In regard to Carpenter's weakly nonlinear theory, based upon careful determination of the physiological parameter values, asymptotic analysis of the governing equations and comparison with invasive pressure measurements, it is submitted that shock-like elastic jumps are unlikely to have any effect in the spinal canal. As a direct consequence, the site of maximum transpial pressure differential due to a cough-induced pulse is most likely to be at the site of pulse origin—not, as supposed, at a distant reflection site. This suggests that there must be some other localising factor more critical to providing the necessary conditions for syrinx formation. On this basis Carpenter's coaxial tube model was modified using Darcy's law to investigate the effects of tissue permeability

on wave propagation. It was shown that permeability plays opposing roles in the SC and pia for wave attenuation; the propagation of a pressure wave is aided by a less-permeable pia but a more-permeable SC. In a healthy cord, it would appear that the tissue properties do not allow wave-induced transpial flow to cause significant pressure attenuation. However, modified pial permeability could arise by disruption to the spinal blood supply, a feature not uncommon in SC pathologies, changing the resistance to perivascular flow. The effect of arachnoid scar tissue is not so well defined, as an increase in pial thickness and stiffness will tend to increase the wave propagation speed as well as the induced damping.

Based on an analysis of wave propagation in SC tissue using Biot's theory of poroelasticity, it is concluded that physiological frequencies are probably too low for poroelastic dissipation to be of significance in such a soft and weak material. However, the speed of the fast dilatational wave is sensitive to porosity, permeability, and the bulk modulus of the porous skeleton—none of which are accounted for in a simple elastic solid representation of the SC. Therefore it is asserted that to simulate syrinx formation in a model that can also be validated by clinical measurements of cough-based pressure waves, a poroelastic representation of the SC is required.

A lumped-parameter model of the cerebrospinal system was constructed with a dynamic pial conductance corresponding to perivascular fluid exchange between the SC and SSS. Varying the phase lag between the pial conductance and a vascular pressure source allows a mean transpial pressure differential to persist such that the pressure in the SC is greater than that in the SSS. This result supports Bilston's phase lag hypothesis for net perivascular inflow to the SC but only on the condition that the SC contains an intrinsic volume compliance; i.e., the SC is not incompressible. Such a compliance may be effected by the displacement of blood volume in the contained vascular bed. This means that the SC cannot store extra fluid by the distension of the pial membrane alone—the induced tensile forces will counter the pressure gradient of the fluid. This is also predicted from the coaxial tube model developed here in which the flexible tube was made permeable. If the phase-lag mechanism is in operation though

then a blockage of the SSS, as occurs at the craniocervical junction by a malformed hindbrain or by scar tissue build-up at a trauma site, will amplify its effect. The same result is predicted by a stiffer pia, as could arise from fibrosis due to arachnoiditis or SC compression from an impinging hindbrain, except that the amplitude of transpial pulsations will also be amplified at the disease location, which suggests a more vigorous fluid exchange between the SC and SSS; the pathological implications are unknown. By comparing the effects of differing length syrinxes, it is submitted that the elongation of a syrinx may be a homeostatic mechanism for alleviating symptoms associated with high syrinx pressures. In regard to surgical treatments for syrinxes associated with Chiari malformations and arachnoiditis, a patent shunt may be effective in equilibrating the mean pressure between the SC and SSS. For arachnoiditis-associated syrinxes the bypass and decompression treatments may not be as effective as the shunt in alleviating the perturbed pressure state.

9.2 Recommendations for future work

In this thesis the mechanical behaviour of the cerebrospinal system was investigated through the development of mathematical models. To confirm or refute the qualitative predictions that have been put forward accurate biological experiments are required. In regard to the coaxial tube models, an experiment needs to be devised to quantify the permeability of the pial membrane and SC parenchyma so that the relation between permeability and the mechanical properties of the tissue can be investigated. The accumulation of a CSF tracer molecule may be useful for this purpose (e.g., horseradish peroxidase; Stoodley *et al.*, 1996) but in addition one needs a measure of the pressure gradient driving any such flow, and therein lies one of the main obstacles in syringomyelia research—direct invasive pressure measurements in the spinal canal are problematic, both for practical as well as ethical reasons. One may speculate on indirect methods of quantifying pressure, such as imaging of a pressure-sensitive molecule that binds to the spinal tissues, for example, but more useful are suggestions for experiments

not needing *in vivo* pressure measurements.

The poroelastic properties of spinal tissue have never been quantified but the suite of laboratory tests described by Wang (2000) for soils could possibly be adapted for excised cord specimens. The main result of the lumped-parameter modelling presented here was in establishing the necessity of an intrinsic SC compliance for the phase-lag mechanism to produce a net perivascular inflow. In an animal model it may be possible, by ligating the appropriate blood vessels and comparing accumulation of CSF tracer over different durations, to test out this mechanical prediction. The protocols of Brodbelt and colleagues would serve as a guide for developing the surgical and histological procedure (e.g., Brodbelt, Stoodley, Watling, Rogan, Tu, Brown, Burke & Jones, 2003).

Syringomyelia is a disease characterised by disparate length and time scales. Pressure waves propagate over fractions of a second which may be accompanied by relatively large displacements of fluid and solid constituents, while syrinxes are the gradual accumulation of small quantities of fluid over very long time scales, of the order of months and years. To resolve this multiscale behaviour computationally with existing methods and technology one may be somewhat restricted by prolonged computing times, thus any progress that can be made analytically is highly desirable. For this task the *method of multiple scales*, a technique in asymptotic analysis, may be a useful starting point (Hinch, 1991). The governing equations should tend to hyperbolic form at short time scales, to reproduce the wave propagation characteristics observed in real time, and tend to parabolic form at long time scales, to be capable of predicting diffusive syrinx formation and progression, and also be well-defined at intermediate time scales. This multiscale behaviour was touched upon in the work presented here on the damped wave equation, which may provide some guidance in a linearised formulation.

In addition to a pathogenesis model, there are many other aspects of syringomyelia that are poorly understood and need further research. Syrinxes form in a variety of shapes and sizes, typically many small cavities rather than a single large cavity. The reason for this is unknown but may be related to minimising strain energy. Using a

finite element approach there is scope for investigating the solid mechanics of different cavity morphologies with the aim of looking for an 'optimal' solution for a given syrinx pressure or volume. Another area of the mechanics that needs further work is in the characterisation of the wave-bearing properties of the spinal canal. The finite geometry models that have been reported to date (e.g., Bertram *et al.*, 2005; 2008; Cirovic, 2009) do not take into account poroelasticity, and the poroelasticity investigation presented here was for an infinite medium. Wisse *et al.* (2007), in their recent work on borehole analysis for geophysics applications, investigated the dispersion behaviour of a poroelastic cylinder immersed in a fluid-filled rigid tube. This may provide a good starting point for investigating wave propagation in a poroelastic model of the spinal canal.

Bibliography

Agarwal, G. C., Berman, B. M. & Stark, L. (1969). A lumped parameter model of the cerebrospinal fluid system, *IEEE Transactions on Biomedical Engineering* **BME-16**: 45–53.

Alciatore, D. G. & Histand, M. B. (2002). *Introduction to Mechatronics and Measurement Systems*, McGraw-Hill Professional.

Allen, A. R. (1911). Surgery of experimental lesion of spinal cord equivalent to crush injury of fracture dislocation of spinal column. A preliminary report, *Journal of the American Medical Association* **57**: 878–880.

Ambarki, K., Baledent, O., Kongolo, G., Bouzerar, R., Fall, S. & Meyer, M.-E. (2007). A new lumped-parameter model of cerebrospinal hydrodynamics during the cardiac cycle in healthy volunteers, *IEEE Transactions on Biomedical Engineering* **54**(3): 483–491.

Assenmacher, D. R. & Ducker, T. B. (1971). Experimental traumatic paraplegia. The vascular and pathological changes seen in reversible and irreversible spinal cord lesions, *The Journal of Bone and joint Surgery. American Volume* **53-A**(4): 671–680.

Awrejcewicz, J. & Krysko, V. A. (2006). *Introduction to Asymptotic Methods*, Chapman Hall, CRC Press.

Ball, M. J. & Dayan, A. D. (1972). Pathogenesis of syringomyelia, *Lancet* **ii**: 799–801.

Barnett, H. J. M. (1973). Syringomyelia associated with spinal arachnoiditis, *in* H. J. M. Barnett, J. B. Foster & P. Hudgson (eds), *Syringomyelia*, Vol. 1 of *Major Problems in Neurology*, W. B. Saunders, pp. 220–224.

Bastian, H. C. (1867). On a case of concussion-lesion with extensive secondary degeneration of the spinal cord, followed by general muscular atrophy, *Medico-Chirurgical Transactions* **50**(XXII): 499–542.

Becker, D. P., Wilson, J. A. & Watson, G. W. (1972). The spinal cord central canal: response to experimental hydrocephalus and canal occlusion, *Journal of Neurosurgery* **36**: 416–424.

Berkouk, K. (1999). *Theoretical and physical models of a pressure pulse propagation in the spinal system*, PhD thesis, School of Engineering, The University of Warwick.

Berkouk, K., Carpenter, P. W. & Lucey, A. D. (2003). Pressure wave propagation in fluid-filled co-axial elastic tubes part 1: basic theory, *Journal of Biomechanical Engineering* **125**(6): 852–856.

Bertram, C. D., Bilston, L. E. & Stoodley, M. A. (2008). Tensile radial stress in the spinal cord related to arachnoiditis or tethering: a numerical model, *Medical & Biological Engineering & Computing* **46**: 701–707.

Bertram, C. D., Brodbelt, A. R. & Stoodley, M. A. (2005). The origins of syringomyelia: numerical models of fluid/structure interactions in the spinal cord, *Journal of Biomechanical Engineering* **127**(7): 1099–1109.

Bilston, L. E., Fletcher, D. F., Brodbelt, A. R. & Stoodley, M. A. (2003). Arterial pulsation-driven cerebrospinal fluid flow in the perivascular space: a computational model, *Computer Methods in Biomechanics & Biomedical Engineering* **6**(4): 235–241.

Bilston, L. E., Fletcher, D. F. & Stoodley, M. A. (2007). Effect of phase differences between cardiac and csf pulse on perivascular flow—a computational model with relevance to syringomyelia, *British Journal of Neurosurgery* **21**(5): 430.

Bilston, L. E. & Thibault, L. E. (1996). The mechanical properties of the human cervical spinal cord in vitro, *Annals of Biomedical Engineering* **24**(1): 67–74.

Biot, M. A. (1941). General theory of three-dimensional consolidation, *Journal of Applied Physics* **12**: 155–164.

Biot, M. A. (1955). Theory of elasticity and consolidation for a porous anisotropic solid, *Journal of Applied Physics* **26**(2): 182–185.

Biot, M. A. (1956a). Theory of deformation of a porous viscoelastic anisotropic solid, *Journal of Applied Physics* **27**: 459–467.

Biot, M. A. (1956b). Theory of propagation of elastic waves in a fluid-saturated porous solid. i. low-frequency range, *The Journal of the Acoustical Society of America* **28**(2): 168–178.

Biot, M. A. (1956c). Theory of propagation of elastic waves in a fluid-saturated porous solid. II. high-frequency range, *The Journal of the Acoustical Society of America* **28**(2): 179–191.

Bloomfield, I. G., Johnson, I. H. & Bilston, L. E. (1998). Effects of proteins, blood cells and glucose on the viscosity of cerebrospinal fluid, *Pediatric Neurosurgery* **28**(5): 246–251.

Boman, K. & Iivanainen, M. (1967). Prognosis of syringomyelia, *Acta Neurologica Scandinavica* **43**(1): 61–68.

Borysowicz, J. (1967). Results of treatment of syringomyelia with nitrogen mustard, *Polish Medical Journal* **6**(3): 728–732.

Bowen, R. M. (1976). Theory of mixtures, *Continuum Physics*, Vol. 3, Academic Press, New York, pp. 1–127.

Bowen, R. M. (1980). Incompressible porous media models by use of the theory of mixtures, *International Journal of Engineering Science* **18**(9): 1129–1148.

Bowen, R. M. (1982). Compressible porous media models by use of the theory of mixtures, *International Journal of Engineering Science* **20**(6): 697–735.

Bozanovic-Sosic, R., Mollanji, R. & Johnston, M. G. (2001). Spinal and cranial contributions to total cerebrospinal fluid transport, *American Journal of Physiology - Regulatory, Integrative and Comparative Physiology* **281**: R909–R916.

Bradbury, M. (1993). *Hydrocephalus*, Oxford University Press, chapter Anatomy and physiology of CSF, pp. 19–47.

Brewis, M., Poskanzer, D. C., Rolland, C. & Miller, H. (1966). Neurological disease in an English city, *Acta Neurologica Scandinavica* **42**(Suppl 24): 1–89.

Brickell, K. L., Anderson, N. E., Charleston, A. J., Hope, J. K. A., Bok, A. P. L. & Barber, P. A. (2006). Ethnic differences in syringomyelia in New Zealand, *Journal of Neurology, Neurosurgery and Psychiatry* **77**: 989–991.

Brodbelt, A. R. (2009). Private communication.

Brodbelt, A. R. & Stoodley, M. A. (2003). Syringomyelia and the arachnoid web, *Acta Neurochirurgica* **145**: 707–711.

Brodbelt, A. R. & Stoodley, M. A. (2007). CSF pathways: a review, *British Journal of Neurosurgery* **21**(5): 510–520.

Brodbelt, A. R., Stoodley, M. A., Watling, A. M., Tu, J., Burke, S. & Jones, N. R. (2003). Altered subarachnoid space compliance and fluid flow in an animal model of posttraumatic syringomyelia., *Spine* **28**(20): E413–E419.

Brodbelt, A. R., Stoodley, M. A., Watling, A. M., Tu, J. & Jones, N. R. (2003). Fluid flow in an animal model of post-traumatic syringomyelia, *European Spine Journal* **12**: 300–306.

Brodbelt, A. R., Stoodley, M. A., Watling, A., Rogan, C., Tu, J., Brown, C. J., Burke, S. & Jones, N. R. (2003). The role of excitotoxic injury in post-traumatic syringomyelia, *Journal of Neurotrauma* **20**(9): 883–893.

Bronson, R. (1973). *Differential Equations*, McGraw Hill.

Brown, P. N., Jackson, P. C., Staddon, G. E., Richardson, R. B. & Griffith, H. B. (1985). Compartmental analysis of cerebrospinal fluid transfer and absorption in simulated hydrocephalus, *Physics in Medicine and Biology* **30**(10): 1113–1121.

Brunner, J. C. (1700). Hydrocephalo, sire hydrope capitis, *in* T. Bonneti (ed.), *Sepulchretum, Miscell. Nat. Curios. III Dec. Ann. I 1688*, ed ii, lib i edn, Cramer & Perachon, Genf, p. 394.

Camus, J. & Roussy, G. (1914). Cavités médullaires et méningites cervicales: étude expérimentale, *Revista de Neurologia* **22**: 213–225.

Carpenter, P., Berkouk, K. & Lucey, A. (1999). A theoretical model of pressure propagation in the human spinal csf system, *Engineering Mechanics* **6**(4): 1–16.

Carpenter, P., Berkouk, K. & Lucey, A. (2003). Pressure wave propagation in fluid-filled coaxial elastic tubes part 2: mechanisms for the pathogenesis of syringomyelia, *Journal of Biomechanical Engineering* **125**(6): 857–863.

Carpenter, P. W., Lucey, A. D. & Berkouk, K. (1996). Progress in theoretical and physical modelling of pressure pulse propagation in the human spinal csf system, *Technical Report 96/1*, Fluid Mechanics Research Centre, The University of Warwick.

Chang, H. S. & Nakagawa, H. (2003). Hypothesis on the pathophysiology of syringomyelia based on simulation of cerebrospinal fluid dynamics, *Journal of Neurology, Neurosurgery & Psychiatry* **74**(3): 344.

Chang, H. S. & Nakagawa, H. (2004). Theoretical analysis of the pathophysiology of syringomyelia associated with adhesive arachnoiditis, *Journal of Neurology, Neurosurgery & Psychiatry* **75**(5): 754–757.

Charcot, J. M. & Joffroy, A. (1869). Deux cas d'atrophie musculaire progressive avec lésions de la substance grise et des faisceaux antérolatéraux de la moelle épinière, *Arch. Physiol. Ser.* **12**: 354–367.

Chiari, H. (1891). Ueber veränderungen des Kleinhirns infolge von Hydrocephalie des Grosshirns, *Deutsche medizinische Wochenschrift (1946)* **42**: 1172–1175.

Chiari, H. (1896). über Veränderungen des Kleinhirns, des Pons und der Medulla oblongata infolge von congenitaler Hydrocephalie des Grosshirns, *Denkschr. Akad. Wiss. Wien.* **63**: 71–116.

Cirovic, S. (2009). A coaxial tube model of the cerebrospinal fluid pulse propagation in the spinal column, *Journal of Biomedical Engineering* **131**(2): 021008.

Cirovic, S., Walsh, C. & Fraser, W. D. (2002). Wave propagation in a system of coaxial tubes flled with incompressible media: a model of pulse transmission in the intracranial artieries, *Journal of Fluids and Structures* **16**(8): 1029–1049.

Cleland, J. (1874). Double-bodied monsters, and the development of the tongue, *Journal of Anatomy and Physiology* **8**(2): 250–260.

Cleland, J. (1883). Contribution to the study of spina bifida, encephalocele, and anencephalus, *Journal of Anatomy and Physiology* **17**(3): 257–291.

Crossman, A. & Neary, D. (2001). *Neuroanatomy: An Illustrated Colour Text*, Churchill Livingstone.

Curschmann, H. (1894). *Klinische Abbildungen*, Springer.
URL: *http://www.artandmedicine.com/index.html*

de Boer, R. (2000). *Theory of Porous Media*, Springer Verlag.

Delherm, L. & Morel-Kahn, M. (1930). treatment of syringomyelia by roentgentherapy, *American Journal of Surgery* **9**(2): 302–314.

Donaldson, H. H. & Davis, D. J. (1903). A description of charts showing the areas of the cross-sections of the human spinal cord at the level of each spinal nerve, *The Journal of Comparative Neurology* **13**: 19–40.

Drake, J. M. & Sainte Rose, C. (1995). *The Shunt Book*, Wiley Blackwell.

Ehlers, W. (1993). Compressible, incompressible and hybrid two-phase models in porous media theories, *Anisotropy and Inhomogeneity in Elasticity and Plasticity*, Vol. AMD-Vol. 158, American Society of Mechanical Engineers, pp. 25–38.

Eide, P. K. & Sorteberg, W. (2007). Association among intracranial compliance, intracranial pulse pressure amplitude and intracranial pressure in patients with intracranial bleeds, *Neurological Research* **29**(8): 798–802.

Ellertsson, A. B. & Greitz, T. (1970). The distending force in the production of communicating syringomyelia, *Lancet* **1**: 1234.

Elliott, H. C. (1945). Cross-sectional diameters and areas of the human spinal cord, *The Anatomical Record* **93**(3): 287–293.

England, M. A. & Wakeley, J. W. (2006). *Color Atlas of the Brain and Spinal Cord: An Introduction to Normal Neuroanatomy*, Mosby.

European Commission (2004). Useful information on rare diseases from an EU perspectives, *Meeting Of The Network Of Competent Authorities For Health Information And Knowledge*, Luxembourg.

Fehlings, M. G., Tator, C. H. & Linden, R. D. (1989). The relationship among the severity of spinal cord injury, motor and somatosensory evoked potentials and spinal cord blood flow, *Electroencephalography and Clinical Neurophysiology* **74**(4): 241–259.

Ferry, D. J., Hardman, J. M. & Earle, K. M. (1969). Syringomyelia and intramedullary neoplasms, *The Medical Annals of the District of Columbia* **38**(7): 363–365.

Fillunger, P. (1913). Der auftrieb von talsperren, teil i-iii. österr [the lift of dams, parts i-iii. oesterr.], *Wochenschrift für den öffentlichen Baudienst [Weekly revue for the public building service]* **7**: 510–532.

Fischbein, N. J., Dillon, W. P., Cobbs, C. & Weinstein, P. R. (1999). The 'presyrinx' state: a reversible myelopathic condition that may precede syringomyelia, *American Journal of Neuroradiology* **20**: 7–20.

Fischbein, N. J., Dillon, W. P., Cobbs, C. & Weinstein, P. R. (2000). The "presyrinx" state: is there a reversible myelopathic condition that may proceed syringomyelia?, *Neurosurgical Focus* **8**(3): 1–13.

Freeman, L. W. & Wright, T. W. (1953). Experimental observations of concussion and contusion of the spinal cord, *Annals of Surgery* **137**(4): 433–443.

Fujiwara, K., Yonenobu, K., Hiroshima, K., Ebara, S., Yamashita, K. & Ono, K. (1988). Morphometry of the cervical spinal cord and its relation to pathology in cases with compression myelopathy, *Spine* **13**(11): 1212–1216.

Gardner, W. J. (1965). Hydrodynamic mechanism of syringomyelia: its relation to myelocele, *Journal of Neurology, Neurosurgery, and Psychiatry* **28**: 247–259.

Gardner, W. J. & Angel, J. (1959). The mechanism of syringomyelia and its surgical correction, *Clinical Neurosurgery, Proceedings of the Congress of Neurological Surgeons, San Francisco, U.S.A., 1958*, Vol. 6, The Williams & Wilkins Company, Baltimore, chapter VI, pp. 131–140.

Gardner, W. J. & Goodall, R. J. (1950). The surgical treatment of Arnold-chiari malformation in adults: an explanation of its mechanism and importance of encephalography in diagnosis, *Journal of Neurosurgery* **7**: 199–206.

Getreuer, P. (2008). *Writing Fast MATLAB Code*.

Gray, H. (1918). *Anatomy of the Human Body*, 20th edn, Lea & Febiger, Philadelphia. **URL:** *http://www.bartleby.com/107/*

Greitz, D. (1995). CSF-flow at the craniocervical junction: increased systolic and diastolic pressure gradients as the cause of cystic cord lesions, *in* J. Kenéz (ed.), *Imaging of the Craniocervical Junction*, Edizione del Centauro, Udine Milano, pp. 19–23.

Greitz, D. (2006). Unraveling the riddle of syringomyelia, *Neurosurgical Review* **29**: 251–264.

Greitz, D., Ericson, K. & Flodmark, O. (1999). Pathogenesis and mechanics of spinal cord cysts. A new hypothesis based on magnetic resonance studies of cerebrospinal fluid dynamics, *International Journal of Neuroradiology* **5**: 61–78.

Greitz, D. & Flodmark, O. (2004). Modern concepts of syringohydromyelia, *Rivista di Neuroradiologia* **17**(3): 360–361.

Grinker, R. R. (1934). *Neurology*, Charles C. Thomas.

Gull, W. (1862). Case of progressive atrophy of the muscles of the hands: enlargement of the ventricle of the cord in the cervical region, with atrophy of the gray matter (hydromyelus), *Guy's Hospital Reports (3rd Series)* **8**: 244–250.

Häckel, M., Beneš, V. & Mohapl, M. (2001). Simultaneous cerebral and spinal fluid pressure recordings in surgical indications of the Chiari malformation without myelodysplasia, *Acta Neurochirurgica* **143**: 909–918.

Hall, P., Turner, M., Aichinger, S., Bendick, P. & Campbell, R. (1980). Experimental syringomyelia: The relationship between intraventricular and intrasyrinx pressures, *Journal of Neurosurgery* **52**: 812–817.

Hall, P. V., Kalsbeck, J. E., Wellman, H. N., Campbell, R. L. & Lewis, S. (1976). Radioisotope evaluation of experimental hydrosyringomyelia, *Journal of Neurosurgery* **45**: 181–187.

Hall, P. V., Muller, J. & Campbell, R. L. (1975). Experimental hydrosyringomyelia, ischaemic myelopathy, and syringomyelia, *Journal of Neurosurgery* **43**: 464–470.

Hassin, G. B. (1920). A contribution to histopathology and histogenesis of syringomyelia, *Archives of Neurology and Psychiatry* **3**: 130–146.

Heiss, J. D., Patronas, N., DeVroom, H. L., Shawker, T., Ennis, R., Kammerer, W., Eidsath, A., Talbot, T., Morris, J., Eskioglu, E. & Oldfield, E. H. (1999). Elucidating the pathophysiology of syringomyelia, *Journal of Neurosurgery* **91**: 553–562.

Henry-Feugeas, M. C., Idy-Peretti, I., Baledent, O., Poncelet-Didon, A., Zannoli, G., Bittoun, J. & Schouman-Claeys, E. (2000). Origin of subarachnoid cerebrospinal fluid pulsations: a phase-contrast mr analysis, *Magnetic Resonance Imaging* **18**(4): 387–395.

Heukamp, F. H., Ulm, F.-J. & Germaine, J. T. (2001). Mechanical properties of calcium-leached cement pastes. triaxial stress states and the influence of the pore pressures., *Cement and Concrete Research* **31**: 767–774.

Hinch, E. J. (1991). *Perturbation Methods*, Cambridge University Press.

Hinsdale, G. (1897). *Syringomyelia, an Essay to which was Awarded the Alvarenga Prize of the College of Philadelphia for the Year 1895*, International Medical Magazine Co., Philadelphia.

Holmes, G. (1915). The Goulstonian Lectures on spinal injuries of warfare: Part I. The pathology of acute spinal injury, *British Medical Journal* **2**: 769–774.

Holmes, G. & Kennedy, R. F. (1909). Two anomalous cases of syringomyelia, *Proceedings of the Royal Society of Medicine* **2**(Neurological Section): 1–11.

Inoue, H., Ohmori, K., Takatsu, T., Teramoto, T., Ishida, Y. & Suzuki, K. (1996). Morphological analysis of the cervical spinal canal, dural tube and spinal cord in normal individuals using ct myelography, *Neuroradiology* **38**: 148–151.

Jackson, J. R. & Williams, B. (1979). Errors in velocity measurement by the Pitot principle in fluids with slowly propagated pressure waves, *Journal of Biomedical Engineering* **1**: 50–54.

Joffroy, A. & Achard, C. (1887). De la myelite cavitaire (observations; reflexions; pathogenie des cavites), *Arch. Physiol. Ser. 3S* **10**: 435–472.

Johnson, D. L. (2001). Theory of frequency dependent acoustics in patchy-saturated porous media, *The Journal of the Acoustical Society of America* **110**(2): 682–694.

Josephson, A., Greitz, D., Klason, T., Olson, L. & Spenger, C. (2001). A spinal thecal sac constriction model supports the theory that induced pressure gradients in the cord cause edema and cyst formation, *Neurosurgery* **48**(3): 636–646.

Kameyama, T., Hashizume, Y. & Sobue, G. (1996). Morphologic features of the normal human cadaveric spinal cord, *Spine* **21**(11): 1285–1290.

Kasantikul, V., Netsky, M. G. & James, A. E. (1979). Relation of age and cerebral ventricle size to central canal in man, *Journal of Neurosurgery* **51**: 85–93.

Kiernan, J. A. (1998). *Barr's the Human Nervous System, an Anatomical Viewpoint*, 7th edn, Lippincott-Raven, Philadelphia.

Klekamp, J. (2002). The pathophysiology of syringomyelia—historical overview and current concept, *Acta Neurochirurgica* **144**: 649–664.

Klekamp, J., Samii, M. & Matthies, C. (2001). *Syringomyelia: Diagnosis and Treatment*, Springer.

Ko, H.-Y., Park, J. H., Shin, Y. B. & Baek, S. Y. (2004). Gross quantitative measurements of spinal cord segments in human, *Spinal Cord* **42**: 35–40.

Kolsky, H. (1953). *Stress Waves In Solids*, Clarendon Press, Oxford.

Levine, D. N. (2004). The pathogenesis of syringomyelia associated with lesions at the foramen magnum: a critical review of existing theories and proposal of a new hypothesis, *Journal of the Neurological Sciences* **220**(1-2): 3–21.

L'Hermitte, J. & Boveri, P. (1912). Sur un cas de cavite medullaire consecutive a une compression bulbaire chez ihomme et etude experimentale des cavites spinales produites par la compression, *Revista de Neurologia* **20**: 385–393.

Liber, A. F. & Lisa, J. R. (1937). Rosenthal fibres in non-neoplastic syringomyelia: a note on the pathogenesis of syringomyelia, *The Journal of Nervous and Mental Disease* **86**(5): 549–558.

Lichtenstein, B. W. (1943). Cervical syringomyelia and syringomyelia-like states associated with Arnold-Chiari deformity and platybasia, *Archives of Neurology and Psychiatry* **49**: 881–894.

Lockey, P., Poots, G. & Williams, B. (1975). Theoretical aspects of the attenuation of pressure pulses within cerebrospinal fluid pathways, *Medical & Biological Engineering & Computing* **13**: 861–869.

Lohle, P. N., Wurzer, H. A. L., Hoogland, P. H., Seelen, P. J. & Go, K. G. (1994). The pathogenesis of syringomyelia in spinal cord ependymoma, *Clinical Neurology and Neurosurgery* **96**: 323–326.

Loth, F., Yardimci, M. A. & Alperin, N. (2001). Hydrodynamic model of cerebrospinal fluid motion within the spinal cavity, *Journal of Biomechanical Engineering* **123**: 71–79.

Marieb, E. N. (2000). *Human Anatomy And Physiology*, 5th edn, Benjamin Cummings.

Marmarou, A., Shulman, K. & LaMorgese, J. (1975). Compartmental analysis of compliance and outflow resistance of the cerebrospinal fluid system, *Journal of Neurosurgery* **43**(5): 523–34.

Martin, B. A., Kalata, W., Loth, F. & Royston, T. J. (2005). Syringomyelia hydrodynamics: an in vitro study based on in vivo measurements, *Journal of Biomechanical Engineering* **127**(7): 1110–1120.

Martin, J. H. (2003). *Neuroanatomy: Text and Atlas*, McGraw Hill.

Martinez-Arizala, A., Mora, J., Green, B. & Hayashi, N. (1990). Dorsal spinal venous occlusion model in the rat: preliminary observations, *Abstracts - Society for Neuroscience* **16**: 992.

Martinez-Arizala, A., Mora, R. J., Madsen, P., Green, B. A. & Hayashi, N. (1995). Dorsal spinal venous occlusion in the rat, *Journal of Neurotrauma* **12**(2): 199–208.

Mazuchowski, E. L. & Thibault, L. E. (2003). Biomechanical properties of the human spinal cord and pia mater, *Proceedings of the Summer Bioengineering Conference*, Key Biscayne, Florida, U.S.A., pp. 1205–1206.

McDonald, D. A. (1974). *Blood Flow in Arteries*, Edward Arnold, chapter 6, pp. 118–145.

McGrath, J. T. (1965). Spinal dysraphism in the dog with comments on syringomyelia, *Pathologia Veterinaria (Supplement)* **2**: 1–36.

McLaurin, R. L., Bailey, O. T., Schurr, P. H. & Ingraham, F. D. (1954). Myelomalacia and multiple cavitations of spinal cord secondary to adhesive arachnoiditis, *Archives of Pathology* **57**: 138–146.

McVeigh, J. F. (1923). Experimental cord crushes: with especial reference to the mechanical factors involved and subsequent changes in the areas of the cord affected, *Archives of Surgery* **7**: 573–600.

Milhorat, T. H. (1999). Is reversible enlargement of the spinal cord a presyrinx state?, *American Journal of Neuroradiology* **20**: 21–22.

Milhorat, T. H. (2000). Classification of syringomyelia, *Neurosurgical Focus* **8**(3): 1–6.

Milhorat, T. H., Kotzen, R. M. & Anzil, A. P. (1994). Stenosis of central canal of spinal cord in man: incidence and pathological findings in 232 autopsy cases, *Journal of Neurosurgery* **80**: 716–722.

Milhorat, T. H., Nobandegani, F., Miller, J. I. & Rao, C. (1993). Noncommunicating syringomyelia following occlusion of central canal in rats. experimental model and histological findings, *Journal of Neurosurgery* **78**(2): 274–279.

Morgagni, G. B. (1769). Of the hydrocephalus, and watry tumours of the spine, *The Seats and Causes of Disease as Investigated by Anatomy (translated by B. Alexander from the latin of 1761)*, Vol. I, Which treats disorders of the head, Miller & Candell Publishers, London, Letter XII, Article 9, 255.

Nakamura, K., Urayama, K. & Hoshino, Y. (1997). Lumbar cerebrospinal fluid pulse wave rising from pulsations of both the spinal cord and the brain in humans, *Spinal Cord* **35**(11): 735–739.

Netsky, M. G. (1953). Syringomyelia: a clinicopathologic study, *Archives of Neurology and Psychiatry* **70**: 741–777.

Nicholson, C. (1999). Structure of extracellular space and physiochemical properties of molecules governing drug movement in brain and spinal cord, *in* T. L. Yaksh (ed.), *Spinal Drug Delivery*, Elsevier Science, chapter 10, pp. 253–269.

Noble, L. J. & Wrathall, J. R. (1989). Correlative analysis of lesion development and functional status after graded spinal cord contusive injuries in the rat, *Experimental Neurology* **103**: 34–40.

Nolte, J. (2002). *The Human Brain: An Introduction to its Functional Anatomy*, Mosby, St Loius.

Ogryzlo, M. A. (1942). The Arnold-Chiari malformation, *Archives of Neurology and Psychiatry* **38**: 30–46.

Okada, Y., Ikata, T., Katoh, S. & Yamada, H. (1994). Morphologic analysis of the cervical spinal cord, dural tube, and spinal canal by magnetic resonance imaging in normal adults and patients with cervical spondylotic myelopathy, *Spine* **19**(20): 2331–2335.

Oldfield, E. H., Murasko, K., Shawker, T. H. *et al.* (1994). Pathophysiology of syringomyelia associated with Chiari I malformation of the cerebellar tonsils. Implications for diagnosis and treatment, *Journal of Neurosurgery* **80**: 3–15.

Ollivier D'Angers, C. P. (1827). *Traité de la moelle épinière et de ses maladies: contenant l'histoire anatomique, physiologique et pathologique de ce centre nerveux chez l'homme*, 2nd edn, Chez Crevot, Paris.

Ozawa, H., Matsumoto, T., Ohashi, T., Sato, M. & Kokuban, S. (2004). Mechanical properties and function of the spinal pia mater, *Journal of Neurosurgery (Spine 1)* **1**: 122–127.

Pearsall, J. (ed.) (1999). *The Concise Oxford English Dictionary*, tenth edn, Oxford University Press Inc., New York.

Plona, T. J. (1980). Observation of a second bulk compressional wave in porous medium at ultrasonic frequencies, *Applied Physics Letters* **36**: 259–261.

Polyanin, A. D. (2002). *Handbook of Linear Partial Differential Equations for Engineers and Scientists*, Chapman Hall.

Prasad, S., Price, R. S., Kranick, S. M., Woo, J. H., Hurst, R. W. & Galetta, S. (2007). Clinical reasoning: A 59-year-old woman with acute paraplegia, *Neurology* **69**: E41–E47.
URL: *http://www.neurology.org/cgi/content/full/69/24/E41*

Rare Diseases Act of 2002, Public Law 107-280, 116 Stat. 1987 (2002) (n.d.).

Redzic, Z. B., Preston, J. E., Duncan, J. A., Chodobski, A. & Szmydynger-Chodobska, J. (2005). The choroid plexus-cerebrospinal fluid system: From development to aging, *in* G. P. Schatten (ed.), *Current Topics in Developmental Biology*, Vol. 71, Academic Press, chapter 1.

Reina, M. A., De León Casasola, O., Villanueva, M. C., López, A., Machés, F. & Antonio De Andrés, J. (2004). Ultrastructural findings in human spinal pia mater in elation to subarachnoid anesthesia, *Anesthesia and Analgesia* **98**: 1479–1485.

Reina, M. A., Dittmann, M., López Garcia, A. & van Zundert, A. (1997). New perspectives in the microscopic structure of human dura mater in the dorsolumbar region, *Regional Anesthesia* **22**(2): 161–166.

Rennels, M. L., Gregory, T. F., Blaumanis, O. R. & Fujimoto, K. (1985). Evidence for a 'paravascular' fluid circulation in the mammalian central nervous system, provided by the rapid distribution of tracer protein throughout the brain from the subarachnoid space, *Brain Research* **326**(1): 47–63.

Rice-Edwards, J. M. (1977). A pathological study of syringomyelia, *Journal of Neurology, Neurosurgery, and Psychiatry* **40**(2): 198.

Riley, H. A. (1930). Syringomyelia or myelodysplasia, *The Journal of Nervous and Mental Disease* **72**(1): 1–27.

Ros, L., Mota, J., Guedea, A. & Bidgood, D. (1998). Quantatative measurements of the spinal cord and canal by MR imaging and myelography, *European Radiology* **8**: 966–970.

Rubin, M. & Safdieh, J. E. (2007). *Netter's Concise Neuroanatomy*, Saunders.

Runza, M., Pietrabissa, R., Mantero, S., Albani, A., Quaglini, V. & Contro, R. (1999). Lumbar dura mater biomechanics: experimental characterization and scanning electron microscopy observations, *Anesthesia and Analgesia* **88**: 1317–1321.

Samii, M. & Klekamp, J. (1994). Surgical results for 100 intramedullary tumors in relation to accompanying syringomyelia, *Neurosurgery* **35**(5): 865–873.

Schanz, M. & Diebels, S. (2003). A comparative study of biots theory and the linear Theory of Porous Media for wave propagation problems, *Acta Mechanica* **161**: 213–235.

Schmaus, H. (1890). Commotio spinalis, *in* O. Lubarsch & R. Ostertag (eds), *Ergebnisse der allgemeinen Pathologie und pathologischen Anatomie des Menschen und der Tiere*, J. F. Bergmann, Wiesbaden, pp. 674–713.

Selçuki, M., Vatansever, S., Inan, S., Erdemli, E., Bağdatoğlu, C. & Polat, A. (2003). Is a filum terminale with a normal appearance really normal?, *Child's Nervous System* **19**: 3–10.

Shampine, L. F. & Gear, C. W. (1979). A user's view of solving stiff ordinary differential equations, *SIAM Review* **21**(1): 1–17.

Simon, T. (1875). Beiträge zur Pathologie und pathologischen Anatomie des Central-Nervensystems, *Archives of Psychiatry* **5**: 108–163.

Smillie, A., Sobey, I. & Molnar, Z. (2005). A hydroelastic model of hydrocephalus, *Journal of Fluid Mechanics* **539**: 417–443.

Smith, F. W. K., Allen, D. G. & Tilley, L. P. (2003). *Stedman's Medical Dictionary*, twenty-seventh edn, Lippincott Williams & Wilkins, Philadelphia, U. S. A.

Smith, J. H. & Humphrey, J. A. C. (2007). Interstitial transport and transvascular fluid exchange during infusion into brain and tumor tissue, *Microvascular Research* **73**: 58–73.

Soleau, S., Tubbs, R. S. & Oakes, W. J. (2007). Chiari malformations, *in* A. L. Albright, P. D. Adelson & I. F. Pollack (eds), *Principles and Practice of Pediatric Neurosurgery*, second edn, Thieme, New York, chapter 14, pp. 217–232.

Sorek, S., Bear, J. & Karni, Z. (1989). Resistances and compliances of a compartmental model of the cerebrovascular system, *Annals of Biomedical Engineering* **17**: 1–12.

Speer, M. C., Enterline, D. S., Mehltretter, L., Hammock, P., Joseph, J., Dickerson, M., Ellenbogen, R. G., Milhorat, T. H., Hauser, M. A. & George, T. M. (2003). Chiari type I malformation with or without syringomyelia: prevalence and genetics, *Journal of Genetic Counseling* **12**(4): 297–311.

Steiner, L. A. & Andrews, P. J. D. (2006). Monitoring the injured brain: Icp and cbf, *British Journal of Anaesthesia* **97**(1): 26–38.

Stoodley, M. A., Brown, S. A., Brown, C. J. & Jones, N. R. (1997). Arterial pulsation-dependent perivascular cerebrospinal fluid flow into the central canal in the sheep spinal cord, *Journal of Neurosurgery* **86**: 686–693.

Stoodley, M. A., Gutschmidt, B. & Jones, N. R. (1999). Cerebrospinal fluid flow in an animal model of noncommunicating syringomyelia, *Neurosurgery* **44**(5): 1065–1077.

Stoodley, M. A., Jones, N. R. & Brown, C. J. (1996). Evidence for rapid fluid flow from the subarachnoid space into the spinal cord central canal in the rat, *Brain Research* **707**(2): 155–164.

Stoodley, M. A., Jones, N. R., Yang, L. & Brown, C. J. (2000). Mechanisms underlying the formation and enlargement of noncommunicating syringomyelia: experimental studies, *Neurosurgical Focus* **8**(3): 1–7.

Syková, E. (2004). Extrasynaptic volume transmission and diffusion parameters of the extracellular space, *Neuroscience* **129**: 861–876.

Tannenberg, J. (1924). über die Pathogenese der Syringomyelie, zugleich ein Beitrag zum Vorkommen von Capillarhaemangiomen im Rueckenmark, *Z. Ges. Neurol. Psychiatr.* **92**: 119–174.

Tarlov, I. M., Klinger, H. & Vitale, S. (1953). Spinal cord compression studies. Experimental techniques to produce acute and gradual compression, *Archives of Neurology and Psychiatry* **70**: 813–819.

Tator, C. H. (1991). Review of experimental spinal cord injury with emphasis on the local and systemic circulatory effects, *Neuro-Chirurgie* **37**: 291–302.

Tator, C. H. & Deecke, L. (1973). Value of normothermic perfusion, hypothermic perfusion and durotomy in the treatment of experimental acute spinal cord trauma, *Journal of Neurosurgery* **39**: 52–64.

Tauber, E. S. & Langworthy, O. R. (1935). A study of syringomyelia and the formation of cavities in the spinal cord, *The Journal of Nervous and Mental Disease* **81**(3): 245–264.

Tenti, G., Drake, J. & Sivaloganathan, S. (2000). Brain biomechanics: mathematical modelling of hydrocephalus, *Neurological Research* **22**: 19–24.

Thijssen, H. O. M., Keyser, A., Horstink, M. W. M. & Meijer, E. (1979). Morphology of the cervical spinal cord on computed myelography, *Neuroradiology* **18**(2): 57–62.

Truesdell, C. & Toupin, R. (1960). *The Classical Field Theories*, Springer Berlin.

Tunturi, A. R. (1977). Elasticity of the spinal cord dura in the dog, *Journal of Neurosurgery* **47**(3): 391–396.

U. S. National Library of Medicine (n.d.). The Visible Human Project ®.
URL: *http://www.nlm.nih.gov/research/visible/visible_human.html*

Urayama, K. (1994). Origin of lumbar cerebrospinal fluid pulse wave, *Spine* **19**(4): 441–445.

Virchow, R. (1863). Die Betheiligung des Rückenmarkes an der Spina bifida und die Hydromyelie, *Virchows Archive* **27**(5-6): 575–578.

von Terzaghi, K. (1923). Die berechnung der durchlässigkeit des tones aus dem verlauf der hydromechanischen spannungserscheinungen [the computation of the permeability of the clay/tone from the process of the hydromechanical stress phenomena], *Sitzungsber. Akad. Wissensch. (Wien): Math.- Naturwiss* **Klasse 132**: 125–138.

Wallace, M. S. (1999). Human spinal drug delivery: methods and technology, *in* T. L. Yaksh (ed.), *Spinal Drug Delivery*, Elsevier Science, chapter 14, pp. 345–370.

Wang, H. F. (2000). *Theory of Linear Poroelasticity with Applications to Geomechanics and Hydrogeology*, Princeton series in geophysics, Princeton University Press.

Weller, R. O. (1999). Reaction of intrathecal and epidural spaces to infection and inflammation, *in* T. L. Yaksh (ed.), *Spinal Drug Delivery*, Elsevier Science, chapter 12, pp. 297–315.

Wiedemayer, H., Nau, H. E., Raukut, F., Gerhard, L., Reinhard, V. & Grote, W. (1990). Pathogenesis and operative treatment of syringomyelia, *Advances in Neurosurgery* **18**: 119–125.

Williams, B. (1969). The distending force in production of communicating syringomyelia, *Lancet* **2**: 189–193.

Williams, B. (1970). Current concepts of syringomyelia, *British Journal of Hospital Medicine* **4**: 331–342.

Williams, B. (1972). Combined cisternal and lumbar pressure recordings in the sitting position using differential manometry, *Journal of Neurology, Neurosurgery, and Psychiatry* **35**: 142–143.

Williams, B. (1974). A Demonstration Analogue for Ventricular and Intraspinal Dynamics (DAVID), *Journal of Neurological Science* **23**: 445–461.

Williams, B. (1976). Cerebrospinal fluid pressure changes in response to coughing, *Brain* **99**: 331–346.

Williams, B. (1980). On the pathogenesis of syringomyelia: a review, *Journal of the Royal Society of Medicine* **73**(11): 798.

Williams, B. (1986). Progress in syringomyelia, *Neurological Research* **8**: 129–144.

Williams, B. (1990). Syringomyelia, *Neurosurgery Clinics of North America* **1**: 653–685.

Wilson, E. O. (1998). *Consilience*, Little, Brown and Co., London.

Wisse, C. J., Smeulders, D. M. J., Chao, G. & van Dongen, M. E. H. (2007). Guided wave modes in porous cylinders: Theory, *Journal of the Acoustical Society of America* **122**(4): 2049–2056.

Yamada, S., Won, D. J., Pezeshkpour, G., Yamada, B. S., Yamada, S. M., Siddiqi, J., Zouros, A. & Colohan, A. R. T. (2007). Pathophysiology of tethered cord syndrome and similar complex disorders, *Neurosurgical Focus* **23**(2): E6, 1–10.

Yang, L., Jones, N. R., Stoodley, M. A., Blumbergs, P. C. & Brown, C. J. (2001). Excitotoxic model of post-traumatic syringomyelia in the rat, *Spine* **26**(17): 1842–1849.

Yezierski, R. P., Santana, M., Part, S. H. & Madsen, P. (1993). Neuronal degeneration and spinal cavitation following intraspinal injections of quisqualic acid in the rat, *Journal of Neurotrauma* **10**: 445–456.

Young, P. A. & Tolbert, D. L. (2007). *Basic Clinical Neuroscience*, second edn, Lippincott Williams & Wilkins.

Yu, Y. L., du Boulay, G. H., Stevens, J. M. & Kendall, B. E. (1985). Morphology and measurements of the cervical spinal cord in computer-assisted tomography, *Neuroradiology* **27**(5): 399–402.

Zaaroor, M., Kósa, G., Peri-Eran, A., Maharil, I., Shoham, M. & Goldsher, D. (2006). Morphological study of the spinal canal content for subarachnoid endoscopy, *Minimally Invasive Neurosurgery* **49**(4): 220–226.

Zauderer, E. (2006). *Partial Differential Equations of Applied Mathematics*, Pure and applied mathematics, third edn, Wiley.

Zeng, Z. (2003). MultRoot — A MATLAB package computing polynomial roots and multiplicities.

URL: *http://www.neiu.edu/~zzeng/multroot.htm*

Part IV

Appendices

Synopsis

This Part provides technical reference information that supplements the body of the thesis. These are a glossary of medical terms (Appendix A), the solution and properties of the damped wave equation (Appendix B), and a derivation of the poroelasticity equations that were solved numerically (Apppendix C).

APPENDIX A

Glossary of Medical Terms

A

anterior Describing or relating to the front. The opposite of posterior. *page 20*

arachnoid mater A translucent, collagenous membrane that, like the dura, loosely envelops the brain and spinal cord. The entanglement of fibres gives a cobweb-like appearance. *page 7*

arachnoid villi The thin-walled outward projections of the arachnoid membrane into the blood-filled sinuses of the dura, acting as a one-way valve for the flow of cerebrospinal fluid from the subarachnoid space into the bloodstream. *page 8*

arachnoiditis An inflammatory process causing thickening and scarring of the arachnoid lining of the spinal canal. *page 13*

Arnold-Chiari deformity See Chiari malformation. *page 13*

atrophy A wasting away or a diminution in the size of a cell, tissue, organ or part. *page 24*

B

basilar invagination Upward deformation of the base of the skull and associated migration of the upper portion of the spine. *page 12*

blood plasma The straw-coloured fluid in which the blood cells are suspended, containing salts and a high concentration of protein. *page 8*

brainstem The enlarged extension upwards within the skull of the spinal cord, functionally divided into the medulla oblongata, the pons and the midbrain. *page 13*

C

cauda equina A bundle of spinal nerve roots which arise from the termination of the spinal cord proper, it comprises the roots of all the spinal nerves below the first lumbar nerve (L1). *page 7*

caudal Denoting a position more toward the cauda or tail, than some specified point of reference. The same as inferior, in human anatomy. *page 34*

CC *central canal* *page 214*

cell rest Cells displaced from their region of origin. *page 18*

central artery An artery that directly supplies the spinal cord, originating from the anterior spinal artery and penetrating the cord parenchyma where it branches mainly within the grey matter. *page 9*

central canal The narrow lumen running the length of the spinal cord. In infants this canal is usually continuous above with the fourth ventricle of the brain but in the adult it is often partially or completely occluded. *page 8*

central nervous system The combination of the brain and spinal cord that function to coordinate the activity of all parts of the body. *page 6*

cerebrospinal fluid A clear, colourless fluid that contains small quantities of glucose and protein. Cerebrospinal fluid fills the ventricles of the brain, the central canal of the spinal cord, and occupies the subarachnoid space that surrounds both the brain and spinal cord. *page 7*

cervical Pertaining to the neck or to the neck of any organ or structure. *page 6*

Chiari I A Chiari malformation characterized by hindbrain tonsilar herniation but with no associated brainstem herniation or supratentorial anomalies. Commonly occurs with syringomyelia but not hydrocephalus. *page 13*

Chiari II A Chiari malformation characterized by herniation of the cerebellum, brainstem and fourth ventricle through the foramen magnum. Almost always associated with myelomeningocele and multiple brain anomalies, and commonly with syringomyelia and hydrocephalus. *page 13*

Chiari malformation This disorder involves distortion of the base of the skull with protrusion of the lower brainstem and parts of the cerebellum through the opening (foramen magnum) for the spinal cord at the base of the skull. The hindbrain effectively forms a tonsil of sorts which partially blocks the upper spinal subarachnoid space thereby interrupting normal cerebrospinal fluid flow. *page 13*

choroid plexus Convoluted strands of vascularised tissue, which constitute the source of cerebrospinal fluid. *page 8*

cine-MRI Dynamic variant of MRI in which a series of scans are retrospectively fitted to a cardiac time signal to produce a cinematic display of CSF movement. *page 12*

cisterna magna One of the three reservoirs in the subarachnoid space, located between the cerebellum and the medulla oblongata. The other two cisterns are the pontine cistern and the interpeduncular cistern. *page 8*

coccygeal Relating to the coccyx. *page 6*

coccyx The last bone of the spinal column just below the sacrum, often called the tailbone. *page 214*

cohort A group of people who share a common characteristic or experience within a defined period. *page 19*

communicating syringomyelia Refers to the condition in which the spinal syrinx is continuous with the fourth ventricle of the brain. Typically the syrinx is a dilatation of the central canal and the connecting passageway is a patent obex. See also syringomyelia. *page 13*

craniocervical junction The articulation of the skull on the top of the spine, and also often denotes the tissue structures surrounding this joint. *page 8*

CSF *cerebrospinal fluid* *page 214*

cyst An abnormal sac or closed cavity lined with epithelium and filled with liquid or semisolid matter. *page 23*

D

decompression A surgical procedure performed to alleviate the compression of soft tissues brought about by abnormal soft tissue growth or insufficient space due to a malformed bony compartment. In the case of a Chiari malformation the procedure involves removing a piece of the base of the skull and enlarging the dural sheath so as to decompress the hindbrain, thereby unblocking the fluid passage between the head and the spinal canal. *page 14*

diastematomyelia A congenital condition that involves splitting of the spinal cord in the longitudinal direction. *page 12*

diastole The phase of the heartbeat when the heart muscle relaxes and allows the chambers to fill with blood; *cf* systole. *page 34*

disc disease Dehydration of the intervertebral discs reducing their shock-absorbing capacity. *page 12*

dura mater The outermost, toughest and most fibrous of the three membranes (meninges) covering the brain and spinal cord. *page 7*

dysraphism The incomplete fusion of vertebral arches. *page 17*

E

ECF *extracellular fluid page 214*

ependyma The thin (epithelial) membrane lining the CSF-filled ventricles in the brain and the central canal in the spinal cord. *page 17*

epidural space The space between the dura mater and the walls of the vertebral canal, contains fat and blood vessels (mainly veins). *page 7*

extra-canalicular syrinx A syrinx located in the spinal cord parenchyma; i.e., not located in the central canal. *page 47*

extracellular fluid A general term for all the body fluids outside the cells, which can be further subdivided into interstitial fluid and intravascular fluid. *page 9*

extracellular space The space outside the cell, collectively this is usually taken to be the fluid-filled space outside the plasma membranes but does not include the noncellular blood volume. *page 9*

exudate Material including pus, fluid and cells that has slowly escaped from intact blood vessels and has been deposited in tissue, often as a result of inflammation. *page 28*

F

filum terminale A long, slender connective tissue (pia mater) strand extending from the extremity of the medullary cone to the internal aspect of the spinal dural sac (filum terminale internum); stout strands of connective tissue attaching the spinal dural sac to the coccyx (filum terminale externum), commonly called the coccygeal ligament. *page 7*

foramen A small opening, perforation, or orifice. Plural: foraminae. *page 13*

foramen magnum The largest hole in the base of the skull through which the spinal cord passes. *page 13*

foramen of Magendie The midline opening of the fourth ventricle of the brain that, together with the foraminae of Luschka, allows exchange of CSF with the subarachnoid space. *page 14*

foraminae of Luschka The two lateral openings of the fourth ventricle of the brain that, together with the foramen of Magendie, allows exchange of CSF with the subarachnoid space *page 14*

forebrain The brain proper, continuous below with the midbrain and the largest component of the central nervous system. *page 6*

fourth ventricle A shallow cavity with a tent-like shape within the brain stem, communicating with the central canal caudally and the cerebral aqueduct rostrally. *page 8*

FT *filum terminale* *page 214*

G

glia Supportive cells of the nervous system which do not conduct eletrical impulses. *page 17*

gliosis A proliferation of glia in damaged areas of the central nervous system that usually leads to the formation of scar tissue. *page 18*

grey matter The component of the central nervous system containing nerve cell bodies, named for its colour. Grey matter is distributed at the surface of the brain and through the central core of the spinal cord. *cf* white matter. *page 7*

H

haematoma A localised collection of blood, usually clotted, in an organ, space or tissue, due to a break in the wall of a blood vessel. More commonly called a blood clot. *page 22*

haemorrhage The escape of blood from the vessels, bleeding. *page 23*

hindbrain The part of the brain comprising the cerebellum, pons and medulla oblongata; continuous above with the midbrain and below with the spinal cord. *page 6*

hindbrain tonsil A rounded lobule on the undersurface of each cerebellar hemisphere, continuous medially with the uvula of the cerebellar vermis. *page 13*

histology The study of the microscopic anatomy of cells and tissues. *page 18*

hydrocephalus A condition marked by dilatation of the cerebral ventricles, most often occurring secondarily to obstruction of the CSF pathways and accompanied by an accumulation of CSF within the skull at elevated pressure. *page 17*

hydromyelia See communicating syringomyelia. *page 13*

I

ICP *intracranial pressure page 214*

interstitial fluid The fluid residing in the spaces between cells (interstices), including the fluid in the perivascular spaces. *page 9*

intracranial pressure The pressure within the skull and thus in the brain tissue and intraventricular CSF. *page 32*

intravascular fluid See blood plasma. *page 9*

ischaemia An inadequate blood supply to a part of the body, caused by constriction or blockage of the blood vessels supplying it. *page 19*

ISF *interstitial fluid page 214*

K

kyphosis Excessive forward curvature of the spine (hump-backed). *page 12*

L

lateral ventricle A horseshoe-shaped chamber, the pair of which are located within the cerebral hemispheres of the brain. They are continuous below with the interventricular foramen. *page 8*

lesion A zone of tissue with impaired function as a result of damage by disease or wounding. *page 22*

ligature A cord or thread that is tied around a blood vessel to slow or stop it from bleeding. *page 20*

lumbar Pertaining to the loins, the part of the back between the thorax and the pelvis. *page 6*

lumbar cistern The enlargement of the subarachnoid space between the conical end of the spinal cord and the lower extent of the filum terminale, occupied by the cauda equina and CSF; site for lumbar puncture. *page 8*

lymphatic system A network of conduits that carry a clear fluid called lymph, the confirmed functions of which include the removal of interstitial fluid from tissues and the transport of fatty acids and fats to the circulatory system. *page 8*

M

magnetic resonance imaging A diagnostic imaging technique based on the detection of electromagnetic waves when the patient is exposed to radiofrequency radiation. *page 12*

medulla See spinal cord. *page 12*

meninges The membranes surrounding the brain and spinal cord. There are three layers: the dura mater (outer), arachnoid mater (middle) and the pia mater (inner layer). *page 7*

meningitis Inflammation of the meninges. When it affects the dura mater, the disease is termed pachymeningitis, when the arachnoid and pia mater are involved, it is

called leptomeningitis or meningitis proper. *page 19*

meningocele A protrusion of the meninges through a gap in the spine due to a congenital defect. *page 32*

midbrain The part of the central nervous system between the forebrain and the hindbrain. The cerebral aqueduct runs through the midbrain, connecting the the third and fourth ventricle. *page 6*

MRI *magnetic resonance imaging page 214*

myelography A specialised method of X-ray examination to demonstrate the spinal canal that involves injection of a contrast medium into the subarachnoid space by lumbar puncture. *page 30*

myelomalacia Softening of the tissues of the spinal cord, most often caused by an impaired blood supply. *page 20*

myelopathy Any disease affecting the spinal cord. *page 30*

N

necrosis The death of some or all of the cells in an organ or tissue caused by disease, injury or interference with the blood supply. *page 20*

neoplasm See tumour. *page 18*

noncommunicating syringomyelia Refers to the condition in which the spinal syrinx has no direct connection with the fourth ventricle of the brain. Suchsyrinxes are often extra-canalicular in location. See also syringomyelia. *page 13*

O

obex The narrow passage connecting the fourth ventricle with the central canal. *page 8*

oedema A condition characterised by an excess of watery fluid collecting in the cavities or tissues of the body. *page 35*

osmosis The movement of water through a semi-permeable membrane, from a region of low solute concentration to one of high concentration. This tends to equalise the concentration on either side of the membrane. *page 36*

P

parenchyma The functional tissue of an organ as distinguished from the connective and supporting tissue. In the brain and spinal cord this is the grey and white matter, as opposed to the meninges. *page 7*

pathogenesis The study of the cause and process of evolution of a disease. *page 6*

peristalsis The propulsion of fluid or solid through a tube by waves of rhythmic contractions; e.g., food in the intestine or possibly CSF in the perivascular spaces. *page 48*

perivascular space The space that lies between the blood vessels and the pia mater that is filled with ISF. *page 9*

pia mater The delicate and highly vascular membrane immediately investing the brain and spinal cord. *page 7*

posterior Of or nearer the rear or hind end. The opposite of anterior. *page 12*

posterior fossa The lower part of the cranial cavity that houses the brainstem and cerrebellum. *page 12*

proprioception The spatial awareness of body position, achieved via inputs from stretch receptors detecting joint positions. *page 4*

PVS *perivascular space(s) page 214*

Q

Queckenstedt test A now-outdated clinical test used for diagnosing blockages of the spinal subarachnoid space. With the patient lying on one side, a lumbar puncture is performed and the quiescent spinal CSF pressure is measured using a column manometer. Next, an assistant compresses the jugular veins, which raises the intracranial pressure. In a healthy person this causes an increase in the pressure of the spinal fluid in the lumbar region within 10 to 12 seconds, and an equally rapid fall to normal on release of the pressure on the vein; when there is a block of the subarachnoid channels, compression of the vein causes little or no increase of pressure in the CSF. *page 30*

R

rhombencephalon See hindbrain. *page 12*

rostral Denoting a position more toward the rostrum or head, than some specified point of reference. The same as superior, in human anatomy. *page 47*

rostrocaudal axis The imaginery line passing from the head to the tail, encompassing the longitudinal axis of the spinal cord. *page 41*

S

sacral Of or pertaining to the sacrum; in the region of the sacrum. *page 6*

sacrum The triangular-shaped bone lying between the 5th lumbar vertebra and the coccyx. It consists of 5 vertebrae fused together and it articulates on each side with the bones of the pelvis (ilium), forming the sacroiliac joints. *page 214*

SC *spinal cord page 214*

scoliosis Sideward curvature of the spine. *page 12*

spina bifida A congenital disorder in which one or more of the bones of the spine do not develop properly, often leaving a portion of the spinal cord exposed. *page 12*

spinal artery One of the three vessels supplying blood to the spinal cord; there are two posterior and one anterior spinal arteries, all of which descend the length of the cord and are adherent to its outer surface. *page 20*

spinal block See spinal stenosis. *page 214*

spinal canal The canal that contains the spinal cord, spinal meninges and related structures. It is formed by the vertebral foramina of successive vertebrae of the articulated vertebral column. *page 13*

spinal cord The portion of the central nervous system enclosed in the vertebral column, consisting of nerve cells and bundles of nerves connecting all parts of the body with the brain. *page 4*

spinal stenosis Blockage of the spinal subarachnoid space inhibiting/preventing CSF flow. *page 12*

SSS *spinal subarachnoid space page 214*

subarachnoid space The space between the arachnoid and pia mater, traversed by delicate fibrous trabeculae and filled with CSF. The large blood vessels supplying the brain and spinal cord lie in the subarachnoid space. *page 7*

subdural space Originally thought to be a narrow fluid-filled interval between the dural and arachnoid; now known to be an artificial space created by the separation of the arachnoid from the dura as the result of trauma or some ongoing pathological process; in the healthy state, the arachnoid is attached to the dura and a naturally occurring subdural space is not present. *page 7*

syringobulbia The term given to the condition of syrinx formation in the brainstem. See also syringomyelia. *page 13*

syringomyelia A disease in which longitudinal, fluid-filled cavities, often referred to as syrinxes, form and enlarge within the spinal cord. It most commonly occurs

in the cervical segments of the spinal cord but can involve the entire length of the cord and occasionally extends upwards to the brainstem. *page 4*

syrinx A fluid-filled cavity in the spinal cord, which may be closed (cyst) or have an open communication to a CSF compartment, such as the subarachnoid space. *page 4*

systole The phase of the heartbeat when the heart muscle contracts and pumps blood from the chambers into the arteries; *cf* diastole. *page 34*

T

tentorium cerebelli An extension of the cranial dura mater that forms the tent-like roof of the posterior fossa. *page 12*

tethered cord syndrome Abnormal tissue attachments that stretch and limit the movement of the spinal cord. *page 12*

thoracic Pertaining to or affecting the chest. *page 6*

transude To discharge through pores in a membrane. *page 23*

tumour Any new and abnormal growth, may be benign or malignant (cancerous). *page 18*

V

Valsalva manoeuvre Any attempted exhalation against a closed glottis or against a closed mouth and nose. For example, the closed-glottis manoeuvre is used when blowing up a balloon or during bowel movements, and the closed-mouth-and-nose variant is used as a pressure equalisation technique by scuba divers and airplane passengers to avoid barotrauma and ear discomfort when moving to a higher pressure breathing environment. *page 30*

ventricle A chamber or cavity. Specifically, the system of irregular cavities in the brain that contain cerebrospinal fluid; there are two lateral ventricles, the third

ventricle and the fourth ventricle. (Also the chambers of the heart that pump blood are ventricles.) *page 8*

vertebral canal See spinal canal. *page 6*

Virchow-Robin space See perivascular space. *page 9*

W

white matter Bundles of nerve fibres (axons) insulated by myelin, a white fatty substance, that connect different areas of gray matter within the central nervous system. *cf* grey matter. *page 7*

APPENDIX B

Solution and properties of the damped wave equation

B.1 General solution

The damped (or dissipative) wave equation is as follows,

$$\frac{\partial^2 u}{\partial t^2} - c^2 \frac{\partial^2 u}{\partial x^2} + \beta \frac{\partial u}{\partial t} = q(x,t); \quad u(x,0) = f(x), \quad \frac{\partial u}{\partial t}(x,0) = g(x). \tag{B.1}$$

Equation (B.1) is in fact a reduced version of the telegraph equation, which governs the propagation of signals on telegraph lines, as the $\mathrm{O}(u)$ term has been omitted.

By making the change of variables $u(x,t) = \exp(-\beta t/2)\, v(x,t)$ equation (B.1) reduces to

$$\frac{\partial^2 v}{\partial t^2} - c^2 \frac{\partial^2 v}{\partial x^2} - \left(\frac{\beta}{2}\right)^2 v = \exp\left(\frac{\beta t}{2}\right) q(x,t); \tag{B.2}$$

i.e. a Klein-Gordon equation[1]. The Cauchy problem for this related system is

$$\frac{\partial^2 v}{\partial t^2} - c^2 \frac{\partial^2 v}{\partial x^2} - \gamma^2 = q^*(x,t); \quad v(x,0) = f^*(x), \quad \frac{\partial v}{\partial t}(x,0) = g^*(x), \tag{B.3}$$

[1]The Klein-Gordon equation, in this case with the substitution $\hat{\gamma} = i\gamma$, is the relativistic version of the Schrödinger equation, which is used to describe the field behaviour of spinless particles in quantum mechanics.

with free-space Green's function given by

$$G^*(x,t;\xi,\tau) = \frac{1}{2c} I_0\Big[(\gamma/c)\sqrt{c^2(t-\tau)^2-(x-\xi)^2}\Big]\; H[c(t-\tau)-|x-\xi|], \tag{B.4}$$

and the general solution

$$\begin{aligned} v(x,t) \;=\; & \frac{1}{2}[f^*(x-ct)+f^*(x+ct)] \\ & + \frac{\gamma t}{2}\int_{x-ct}^{x+ct} \frac{I_1\Big[(\gamma/c)\sqrt{c^2t^2-(x-\xi)^2}\Big]}{\sqrt{c^2t^2-(x-\xi)^2}} f^*(\xi)\,d\xi \\ & + \frac{1}{2c}\int_{x-ct}^{x+ct} I_0\Big[(\gamma/c)\sqrt{c^2t^2-(x-\xi)^2}\Big]\, g^*(\xi)\,d\xi \\ & + \frac{1}{2c}\int_0^t\int_{x-c(t-\tau)}^{x+c(t-\tau)} I_0\Big[(\gamma/c)\sqrt{c^2(t-\tau)^2-(x-\xi)^2}\Big]\, q^*(\xi,\tau)\,d\xi\,d\tau, \end{aligned} \tag{B.5}$$

where $H(x)$ is the Heaviside step function and $I_n(x)$ are nth-order modified Bessel functions of the first kind.

Making use of this result one may obtain the free-space Green's function for (B.1)

$$\begin{aligned} G(x,t;\xi,\tau) \;=\; & \frac{1}{2c}\exp\left[-\frac{\beta(t-\tau)}{2}\right] \\ & I_0\Big[(\beta/c)\sqrt{c^2(t-\tau)^2-(x-\xi)^2}\Big]\; H[c(t-\tau)-|x-\xi|] \end{aligned} \tag{B.6}$$

and, noting that $f^*(x) = f(x)$ and $g^*(x) = \frac{\beta}{2}f(x) + g(x)$, the corresponding general

solution takes the form

$$\begin{aligned} u(x,t) &= \frac{1}{2}\exp\left(-\frac{\beta t}{2}\right)\left[f(x-ct)+f(x+ct)\right] \\ &\quad +\frac{\beta t}{4}\exp\left(-\frac{\beta t}{2}\right)\int_{x-ct}^{x+ct}\frac{I_1\left[(\beta/2c)\sqrt{c^2t^2-(x-\xi)^2}\right]}{\sqrt{c^2t^2-(x-\xi)^2}}f(\xi)\,d\xi \\ &\quad +\frac{1}{2c}\exp\left(-\frac{\beta t}{2}\right)\int_{x-ct}^{x+ct} I_0\left[(\beta/2c)\sqrt{c^2t^2-(x-\xi)^2}\right]\left[\frac{\beta}{2}f(\xi)+g(\xi)\right]d\xi \\ &\quad +\frac{1}{2c}\int_0^t\int_{x-c(t-\tau)}^{x+c(t-\tau)}\exp\left[-\frac{\beta(t-\tau)}{2}\right] \\ &\qquad\qquad I_0\left[(\beta/2c)\sqrt{c^2(t-\tau)^2-(x-\xi)^2}\right]q(\xi,\tau)\,d\xi\,d\tau. \end{aligned} \tag{B.7}$$

For further details the interested reader is referred to Polyanin (2002) and Zauderer (2006; pp. 464–470).

B.2 Multiscale analysis

Let $c=\beta=1$ so that the differential operator becomes

$$L=\frac{\partial^2}{\partial t^2}-\frac{\partial^2}{\partial x^2}+\frac{\partial}{\partial t}. \tag{B.8}$$

We introduce a scaled set of time and length variables

$$\tau=\frac{t}{\varepsilon^m} \qquad \text{and} \qquad \chi=\frac{x}{\varepsilon^n} \tag{B.9}$$

where $\varepsilon \ll 1$ and $m,n\in\Re$. If $m,n>0$ then (τ,χ) represent small time and length scales; likewise large scales correspond to $m,n<0$, respectively. Applying the chain

rule:

$$\frac{\partial}{\partial t} = \frac{\partial \tau}{\partial t}\frac{\partial}{\partial \tau} = \frac{1}{\varepsilon^m}\frac{\partial}{\partial \tau}, \tag{B.10a}$$

$$\frac{\partial^2}{\partial t^2} = \frac{\partial}{\partial t}\left\{\frac{1}{\varepsilon^m}\frac{\partial}{\partial \tau}\right\} = \frac{1}{\varepsilon^{2m}}\frac{\partial^2}{\partial \tau^2}, \tag{B.10b}$$

$$\frac{\partial^2}{\partial x^2} = \frac{1}{\varepsilon^{2n}}\frac{\partial^2}{\partial \chi^2}; \tag{B.10c}$$

the differential operator becomes

$$L = \frac{1}{\varepsilon^{2m}}\frac{\partial^2}{\partial \tau^2} - \frac{1}{\varepsilon^{2n}}\frac{\partial^2}{\partial \chi^2} + \frac{1}{\varepsilon^m}\frac{\partial}{\partial \tau}. \tag{B.11}$$

The system L will behave as a classic wave equation — undamped — if the coefficients of the first two terms are of the same order, and if the coefficient of the third term is small by comparison. Therefore

$$\frac{\varepsilon^{-2m}}{\varepsilon^{-2n}} = 1 \implies m = n, \tag{B.12a}$$

$$\frac{\varepsilon^{-m}}{\varepsilon^{-2m}} = \varepsilon^p,\ p > 0 \implies n = p, \tag{B.12b}$$

and $m = n > 0$. Thus wave behaviour dominates at short time and length scales. Damping comes into effect when all three terms of L are of equal order:

$$\frac{\varepsilon^{-2m}}{\varepsilon^{-2n}} = 1 \implies m = n, \tag{B.13a}$$

$$\frac{\varepsilon^{-m}}{\varepsilon^{-2m}} = 1 \implies m = 0, \tag{B.13b}$$

and $m = n = 0$. Thus wave propagation and dissipation compete on equal terms at intermediate time and length scales, with L describing the damped wave equation. Finally, damping will overwhelm the system when the coefficients of terms two and

Table B.1: Order of magnitude of terms in the damped wave equation; $\varepsilon \ll 1$ and $m > 0$.

t	x	x/t	u_{tt}	u_{xx}	u_t	behaviour
ε^m	ε^m	1	1	1	ε^m	wave
1	1	1	1	1	1	dissipative wave
ε^{-m}	$\varepsilon^{-m/2}$	$\varepsilon^{m/2}$	ε^m	1	1	diffusion

three are of equal order and greater than that of the first term. That is,

$$\frac{\varepsilon^{-2n}}{\varepsilon^{-m}} = 1 \quad \Longrightarrow \quad m = 2n, \tag{B.14a}$$

$$\frac{\varepsilon^{-2m}}{\varepsilon^{-m}} = \varepsilon^p, \; p > 0 \quad \Longrightarrow \quad m = -p, \tag{B.14b}$$

and $m = 2n = -2p$. Thus the system reduces to pure diffusion at large length and even larger time scales.

The behaviour of the damped wave equation is summarised in Table B.1. One could also solve the damped wave equation using asymptotic methods, the possible benefit being an explicit analytical solution, but the scale-dependent behaviour demonstrated above demands that one of the more specialised approaches based on singular perturbation theory be applied [e.g., Hinch (1991; Ch. 7); Awrejcewicz & Krysko (2006; Ch. 3)].

APPENDIX C

Derivation of the Biot equations

By substituting the solution (4.6a,b) into the curl of equations (4.1a,b), and eliminating constants C_1 and C_2, one obtains $Nl^2/\rho\alpha^2 = E_\mathrm{r} - iE_\mathrm{i}$, with

$$E_\mathrm{r} = \frac{1+\gamma_{22}\frac{(\gamma_{11}\gamma_{22}-\gamma_{12}^2)}{(\gamma_{12}+\gamma_{22})^2}\left(\frac{f}{f_\mathrm{c}}\right)^2}{1+\left(\frac{\gamma_{22}}{\gamma_{12}+\gamma_{22}}\right)^2\left(\frac{f}{f_\mathrm{c}}\right)^2}, \tag{C.1a}$$

$$E_\mathrm{i} = \frac{(\gamma_{12}+\gamma_{22})}{1+\left(\frac{\gamma_{22}}{\gamma_{12}+\gamma_{22}}\right)^2\left(\frac{f}{f_\mathrm{c}}\right)^2}\left(\frac{f}{f_\mathrm{c}}\right), \tag{C.1b}$$

and

$$\gamma_{11} = \frac{\rho_{11}}{\rho}, \tag{C.2a}$$

$$\gamma_{22} = \frac{\rho_{22}}{\rho}, \tag{C.2b}$$

$$\gamma_{12} = \frac{(1-\gamma_{11}-\gamma_{22})}{2}. \tag{C.2c}$$

The nondimensional phase speed and attenuation coefficient of shear waves are then

$$\frac{v_\mathrm{r}}{V_\mathrm{r}} = \frac{\sqrt{2}}{\left[(E_\mathrm{r}^2+E_\mathrm{i}^2)^{1/2}+E_\mathrm{r}\right]^{1/2}}, \tag{C.3a}$$

$$\frac{L_\mathrm{r}}{x_\mathrm{a}} = \frac{\left[(E_\mathrm{r}^2+E_\mathrm{i}^2)^{1/2}-E_\mathrm{r}\right]^{1/2}}{\sqrt{2}}\left(\frac{f}{f_\mathrm{c}}\right). \tag{C.3b}$$

Similarly, by substituting the solution (4.9a,b) into the divergence of equations

(4.1a,b), and eliminating constants C_3 and C_4, one obtains the complex quadratic

$$(z - z_1)(z - z_2) + iM(z - 1) = 0 \tag{C.4}$$

for the nondimensional variable $z = V_c^2 l^2/\alpha^2$; M is given by

$$M = \frac{b}{\alpha\rho(\sigma_{11}\sigma_{22} - \sigma_{12}^2)}, \tag{C.5}$$

the elastic parameters are defined as

$$\sigma_{11} = \frac{P}{H}, \tag{C.6a}$$

$$\sigma_{22} = \frac{R}{H}, \tag{C.6b}$$

$$\sigma_{12} = \frac{(1 - \sigma_{11} - \sigma_{22})}{2}, \tag{C.6c}$$

and z_1 and z_2 are the complex roots of

$$(\sigma_{11}\sigma_{22} - \sigma_{12}^2)z^2 - (\sigma_{11}\gamma_{22} + \sigma_{22}\gamma_{11} - 2\sigma_{12}\gamma_{12})z + (\gamma_{11}\gamma_{22} - \gamma_{12}^2) = 0. \tag{C.7}$$

The complex pair of roots of (C.4) are designated z_{I} and z_{II}, from which we define

$$(z_{\mathrm{I}})^{1/2} = \mathcal{R}_{\mathrm{I}} + i\mathcal{T}_{\mathrm{I}} \quad \text{and} \quad (z_{\mathrm{II}})^{1/2} = \mathcal{R}_{\mathrm{II}} + i\mathcal{T}_{\mathrm{II}}. \tag{C.8a,b}$$

Finally, the nondimensional phase speed and attenuation coefficient are given for the first dilatational wave

$$\frac{v_{\mathrm{I}}}{V_c} = \frac{1}{|\mathcal{R}_{\mathrm{I}}|}, \tag{C.9a}$$

$$\frac{L_c}{x_{\mathrm{I}}} = |\mathcal{T}_{\mathrm{I}}| \left(\frac{f}{f_c}\right), \tag{C.9b}$$

and the second dilatational wave

$$\frac{v_{\mathrm{II}}}{V_{\mathrm{c}}} = \frac{1}{|\mathcal{R}_{\mathrm{II}}|}, \tag{C.10a}$$

$$\frac{L_{\mathrm{c}}}{x_{\mathrm{II}}} = |\mathcal{T}_{\mathrm{II}}| \left(\frac{f}{f_{\mathrm{c}}} \right). \tag{C.10b}$$

For a full derivation of the above equations see Biot (1956b).

To compute the terms (C.3a,b), (C.9a,b) and (C.10a,b) the equations (C.4) and (C.7) were solved using the MultRoot package (Zeng, 2003) for MATLAB. To validate the computational code the curves from Figures 1–6 of Biot (1956b) were reproduced from the given parameter values therein (Biot, 1956b; Table 1), and plotted on digitized versions of the original figures; all computed curves matched the originals.